Università degli Studi di Torino
Doctoral School of Sciences and Innovative Technologies
PhD Program in Chemical and Material Sciences XXX Cycle

Tailoring the surface properties of TiO_2: shape controlled nanoparticles for the optimization of functional properties

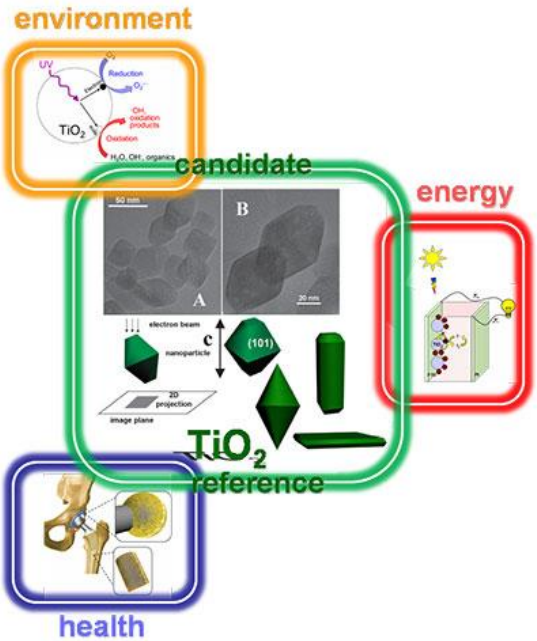

Francesco Pellegrino

Supervisor:
Prof. Valter Maurino

Università degli Studi di Torino

Doctoral School of Sciences and Innovative Technologies

PhD Programme in Chemical and Materials Sciences XXX cycle

Tailoring the surface properties of TiO_2: shape controlled nanoparticles for the optimization of functional properties

Candidate: **Francesco Pellegrino**

Supervisor: Prof. **Valter Maurino**

Jury Members: Prof. **Giuseppe Spoto**
Università degli Studi di Torino
Dipartimento di Chimica

Prof. **Barbara Bonelli**
Politecnico di Torino
Dipartimento di Scienza Applicata e Tecnologia

Dr. **Massimiliano D'Arienzo**
Università degli Studi di Milano - Bicocca
Dipartimento di Scienze dei Materiali

Head of the Doctoral School: Prof. Massimo Maffei
PhD Programme Coordinator: Prof. Mario Chiesa

Torino, 2017

Contents

Preface

Environmental pollution caused by human activities is posing serious problems for the protection of the environment and the protection of human health; the most important environmental receptors are surface and groundwater bodies as well as air, because they are the primary sources of contact for humans with numerous classes of pollutants. The general categories of contaminants include solvents, volatile organic compounds (VOCs), volatile chlorinated organic compounds, dioxins, dibenzofurans, pesticides, PCBs, asbestos, heavy metals, arsenic compounds, etc. It is therefore urgent to develop new advanced methods of detoxification that can treat non-biodegradable compounds that result in the total destruction of the pollutants.

Metal oxides are valid materials for their versatility and functional properties that can be exploited in several fields of application. Metals are able to generate a lot of different oxides compounds, and the different structures and electronic properties of these materials can lead to insulator, semiconductor or conductor character. These different characteristichs can be exploited in many technological applications such as the fabrication of fuel cells, microelectronic circuits, sensors, coatings against corrosion and, of course, catalysts.

The need of an energy saving, together with an ever-higher environmental consciousness, led to enhanced interest in the miniaturization of the technologies with a consequent more and more higher interest for nanomaterials and nanotechnologies. Metal oxide nanomaterials are among the most studied nanomaterials. The peculiar properties of these materials,

due to their limited dimensions, opened an extensive research field in the synthesis and characterization of nano-metal oxides. Indeed, the sizes can affect the metal oxides functional properties and, the control of the size could lead to an optimization of the energetic efficiency rather than an improvement of the catalytic performances, etc. The effect of the decreasing are structural distortions associated with changes in cell parameters, the production of stress, defects and perturbations on structure of the nanomaterials. The electronic properties themselves can change due to the size reduction, manifesting in quantum confinement effect, modifications on the band gap of semiconductor and/or the optimization of the ratio between the interfacial transfer and the recombination of electrons and holes in the case of photoactive materials. Moreover, as small are the dimensions, as high become the importance of the surfaces. Shape can be modified in order to synthetized nanoparticles with defined surfaces using specific capping agent able to change the free energies of different facets. Again, different surfaces have different characteristics, which could have an impact in many applications of these nanomaterials. Among metal oxides, TiO_2 have a central role due to his multifaceted that allows an extended applicability in several scientific and technological fields. TiO_2 nanoparticles were deeply investigated in the last decades, studying the correlation between the morphological and functional properties of this semiconductor.

In Chapter 1 a general introduction on the TiO_2 main characteristics and properties are reported, with an overview of the physical properties of TiO_2, his applications and the light-driven processes that occur in the nanoparticles under a properly irradiation. Chapter 2 is dedicated to the

synthetic methodologies of TiO_2 nanoparticles. In the first paragraph a brief view on the main synthetic methods. The second paragraph is devoted to a general description of the surfaces exposed by TiO_2 and the state of the art on the synthesis of shape-controlled nanoparticles. Moving to the experimental section, in Chapter 3 are described the synthetic procedures carried out to obtain shape controlled nanoparticles and all the characterization done on the nanoparticles. Finally, in Chapter 4 are shown the results of the photocatalytic tests performed on selected synthetic TiO_2 nanoparticles and then, in the last pages, the conclusions of the entire work are summarized.

Introductory Section

Chapter 1

1.1. Titanium Dioxide – TiO_2

Titanium dioxide (TiO_2, titania) is one of the most studied semiconductor oxides due to potential multisectorial applications of TiO_2 NPs[1] in several technological fields, including energy, healthcare/medical, engineering and consumer goods domains[2]. The awareness of emerging needs and challenges in strategic sectors for humanity, like energy production and employment, sustainable development, healthcare systems, is increasing a new and renewed interest towards the possibility to use TiO_2, and in special way systems based on nano-TiO_2, to attain real and efficient innovation.

The commercial production of TiO_2 grew during the twentieth century in order to meet the world's need in several applications like pigments, toothpaste and sunscreens. Fujishima and Honda gave a new impulse to research after the discovery of the photocatalytic water splitting on TiO_2 electrodes in 1972[3]. Moreover, the increasing of energetic demand and environmental pollution result in new applications for TiO_2 like heterogeneous photocatalysis (for the clean-up of environmental compartments exploiting the sunlight throughout the so-called Advanced Oxidation Processes (AOP)) and electrical energy production with the Dye Sensitized Solar Cell, which exploits the coupling of a dye with a TiO_2 nanoparticles film for producing energy. Nevertheless, TiO_2 nanoparticles are exploited for the production of smart materials with super-hydrophilic or super-hydrophobic surfaces or coatings for human bone implants.

The pioneering works of Fujishima and Honda[3] and O'Regan and Graetzel[4] have highlighted the role of TiO_2 as a key material for the exploitation of sunlight irradiation in a crucial sector such as the energetic one. Furthermore, the interaction with "light" enables the use of TiO_2 as photocatalyst for the abatement of air and water pollutants[5].

Titanium (and titanium alloys) are among the few metals in which the oxidized surface can support osseointegration, which can be (and positively) affected significantly by the nanostructuration of the surface oxidic layer[6]. Improvement of the effectiveness of healthcare treatments, indeed the development of implants or restoration materials with a better prognosis, a longer durability and with less failures is achievable only with a good understanding of TiO_2 surface properties[7].

These inputs are resulting in a flourish of both fundamental and technological studies devoted to TiO_2, with in a consequent increase in reports dealing with new functional behaviors and improved performances. However, it can be difficult to attain an objective and comprehensive evaluation of the impact of the proposed novelties, due to the wide heterogeneity of measurement conditions of the functional performances of these systems and of the material used. An example of such difficulties occurs in the field of heterogeneous photocatalysis, where an emerging issue was the establishment of true photocatalytic normalized tests to prove the real catalytic activity of the materials[8]. Furthermore, the possibility to perform a critical assessment of properties and performances of nanomaterials and derived nanosystems is among the basic requirements for an effective knowledge transfer from the nanoscience to a nanotechnological expertise, scalable at industrial level.

1.1.1. Physical and Chemical Properties

Titanium dioxide presents as mineral under three distinct allotropic forms: rutile, anatase and brookite. The three polymorphs have a TiO_6^{2-} distorted octahedral structure. The three forms differ both for the structure distortion extent and for the type of elementary cell in which these structures are organized. Anatase and rutile have a tetragonal cell (Anatase: a = b = 4,584 Å ec = 2,953 Å; Rutile: a = b = 3,782 Å ec = 9,502 Å), brookite has an orthorhombic cell (a = 5,436 Å = b = 9.166 Å; c = 5.135 Å). Figure 1 shows the tetragonal cells of rutile and anatase and the respective representation of the crystalline structures.

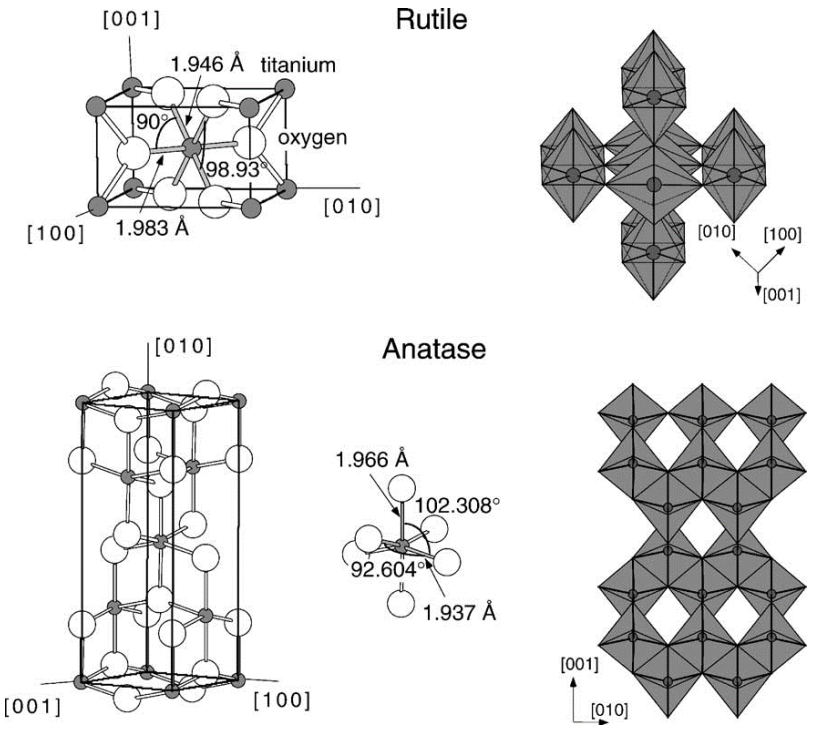

Figure 1. Rutile and anatase tetragonal cells and crystalline structures [9]

The more stable phase of titanium dioxide is rutile, but anatase although less stable is kinetically very stable, so its transformation to rutile at room temperature is negligible. Only reaching temperatures above 873K the processing rate becomes appreciable[10]. This represents the limit temperature, above which the phase transformation from anatase to rutile occurs[11,12]. Moreover, this transition is strongly influenced by particle size, pressure and concentration of surface and bulk defects.

From a chemical point of view, the acid-base properties of TiO_2 surfaces are of primary importance in determining the surface behavior. The most stable (not reconstructed) surfaces of rutile (100) and anatase (101) contain penta-coordinated titanium atoms that are able to adsorb water in both dissociated and non-dissociated form. The most important surface groups are therefore surface hydroxides, which are involved in two base acid equilibria:

$$\equiv TiOH_2^+ \overset{pK_1}{\Longleftrightarrow} \equiv TiOH \overset{pK_2}{\Longleftrightarrow} \equiv TiO^-$$

Therefore, when TiO_2 is in contact with an aqueous solvent, its surface may be positively or negatively charged depending on pH of the aqueous solution. Hydroxide ions establish an interaction with Ti^{4+} atoms that are Lewis acids, while protons interact with sites that act as Lewis bases, i.e. O^{2-} atoms (Figure 2). And they are the most important potential determining ions.

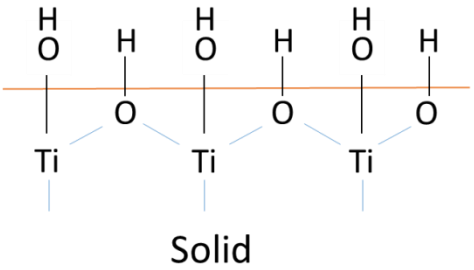

Figure 2. Surface of TiO_2 crystal

The study of the surface characteristics is fundamental, especially in photocatalysis where the surface properties influence the ions adsorption on the surface of the oxide which in turn change the surface electronic states.

A complete knowledge of all the TiO_2 surface aspects is still far from complete understanding, in particular for nanocrystals in which the presence of a wide heterogeneity of surface sites can play different roles on the surface reactivity. Moreover, surface roughness and edges imply the presence of defective sites that result in a different reactivity and behavior in the interaction with molecules. Finally, different crystallographic surfaces have different properties due to the different structures and surface electronic states; these properties imply a difference in the surface behavior in several applications.[9,11]

The possibility to study TiO_2 nanocrystals with a defined shape allows setting a relation among the functional properties of a TiO_2 nanoparticle and his shape. In turn the properties of TiO_2 NPs can be engineered for a given application.

1.2. Light Driven Processes on TiO_2 – A Brief Introduction

Figure 3 shows a scheme of the light driven processes that could take place on TiO_2 when a photon with energy greater than the band gap is absorbed and an electron–hole couple is generated (a). The charge carriers can then migrate towards the surface of the nanoparticles where they can be trapped and/or react with species at the surface (d) (e). Reactive Oxygen Species (ROS) can be generated, and the degradation of pollutants occurs. From the environmental point of view, this phenomenon can be very useful and effective, since the harmful pollutant is often decomposed to non-harmful inorganic compounds. Often though, photogenerated electrons and holes can undergo a mechanism of recombination in the bulk (b) or at the surface (c) of the nanoparticles. These recombinations decrease the photonic efficiencies of the TiO_2 nanoparticles and consequently the efficiency of the photocatalytic mechanism.

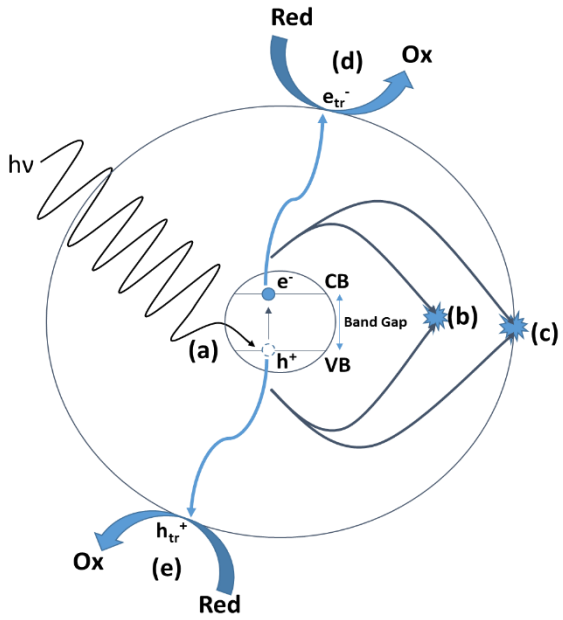

***Figure 3.** Processes occurringonTiO_2 under UV irradiation: (a) UV light absorption and electron-hole couple generation; (b) bulk recombination; (c) surface recombination; (d) electron migration to the surface, trapping and reaction with species in solution; (e) hole migration to the surface, trapping and reaction with species in solution.*

The commercial and industrial exploitation of technologies based on these photoeffects at TiO_2 NPs is indeed due to:[13,14]

- ✓ the light absorption is limited by the fact that TiO_2 is an indirect band gap semiconductor
- ✓ TiO_2 has a wide band gap (Figure 4), so the light absorption is limited only at the UV fraction of the solar spectrum
- ✓ TiO_2 has a quite high refractive index and light absorption is limited by light reflection at the surface of the crystal
- ✓ the efficiencies are limited by the high rate of the charge carriers recombination
- ✓ the morphological characteristics of the nanoparticles could affect the amount of the absorbed light like the crystallographic phase[9], the carrier mobility inside the crystal[15], the aggregation/agglomeration level[16], etc.

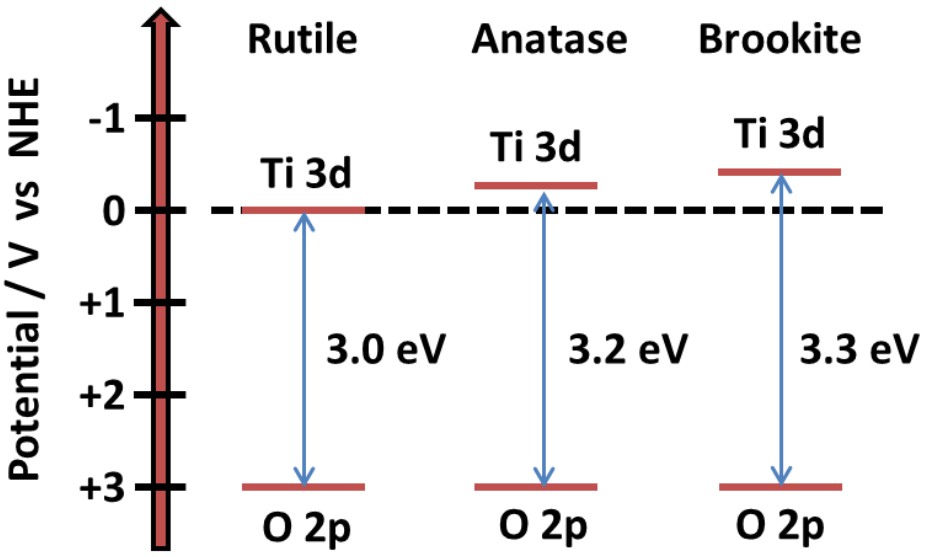

Figure 4. Band Gaps of the three different polymorphs of TiO_2 at pH = 0 [17]

In order to improve all aspects that limit the efficiency of the light driven processes on TiO_2, several solutions were proposed. For example, the TiO_2 doping with cations or anions can reduce the band gap of the semiconductor, extending the band gap absorption into the visible portion of the solar spectrum. Moreover, it is possible the coupling of the TiO_2 with organic dyes (like in the DSSC, Dye-Sensitized Solar Cell) or metals (Ag, Pd, Au, etc.) able to absorb light in the Vis range and then transfer the electrons to the TiO_2, favoring charge separation processes versus the recombination. Moreover, it is possible to act directly on the morphological characteristics of the TiO_2 crystals; it is known that anatase is the more active allotropic form due to his structure that allow a higher mobility of the charge carriers[15]. Other way are the control of the shape and of the size, that could minimize the electron-hole couple recombination, promoting the interfacial transfer of the charge carriers, and favor oxidative or reductive processes depending on which surface is most exposed[18].

1.3. The Photocatalytic Processes on TiO_2

The term "photocatalysis" refers to a catalyzed reaction that involves light adsorption by a catalyst in order to activate/accelerate the process itself. In this work the term "photocatalysis" will be used to identify all the processes activated on a semiconductor by the adsorption of a photon with energy higher than its band gap.[19]

The heterogeneous photocatalytic process is pretty complex, in order to rationalize the entire mechanism; we can split it in several single elementary steps that can take place in different space-time locations. I

order to optimize the process, a spatial and kinetic control of each single step is mandatory, with the final aim to avoid or at least minimize the recombination of the charge carriers generated at the beginning of the process. The first photochemical step is the absorption of a photon with $h\nu \geq E_g$ by the semiconductor particle, where E_g indicates the energy band gap (reaction 1.1). The absorption allows to generate an electron/hole couple (the so-called exciton, $e^-_b\ h^+_b$) which can dissociate to generate thermalized conduction band electron (e^-_{cb}) and valence band hole (h^+_{vb}) (reaction 1.2).[19]

Light Absorption

$$TiO_2 + h\nu \geq E_g \rightarrow e^-_b + h^+_b \qquad (1.1)$$

Thermalization of hot carriers

$$e^-_b \rightarrow e^-_{cb} \qquad h^+_b \rightarrow h^+_{vb} \qquad (1.2)$$

The thermalized carriers can either recombine in the bulk or migrate to the surface where they are trapped or can recombine. The main recombination processes are:

1) Radiative recombination, in which a photon is emitted with the wavelength corresponding to the energy released. Because the photon carries relatively little momentum, radiative recombination is significant only in direct band-gap materials (for indirect band semiconductor like TiO_2 is not allowed);
2) Defect mediated recombination in the bulk of the crystal, a non-radiative process described by the Shockley-Read-Hall mechanism. Briefly, the carrier in transition between the bands passes through a

localized state created within the band gap due to the presence of an impurity in the lattice (defects). The localized states can absorb differences in momentum between the carriers, and so this process is the dominant generation and recombination process in indirect bandgap materials;

3) Auger recombination, a non-radiative process in which an electron and a hole recombine in a band-to-band transition, but now the resulting energy is given off to another electron or hole instead of just emitting the energy as a photon. The newly excited electron then gives up its additional energy in a series of collisions with the lattice, relaxing back to the edge of the band. The process involves three particles and therefore scales with the third power of the carrier densities.

The classification of the different type of recombination is very important in this context because often, in heterogeneous photocatalysis, is hiring a priori that free charge carriers recombination happens through a second order process. The recombination mediated by the presence of defects that act like recombination centers, is often completely ignored.[19] In fact, some must be taken into account:

i) for recombination event mediated by a recombination center there are no restriction from momentum conservation and energy conservation laws. In fact, as reported by Serpone[20], band-to-band recombination requires the fulfillment of two conditions: (1) the conservation of energy, and (2) the conservation of momentum, both of which significantly decrease the efficiency of the band-to-band recombination process. The first condition is, in

the radiative process, easily respected by the emission of a photon with corresponding energy. Conversely, the momentum conservation law requires that the algebraic sum of two rather large values must be very small to be equal to the momentum of the photon. However, because the momentum of the photons is nearly zero in comparison to the momentum of free charge carriers, the possibility for recombination through the band-to-band pathway is restricted only to those electrons and holes that possess the same momentum. Therefore, the number of charge carriers having the same momentum will be very small.[20]

ii) In wide band gap semiconductor, like TiO_2, the overlap between the wave functions of the levels at the bottom of the conduction band and at the top of the valence band is low.

Migration to the surface

$$e^-_{cb} \rightarrow e^-_s \quad h^+_{vb} \rightarrow h^+_s \tag{1.3}$$

Surface charges trapping

$$e^-_s \rightarrow e^-_{tr} \ (e^-_s + \equiv Ti{-}OH \rightarrow \equiv Ti^{III} + OH^-) \tag{1.4}$$

$$h^+_s \rightarrow h^+_{tr} \ (h^+_s + \equiv Ti{-}OH \rightarrow \equiv Ti\text{-}O^{\bullet} + H^+) \tag{1.5}$$

Surface recombination

$$e^-_s + \equiv Ti\text{-}O^{\bullet} + H^+ \rightarrow \equiv Ti{-}OH \tag{1.6}$$

$$h^+_s + \equiv Ti^{III} + OH^- \rightarrow \equiv Ti{-}OH \tag{1.7}$$

The chemical nature of trapped charge carriers was deeply investigated. For example, Hoffmann and co-workers[21,22] carried out some laser flash photolysis measurements and they concluded that electrons present in the conduction band can be trapped in two different Ti^{III} sites:

$$e^-_{cb} + \equiv Ti^{IV}–OH \leftrightarrows \equiv Ti^{III}\text{-}OH \quad (1.8)$$

$$e^-_{cb} + \equiv Ti^{IV} \leftrightarrows \equiv Ti^{III} \quad (1.9)$$

where $\equiv Ti^{III} –OH$ is a surface trapped electron, while $\equiv Ti^{III}$ denoted a bulk or subsurface trapped electron.

The assignment of a well-defined chemical nature to the trapped holes is more difficult. Some works reported that the holes are trapped at the surface as weakly adsorbed hydroxyl radicals (reaction 1.10):

$$h^+_{vb} + Ti^{IV}\text{-}O^{2-}\text{-}Ti^{IV}\text{-}OH \rightarrow Ti^{IV}–O^{2-}\text{-}Ti^{IV}\text{-}OH\cdot \quad (1.10)$$

Others reported that the holes are trapped either in surface bridged oxygen anions (reaction 1.11) or in terminal hydroxyl groups (reaction 1.12).[23]

$$h^+_{vb} + Ti^{IV}\text{-}O^{2-}\text{-}Ti^{IV}\text{-}OH \rightarrow Ti^{IV}–O^{\cdot -}\text{-}Ti^{IV}\text{-}OH \quad (1.11)$$

$$h^+_{vb} + Ti^{IV}\text{-}O^{2-}\text{-}Ti^{IV}\text{-}OH \rightarrow Ti^{IV}–O^{2-}\text{-}Ti^{IV}\,{}^{\cdot}O + H^+ \quad (1.12)$$

Photogenerated charges, free or trapped at the surface, can then react with electron acceptors A (often is O_2) or electron donors D (e.g. an organic substrates, RH) absorbed or near the surface. The adsorbed species can also act as surface recombination centers, this process is defined Back Reaction, and can have relevant role in the decrease of the photocatalytic process efficiency.[19,24]

Donor reaction with free or trapped holes

$D + h^+ \rightarrow D^{\bullet+}$ (e.g. $\equiv Ti\text{-}O^{\bullet} + RH \rightarrow \equiv Ti\text{-}OH + R^{\bullet+}$) (1.13)

Donor back reaction (donor mediated recombination)

$D^{\bullet+} + e^- \rightarrow D$ (e.g. $\equiv Ti^{III} + R^{\bullet+} + H_2O \rightarrow \equiv Ti\text{-}OH + RH$) (1.14)

Acceptor reaction with free or trapped electrons

$A + e\text{-} \rightarrow A^{\bullet-}$ (e.g. $O_2 + e^- \rightarrow O_2^{\bullet-}$) (1.15)

Acceptor back reaction (acceptor mediated recombination)

$A^{\bullet-} + h^+ \rightarrow A$ (e.g. $O_2^{\bullet-} + \equiv Ti\text{-}O^{\bullet} + H^+ \rightarrow O_2 + \equiv Ti\text{-}OH$) (1.16)

Three different mechanisms of the interfacial charge transfer can be envisaged:

- *Inner sphere or Direct*: acceptors or donors form inner sphere complexes with surface groups and are located at Inner Helmholtz Plane (IHP). The efficiency of this charge transfer is usually high because the substrates are directly adsorbed to the photocatalyst surface in close proximity of the reagent (e_{cb}^- or h_{vb}^+);
- *Outer sphere or Indirect*: donor and/or acceptor substrates are located at the Outer Helmholtz Plane (OHP), in contact with the photocatalyst surface with their hydration shell. A substrate that reacts mainly through an outer sphere mechanism should conform to the Marcus-Gerisher theory of electron transfer[25-29] showing a quadratic dependence between the logarithm of apparent kinetic constant and the standard free energy of the process.

- *Mediated charge transfer*: the transfer of the charge carriers to the substrates is mediated by adsorbed reactive species generally formed by inner sphere electron or hole transfer to some adsorbates (mainly water). Those species, that are equivalent to surface holes or electrons traps, mediate the electron transfer to the substrates.

Clearly, a main transfer mechanism does not exclude the presence of the others.[19]

The radicals formed during the first steps of the photocatalytic process are further transformed by:

i) subsequent reactions with photogenerated active species ($O_2^{-\bullet}$, H_2O_2, $OH^{\bullet}$, $^1O_2$…) or with solvent;
ii) elimination of molecular groups/ions;
iii) dimerization.[30,31]

Donor-Acceptor radical ions reaction

$$A^{\cdot-} + D^{\cdot+} \rightarrow AD \qquad (1.17)$$

Dimerization

$$D^{\cdot+} + D^{\cdot+} \rightarrow D_2 \qquad (1.18)$$

$$A^{\cdot-} + A^{\cdot-} \rightarrow A_2 \qquad (1.19)$$

The photocatalytic process is formed from a complex network of elementary steps each having its own kinetic characteristics strictly dependent by the process variables (illumination intensity, intrinsic

surface properties, presence of adsorbates, the activity of surface potential determining ions (PDI), presence of bulk defects, etc…). In this respect, some complex kinetic models, with a good predictable capacity, were proposed [20,24,32-36], but the complexity of the system lead to an incomplete description of the phenomenon.[19]

In the primary step of the process, kinetics of degradations and products analysis reveal that several organic compounds directly react with e_{cb}^- either through inner sphere or through outer sphere mechanism. For example, 1,4-benzoquinone[37], tetrachlorometane[38], alomethanes[31,39], tetranitromethane[40] and several nitro aromatic compounds[41] follow a reductive pathway, with a direct electron transfer from the nanoparticles to the organic substrates. The direct hole transfer was also reported in many cases. The chloride ions seem to be directly oxidized by h^+_{vb}, the formed radical can then react with another chloride ion to give the radical anions $Cl_2^{\bullet -}$ able to oxidize organic substrate like phenol.[42] Direct hole transfer was also observed with dichloroacetate[43], quinoline[44], 2,4-dichlorophenoxyacetic acid[45], biphenyl derivatives[46], aromatic sulfides[47] and the dye X3B[48], presumably through an inner sphere mechanism. The direct electron transfer is, as outlined, a possible mechanism, but usually the main part of the photocatalyzed degradations happen via mediated oxidation.[19]

Hydroxyl Radical, OH·

Hydroxyl radical are probably the principal reactive species in photocatalysis. It can be present in two different forms: free in solution or bound to the surface as trapped hole. $OH^{\bullet}/OH^-$ has a standard redox

potential of 1.9 V vs NHE in homogeneous solution, potential that is estimated 1.6 V vs NHE when bound at the TiO_2 surface[40]. In each case, the hydroxyl radicals are strong oxidants, they are able to start the oxidative degradation of several organic substrates. The presence of free hydroxyl radicals in irradiated TiO_2 suspension was demonstrated by several ESR (Electronic Spin Resonance) spectroscopy experiments[49-53] and by the detection of the principal products of the photocatalytic degradation of organic substrates, which are usually hydroxylated. But, it should be noted that, from the latter evidences, the observation of hydroxylated products, may not lead to distinguish between a $OH^{\bullet}$ mediated vs direct hole injection mechanism, because the product of oxidation can be in some cases the same. Indeed, Nosaka and co-workers proposed that the hydroxylated DMPO (5,5-Dimethyl-1-Pyrroline-N-Oxide) product can be also obtained from the direct hole transfer to the DMPO, followed by the reaction of the oxidized species with water.

$$DMPO + h^{+} \rightarrow DMPO^{\bullet+} \qquad (1.20)$$

$$DMPO^{\bullet+} + H_2O \rightarrow DMPO{-}OH^{\bullet} + H \qquad (1.21)$$

The EPR (Electronic Paramagnetic Resonance) evaluation of the hydroxyl radical concentration by DMPO as spin trapping agent can overestimate the role of this ROS (Reacting Oxygen Species).[54]

Hydroxyl radicals can be also been detected in the gas phase using the Laser Induced Fluorescence (LIF) method. This high sensitivity technique exploits a pulsed laser irradiation (355 nm) in order to start the photocatalytic process. The OH radicals released from irradiated

TiO_2 are then irradiated with a Dye Laser (281-284 nm) and their fluorescence appearing at 310 nm.[55,56] The LIF application is limited to the gas phase, due to OH radicals fluorescence quenching by water molecules.

Hydroxyls radicals can be detected also exploiting the fluorescence emitted by the hydroxylated products generated during the photocatalytic process, for example such as 3-(p-hydroxyphenyl) fluorescein (HPF), Terephtalic Acid and Coumarin are used as molecular probes for OH radicals (Figure 5).[56]

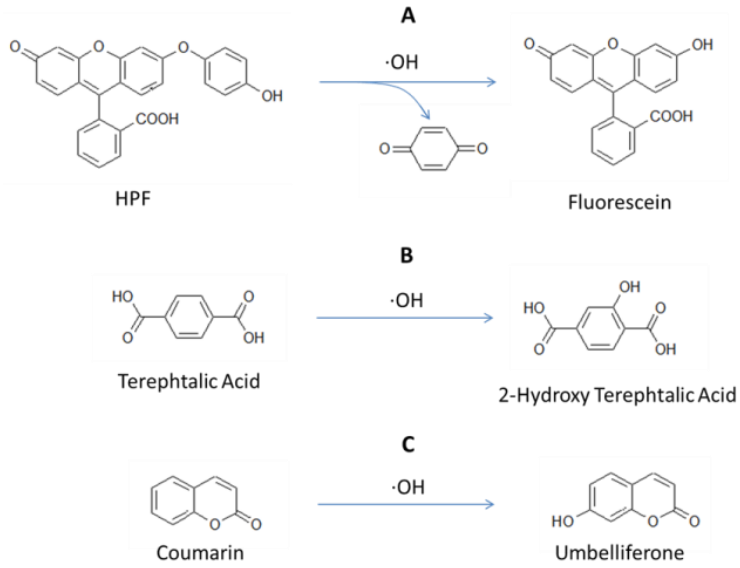

Figure 5. Reactions for detection of OH radical with fluorescence probes, (A) 3-(p-hydroxyphenyl) fluorescein (HPF), (B) Terephtalic Acid and (C) Coumarin.[56]

The main pathways of $OH^{\bullet}$ radicals formation are the photo-oxidation of the hydroxyl group or of the adsorbed water (reaction 1.22a, b). Nevertheless, hydroxyl radicals can also be formed via a reductive

mechanism from H_2O_2 via the superoxide $O_2^{-\bullet}$ radical anion (reactions 1.23 and 1.24) and by photolysis of H_2O_2 (reaction 1.25).[57]

$$h^+_{vb} + (Ti^{IV}\text{-}O^{2-}\text{-}Ti^{IV})\text{-}OH \rightarrow (Ti^{IV}\text{-}O^{2-}\text{-}Ti^{IV})\text{-}OH^{\bullet} \quad (1.22a)$$

$$h^+_{vb} + (Ti^{IV}\text{-}O^{2-}\text{-}Ti^{IV})\text{-}OH_2 \rightarrow (Ti^{IV}\text{-}O^{2-}\text{-}Ti^{IV})\text{-}OH^{\bullet} + H^+ \quad (1.22b)$$

$$O_{2(ads)} + e^- \rightarrow O_2^{\bullet -}{}_{(ads)} \quad (1.23)$$

$$H_2O_2 + O_2^{\bullet -} \rightarrow OH^{\bullet} + OH^- + O_2 \quad (1.24)$$

$$H_2O_2 + hv \rightarrow 2OH^{\bullet} \quad (1.25)$$

The possibility of several reaction paths and the influence of several variables on the process have hindered the formulation of a widely accepted mechanism of the photocatalytic process. For example $OH^{\bullet}$ radicals can or cannot be involved, also depending on the substrate type.[56]

Superoxide Radical, $\cdot O_2^-$

The radical anion $\cdot O_2^-$, obtained from the O_2 reduction at the titania surface (reaction 1.23), can be further reduced to the hydrogen peroxide, H_2O_2 (reaction 1.26). The same product can be obtained by the hydroxyl radical coupling with the formation of adsorbed peroxo-species (reactions 1.27 and 1.28) or by the dismutation of $\cdot O_2^-$ (reaction 1.29).

$$\cdot O_2^-{}_{(ads)} + e^- \rightarrow O_2^{2-} \quad (1.26)$$

$$2(OH\cdot)_{surface} \rightarrow (H_2O_2)_{surface} \quad (1.27)$$

$$(H_2O_2)_{surface} \leftrightarrows O_2^{2-} + 2H^+ \quad (1.28)$$

$$2{\cdot}O_2^-{}_{(ads)} + 2H^+ \rightarrow O_{2(ads)} + (H_2O_2)_{surface} \quad (1.29)$$

The superoxide radical anion is a Brønsted base that at pH < 3 gives the hydroperoxyl radical, $HO_2^{\bullet}$ (pK_a 4.88, reaction 1.30.[58] Other possible reactions involving these species are:

$${\cdot}O_2^-{}_{(ads)} + H^+ \leftrightarrows O_2^{2-}{}_{(surface)} \quad (1.30)$$

$$2HO_2{\cdot} \rightarrow H_2O_2 + O_2 \quad (1.31)$$

$${\cdot}O_2^- + HO_2{\cdot} + H_2O \rightarrow O_2 + H_2O_2 + OH^- \quad (1.32)$$

Hydrogen Peroxide, H_2O_2

Hydrogen Peroxide (H_2O_2) is another species that is involved in the photocatalytic process. Among ROS, is the only relatively stable molecule. Therefore, it could be easily detected after the other ROS decay.[19]

The generation of H_2O_2 can occurs through two different pathways, the two-electron reduction of O_2 and the two-hole oxidation of H_2O.[56] The reductive path seems to be the dominant one. The processes involved in the H_2O_2 production are summarized by the following reaction:

Reductive Route

$${\cdot}O_2^- + HO_2{\cdot} + H_2O \rightarrow O_2 + H_2O_2 + OH^- \quad (1.32)$$

$${\cdot}O_2^- + e^- + 2H^+ \rightarrow H_2O_2 \quad (1.33)$$

Oxidative Route

$$2H_2O + 2h^+ \rightarrow H_2O_2 + 2H^+ \quad (1.34)$$

$$H_2O + h^+ \rightarrow {}^{\cdot}OH + H^+ \quad (1.35)$$

$$2OH^{\cdot} \rightarrow H_2O_2 \quad (1.36)$$

The photogenerated H_2O_2 can then follow disproportionation to generate H_2O and O_2 (reaction 1.37), but it can be also been oxidized to $\cdot O_2^-$ (reaction 1.38) or generate OH radical due to a reductive mechanism (reaction 1.39).[56]

$$2H_2O_2 \rightarrow O_2 + H_2O \quad (1.37)$$

$$H_2O_2 + h^+ \rightarrow \cdot O_2 - + 2H^+ \quad (1.38)$$

$$H_2O_2 + e^- \rightarrow \cdot OH + OH^- \quad (1.39)$$

Hydrogen peroxide can also react with hydroxyl radical to generate superoxide radical (reaction 1.40).

$$H_2O_2 + \cdot OH \rightarrow \cdot O_2^- + H_2O + H^+ \quad (1.40)$$

Several works studied the effect of an external addition of H_2O_2 in a TiO_2 suspension (rutile, anatase or mixed phase). Usually, the adding of hydrogen peroxide enhances (not always) the photocatalytic process rate both for anatase and rutile, but the value of this increment depends from the catalyst characteristics and the substrate nature.[56]

Singlet Oxygen, $^1O_2$

The formation of singlet oxygen under irradiated semiconductor was predicted by Munuera and co-workers nearly forty years ago[59]. The

presence of this ROS has been a simple hypothesis till Nosaka and co-workers[60] demonstrated its existence detecting the near infrared phosphorescence at 1270 nm of $^1O_2$ in a TiO_2 suspension under irradiation. They suggested that $^1O_2$ is the product of the oxidation of $O_2^{\bullet -}$ from the valence band hole (reaction 1.41).

$$\cdot O_2^- + h^+ \rightarrow {}^1O_2 \qquad (1.41)$$

This mechanism of $^1O_2$ generation is supported by experiments conducted on different kind of TiO_2 powders, in which the materials that produce higher amount of $\cdot O_2^-$, give a higher generation of $^1O_2$.[61] Comparing anatase and rutile, the generation rate for anatase was reported to be 15-fold higher than rutile.[56,62]

1.3.1. Photocatalyst surface properties

The complexity of the photocatalytic processes depends not only from the catalyst, but also from the surface properties among the same kind of photocatalyst. In the following it will be highlighted the role of the extrinsic and intrinsic surface properties of the material on the photocatalytic process. With the term intrinsic surface properties (ISPs) it is usually denoted all the properties of the surface catalysts intrinsically related to their surface structure, i.e. exposed crystallographic planes, surface crystallographic phase and the degree of hydration/hydroxylation. Instead, the extrinsic surface properties (ESPs) are the properties related to the external environment of the catalyst, like pH, adsorption phenomena, ionic strength, surface complexation and so on.[19]

1.3.1.1. Intrinsic Surface Properties, ISPs

Titanium dioxide shows a marked polymorphism, in nature the stable forms are anatase, rutile and brookite. The most stable allotrope is polymorph rutile. However, anatase is the most stable phase for very small nanoparticles (radius below 11 nm)[9], while rutile is the predominant phase for particles above 35 nm in size. However, the crystallographic form is strictly related to the synthesis mechanism, so often the above reported rules are not observed.[19]

From a photocatalytic point of view only anatase and rutile show high photocatalytic activity, while brookite usually shows a negligible photoactivity. Moreover, often anatase is more active than rutile despite the higher band gap (3.2 eV vs 3.0 eV). One of the explanations at this apparent contradiction goes back to the different carriers' mobility inside the two polymorphs, decidedly higher for anatase. This different behavior is due to the different hybridization of the orbitals in the two phases, for which the effective mass of the electrons for anatase results definitely lower than for rutile. Consequently, the lightest carriers of anatase have a higher mobility, increasing the transport to the surface and decreasing the recombination. Obviously, this is not the only reason, indeed the CB level of rutile is slightly lower than anatase, it follows that rutile is not able to reduce O_2 to $O_2^{\cdot-}$, favoring the recombination.

The study of the relationship between surface and photocatalytic properties should start from the definitions of the most stable crystallographic planes for each allotrope.

Rutile crystal shows three low index crystallographic faces. The (110) and (100) have the lowest surface energy and for this reason are those considered more important and more studied in powder materials. When considering a non-reconstructed and unrelaxed surface in contact with vacuum, (110) is the most stable. The third rutile low index face is the (001) which is thermodynamically less stable and restructures above 748K.[63] A deep investigation on the photocatalytic properties of the Rutile phase is beyond the aim of this work and the reader should refer to specific literature.[9]

For anatase, the polymorph with the highest photocatalytic activity, the principal crystallographic planes are the (101) and (001), which are the faces that natural anatase crystals usually expose. How the crystallographic facets of anatase nanoparticles can affect the photocatalytic activity is the main purpose of the next chapters (Chapter 2 and Chapter 4) of this thesis.[19]

1.3.1.2. Extrinsic Surface Properties, ESPs

The principal extrinsic surface properties that can affect the entire photocatalytic process are:

- pH;
- Ionic Strength
- Adsorption Phenomena
- Surface complexation.

All these parameters have an influence on the semiconductor/electrolyte interface. First, the principal surfaces Potential Determining Ions (PDI) for the semiconductor oxide surface are H_3O^+ and OH^-. It follows that changing the pH of the solution, it is possible affect the energetic position of the electronic bands modifying the oxidative and reductive electrochemical potentials of h^+_{vb} and e^-_{cb}, respectively. The shift in the electrochemical potentials changes the driving force of the photochemical process, favoring or disfavoring it.[19]

At the semiconductor/electrolyte interface, it is possible define three different charge layers: one is the space charge region inside the semiconductor in contact with the solution, the others are called Helmholtz and Gouy-Chapmann layers, and they are generated at the semiconductor surface and at the structured electrolyte zone near the surface. It must be noted that: a) the capacity and charge of the three layers are interdependent; b) specific adsorption of ions influences the charge located at the semiconductor surface.[19]

The specific adsorption of ions can play a key role on the TiO_2 photocatalytic activity,[64] increasing or decreasing the rate of the photocatalytic process.[64-66] This derives from the influence of the adsorption on several properties of the semiconductor/electrolyte interface, i.e.:

I. the surface charge build-up at a given pH [67-70];
II. the flat band potential and consequently the band edge position[71];

III. the adsorption of substrates which either compete with the ions for the same sites or, if charged, are affected by the change in surface charge[72];

IV. the electron transfer kinetic, indeed adsorbed ions could introduce surface states that can act as carrier trapping sites or recombination centers. Moreover, redox active ions can generate reactive species and lead to the formation of undesirable reaction intermediates.[73]

For all these reasons, tuning the surface properties of a photocatalyst can be a way to improve and optimize his efficiency, but it can be also a tool to study the photocatalytic process, in particular the pathways of the charge transfer.[19]

Surface fluorination is one of the most studied cases of effects of an external ion on the heterogeneous photocatalysis. Minero and co-workers reported a relevant effect of the surface fluorination on the photocatalytic process.[74] Fluorides adsorption occurs via a ligand exchange reaction between surface hydroxyl groups and the fluoride ions and it is pH dependent[75]. Minero et al. tested the effect of fluoride ions on the photocatalytic degradation of phenol in aqueous TiO_2 suspensions at several pH values, observing an increase of the degradation rate on fluorinated TiO_2.[19] Competition degradation experiments on fluorinated titania between phenol and different alcohols permitted to estimate the relative weight that the direct hole transfer and the hydroxyl radical mediated oxidation have on the total degradation rate.[74] In fact, over fluorinated TiO_2, the photocatalytic process seems to involve prevalently free hydroxyl radicals, while direct reaction with holes was suppressed. The published results show that the fluorination can have opposite effects,

increasing or decreasing the degradation rate of different substrates. The fluorides coverage increases the degradation rate of substrates like Acid Orange 7[76], Acid Red 1[53,77] benzoic acid[77,78], organic dye X3B[48], Rhodamine B[79] and gaseous acetaldehyde[80] and acetone[81]. Conversely, on fluorinated catalysts the degradation rate of hydrogen peroxide[82], cathecol[74], dichloroacetate[76] and formic acid[77] are depressed.

Park and Choi observed an increase of the remote photocatalytic degradation rate of stearic acid in the proximity of a fluorinated thin film of catalyst and correlated this to an increase of the concentration of hydroxyl radicals in the gaseous phase because of the fluoride coverage[83]. Maurino et al. observed an increase of the hydrogen peroxide accumulation on fluorinated surfaces in the presence of oxygen and formic acid as hole scavenger[82]. Mrowetz and Selli successively confirmed this finding during the photocatalytic transformation of Acid Red 1, benzoic acid and formic acid[77]. Xu and co-workers[84] studied the phenol photocatalytic degradation in the presence and in the absence of fluoride over different anatase and rutile powders. The presence of fluorides clearly affected the degradation rate of phenol, increasing or decreasing the transformation rate depending on the TiO_2 nature.[19]

From the analysis of all the above-cited data and the relative considerations reported until now, some conclusions can be drawn:

a) the formation of free $OH^{\bullet}$ radicals seems to be enhanced on fluorinated TiO_2, as described by Mrowetz and Selli by using spin-probe EPR spectroscopy[53] or, recently, by Yu and coworkers by photoluminescence technique[81] using terephtalic acid as probe molecule. As a consequence,

the degradation of substrates that react predominantly by $OH^{\bullet}$ radicals mediated oxidation seems to be favored over fluorinated TiO_2;

b) the fluorination alters profoundly the surface OH population of the TiO_2. The fluoride induces strong modifications to the surface titania speciation with a decrease of the surface charge in the acidic pH, because the dominant surface species shift from $>Ti-OH_2^+$ to $>Ti-F$. Marked change in the electrostatic interaction between the surface and charged substrate are expected;

c) over fluorinated catalysts, substrates whose degradation is started by a direct hole transfer (through an inner sphere mechanism, ISM) show slower degradation kinetics because the complexation of fluoride toward surface Ti^{IV} ions hinders the specific adsorption of substrates;

d) fluorides inhibit the surface complexation of superoxide/peroxide species, derived from the e^-_{CB} reduction of O_2, thus in turn inhibiting H_2O_2 degradation and so promoting its accumulation;

e) the inhibition of the substrates adsorption of species that are able to back react with e^-_{CB} improves the photocatalytic efficiency enhancing the degradation rate especially at high substrate concentration;

f) fluoride ions at the surface decrease the energy of empty surface electron traps (Ti^{III}–OH vs Ti^{III}–F) slowing down both surface recombination and electron transfer to molecular oxygen[85] and enhancing anodic photocurrents[86] as observed studying the photo electrochemical behavior of polycrystalline TiO_2 films.

In the experimental section of this work, it will be shown some results that are in agreement with the just "listed conclusions", but other results deny it. It follows that the photocatalytic mechanism of these kinds of systems is

far from being completely unveiled and rationalized. This is due to the complexity of the interactions between catalyst, substrate and external species. The change of one or more of these factors can lead to results very different from each other.[19]

1.4. Photocatalytic Hydrogen Production

The increase of the world population and, consequently, of the global energy consumption (15 TW, 2004) lead to a diminishing of fossil fuels resources, raising their price and giving rise to various economic-political instabilities. Moreover, several predictions show that the demand will probably exceed the supply possibilities within a few years. Actually, near the 80% of the energy comes from fossil fuels, so governments are every day more attracted by renewable sources, developing new strategies for energy production that could be economically and environmentally sustainable.

In this context, hydrogen is one of the solutions that can contribute to solve the energy problem. Indeed, the reaction between molecular hydrogen and oxygen in a fuel cell is able to transform chemical energy in an electric work, leaving as byproduct only heat and water. Nevertheless, the impact of the hydrogen production is close to zero if produced starting from renewable source.

Beside these advantages, there are still some problems:

1. There is no molecular hydrogen on the Earth (escape velocity too high in the atmosphere) although it is the main gas in the universe;
2. Its exploitation requires good purity level and it has to be generated in an efficient way;
3. There are still problems concerning the storage technology and transport/distribution network avoiding leaks. Actually, this problem has been bypassed replacing H_2 distribution infrastructures with on-board form;
4. Uncertain debates are still open on the consequences of an unmeant lacks into the atmosphere (interaction with the ozone cycle and increase of the water vapor).

Nowadays, fossil fuels are the main resource for the hydrogen production (nearly 95%). The principal technique is the reforming of methane, for which exist two main routes in order to obtain useful products. The first one is called *indirect*, it consists in the transformation of the natural gas into syngas, a mixture of H_2 and CO at different ratios).[87] The syngas can be then used as raw material for the production of other valuable products such as methanol, formaldehyde, ammonia and olefins. Conversely, also a *direct* route exist, it consist in a one-step process in which the methane is directly converted to the final products. Of course, the direct method is preferred to the indirect one, but his applicability can be limited by low conversion efficiency and low selectivity.[87]

As already mentioned, the importance of the hydrogen as fuel it will become gradually greater if it will be possible untie its production from fossil fuel as methane. Therefore, great efforts are actually devoted to implement methods and technologies in order to produce hydrogen starting

from renewable resources (biomass steam reforming and gasification, photochemical approaches, etc.[87-92]). The black mark is that, at the current state, these methods have some limitations (low efficiency and high energy demand) that impose hard conditions. The big advantage, especially for the photoelectrochemicals methods, is the possibility to exploit the sunlight as infinite energy source (at no cost).

The process which makes it possible is the photocatalysis, already widely discussed in this chapter. Starting from the photon absorption and the generation of the electron-hole couple, whereas the holes present in the valence band of the catalyst have the potential for oxidize the water (producing hydroxyl radicals), at the same time electrons in the conduction band are involved in the H_2 production. Obviously, for this to happen the CB potential of the catalyst must be more negative than the H^+/H_2 reduction potential (E_{H^+/H_2} = 0.00 V vs NHE at pH 0). Simultaneously, the VB potential must be more positive than the oxidation potential of H_2O so that oxygen can be generated from water (E_{O_2/H_2O} = 1.23 V vs NHE at pH 0).[87] This process is the so-called *photo-water-splitting*, in which a catalyst, suffering the light absorption, splits water molecule into hydrogen and oxygen. The limitation of the entire process is again the efficiency, due to recombination processes in the catalyst and the backward reaction among the two gases.

In this context, a big step forward has been made studying the *photoreformig* process (see Figure 6), in which an organic substrate is used as a sacrificial reagent (often hole scavenger) because it is more easily oxidized than water from the hole in the VB, meanwhile the hydrogen reductive process remains untouched. The possibility to choose among

different sacrificial agents (often alcohols but even other pollutants) and to control the process in order to increase the selectivity is the main advantages of the photoreforming. Moreover, in such kind of systems usually a co-catalyst is utilized in order to decrease the electron-hole couple recombination.

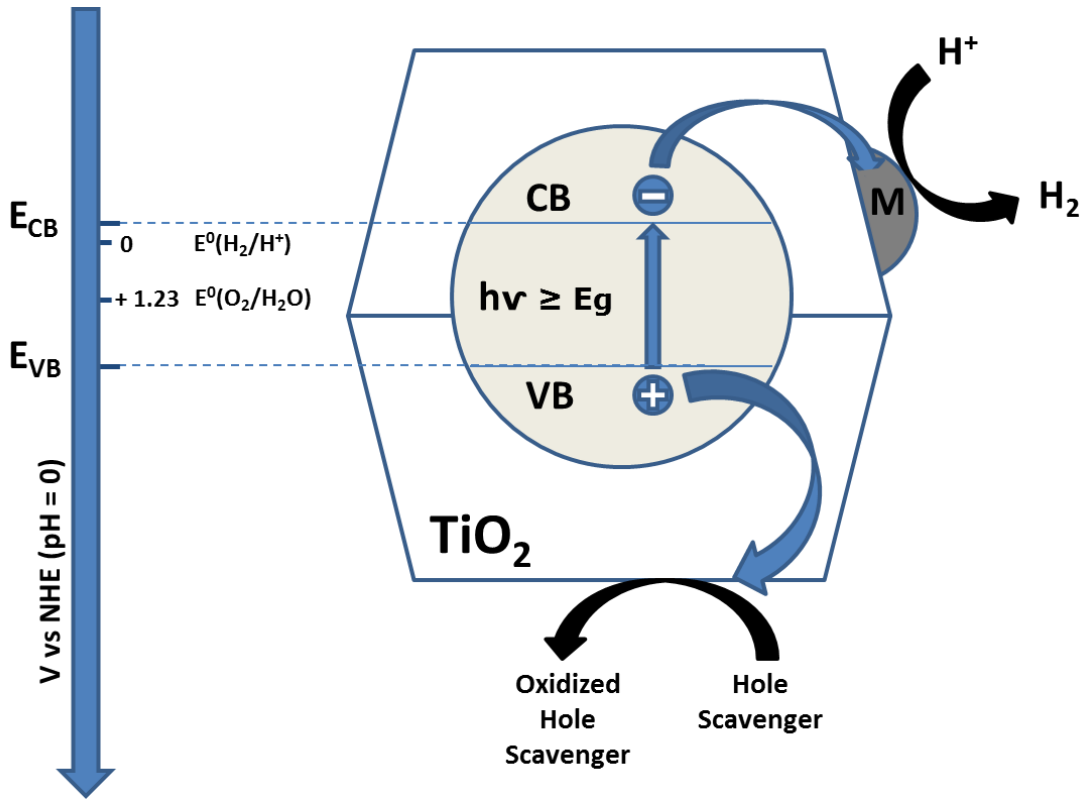

Figure 6. Photoreforming process using a hole scavenger for the H_2 production

1.4.1. Photocatalytic Hydrogen Production from TiO_2

The photocatalytic production of hydrogen can be performed using several catalysts; in this paragraph we will limit our description only to TiO_2 for H_2 evolution. In the last decade, several works have been devoted to the influence of the TiO_2 structure, dimension and morphology in order to maximize the charge carrier separation. Similarly, studies on the properties of the co-catalyst deposed on the oxide surface and the role of the sacrificial agent were carried out. Nevertheless, the pH, influencing the surface properties of the catalyst, can have an important impact on the H_2 evolution from TiO_2 slurries.

In 2011, Yi and coworkers[93] investigated the role of the TiO_2 nanoparticles shape in the photocatalytic hydrogen evolution. They compared nano-spheres and nanorods using Pt as co-catalyst (1 wt %) and ethanol as sacrificial agent. They found that TiO_2 nanorods have a higher photocatalytic activity due to a decreased probability of e^-/h^+ recombination. The authors, however, didn't investigate the role of different surfaces present in their materials, probably responsible of the different electron hole recombination.

A more accurate work carried out by D'Arienzo et al. in 2015[94], tried to study the relationship between the different anatase surface and the H_2 generation yield in methanol photo-steam reforming. They synthesize three different anatase crystals with shape nearly rectangular (RC), rhombic (R) and nanobar (NB). They expose {101}, {001} and, only for the RC, the

{010} surfaces. They carried out some EPR experiments, correlating the amount of Ti^{3+} (electron traps) with the H_2 evolution rate, indeed the hydrogen production involves an electron transfer to a proton. So, higher is the Ti^{3+} EPR signal, higher is the H_2 evolution rate. As we will see in the next chapter, the {101} surface for anatase seems to be a reductive surface, it follows that an high exposition of this kind of facet should induce a higher presence of Ti^{3+} centers under illumination and, therefore, a higher H_2 production. From their results, the RC materials are the more active in the methanol photoreforming and with the higher presence of Ti^{3+} centers, however this material has also the lower {101} surface area, exposing preferentially the {010} surface. This points out that the H_2 production cannot can't be related only to the reductive {101} surface, but also the presence of the {010} facet play a role. They suggest the presence of a "surface hetero-junction" between the {101}, {010} and {001} facets which drives the electrons photogenerated on the {001} not just toward the {101} but also to the {010}, favoring the charge separation.

The importance of the exposed surfaces is highlighted also in a recent paper of Liu, Page and coworkers[95]. They synthetized anatase NPs with different relative amount of the {101} and {001} surfaces. They obtained that the catalyst with an intermediate amount of the {101} and {001} surfaces, normalizing for the SSA, shows the best photocatalytic activity in the H_2 production from a methanol solution. They conclude that a synergistic effect may exist between {001} and {101} facets.

The photocatalytic production of hydrogen from methanol steam reforming was also investigated over a series of fluorinated Pt/TiO_2 samples (F for O nominal molar substitution ranging from 5 to 15%) synthesized by flame

spray pyrolysis by Chiarello et al. in a work published in 2014[96]. A substitution lower than 10% leads to an increase of surface hydroxylation which can favor an indirect hydroxyl mediated mechanism, with the consequent increase of hydrogen production rate. Conversely, fluorination higher than 10% introduces an excess of bulk structural defects that can act as electron–hole recombination centers. Moreover, an excess of fluorination increases the F-induced surface electronegativity, inhibiting CB electron transfer. Both these effects lead to a lower photocatalytic hydrogen production rate.

In 2012 Gordon et al.[97] used TiF_4 as precursor in the anatase nanocrystals synthesis, in order to produce HF in situ during the reaction and having a controlled release of the acid and allowing an high control of the crystals shape. Moreover, changing the ratio of TiF_4 precursor in combination with $TiCl_4$ and the type of surfactant (oleylamine or octadecanol), a tunability of the titania shape based on bipyramidal geometry was demonstrated. The percentage of {101} and {001} facets was therefore well controlled and depended on the amount of HF released during the reaction, resulting in samples where F was still present on the surface. Then, a ligand exchange procedure with NaOH solution exchanged the fluorides at the surface with OH groups. The materials were then tested for H_2 production in the presence of methanol as sacrificial agent and photo-deposited Pt as co-catalyst under simulated solar light. The results show that the samples with higher content of {101} facets were better than {001} for this particular reaction, both with and without fluorine on the surface. This clearly demonstrates the importance of the presence of the {101} reductive facets for these kind of systems.

Bibliography

*(1) Chen, X.; Mao, S. S. Chemical reviews **2007**, 107, 2891.*

*(2) Wang, Z.; Saxena, S. K.; Pischedda, V.; Liermann, H. P.; Zha, C. S. Journal of Physical Condensed Matter **2001**, 13, 8317.*

*(3) Fujishima, A.; Honda, K. Nature **1972**, 238, 37.*

*(4) O'Regan, B.; Gratzel, M. Nature **1991**, 353, 737.*

*(5) Zhang, Q.; Gao, L. Langmuir **2003**, 19, 967.*

*(6) Wanga, D.; Yu, B.; Zhoua, F.; Wang, C.; Liua, W. Materials Chemistry and Physics **2009**, 113, 602.*

*(7) Zhou, Y.; Huang, Y.; Li, D.; He, W. Materials Research Bulletin **2013**, 48, 2420.*

*(8) Herrmann, J.-M. Journal of Photochemistry and Photobiology A Chemistry **2010**, 216, 85.*

*(9) Diebold, U. Surf. Sci. Rep. **2003**, 48, 53.*

*(10) Shannon, R. D.; Pask, J. A. Journal of the Ceramic American Society **1965**, 48, 391.*

*(11) Deiana, C.; Fois, E.; Coluccia, S.; Martra, G. The Journal of Physical Chemistry C **2010**, 114, 21531.*

*(12) Cerrato, G.; Marchese, L.; Morterra, C. Applied Surface Science **1993**, 70, 200.*

*(13) Fujishima, A.; Zhang, X.; Tryk, D. A. Surf. Sci. Rep. **2008**, 63, 515.*

*(14) Gaya, U. I.; Abdullah, A. H. Journal of Photochemistry and Photobiology C: Photochemistry Reviews **2008**, 9, 1.*

*(15) Luttrell, T.; Halpegamage, S.; Tao, J.; Kramer, A.; Sutter, E.; Batzill, M. Scientific Reports **2014**, 4.*

*(16) Pellegrino, F.; Pellutiè, L.; Sordello, F.; Minero, C.; Ortel, E.; Hodoroaba, V. D.; Maurino, V. Appllied Catalysis B: Environmental **2017**, 216, 80.*

*(17) Shimura, K.; H.Yoshida Energy & Environmental Science **2011**, 4, 2467.*

*(18) D'Arienzo, M.; Carbajo, J.; Bahamonde, A.; Crippa, M.; Polizzi, S.; Scotti, R.; Wahba, L.; Morazzoni, F. Journal of American Chemical Society **2011**, 133, 17652.*

(19) Minella, M. PhD Thesis, University of Turin, 2010.

*(20) Emeline, A. V.; Ryabchuk, V. K.; Serpone, N. The Journal of Physical Chemistry B **2005**, 109, 18515.*

*(21) Martin, S. T.; Herrmann, H.; Choi, W.; Hoffmann, M. R. J. Chem. Soc., Faraday Trans. **1994**, 90, 3315.*

(22) Martin, S. T.; Herrmann, H.; Hoffmann, M. R. J. Chem. Soc., Faraday Trans. ***1994****, 90, 3323.*

(23) Robertson, P. K. J.; Bahnemann, D. W.; Robertson, J. M. C.; Wood, F. In Environmental Photochemistry Part II; Springer Berlin Heidelberg: 2005, p 367.

(24) Minero, C.; Vione, D. Applied Catalysis B: Environmental ***2006****, 67, 257.*

(25) Marcus, R. A. The Journal of Chemical Physics ***1956****, 24, 966.*

(26) Marcus, R. A. The Journal of Chemical Physics ***1957****, 26, 872.*

(27) Marcus, R. A. The Journal of Chemical Physics ***1956****, 24, 979.*

(28) Marcus, R. A. The Journal of Chemical Physics ***1957****, 26, 867.*

(29) Marcus, R. A. The Journal of Chemical Physics ***1965****, 43, 679.*

(30) Piccinini, P.; Minero, C.; Vincenti, M.; Pelizzetti, E. Journal of the Chemical Society, Faraday Transactions ***1997****, 93, 1993.*

(31) Calza, P.; Minero, C.; Pelizzetti, E. Environ Sci Technol ***1997****, 31, 2198.*

(32) Lewandowsky, M.; Ollis, D. F. ***2003****, 43, 309.*

(33) Lewandowski, M.; Ollis, D. F. Appl Catal B-Environ ***2003****, 45, 223.*

(34) Ollis, D. F. Journal of Physical Chemistry B ***2005****, 109, 2439.*

(35) Serpone, N. J Adv Oxid Technol ***2007****, 10, 111.*

(36) Minero, C. Catalysis Today ***1999****, 54, 205.*

(37) Richard, C. New Journal of Chemistry ***1994****, 18, 443.*

(38) Choi, W.; Hoffmann, M. R. Environ Sci Technol ***1995****, 29, 1646.*

(39) Calza, P.; Minero, C.; Pelizzetti, E. J Chem Soc Faraday T ***1997****, 93, 3765.*

(40) Minero, C.; Piccinini, P.; Calza, P.; Pelizzetti, E. New Journal of Chemistry ***1996****, 20, 1159.*

(41) Nahen, M.; Bahnemann, D.; Dillert, R.; Fels, G. Journal of Photochemistry and Photobiology A: Chemistry ***1997****, 110, 191.*

(42) Grabner, G.; Li, G.; Quint, R. M.; Quint, R.; Getoff, N. Journal of the Chemical Society, Faraday Transactions ***1991****, 87, 1097.*

(43) Bahnemann, D. W.; Hilgendorff, M.; Memming, R. The Journal of Physical Chemistry B ***1997****, 101, 4265.*

(44) Cermenati, L.; Pichat, P.; Guillard, C.; Albini, A. The Journal of Physical Chemistry B ***1997****, 101, 2650.*

(45) Sun, Y.; Pignatello, J. J. Environ Sci Technol ***1995****, 29, 2065.*

*(46) Tachikawa, T.; Tojo, S.; Fujitsuka, M.; Majima, T. Langmuir **2004**, 20, 2753.*

*(47) Tachikawa, T.; Tojo, S.; Fujitsuka, M.; Majima, T. The Journal of Physical Chemistry B **2004**, 108, 11054.*

*(48) Lv, K.; Xu, Y. The journal of physical chemistry. B **2006**, 110, 6204.*

*(49) Jaeger, C. D.; Bard, A. J. The Journal of Physical Chemistry **1979**, 83, 3146.*

(50) Fox, M. A.; Draper, R. B.; Dulay, M.; O'Shea, K. In Photochemical Conversion and Storage of Solar Energy; Kluwer: Dordrecht, 1991.

*(51) Howe, R. F.; Gratzel, M. The Journal of Physical Chemistry **1987**, 91, 3906.*

*(52) Anpo, M.; Shima, T.; Kubokawa, Y. Chemistry Letters **1985**, 14, 1799.*

*(53) Mrowetz, M.; Selli, E. Physical chemistry chemical physics : PCCP **2005**, 7, 1100.*

*(54) Nosaka, Y.; Komori, S.; Yawata, K.; Hirakawa, T.; Nosaka, A. Y. Phys. Chem. Chem. Phys. **2003**, 5, 4731.*

(55) Nosaka, Y. In Environmentally Benign Photocatalysts: Applications of Titanium Oxide-based Materials; Anpo, M., Kamat, P. V., Eds.; Springer New York: New York, NY, 2010, p 205.

*(56) Nosaka, Y.; Nosaka, A. Y. Chemical reviews **2017**, 117, 11302.*

*(57) Pelizzetti, E.; Minero, C. Comments on Inorganic Chemistry **1994**, 15, 297*

*(58) Sawyer, D. T.; Gibian, M. J. Tetrahedron **1979**, 35, 1471.*

*(59) Munuera, G.; Navio, A.; Rives-Arnau, V. Journal of the Chemical Society, Faraday Transactions **1981**, 177, 2747.*

*(60) Nosaka, Y.; Daimon, T.; Nosaka, A. Y.; Murakami, Y. Physical Chemistry Chemical Physics **2004**, 6, 2917.*

*(61) Daimon, T.; Nosaka, Y. The Journal of Physical Chemistry C **2007**, 111, 4420.*

*(62) Zoltan, T.; Rosales, M. C.; Yadarola, C. Journal of Environmental Chemical Engineering **2016**, 4, 3967.*

*(63) Ramamoorthy, M.; Vanderbilt, D.; King-Smith, R. D. Physical review. B, Condensed matter **1994**, 49, 16721.*

*(64) Kormann, C.; Bahnemann, D. W.; Hoffmann, M. R. Environ Sci Technol **1991**, 25, 494.*

*(65) Abdullah, M.; Low, G. K. C.; Matthews, R. W. The Journal of Physical Chemistry **1990**, 94, 6820.*

*(66) D'Oliveira, J. C.; Al-Sayyed, G.; Pichat, P. Environ Sci Technol **1990**, 24, 990.*

(67) Stumm, W. Chemistry of the Solid-Water Interface: Processes at the Mineral-Water and Particle-Water Interface in Natural Systems, 1992.

(68) Dzombak, D. A.; Morel, F. M. M. Surface Complexation Modeling: Hydrous Ferric Oxide; Wiley, 1990.

*(69) James, R. O.; Healy, T. W. Journal of Colloid and Interface Science **1972**, 40, 53.*

*(70) Nelson, B. P.; Candal, R.; Corn, R. M.; Anderson, M. A. Langmuir **2000**, 16, 6094.*

(71) Graetzel, M. In Photocatalysis: Fundamentals and Applications; Pelizzetti, E., Serpone, N., Eds.; Wiley Interscience: New York, 1989, p 123.

*(72) Maurino, V.; Minero, C.; Pelizzetti, E.; Mariella, G.; Arbezzano, A.; Rubertelli, F. Res Chem Intermediat **2007**, 33, 319.*

*(73) Vione, D.; Maurino, V.; Minero, C.; Vincenti, M.; Pelizzetti, E. Environ. Sci. Pollut. Res. Int. **2003**, 10, 321.*

*(74) Minero, C.; Mariella, G.; Maurino, V.; Vione, D.; Pelizzetti, E. Langmuir **2000**, 16, 8964.*

*(75) Minella, M.; Faga, M. G.; Maurino, V.; Minero, C.; Pelizzetti, E.; Coluccia, S.; Martra, G. Langmuir **2010**, 26, 2521.*

*(76) Park, H.; Choi, W. The Journal of Physical Chemistry B **2004**, 108, 4086.*

*(77) Mrowetz, M.; Selli, E. New Journal of Chemistry **2006**, 30, 108.*

*(78) Vione; Minero; Maurino; Carlotti; Picatonotto; Pelizzetti Applied Catalysis B: Environmental **2005**, 58.*

*(79) Wang, Q.; Chen, C.; Zhao, D.; Ma, W.; Zhao, J. Langmuir **2008**, 24, 7338.*

*(80) Kim, H.; Choi, W. Applied Catalysis B: Environmental **2007**, 69, 127.*

*(81) Yu, J.; Wang, W.; Cheng, B.; Su, B.-L. The Journal of Physical Chemistry C **2009**, 113, 6743.*

*(82) Maurino, V.; Minero, C.; Mariella, G.; Pelizzetti, E. Chemical communications **2005**, 2627.*

*(83) Park, J. S.; Choi, W. Langmuir **2004**, 20, 11523.*

(84) Xu, Y.; Lv, K.; Xiong, Z.; Leng, W.; Du, W.; Liu, D.; Xue, X. The Journal of Physical Chemistry C ***2007****, 111, 19024.*

(85) Monllor-Satoca, D.; Gómez, R. The Journal of Physical Chemistry C ***2008****, 112, 139.*

(86) Cheng, X. F.; Leng, W. H.; Liu, D. P.; Xu, Y. M.; Zhang, J. Q.; Cao, C. N. The Journal of Physical Chemistry C ***2008****, 112, 8725.*

(87) Cargnello, M. PhD Thesis, University of Trieste, 2011.

(88) Cortright, R. D.; Davda, R. R.; Dumesic, J. A. Nature ***2002****, 418, 964.*

(89) Holladay, J. D.; Hu, J.; King, D. L.; Wang, Y. Catalysis Today ***2009****, 139, 244.*

(90) Huber, G. W.; Iborra, S.; Corma, A. Chemical reviews ***2006****, 106, 4044.*

(91) Navarro, R. M.; Pena, M. A.; Fierro, J. L. Chemical reviews ***2007****, 107, 3952.*

(92) Huber, G. W.; Shabaker, J. W.; Dumesic, J. A. Science ***2003****, 300, 2075.*

(93) Yun, H. J.; Lee, H.; Jool, J. B.; Kim, N. D.; Yi, J. Journal of nanoscience and nanotechnology ***2011****, 11, 1688.*

(94) D'Arienzo, M.; Dozzi, M. V.; Redaelli, M.; Di Credico, B.; Morazzoni, F.; Scotti, R.; Polizzi, S. J Phys Chem C ***2015****, 119, 12385.*

(95) Liu, J.; Olds, D.; Peng, R.; Yu, L.; Foo, G. S.; Qian, S.; Keum, J.; Guiton, B. S.; Wu, Z. L.; Page, K. Chem Mater ***2017****, 29, 5591.*

(96) Chiarello, G. L.; Dozzi, M. V.; Scavini, M.; Grunwaldt, J. D.; Selli, E. Appl Catal B-Environ ***2014****, 160, 144.*

(97) Gordon, T. R.; Cargnello, M.; Paik, T.; Mangolini, F.; Weber, R. T.; Fornasiero, P.; Murray, C. B. J Am Chem Soc ***2012****, 134, 6751.*

Chapter 2

2.1. Synthetic methods of nanoscale TiO_2

TiO_2 nanoparticles can be synthetized by a wide variety of methods. In this paragraph, a brief view on the main TiO_2 nanoparticles synthesis techniques is reported. The different methods could result in different TiO_2 nanostructures such as bipyramids, nanosheets, nanotubes, nanowires, nanorods and mesoporous structures. In this work, TiO_2 nanoparticles were synthetized using hydrothermal and solvothermal methods, as it will be described in Chapter 3.

2.1.1. Hydrothermal Synthesis

Hydrothermal synthesis is a method for obtaining TiO_2 nano and micro crystals; it exploits the solubility of minerals in hot water under high pressure. It is carried out in high pressure reactor, in which a precursor is supplied along with aqueous solution and eventually a shape controller, under controlled temperature and/or pressure values. The method allows to synthetize good-quality crystals with a good control over their composition and morphology. TiO_2 nanoparticles can be obtained by hydrothermal treatment of peptized precipitates of a titanium precursor with aqueous solution. By this method TiO_2 in form of nanoparticles[1], nanorods[2], nanowires[3], etc. are synthetized.

2.1.2. Solvothermal Synthesis

Solvothermal synthesis is very similar to the hydrothermal route, the only difference being that the precursor solution is not aqueous. The temperature can be increased more than in hydrothermal method, since a variety of organic solvents with higher boiling points can be chosen. Using solvothermal methods, it is possible to gain the benefits of both the sol-gel and hydrothermal routes. The solvothermal methods normally has high control on the size and shape distributions of the nanoparticles and on the crystallinity of the TiO_2.[4] These characteristics can be altered by modifying certain experimental parameters, including reaction temperature, reaction time, solvent type, surfactant type, and precursor type.

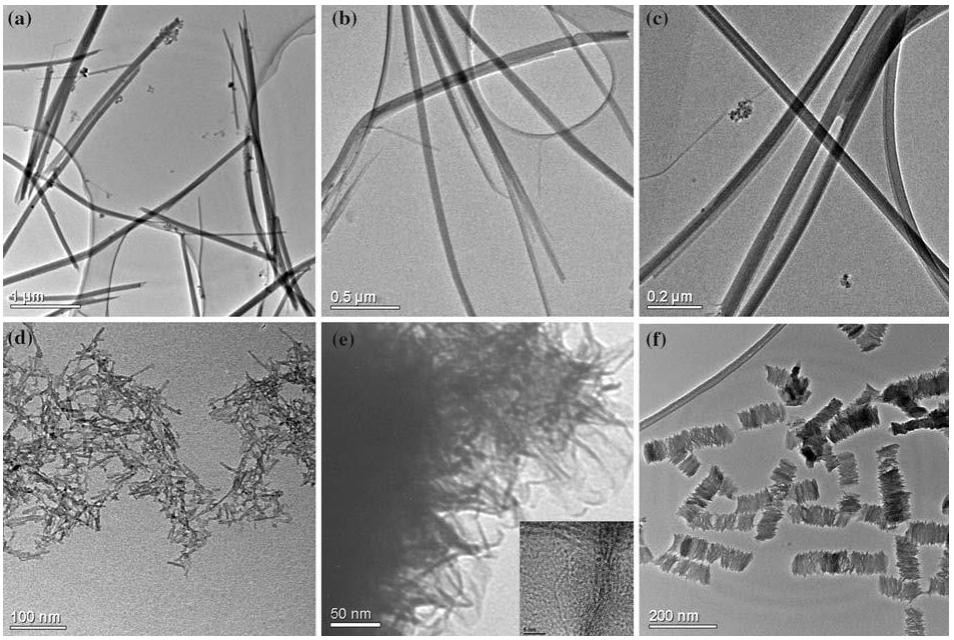

Figure 7. TEM images of TiO_2 nanomaterials in EG–DEA system: (a) 40 nm, (b) 30 nm, and (c) 22 nm diameter wires, (d) 5 nm diameter rods, (e) 2 nm diameter fibers, and (f) nanofiber arrays (from ref.4)

2.1.3. Direct Oxidation

Nanostructured TiO_2 can be obtained by direct oxidation of titanium metal using oxidants[5] or anodization[6]. Using oxidant (such as H_2O_2), the formation of crystalline TiO_2 nanorods occurs through a dissolution and precipitation mechanism[5]. The addition of inorganic salts allows controlling the crystalline phase of the TiO_2. The addition of F^- and SO_4^{2-} helps the formation of pure anatase, while the addition of Cl^- favours the formation of rutile. Anodization is realized with a Ti sample in a solution of 0.5 wt% NH_4F and malonic acid using Pt as a counter electrode. Voltages from 5 V to 20 V were applied and anodizing time from 1 min to 6h.

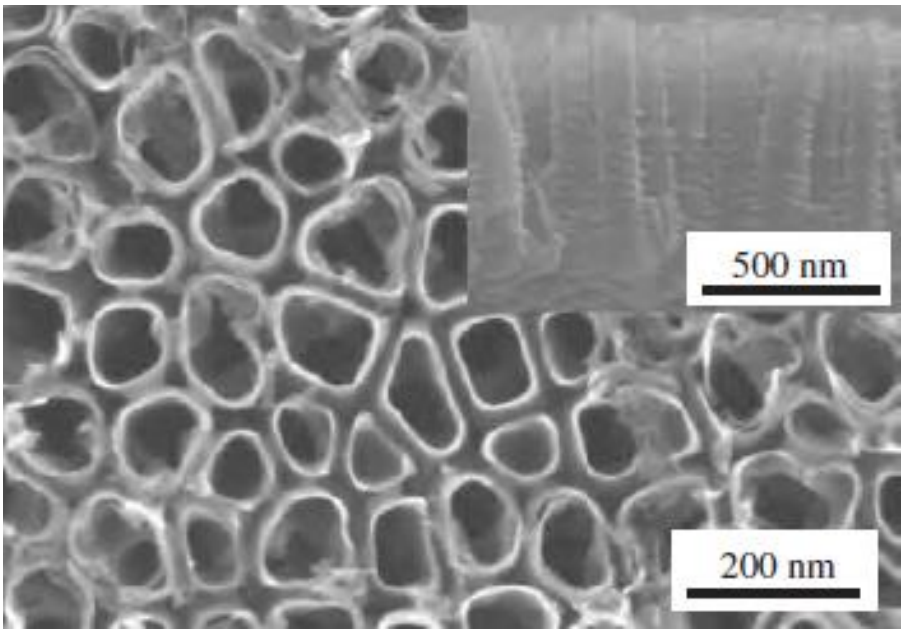

Figure 8. Surface and cross-sectional morphologies of TiO_2 nanotubes obtained from anodizing Ti for 1 h in a solution of 0.5 wt% NH_4F and 1 M malonic acid at 20 V (from ref.6)

2.1.4. Chemical Vapor Deposition

The term "Vapor deposition" is referred to any process in which a material in a vapor state is condensed in order to generate a solid-phase material. These processes are exploited to produce coatings that are able to alter the mechanical, electrical, thermal, optical, corrosion resistance, and wear resistance properties of various substrates.

If no chemical reaction occurs, this process is called Physical Vapor Deposition (PVD); otherwise, it is called Chemical Vapor Deposition (CVD). In CVD processes, thermal energy heats the gases in the coating chamber and drives the deposition reaction. In CVD, flow rate, gas composition, deposition temperature, pressure and deposition chamber geometry are the process parameters by which deposition can be controlled to have materials with a desired morphology[7-9]. Moreover, the nature of substrates could influence the size and distribution of grains in the films. Currently, the use of a modified CVD method in which the process parameters are adjusted such that nanoparticles are formed instead of films is a topic of high interest[7]. It has been shown that variations of precursor delivery and time-temperature profile in CV synthesis have an influence on the particle and powder characteristics (Figure 9)[9].

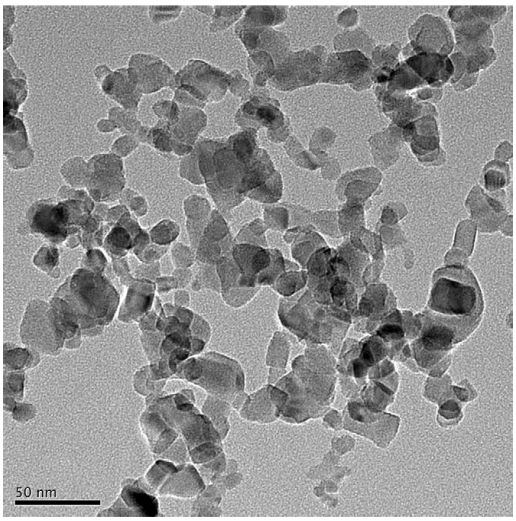

Figure 9. Synthesis of TiO_2 nanoparticles by the oxidation of titanium tetrachloride ($TiCl_4$) in industrial propane/air turbulent flame (from ref. 9)

2.1.5. Electrodeposition

Electrodeposition is a methodology commonly employed in order to produce coatings of TiO_2. The substrate to be coated is used as cathode and immersed into a solution that contains a salt of Ti to be deposited. With the use of the template of an anodic alumina membrane (AAM),[10,11] TiO_2 nanowires can be obtained by electrodeposition. In a typical process, the electrodeposition is carried out using a solution of $TiCl_3$ 0.2 M at pH = 2, then with a pulsed electrodeposition approach the titanium and/or its compound are deposited into the pores of the AAM. By heating the above-deposited template at 500 ºC for 4 h and removing the template, pure anatase TiO_2 nanowires can be obtained[11].

2.1.6. Sonochemical Methods

A wide range of nanostructured materials is successfully synthetized by means of ultrasound. The effects of ultrasound do not ensue from a direct interaction with the molecular species in solution. Instead, the use of the sonochemistry in the synthesis of metal oxide arises from the exploitation of the acoustic cavitation effect, which provides the formation, growth, and implosive collapse of bubbles in a liquid.

Different groups have applied the sonochemical method to prepare various TiO_2 nanomaterials[12-16].

2.1.7. Microwave Methods

A dielectric material can be treated with high-frequency electromagnetic waves. The principal frequencies of microwave heating are between 900 and 2450 MHz. At lower microwave frequencies, the conductive currents that flow within the material due to the ions movement can directly transfer energy from the microwave field to the material. At higher frequencies, the energy absorption is primarily due to molecules with a permanent dipole, which tend to be re-orientated under the influence of a microwave electric field. Microwave radiation is applied to prepare various TiO_2 nanoparticles[16-19]. The advantages of this method are the high heating rate due to the direct absorption of the microwave radiation that allows reaching extremely high temperature in a short time. Therefore, synthesis of high crystalline nanoparticles can be quickly performed. Corradi et al. found that colloidal titania nanoparticle suspensions could be prepared within 5 min to 1 h with microwave radiation, while 1 to 32 h was needed for the conventional synthesis method of forced hydrolysis at 468K.[17]

2.1.8. Sol-Gel Methods

Sol-gel method is one of the most convenient ways to synthesize various metal oxides due to low cost, ease of fabrication and low processing temperatures. It is widely used to prepare TiO2 for films, particles or monoliths. The sol-gel process is one of the main methods for the manufacture of ceramic materials, typically metal oxides. The process involves the synthesis of colloidal solutions (sol) (usually from inorganic metal salts or metal organic compounds such as metal alkoxides) which are

the precursors for the subsequent formation of a gel through hydrolysis and condensation reactions. Post-thermal drying and solidifying treatments are generally employed in order to eliminate the liquid phase and lead to a complete transition from the liquid sol to the solid gel phase. The homogeneity of the gels depends on the solubility of reagents in the solvent, the sequence of addition of reactants, the temperature and the pH of the colloidal solution. The precursors normally used for the synthesis and doping of nanoparticles are organic alkoxides, acetates and/or acetyl-acetonates as well as inorganic salts such as chlorides. Among the solvents, alcohols are largely used but other solvents may also be used. Nanostructured TiO_2 has been synthesized with the sol-gel method from hydrolysis of a titanium precursor[20,21]. This process normally proceeds via an acid-catalyzed hydrolysis step of the titanium (IV) alkoxide, followed by condensation. The generation of Ti-O-Ti chains is favored by low contents of water, low hydrolysis rates and with an excess titanium alkoxide in the reaction mixture.

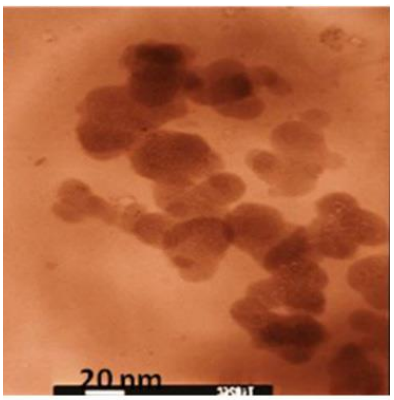

Figure 10. Transmission electron microscopy of TiO_2 prepared by sol gel method and calcined at 673K (from ref.20)

2.1.9. Laser Ablation Methods

Pulsed laser ablation of metal targets in liquid (PLAL) recently become a promising and efficient physical technique for the production of nanoparticles, due to a number of advantages such as simplicity, low

production cost, the absence of chemical reagents in solution, a better control over stoichiometry and the possibility to synthetize a variety of materials[22-26]. Moreover, the nanoparticles collecting in liquid allow avoiding the use of vacuum equipment. PLAL operates in water or organic liquids under ambient conditions. The solvent can provide positive physical and chemical effects such as plasma confinement, cooling actions, oxidation or reduction leading to enhancement of ablation efficiency[27-30]. The process proceeds in one step and results in immediate formation of nanoparticles in the liquid in which the target is immersed. For this reason laser ablation of solids in liquids can be considered as a method of nanoparticle synthesis alternative to chemical methods. The formation of the mentioned oxides with certain structural and physical properties is mainly affected by the laser type (milli-/nano-/pico-/femto-second) and preparation conditions (frequency, pulse energy, duration of ablation, etc.)[31-34]. Some authors assume that the usage of femtosecond lasers can effectively control the nanoparticle size in comparison to nanosecond laser ablation, and minimizes laser–plume interaction as well as reduces the heat affected zones.[35,36]

2.1.10. Seeded Growth Methods

In seeded growth method, preformed seeds provide the nuclei for subsequent growth of metallic nanoparticles. It is not necessary that the seeds have the same composition of the material deposited upon them. Seeded growth suits the criteria of separated nucleation and growth kinetics and may offer a valid strategy for the synthesis of a wide variety of monodisperse metallic nanoparticles of controlled size. Seeded growth has

been employed in a few cases for the growth of large metallic nanoparticles on seeds of the same metal (homogeneous seeded growth).[37-40] it has also been used to prepare core-shell bimetallic nanoparticles in which the cores constitute a substantial volume fraction of the nanoparticles (heterogeneous seeded growth)[41]. In the case of TiO_2, this kind of approach was used by Gordon et al.[42] to synthetized shape controlled anatase nanoparticles in an inert atmosphere starting from TiF_4 and/or $TiCl_4$ as precursor and 1-octadecanol or oleylamine as co-surfactant. The use of the seeded growth method leads to synthetize very shape defined nanoparticles with a high size evenness (Figure 11). Instead, Buonsanti et al. exploited the seeded growth method to synthetize shape controlled brookite nanorods[43]. Phase-controlled nanorods were first prepared in an independent synthesis step and then employed as the starting seeds for producing comparatively larger nanorods in fresh $TiCl_4$/Oleic Acid/Oleylamine mixture.

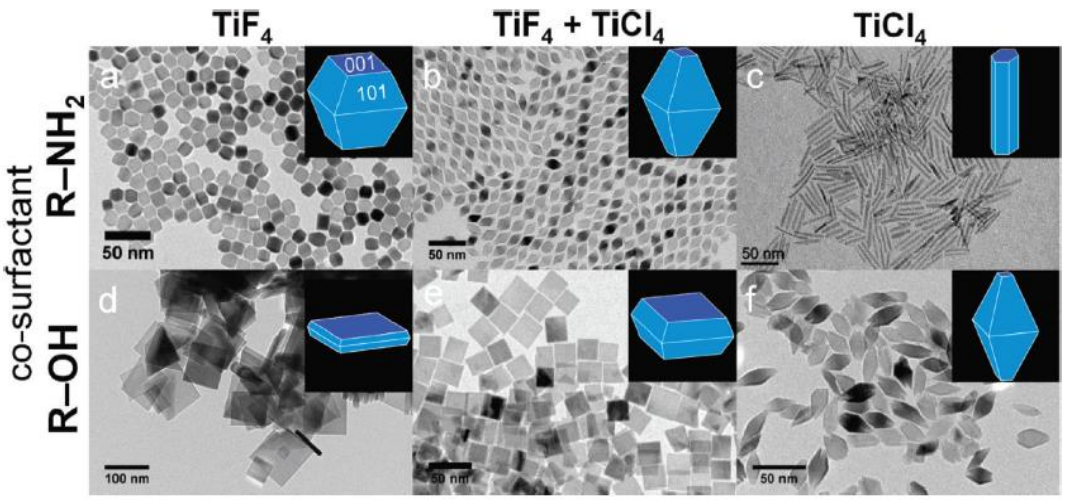

Figure 11. TEM images of TiO_2 NCs synthesized using the precursor TiF_4 (a,d), a mixed precursor of TiF_4 and $TiCl_4$ (b,e), and $TiCl_4$ (c,f). Those depicted in a–c and d–f are synthesized in the presence of oleylamine and 1-octadecanol, respectively[42]

2.1.11. Microemulsions Methods

The microemulsion method is often employed to synthesize nanoparticles with specific size and morphology. The advantage of the method is the possibility to control particle size with narrow size distribution. Microemulsions are used as nano-reactors for the synthesis of nanoparticles, without needing expensive or specialized equipment comparing with other synthesis techniques such as plasma or chemical vapor deposition. The synthesis take advantage of reverse micelles characteristics, where it is favored the formation of small crystallites. It is important in the case of nanoparticles' preparation the choice of the adapt microemulsion system, which has to be stable at the temperature needed for the synthesis. There are two main ways of preparation in order to obtain nanoparticles from microemulsions:

- By mixing two microemulsions, one is containing the precursor and the other the precipitating agent;
- By adding the precipitating agent directly to the microemulsion containing the metal precursor.

The size of the final particle will depend on the size of the droplets in the microemulsion. The microemulsion is a dynamic system, which means that during the process a constant collision of the aggregates takes place. Consequently, the formation of particles proceeds in two steps:

1. first the nucleation process inside the droplet;
2. then the aggregation process to form the final particle.

The rate of particle growth is controlled by the presence of surfactants, which sterically prevents the too fast nuclei growth. Therefore, the growth rate is the same for all the nanoparticles, resulting in the formation of particles of homogeneous size distribution. The size of the droplet will influence the size of the nuclei but the surrounding surfactant molecules will control the size of the final particle. Regarding to titania nanoparticles, in the last few years reverse micelle method was successfully applied to synthesize nanosized titania particles in reverse micelles or water/oil (W/O) microemulsion systems using titanium alkoxides as starting materials[44,45].

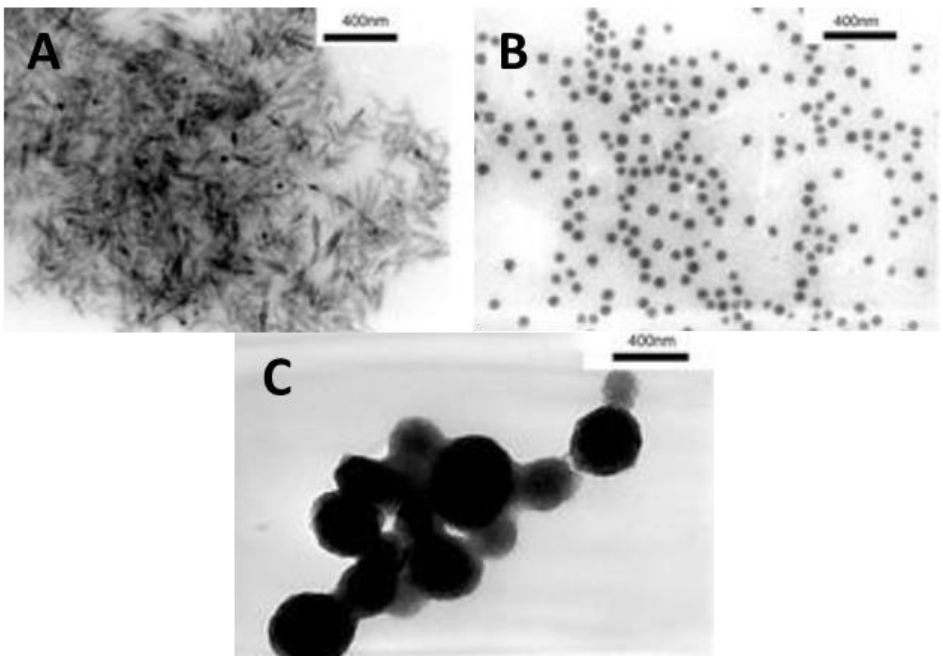

Figure 12. TEM micrographs of TiO_2 NCs prepared by reverse micelle method from titaniumbutoxide in the presence of different acids: (A) nitric acid, (B) sulfuric acid, and (C) phosphoric acid.[46]

2.2. Shape Controlled TiO_2 NPs – State of the art

Engineering the shapes of some materials to desirable morphologies was actively pursued. Many applications, such as heterogeneous catalysis, molecule adsorption, gas sensing and energy conversion are strongly dependent from surface atomic structures, which can be finely tailored by morphology control. Meaningful advancements in this area have been achieved.[42,43,47-54] Albeit a large amount of both experimental and theoretical studies have been carried out on the characteristics and reactivity of different surfaces of metal oxides,[55-63] less attention was paid on the dependence of functional properties on crystal surfaces exposed by metal oxides.[64,65] By tuning the ratio of different facets, the functional properties correspondingly change.

It is generally that a surface with a high percentage of under-coordinated atoms has a greater reactivity compared to those with a lower percentage of under-coordinated atoms[66-69]. A cooperative mechanism involving both favorable surface atomic structures and surface electronic structures has been recently proposed in order to explain the differences in reactivity[70]. Unluckily, surface with higher reactivity usually have a high surface energy, so the possibility to obtain a pristine facet without the use of adsorbates was questioned[68], and upon removing the adsorbates the surface can reconstruct. Obtaining reactive facets is highly desirable for improving and tuning functional properties. The shape evolution during the crystal growth is driven by the continue decrease of the total surface energy until the

minimum surface energy point. Such process is conditioned by the species presents in the reaction environment and their concentrations. The growth of nanocrystals with high percentage of reactive facets is realized using two different approaches:

- non equilibrium methods, that rely on fast quenching of high temperature precursors;
- methods with bottom-up or top-down approaches.

In the first case is difficult accurately control all the relevant process parameters in order to obtain nanoparticles with low polydispersity both of shape and size. Ohtani et al. used controlled flame pyrolysis of $TiCl_4$ for the preparation of truncated anatase bipyramids with reasonable polydispersity.[71] $TiCl_4$ vapors were mixed with an oxygen stream, and feeding into a quartz glass tube heated uniformly and rapidly until 1573 K. In this manner, it possible to obtain a homogeneous nucleation and the subsequent growth of well faceted crystals with few defects is favored. The synthesis of aggregates and large particles is avoided thanks to the low concentration of $TiCl_4$ and the narrow heating zone.

Bottom-up approach entails the nucleation and growth of shape controlled nanoparticles. Instead, top-down method occurs with selective etching of preformed crystal until a desirable shape. These methods are intrinsically near to the thermodynamic equilibrium, so it is necessary stabilize the desired surface in the hydrothermal medium using the so called "shape controllers". Usually these adsorbates or solvents strongly interact with a defined surface, supporting the selective growth of a given type of surface. The pioneering work of Yang et al. used for the first time this paradigm for

stabilizing the {001} surface of TiO_2 during crystal growth using fluorides as capping agent.[72]

Concerning the bottom-up approach, the reaction environment strongly influences the density, the size distribution and the surface chemistry of the nuclei. Consequently, the growth of the surviving nucleus after the coarsening and thus the final shape can be very different depending on the synthesis parameters. Solvents and potential adsorbates act as shape controllers, capping and inhibiting the growth of the nanoparticles along given crystallographic axes[73-76]. The solvent effect is generated via the different interactions with different crystal planes, stabilizing preferentially one of them[77]. Due to the interaction between shape controllers and surfaces with different atomic arrangements, additives can tune the growth rates along different axes, tailoring the shape of the crystal.

The top-down route can also be used in order to control the facets of single crystal particles. This approach has been adopted for the synthesis of some metal oxide such as Fe_2O_3[78], WO_3[79] and TiO_2[80]. In this case a partial dissolution of preformed crystals occurs. The key point is the selection of an appropriate etching and capping agents. Depending on the properties of the pre-existing crystal, the etchant and capping agent, the resulting shape can vary substantially. For example, the etching of TiO_2 anatase microcrystals with H_2SO_4 lead to the formation of high index {112} surfaces[80].

2.2.1. The Wulff construction

The equilibrium shape of crystal structures can be predicted by using the Wulff construction, taking into account the surface energies of the crystal surfaces in the growth medium, if they are available. In the Wulff construction, surface energy minimization is used in order to optimize the composition of the crystal surface. The disadvantage is that only the surface energies for clean crystal planes in vacuum are readily available, and only in these conditions the equilibrium shape obtained is valid. As said in the previous paragraph, the presence of a liquid phase, electrolytes and adsorbates can change the equilibrium shape. TiO_2 polymorphs are anatase, rutile and brookite. All three phases are constituted by TiO_6 octahedra, but in the case of anatase and rutile the crystal system is tetragonal, while for brookite is orthorhombic. The TiO_6 octahedra have different arrangements in the three polymorphs, it follows that the surface terminations in various orientations are different, as well as the equilibrium morphologies of the crystals.

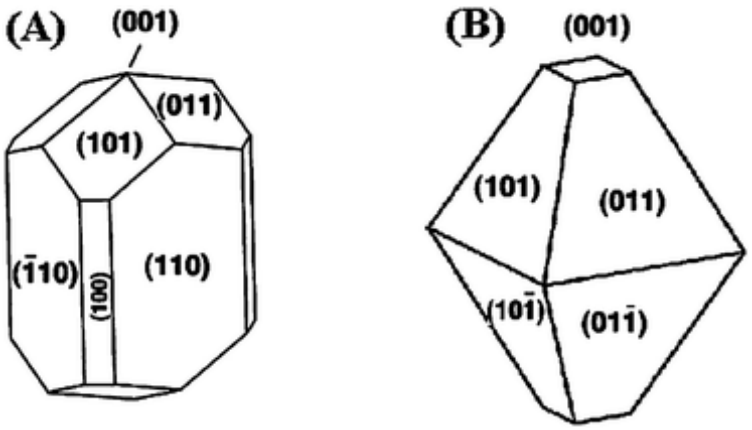

Figure 13. Equilibrium shape using Wulff construction for macroscopic crystals of rutile (A) and anatase (B) [56,81]

According to the Wulff construction, the equilibrium shape of the anatase is a lightly truncated bipyramid enclosed with eight trapezoidal {101} surfaces (>94%) and two top squares {001} surfaces, as shown in Figure 13. Regarding rutile, the predicted equilibrium shape of a macroscopic crystal contains (110), (100), (001) and (011) faces (Figure 13)[82].

All the above equilibrium shapes predicted must be considered only in vacuum at absolute zero temperature, which is clearly different from possible hydrothermal/solvothermal conditions. Barnard et al., by means of theoretical approaches, found that the presence of water could influence the equilibrium shapes by changing the size and the aspect ratio of anatase {001} and rutile[83]. Despite the high differences among vacuum conditions used in the calculations and real conditions for crystal growth, the most stable facets predicted usually represent the largest fraction also in the real crystal surfaces.

In hydrothermal/solvothermal conditions, TiO_2 crystals are synthetized in either acidic or alkaline conditions, their morphologies varies with the surface chemistry involved and therefore with the pH of the synthesis environment. Based on surface free energies and interfacial tensions, again Barnard et al.[84] studied the effects of acidic or alkaline conditions on the morphologies of anatase and rutile nanoparticles. As shown in Figure 14, in acidic conditions the surface termination by hydrogen result in a little change in the shapes of both polymorphs relative to vacuum conditions. However, in water terminated surfaces and/or hydrogen-poor surfaces, both polymorphs seem to be elongated. New {010} surfaces appear in the crystal shape of anatase. These predictions are very important to fine-tune the morphology by controlling surface chemistry.

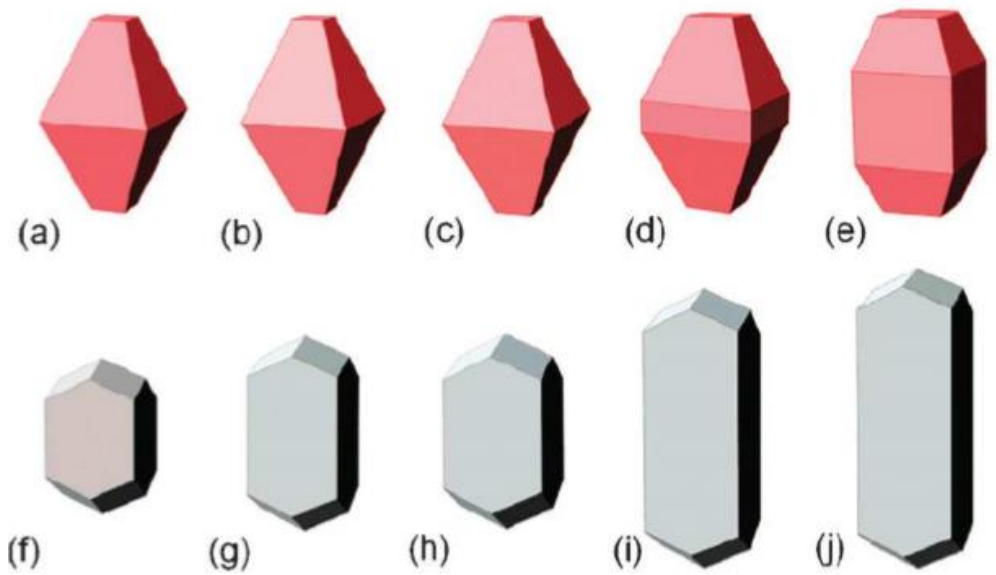

Figure 14. Crystal shape predicted for anatase (top) with (a) hydrogenated surfaces, (b) with hydrogen-rich surface adsorbates, (c) hydrated surfaces, (d) hydrogen-poor adsorbates and (e) oxygenated surfaces, and rutile (bottom) with (f) hydrogenated surfaces, (g) with hydrogen rich surface adsorbates, (h) hydrated surfaces, (i) hydrogen-poor adsorbates and (j) oxygenated surfaces. Adapted from ref. 84.

Rapid growth rates usually lead to crystals exposing a large percentage of high surface energies facets. Moreover, appropriate shape controllers may relevantly decrease the surface energy of defined facets and thus lead to crystal shapes with relatively high percentage of high-energy surfaces. Yang et al.[72] theoretically investigate the influence of some non-metal atoms on the surface energies of anatase (101) and (001), and found that surface terminated fluorine could effectively reverse the stabilities of (101) and (001). Their subsequent experimental results confirmed the key role of surface fluorine in stabilizing {001}.

2.2.2. Anatase NPs with high percentage of {101} surface

{101} facets dominate the surface of most anatase nanoparticles. Through the Ostwald ripening of amorphous hydrated TiO_2 it is possible to obtain regular {101} facets. As early as 1999, lightly truncated bipyramidal crystals with well-defined {101} surfaces were synthetized by coarsening pristine titania particles using sol–gel routes under various hydrothermal conditions[85]. The percentage of (101) can be varied changing the growth rates along <001> and <101> directions during different growth stages. In all cases, the driving force is the reduction in surface energy. Minimizing the presence of high energy surfaces allows reducing surface energy, inducing the morphology evolution. Recently, approaches using titanates as feeder have been reported to obtain anatase with a high percentage of {101}. Ohtani et al.[86,87] reported a hydrothermal transformation directly from potassium titanate nanowires to bipyramidal anatase single crystals with predominant {101} surface.

The role of the water in promoting the growth of bipyramidal nanoparticles that largely expose {101} facets in acidic or neutral media is confirmed by Liu et al.[88], who obtained anatase bipyramids treating at 453 K a suspension of amorphous $Ti(OH)_4$ in water/ethanol solution. They proposed to control the shape of the final anatase nanoparticles by adding a capping reagent able to control the crystal growth. The presence of fluorides increase the truncation level of the bipyramids, increase the amount of {001} surface to 30-40%, whereas sulphates allow to synthetize nanorods

with high percentage of (100) facets. Using oxalate and lactate the solvothermal treatment leads to rutile and brookite nanorods, respectively.

Dai et al.[89] employed small particles of amorphous TiO_2 obtained by electrospinning as precursor to prepare truncated bipyramids of anatase via a hydrothermal route. Low pH leads to percentages of {101} near 90%.

Sugimoto et al. proposed the use of a gel-sol technique, involving the jellification of a concentrated water solution of a Ti(IV)-triethanolammine complex at 373 K. Then the gel is treated at 413 K. Changing the pH from 0.6 to 10 the anatase NPs size increased from 5 to 24 nm, but the shape seem to remain cuboidal[90,91]. Over pH 10 "ellipsoidal" nanoparticles where synthetized due to the adsorption of triethanolammine along the planes parallel to the c-axis.

Recently the reproducible preparation of anatase bipyramids with high percentage of {101} exposed was achieved by hydrothermal treatment of Ti(IV)-triethanolammine complex aqueous solution at 423-483 K[1]. Variation of the temperature allows the control of particle size. At 453 K, uniform bipyramids with 20 nm hydrodynamic radius are obtained.

2.2.3. Anatase NPs with high percentage of {001} surface

Anatase nanoparticles with a large percentage of {001} facets has become a target in the synthesis of anatase TiO_2 crystals since Yang et al. realized the first case of 47% (001) in uniform crystals. Synthesis procedures

leading to NPs have been developed with higher {001} percentages.[42,71,89,92-100]

Controlling the concentrations of precursors and fluorine species, also with the synergistic effects of other capping agents, the relative percentage of (001) surfaces can be tuned. For example, the percentage of {001} increases from 18% to 72% decreasing the concentration of $Ti(SO_4)_2$ from 100 to 10 mM.[93] Zhang et al.[101] showed that the percentage gradually improved with increasing amount of 1-butyl-3-methylimidazolium tetrafluoroborate.

It was found that the increase of the surface coverage fractions of fluorine increase the percentage of (001). Theoretically, different surface coverage fractions can greatly affect the surface energy and thus the percentage of {001} during the growth of crystals[93].

By employing alcohol as synergistic capping agent, the percentage can be further improved.[94,96]

The sources of fluorine includes the most frequently used hydrofluoric acid (HF), 1-butyl-3- methylimidazolium tetrafluoroborate[102], ammonium bi-fluoride[103], ammonium fluoride[104], and titanium tetrafluoride (TiF_4) precursor itself[105]. It seems that all precursors can be used for tailoring both the percentage of {001} facets and particle size. Therefore, the type of precursors is not a decisive factor in growing the desired pure anatase crystals.

Two other methods have also been developed to synthetize anatase nanoparticles with a high percentage of {001} facets. The first one

provides the direct conversion of amorphous TiO_2 nanotube arrays on Ti foil to anatase crystals with well-defined {101} and {001} by calcining at a temperature above 673 K in air for 2 h[104]. The other is to use a gas phase reaction of $TiCl_4$ with O_2 in a non-equilibrium method with fast quenching of the system from 1473 K as described in the preceding section[71]. In this way, small TiO_2 particles (50–250 nm) could be obtained at such high temperature without using fluorine-containing reactants.

Besides fluoride, other shape controllers were proposed to grow anatase nanoparticles with high exposition of {001} surfaces. Chen et al. proved that diethylenetriamine in isopropyl alcohol could act as an alternative morphology controlling agent in a solvothermal system[106]. The freshly prepared TiO_2 microspheres consisting of {001} dominant sheets are poor in crystallinity. Post-calcination at 673 K in air leads to increased crystallinity without morphology change.

2.2.4. Anatase NPs with high percentage of {010} surface

Compared to the widely investigated {101} and {001}, the {010} facets are experimentally less studied. Actually, as far as the density of surface unsaturated Ti atoms is concerned, {010} has the same 100% Ti_{5c} as {001}. So, {010} surfaces are considered favorable for heterogeneous reactions, suggesting an improvement of functional properties. Furthermore, theoretical results have predicted that, water molecules can be adsorbed dissociatively on (010) face, whereas is molecularly absorbed on (101) face and partially dissociates on the (001) face.[107]

Fabrication of anatase crystals with 43.4% of {010} facets was reported by Wu et al.[108]. Dinh et al. also reported routes to prepare anatase crystals in various shapes[109]. In their approach, the use of water vapor as hydrolysis agent to accelerate the reaction is crucial, together with the use of both oleic acid and oleylamine as capping surfactants. Different shapes such as rhombic, truncated rhombic, spherical, dog-bone, truncated and elongated rhombic and bars could be synthetized. Although the authors did not identify crystallographic facets of the exposed surface, it is possible to conclude, based on the symmetries and predicted morphologies of anatase, that the elongated crystals expose (010) facets.

Li et al. used sodium titanate nanotubes to prepare uniform anatase nanorods with a large percentage of (010) facets by a hydrothermal process in basic solution[110]. The proposed growth mechanism involves the formation of $Ti(OH)_4$ fragments from titanate nanotubes and subsequent anatase crystal nuclei by dehydration reaction between Ti–OH and HO–Ti. The continuous release of OH- during the hydrothermal process plays a key role in generating (010) facets. Barnard et al.[84] showed that O-terminated (010) had a lower surface energy than O-terminated (101) and (001). It was believed that the preferential adsorption of hydroxyl ion on (010) face contributed to stabilize the (010) faces.

By controlling carefully the preparation parameters, Pan et al.[70] prepared anatase single crystals with a predominance of {101}, {001} and {010}, respectively. The synthesis are carried out mixing different amount of HF solutions (120, 80 and 40 mM) with different quantities of $TiOSO_4$ precursor (64, 32 and 32 mg) and heating at 453K for 12,12 and 2 hours respectively.

Bibliography

(1) Deiana, C.; Minella, M.; Tabacchi, G.; Maurino, V.; Fois, E.; Martra, G. *Physical Chemistry Chemical Physics* **2013**, *15*, 307.

(2) Zhang, Q.; Gao, L. *Langmuir* **2003**, *19*, 967.

(3) Wanga, D.; Yu, B.; Zhoua, F.; Wang, C.; Liua, W. *Materials Chemistry and Physics* **2009**, *113*, 602.

(4) Xie, R. C.; Shang, J. K. *Journal of Materials Science* **2007**, *42*, 6583.

(5) Wu, J. M. *J Cryst Growth* **2004**, *269*, 347.

(6) Ryu, W. H.; Park, C. J.; Kwon, H. S. *Journal of nanoscience and nanotechnology* **2008**, *8*, 5467.

(7) Djenadic, R.; Winterer, M. In *Nanoparticles from the Gas Phase*; Lorke, A., Winterer, M., Schmechel, R., Schulz, C., Eds.; Springer-Verlag Berlin Heidelberg: 2012, p 49.

(8) Lee, H.; Song, M. Y.; Jurng, J.; Park, Y. K. *Powder Technol* **2011**, *214*, 64.

(9) Xie, H. Y.; Gao, G. L.; Tian, Z.; Bing, N.; Wang, L. J. *Particuology* **2009**, *7*, 204.

(10) Lei, Y.; Zhang, L. D.; Fan, J. C. *Chem Phys Lett* **2001**, *338*, 231.

(11) Liu, S. Q.; Huang, K. L. *Sol Energ Mat Sol C* **2005**, *85*, 125.

(12) Blesic, M.; Saponjic, Z. V.; Nedeljkovic, J. M.; Uskokovic, D. P. *Materials Letters* **2002**, *54*, 298.

(13) Guo, W.; Lin, Z.; Wang, X.; Song, G. *Microelectronic Engineering* **2003**, *66*, 95.

(14) Huang, W. P.; Tang, X. H.; Wang, Y. Q.; Koltypin, Y.; Gedanken, A. *Chemical communications* **2000**, 1415.

(15) Meskin, P. E.; Ivanov, V. K.; Barantchikov, A. E.; Churagulov, B. R.; Tretyakov, Y. D. *Ultrasonics sonochemistry* **2006**, *13*, 47.

(16) Chen, X.; Mao, S. S. *Chemical reviews* **2007**, *107*, 2891.

(17) Corradi, A. B.; Bondioli, F.; Focher, B.; Ferrari, A. M.; Grippo, C.; Mariani, E.; Villa, C. *J Am Ceram Soc* **2005**, *88*, 2639.

(18) Gressel-Michel, E.; Chaumont, D.; Stuerga, D. *J Colloid Interface Sci* **2005**, *285*, 674.

(19) Ma, G. B.; Zhao, X. N.; Zhu, J. M. *Int J Mod Phys B* **2005**, *19*, 2763.

(20) Del Angel-Sanchez, K.; Vazquez-Cuchillo, O.; Aguilar-Elguezabal, A.; Cruz-Lopez, A.; Herrera-Gomez, A. *Materials Chemistry and Physics* **2013**, *139*, 423.

(21) Del Angel-Sanchez, K.; Vazquez-Cuchillo, O.; Salazar-Villanueva, M.; Sanchez-Ramirez, J. F.; Cruz-Lopez, A.; Aguilar-Elguezabal, A. *J Sol-Gel Sci Techn* **2011**, *58*, 360.

(22) Kabashin, A. V.; Meunier, M. *J Phys Conf Ser* **2007**, *59*, 354.

(23) Mafune, F.; Kohno, J. Y.; Takeda, Y.; Kondow, T. *Journal of Physical Chemistry B* **2002**, *106*, 7575.

(24) Musaev, O. R.; Dusevich, V.; Wieliczka, D. M.; Wrobel, J. M.; Kruger, M. B. *J Appl Phys* **2008**, *104*.

(25) Musaev, O. R.; Midgley, A. E.; Muthu, D. V. S.; Wrobel, J. M.; Kruger, M. B. *Materials Letters* **2009**, *63*, 893.

(26) Tsuji, T.; Tatsuyama, Y.; Tsuji, M.; Ishida, K.; Okada, S.; Yamaki, J. *Materials Letters* **2007**, *61*, 2062.

(27) Tsuji, T.; Tsuboi, Y.; Kitamura, N.; Tsuji, M. *Applied Surface Science* **2004**, *229*, 365.

(28) Tsuji, T.; Thang, D. H.; Okazaki, Y.; Nakanishi, M.; Tsuboi, Y.; Tsuji, M. *Applied Surface Science* **2008**, *254*, 5224.

(29) Hong, S. M.; Lee, S.; Jung, H. J.; Yu, Y.; Shin, J. H.; Kwon, K. Y.; Choi, M. Y. *B Korean Chem Soc* **2013**, *34*, 279.

(30) Liu, P. S.; Cai, W. P.; Wan, L. X.; Shi, M. D.; Luo, X. D.; Jing, W. P. *T Nonferr Metal Soc* **2009**, *19*, S743.

(31) Mahdieh, M. H.; Fattahi, B. *Applied Surface Science* **2015**, *329*, 47.

(32) Papadopoulou, E. L.; Intartaglia, R.; Scarpellini, A.; Rodio, M.; Bayer, I. S.; Athanassiou, A. *Laser Phys Lett* **2015**, *12*.

(33) Sajti, C. L.; Sattari, R.; Chichkov, B. N.; Barcikowski, S. *J Phys Chem C* **2010**, *114*, 2421.

(34) Yang, C. J.; Tian, Y. L.; Cui, L. Y.; Zhang, D. W. *Radiat Eff Defect S* **2015**, *170*, 528.

(35) Alnassar, S. I.; Akman, E.; Oztoprak, B. G.; Kacar, E.; Gundogdu, O.; Khaleel, A.; Demir, A. *Opt Laser Technol* **2013**, *51*, 17.

(36) Tan, D. Z.; Lin, G.; Liu, Y.; Teng, Y.; Zhuang, Y. X.; Zhu, B.; Zhao, Q. Z.; Qiu, J. R. *J Nanopart Res* **2011**, *13*, 1183.

(37) Brown, K. R.; Natan, M. J. *Langmuir* **1998**, *14*, 726.

(38) Shirtcliffe, N.; Nickel, U.; Schneider, S. *Journal of Colloid and Interface Science* **1999**, *211*, 122.

(39) Jana, N. R.; Wang, Z. L.; Sau, T. K.; Pal, T. *Curr Sci India* **2000**, *79*, 1367.

(40) Henglein, A.; Meisel, D. *Langmuir* **1998**, *14*, 7392.

(41) Schmid, G.; West, H.; Malm, J. O.; Bovin, J. O.; Grenthe, C. *Chem-Eur J* **1996**, *2*, 1099.

(42) Gordon, T. R.; Cargnello, M.; Paik, T.; Mangolini, F.; Weber, R. T.; Fornasiero, P.; Murray, C. B. *J Am Chem Soc* **2012**, *134*, 6751.

(43) Buonsanti, R.; Grillo, V.; Carlino, E.; Giannini, C.; Kipp, T.; Cingolani, R.; Cozzoli, P. D. *J Am Chem Soc* **2008**, *130*, 11223.

(44) Gao, X.; Li, J.; Gao, W. *Colloid Journal* **2008**, *70*, 392.

(45) Hada, R.; Amritphale, A.; Amritphale, S. S.; Dixit, S. *The Open Mineral Processing Journal* **2010**, *3*, 68.

(46) Zhang, D. B.; Qi, L. M.; Ma, J. M.; Cheng, H. M. *J Mater Chem* **2002**, *12*, 3677.

(47) Habas, S. E.; Lee, H.; Radmilovic, V.; Somorjai, G. A.; Yang, P. *Nat Mater* **2007**, *6*, 692.

(48) Tsung, C. K.; Kuhn, J. N.; Huang, W.; Aliaga, C.; Hung, L. I.; Somorjai, G. A.; Yang, P. *J Am Chem Soc* **2009**, *131*, 5816.

(49) Tao, A.; Sinsermsuksakul, P.; Yang, P. *Angewandte Chemie* **2006**, *45*, 4597.

(50) Hochbaum, A. I.; Yang, P. *Chemical reviews* **2010**, *110*, 527.

(51) Xia, Y.; Xiong, Y.; Lim, B.; Skrabalak, S. E. *Angewandte Chemie* **2009**, *48*, 60.

(52) Lim, B.; Kobayashi, H.; Yu, T.; Wang, J.; Kim, M. J.; Li, Z. Y.; Rycenga, M.; Xia, Y. *J Am Chem Soc* **2010**, *132*, 2506.

(53) Yin, Y.; Erdonmez, C.; Aloni, S.; Alivisatos, A. P. *J Am Chem Soc* **2006**, *128*, 12671.

(54) Feng, X.; Zhai, J.; Jiang, L. *Angewandte Chemie* **2005**, *44*, 5115.

(55) Yi, Z.; Ye, J.; Kikugawa, N.; Kako, T.; Ouyang, S.; Stuart-Williams, H.; Yang, H.; Cao, J.; Luo, W.; Li, Z.; Liu, Y.; Withers, R. L. *Nat Mater* **2010**, *9*, 559.

(56) Diebold, U. *Surf. Sci. Rep.* **2003**, *48*, 53.

(57) Gong, X. Q.; Selloni, A.; Batzill, M.; Diebold, U. *Nat Mater* **2006**, *5*, 665.

(58) Setvin, M.; Hulva, J.; Wang, H. H.; Simschitz, T.; Schmid, M.; Parkinson, G. S.; Di Valentin, C.; Selloni, A.; Diebold, U. *J Phys Chem C* **2017**, *121*, 8914.

(59) Selcuk, S.; Selloni, A. *Nat Mater* **2016**, *15*, 1107.

(60) Setvin, M.; Aschauer, U.; Hulva, J.; Simschitz, T.; Daniel, B.; Schmid, M.; Selloni, A.; Diebold, U. *J Am Chem Soc* **2016**, *138*, 9565.

(61) Setvin, M.; Buchholz, M.; Hou, W. Y.; Zhang, C.; Stoger, B.; Hulva, J.; Simschitz, T.; Shi, X.; Pavelec, J.; Parkinson, G. S.; Xu, M. C.; Wang, Y. M.; Schmid, M.; Woll, C.; Selloni, A.; Diebold, U. *J Phys Chem C* **2015**, *119*, 21044.

(62) Dulub, O.; Batzilln, M.; Solovev, S.; Loginova, E.; Alchagirov, A.; Madey, T. E.; Diebold, U. *Science* **2007**, *317*, 1052.

(63) Li, S.-C.; Chu, L.-N.; Gong, X.-Q.; Diebold, U. *J. Mater. Chem.* **2010**, *20*, 10319.

(64) Kavan, L.; Gratzel, M.; Gilbert, S. E.; Klemenz, C.; Scheel, H. J. *J Am Chem Soc* **1996**, *118*, 6716.

(65) Jang, E. S.; Won, J. H.; Hwang, S. J.; Choy, J. H. *Adv Mater* **2006**, *18*, 3309.

(66) Gong, X. Q.; Selloni, A. *The journal of physical chemistry. B* **2005**, *109*, 19560.

(67) Vittadini, A.; Selloni, A.; Rotzinger, F. P.; Gratzel, M. *Phys Rev Lett* **1998**, *81*, 2954.

(68) Selloni, A. *Nat Mater* **2008**, *7*, 613.

(69) Vittadini, A.; Casarin, M.; Selloni, A. *Theor Chem Acc* **2007**, *117*, 663.

(70) Pan, J.; Liu, G.; Lu, G. Q.; Cheng, H. M. *Angewandte Chemie* **2011**, *50*, 2133.

(71) Amano, F.; Prieto-Mahaney, O. O.; Terada, Y.; Yasumoto, T.; Shibayama, T.; Ohtani, B. *Chem Mater* **2009**, *21*, 2601.

(72) Yang, H. G.; Sun, C. H.; Qiao, S. Z.; Zou, J.; Liu, G.; Smith, S. C.; Cheng, H. M.; Lu, G. Q. *Nature* **2008**, *453*, 638.

(73) Davey, R. J. *J Cryst Growth* **1986**, *76*, 637.

(74) Bourne, J. R.; Davey, R. J. *J Cryst Growth* **1976**, *36*, 278.

(75) Bourne, J. R.; Davey, R. J. *J Cryst Growth* **1976**, *36*, 287.

(76) M., L.; L., L. *Chemical Engineering Science* **2001**, *56*, 2245.

(77) Lovette, M. A.; Browning, A. R.; Griffin, D. W.; Sizemore, J. P.; Snyder, R. C.; Doherty, M. F. *Ind Eng Chem Res* **2008**, *47*, 9812.

(78) Chen, J. S.; Zhu, T.; Yang, X. H.; Yang, H. G.; Lou, X. W. *J Am Chem Soc* **2010**, *132*, 13162.

(79) Zhao, Z. G.; Liu, Z. F.; Miyauchi, M. *Chem Commun (Camb)* **2010**, *46*, 3321.

(80) Taguchi, T.; Saito, Y.; Sarukawa, K.; Ohno, T.; Matsumura, M. *New Journal of Chemistry* **2003**, *27*, 1304.

(81) Lazzeri, M.; Vittadini, A.; Selloni, A. *Physical Review B* **2003**, *66*, 1199011.

(82) Ramamoorthy, M.; Vanderbilt, D.; King-Smith, R. D. *Physical review. B, Condensed matter* **1994**, *49*, 16721.

(83) Barnard, A. S.; Zapol, P.; Curtiss, L. A. *J. Chem. Theo. Comput.* **2005**, *1*, 107.

(84) Barnard, A. S.; Curtiss, L. A. *Nano letters* **2005**, *5*, 1261.

(85) Penn, R. L.; Banfield, J. F. *Geochim Cosmochim Ac* **1999**, *63*, 1549.

(86) Amano, F.; Yasumoto, T.; Prieto-Mahaney, O. O.; Uchida, S.; Shibayama, T.; Ohtani, B. *Chem Commun (Camb)* **2009**, 2311.

(87) Wei, Z. S.; Kowalska, E.; Ohtani, B. *Chemistry Letters* **2014**, *43*, 346.

(88) Liu, L. C.; Gu, X. R.; Ji, Z. Y.; Zou, W. X.; Tang, C. J.; Gao, F.; Dong, L. *J Phys Chem C* **2013**, *117*, 18578.

(89) Dai, Y.; Cobley, C. M.; Zeng, J.; Sun, Y.; Xia, Y. *Nano letters* **2009**, *9*, 2455.

(90) Sugimoto, T.; Zhou, X.; Muramatsu, A. *J Colloid Interface Sci* **2003**, *259*, 43.

(91) Sugimoto, T.; Zhou, X.; Muramatsu, A. *J Colloid Interface Sci* **2003**, *259*, 53.

(92) Han, X.; Kuang, Q.; Jin, M.; Xie, Z.; Zheng, L. *J Am Chem Soc* **2009**, *131*, 3152.

(93) Liu, G.; Sun, C.; Yang, H. G.; Smith, S. C.; Wang, L.; Lu, G. Q.; Cheng, H. M. *Chem Commun (Camb)* **2010**, *46*, 755.

(94) Yang, H. G.; Liu, G.; Qiao, S. Z.; Sun, C. H.; Jin, Y. G.; Smith, S. C.; Zou, J.; Cheng, H. M.; Lu, G. Q. *J Am Chem Soc* **2009**, *131*, 4078.

(95) Yang, W.; Li, J.; Wang, Y.; Zhu, F.; Shi, W.; Wan, F.; Xu, D. *Chem Commun (Camb)* **2011**, *47*, 1809.

(96) Zhu, J. A.; Wang, S. H.; Bian, Z. F.; Xie, S. H.; Cai, C. L.; Wang, J. G.; Yang, H. G.; Li, H. X. *Crystengcomm* **2010**, *12*, 2219.

(97) Yang, X. H.; Li, Z.; Sun, C. H.; Yang, H. G.; Li, C. Z. *Chem Mater* **2011**, *23*, 3486.

(98) Zhang, J.; Wang, J.; Zhao, Z.; Yu, T.; Feng, J.; Yuan, Y.; Tang, Z.; Liu, Y.; Li, Z.; Zou, Z. *Physical chemistry chemical physics : PCCP* **2012**, *14*, 4763.

(99) Wang, W.; Lu, C. H.; Ni, Y. R.; Xu, Z. Z. *Crystengcomm* **2013**, *15*, 2537.

(100) Ong, W. J.; Tan, L. L.; Chai, S. P.; Yong, S. T.; Mohamed, A. R. *Nanoscale* **2014**, *6*, 1946.

(101) Zhang, D. Q.; Li, G. S.; Wang, H. B.; Chan, K. M.; Yu, J. C. *Cryst Growth Des* **2010**, *10*, 1130.

(102) Zhang, D.; Li, G.; Yang, X.; Yu, J. C. *Chem Commun (Camb)* **2009**, 4381.

(103) Yu, J. G.; Xiang, Q. J.; Ran, J. R.; Mann, S. *Crystengcomm* **2010**, *12*, 872.

(104) Alivov, Y.; Fan, Z. Y. *J Phys Chem C* **2009**, *113*, 12954.

(105) Ma, X. Y.; Chen, Z. G.; Hartono, S. B.; Jiang, H. B.; Zou, J.; Qiao, S. Z.; Yang, H. G. *Chemical communications* **2010**, *46*, 6608.

(106) Chen, J. S.; Tan, Y. L.; Li, C. M.; Cheah, Y. L.; Luan, D. Y.; Madhavi, S.; Boey, F. Y. C.; Archer, L. A.; Lou, X. W. *J Am Chem Soc* **2010**, *132*, 6124.

(107) Sumita, M.; Hu, C.; Tateyama, Y. *The Journal of Physical Chemistry C* **2010**, *114*, 18529.

(108) Wu, B.; Guo, C.; Zheng, N.; Xie, Z.; Stucky, G. D. *J Am Chem Soc* **2008**, *130*, 17563.

(109) Dinh, C. T.; Nguyen, T. D.; Kleitz, F.; Do, T. O. *ACS nano* **2009**, *3*, 3737.

(110) Li, J.; Xu, D. *Chem Commun (Camb)* **2010**, *46*, 2301.

Aims of the Thesis

The PhD work is carried out in the framework of a European project named SETNanoMetro. The project stems from the importance to establish validated methods and instrumentations for detection, characterization and analysis of nanoparticles. Central is the development of new synthetic procedures and paradigms for the production of shape and size controlled sets of TiO_2 NPs. The use of various measurement techniques for the determination of the NPs properties allowed moving from the "trial and error" approach toward the development of well-defined and controlled protocols for the production of TiO_2 NPs.

In this work, different shape and size TiO_2 nanoparticles were synthetized by hydrothermal and solvothermal methods. These methods were chosen due to the possibility to produce good-quality crystals with a good control over their composition and morphology. Furthermore, the hydro/solvo-thermal growth of nanoparticles can be easily modeled for obtaining designed rules for shape and size controlled crystals. Nanoparticles were then fully characterized from a physico-chemical point of view and a model was developed in order to predict the shape and the size of TiO_2 nanoparticles using a hydrothermal method. Moreover, the functional properties of selected materials were studied, investigating in particular how the exposition of different surfaces can affect the TiO_2 NPs photocatalytic behavior in heterogeneous photocatalysis, revealing the mechanisms of degradation of different pollutants both in gas/solid and liquid/solid systems, and in the photocatalytic production of hydrogen by formic acid photoreforming, establishing a correlation between developed hydrogen amount and TiO_2 shape.

Experimental Section

Chapter 3

3.1. Hydrothermal Synthesis of TiO_2 Bipyramidal NPs

The synthesis of TiO_2 nanoparticles (NPs) with well-defined morphology and size is fundamental for the development of advanced nanomaterials in various application fields. Synthetic routes were developed for bipyramidal TiO_2 facet-controlled anatase NPs with low truncation along the c-axis and acicular morphology, through hydrothermal treatments of aqueous solutions of Ti^{IV}(triethanolamine)$_2$ complex.[1,2] The compounds that are formed by the complexation of Ti with triethanolamine are called titanatranes. Titanatranes were studied in detail in the last decades,[3,4] due to their potential use in the preparation of fine titania particles.[2,5-7] Triethanolamine in these compounds acts as a chelating ligand, with the three alkoxy groups that are able to coordinate the central Ti atom. This type of bonding results in moderate stability toward hydrolysis. Moreover, triethanolamine is able to displace ligands present in common titanium precursors, such as alkoxy groups, halides, and amides, allowing the easy production of the stable titanatrane.[1,8]

3.1.1. Precursor and Shape Controller

The precursor used for the hydrothermal synthesis of TiO_2 nanoparticles is a complex of Ti(IV) with $TeoaH_3$ with molar ratio 1:2. The synthesis of the precursor is carried out as follows: in a three-necked (ground joints) round-bottomed flask a certain amount of $TeoaH_3$ (Aldrich Reagent grade 98%) is poured. One of the grounds joint is equipped with a dropping funnel loaded with the required quantity of Ti(IV) isopropoxide (Aldrich reagent grade 98%). The flask and the funnels are maintained under a N_2 flow (O_2 concentration under 0.1% mol/mol). The Ti(IV) isopropoxide is then dropped into the triethanolamine under vigorous stirring. A vacuum pump is attached to the flask, maintaining a gentle flow of N_2, until the isopropyl alcohol is distilled off. The synthesis product is a pale yellow viscous liquid, to be stored at 277K under N_2. A reaction scheme is reported in Figure 15.

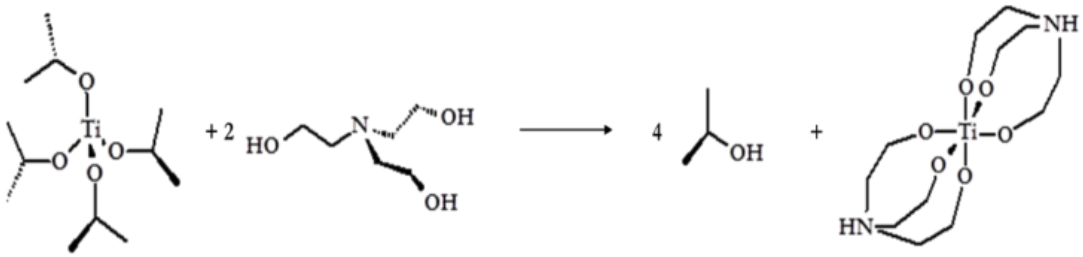

Figure 15. Synthesis of the Ti(IV) – $TeoaH_3$ 1:2 complex

The nominal Ti(IV) content of pure $[Ti(TeoaH)_2]$ is 14.00%. However the product IS titrated to determine the Ti content[9,10].

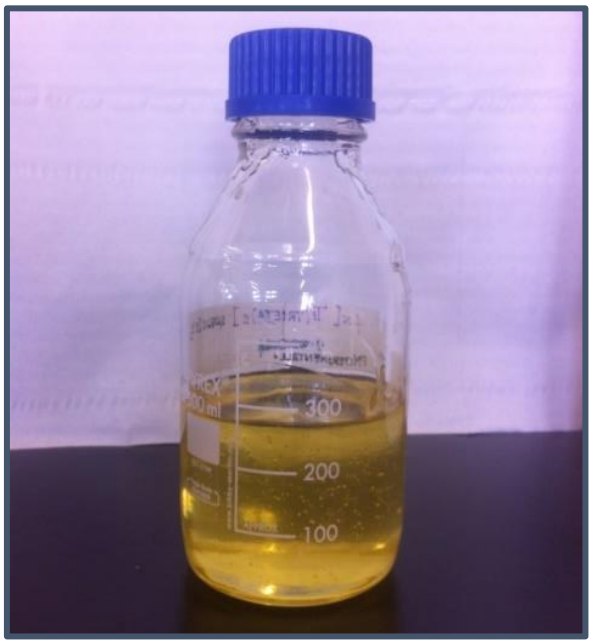

Figure 16. Picture of the yellow viscous liquid obtained in the Ti(IV) complex synthesis

3.1.1.1. Characterization of the Ti(IV)-TeoaH$_3$ species

A freshly prepared 40 mM Ti(TeoaH)$_2$ solution in water is diluted 1:100 with methanol and analysed by ESI-HRMS in order to characterize the Ti(IV) solution species. The spectrum is reported in Figure 17. The signal at m/z 172.0848 is the TeoaH$_3$ - Na^+ adduct ($C_6H_{15}O_3NNa$, Δmmu = -9.575). It is present also the signal of protonated TeoaH$_3$ at m/z 150.1040 ($C_6H_{16}O_3N$, Δmmu = -8.48). The presence of free TeoaH$_3$ signals means that the Ti(TeoaH)$_2$ complex is partially decomposed. The clusters centred at m/z 343.1126, 365.0963, 381.0693 have all the isotopic pattern of a molecule containing an atom of Ti (Figure 18). The first signal corresponds to the empirical formula $C_{12}H_{27}O_6N_2Ti$, the second to $C_{12}H_{26}O_6N_2TiNa$, the third to $C_{12}H_{26}O_6N_2TiK$, so they are the Ti(TeoaH)$_2$ complex cationized with H^+, Na^+ and K^+ respectively.

The clusters centred at m/z 536.1268, 558.1074, 574.0802 have all an isotopic pattern of a molecule containing two Ti atoms (Figure 19). The m/z ratios correspond to the empirical formulas $C_{18}H_{38}O_9N_3Ti_2$, $C_{18}H_{37}O_9N_3Ti_2Na$ and $C_{18}H_{37}O_9N_3Ti_2K$, so they can be attributed to the complex $Ti_2H(Teoa)_3$ cationized with H^+, Na^+ and K^+ respectively. It is worth to note that the mass difference between $Ti(TeoaH)_2$ and $Ti_2H(Teoa)_3$ is 193.0112, that, obviously, correspond to the mass of Ti plus Teoa (not $TeoaH_3$) minus the mass of a hydrogen. The series is completed by the clusters centred at 729.1384, 751.1193 and 767.2993, which correspond to $Ti_3(Teoa)_4$ ($C_{24}H_{48}O_{12}N_4Ti_3$) cationized by H^+, Na^+ and K^+ respectively. It is not possible to continue the sequence because $Ti_3(Teoa)_4$ has no longer mobile hydrogens. So the cluster centred at 938.3310 can't be assigned to protonated $Ti_4(Teoa)_5$. The mass difference between this ion and protonated $Ti_3(Teoa)_4$ at m/z 729.1384 is no longer 193.0112, but 209.1926. This corresponds to Ti plus Teoa plus oxygen minus hydrogen. So with this multinuclear complex the hydrolysis of Ti(IV) is starting. This is in partial agreement, at least with the stoichiometry, with the reported structures of titanatranes crystallized from organic solvents[11].

In conclusion, the solutions of $Ti(TeoaH)_2$ are not thermodynamically stable already at ambient temperature. However the hydrolysis in these conditions is slow and it could take days to go to completion. Taking into account that apparent activation energies of Ti-alkoxides hydrolysis are of the order of 30 kJ mol^{-1} ,[12] an increase of temperature of 100 K should increase the hydrolysis rates of three orders of magnitude in basic conditions, so the reaction goes to completion within minutes.

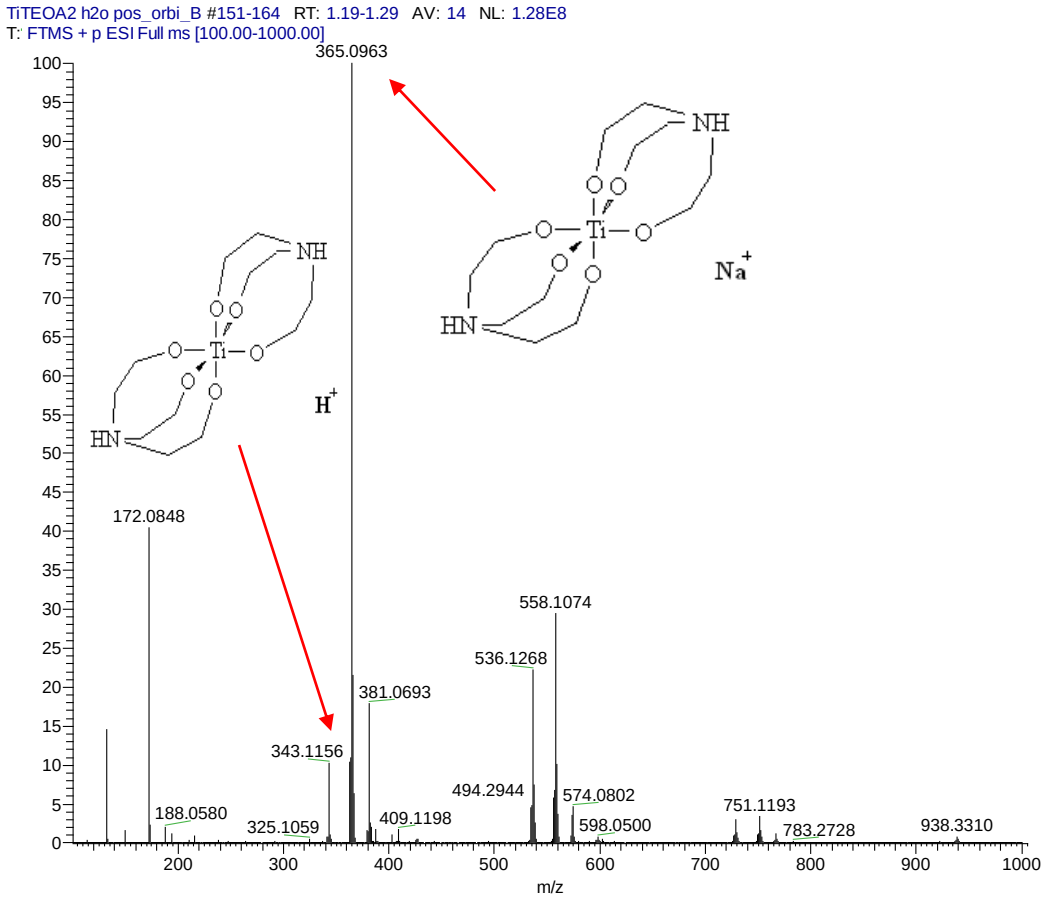

Figure 17. ESI-HRMS spectrum of a 40 mM aqueous solution of Ti(TeoaH)$_2$ diluted 1:100 in methanol.

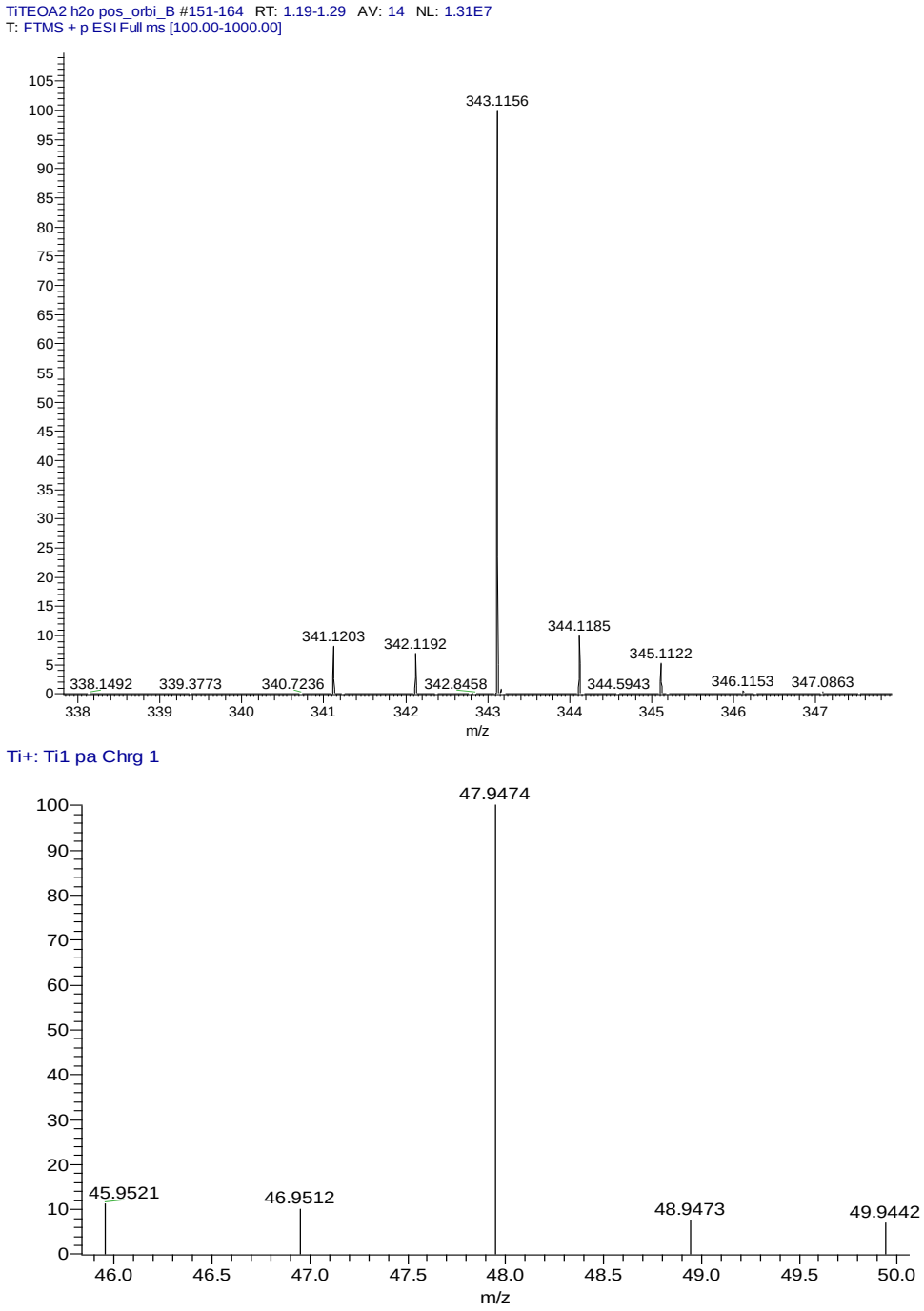

Figure 18. Isotopic pattern of the peak at m/z 226.0535 ($C_7H_{16}O_4NTi$), at 343.1313 ($C_{12}H_{26}O_6N_2Ti$, protonated) in the ESI-HRMS spectrum of the methanolic Ti(TeoaH)$_2$ solution (top) and the isotopic pattern of Ti (below).

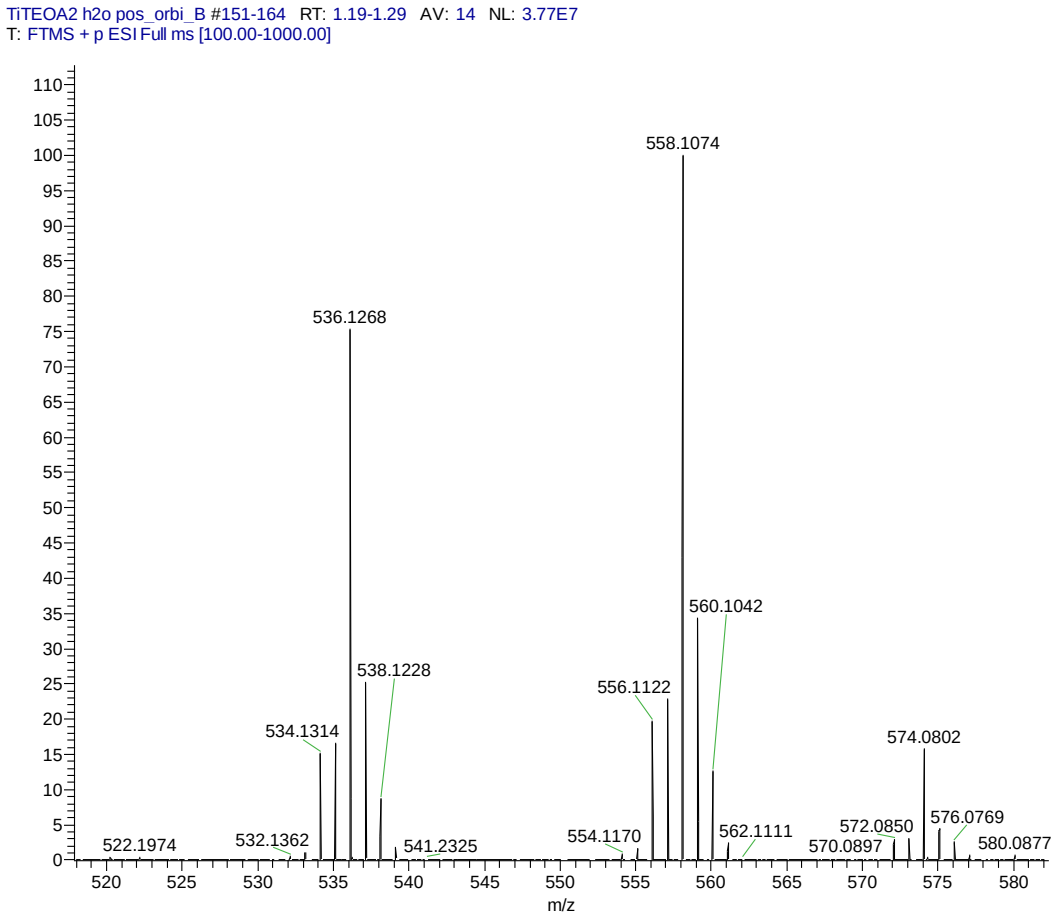

Figure 19. Isotopic patterns of the $Ti_2H(Teoa)_3$ complex cationized with H^+, Na^+ and K^+.

3.1.2. Synthesis and clean-up procedures

The syntheses were carried out in a 200 mL Teflon lined stainless steel high-pressure reactor mod DAB3 (Berghof, Tuebingen, Germany) (Figure 20). The heating/stirring was carried out with an heating mantle mounted on a magnetic stirrer/heater (Heidolph, Germany, mod MR-HEI standard) and a temperature controller/programmer mod BTC-3000 (Berghof,

Germany) equipped with a type K thermocouple (see Figure 20 for the complete assembly). In Table 1 all the relevant conditions and dimensions of the high pressure reactors are reported.

Figure 20. Berghof DAB3 Teflon lined stainless steel high-pressure reactor.

Table 1. Characteristics of the high-pressure reactor and of the magnetic stirrer.

High pressure reactor Description	
internal height (mm)	100.5
internal diameter (mm)	51.5
volume of liquid (ml ± 10 ml)	150
Magnetic stir bar	
length (mm)	30
diameter (mm)	6
stirring speed (rpm)	750

The exact conditions for the preparation of $[Ti(TeoaH)_2]$ solutions for each type of NPs are reported in Table 2. In general, after dissolution of the required mass of $[Ti(TeoaH)_2]$ and (possibly) of shape controller ($TeoaH_3$) in ultrapure water (resistivity > 18.2 MΩ cm^{-1}, TOC < 5 ppb, produced with a Millipore MilliQ apparatus), pH is adjusted with 1 M carbonate-free NaOH or 1 M HCl, as required. The solution is then filtered through a 0.45 μm cellulose acetate membrane filter. The presence of iron in the $[Ti(TeoaH)_2]$ solution before hydrothermal treatment is checked by the thiocyanate test (Fe(III) < 0.2 mg L^{-1}). The solution is N_2 purged for at least 10 minutes in order to eliminate O_2 before sealing the hydrothermal reactor. The purging time should be adjusted in order to ensure an O_2 content of the gaseous phase in the reactor under 1% mol/mol. The reactor is heated to 313 K for 30 minutes, then to the chosen temperature for the treatment (±1 K) at 1 K min^{-1}. The temperature is kept for 50 hours. The reactor is then cooled in air.

At the end of the hydrothermal treatment the nanoparticles suspension is concentrated using a rotovapor system and then cleaned by dialysis and recovered by freeze drying.

The choice to carry out dialysis and Freeze-drying in order to wash the NP and eliminate the solvent was made taking into account that:

- Dialysis and freeze-drying allows recovering all the particles without changing the size distribution. Centrifugation or filtration can selectively loose particles on the fine side of the size distribution.

- Freeze-drying allows the elimination of water without any thermal treatment, making no variation in the surface properties of the nanoparticles.

3.1.3. Experimental Design

Starting from a previously developed synthetic procedure for obtaining TiO_2 bipyramidal nanoparticles,[2] the synthesis conditions were modified by means of an experimental design. The experimental design technique used is based on the Responses Surface Method, by using the Box Wilson central composite designs (CCD) which allows the optimization. According to the design of experiments theory, a central composite design is a factorial designs with center points, with a group of axial points, called "star points", that allow the estimation of the response surface curvature. If n is the number of factors, the 2n corner points having the normalized coordinates +/- 1 while the star points are created by drawing a line from the center orthogonal on each face. The star points represent new extreme values (low and high) for each factor in the design.

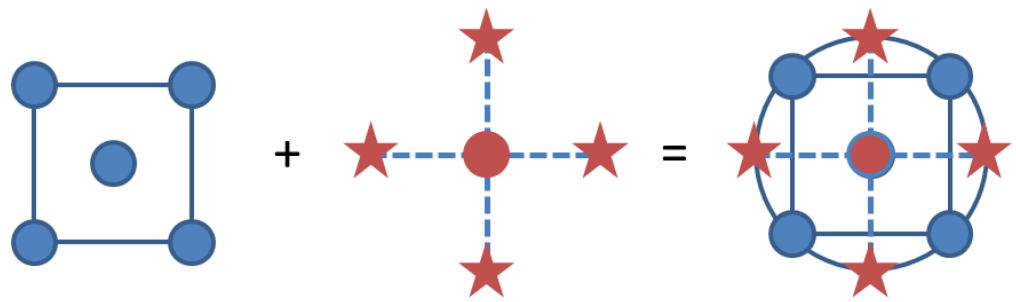

Figure 21. Example of the generation of a Central Composite Design for Two Factors (CCC = Circumscribed Central Composite).

In our case the chosen factors are 4 (n=4) as described below, so the number of the "star points" is 2n = 8. The distance α from the center of the eight "star points", for an orthogonal experiment, in normalized coordinates, is calculated from the relation[13]:

$$\alpha^4 + 2^{n-1}\alpha^2 - 2^{n-2}(n + 0.5N_0) = 0$$

where n is the number of factors (n=4), and N_0 the number of center points (N_0 = 4).

The experimental plan considers the four independent variables (factors) that mainly influence the characteristics of the product:

- Z_1 - [$Ti(TeoaH)_2$] initial concentration;
- Z_2 - Added $TeoaH_3$ concentration as shape controller;
- Z_3 - Initial pH;
- Z_4 - operating temperature.

The predictive soft model developed considers three output variables, hydrodynamic radius (Y_1), polydispersity index (Y_2) and a shape parameter (Y_3, see below for its definition and measurement). The polynomial model is in the functional form $Y_j=f_j(X_1, X_2, X_3, X_4)$. The variables X_1, X_2, X_3, X_4 are the coded factors corresponding to the natural variables Z_k (k = 1, 2, 3, 4). The coded factors are obtained using the general relations:

$$z_k^0 = 0.5\left(z_k^{max} + z_k^{min}\right);\quad \Delta z_k = \frac{z_k^{max} - z_k^0}{\alpha};\quad x_k = \frac{z_k - z_k^0}{\Delta z_k};\qquad (k = 1,2,3,4)$$

Where z_k^0 are the central point coordinates (values chosen slightly modifying the reference synthesis)[2]:

$z_1^0 = 65\ mM;\ \ z_2^0 = 40\ mM;\ \ z_3^0 = 10\ pH;\ \ z_4^0 = 443\ K$

Δz_k represents the distances from the central point:

$\Delta z_1 = 36.07\ mM;\ \ \Delta z_2 = 26.24\ mM;\ \ \Delta z_3 = 1.31\ pH;\ \ \Delta z_4 = 305{,}94\ K$

and x_k represents the values of the work matrix of the experimental program expressed in normalized coordinates (Table 5).

The experimental ranges studied were from 28.03 to 120 mM [$Ti(TeoaH)_2$], from 0 to 66.24 mM added $TeoaH_3$, pH between 8.69 and 12.28 and temperature values from 410 to 493 K. Taking into account the great complexity of the experimental work involved, a fractional central composite design was selected with 8 factorial points, 8 star points and 4 central points. For the selected experiment plan $\alpha = 1.525$. The orthogonal fractional centered composite design, expressed in real factor values, is shown in Table 2.

The experimental program adopted allows the investigation in a large range of operating parameters using a limited number of experiments. This will give the possibility of process analysis and mathematical modeling in order to predict final product characteristics in various operating conditions, and identify the synthesis conditions for a product with predefined final properties.

Table 2. Work matrix for the experimental program, based on orthogonal fractional design Box Wilson (CCD). In the table are also reported the final pH of the synthesis and the crystallographic phase. HT stands for HydroThermal

Name	Z_1 $Ti(TeoaH)_2$ (mM)	Z_2 $TeoaH_3$ (mM)	Z_3 initial pH	Final pH	Z_4 T (K)	$[TeoaH_3]/[Ti]$	Crystallographic Phase
HT01	28.93	13.76	8.69	8.77	410	2.49	anatase
HT02	28.93	13.76	11.31	11.56	476	2.48	anatase
HT03	28.93	66.24	8.69	/	476	4.21	anatase
HT04	28.93	66.24	11.31	11.62	410	4.29	anatase & traces of brookite
HT05	101.07	13.76	8.69	8.87	476	2.14	anatase
HT06	101.07	13.76	11.31	12.11	410	2.14	anatase & traces of brookite
HT07	101.07	66.24	8.69	8.78	410	2.66	anatase
HT08	101.07	66.24	11.31	12.18	476	2.66	anatase & traces of brookite
HT09	10.00	40.00	10.00	10.06	443	5.92	anatase
HT10	120.00	40.00	10.00	11.58	443	2.34	anatase
HT11	65.00	0.00	10.00	11.24	443	2.00	anatase
HT12	65.00	80.00	10.00	11.48	443	3.25	anatase
HT13	65.00	40.00	8.00	8.19	443	2.61	anatase
HT14	65.00	40.00	12.00	12.28	443	2.61	anatase & brookite
HT15	65.00	40.00	10.00	10.09	393	2.62	anatase
HT16	65.00	40.00	10.00	10.97	493	2.62	anatase
HT17	65.00	40.00	10.00	11.36	443	2.62	anatase
HT18	65.00	40.00	10.00	11.31	443	2.62	anatase
HT19	65.00	40.00	10.00	11.38	443	2.61	anatase
HT20	65.00	40.00	10.00	11.39	443	2.62	anatase

3.1.4. Characterization and Image Elaboration

Determination of the crystallographic phase is carried out through X-Ray Diffraction (XRD) measurements with an Analytical X'Pert Pro equipped with an X'Celerator detector powder diffractometer using Cu K radiation. In Table 2 the X-ray diffraction analysis results are summarized. All the materials synthesized at an initial pH $\leq$ 10 contain only the anatase phase. The materials synthesized at an initial pH between 11 and 12 contain anatase along with traces of brookite, with the exception of the HT02 material and of the HT08 material (this last one contains a quite negligible amount of the brookite phase). These two materials were synthesized at 476 K, whereas those containing detectable traces of brookite were synthesized at 410 K. At an initial pH $\geq$ 12 the brookite content was substantial (HT14, 443 K), so pH > 12 and temperatures < 443 K favor the formation of the brookite phase. Brookite could come from the large concentration of Na, indeed for obtaining high value of pH NaOH is used; and Na^+ stabilizes the brookite polymorph.[14,15] Figure 22 shown all the XRD patters of all the synthetized materials.

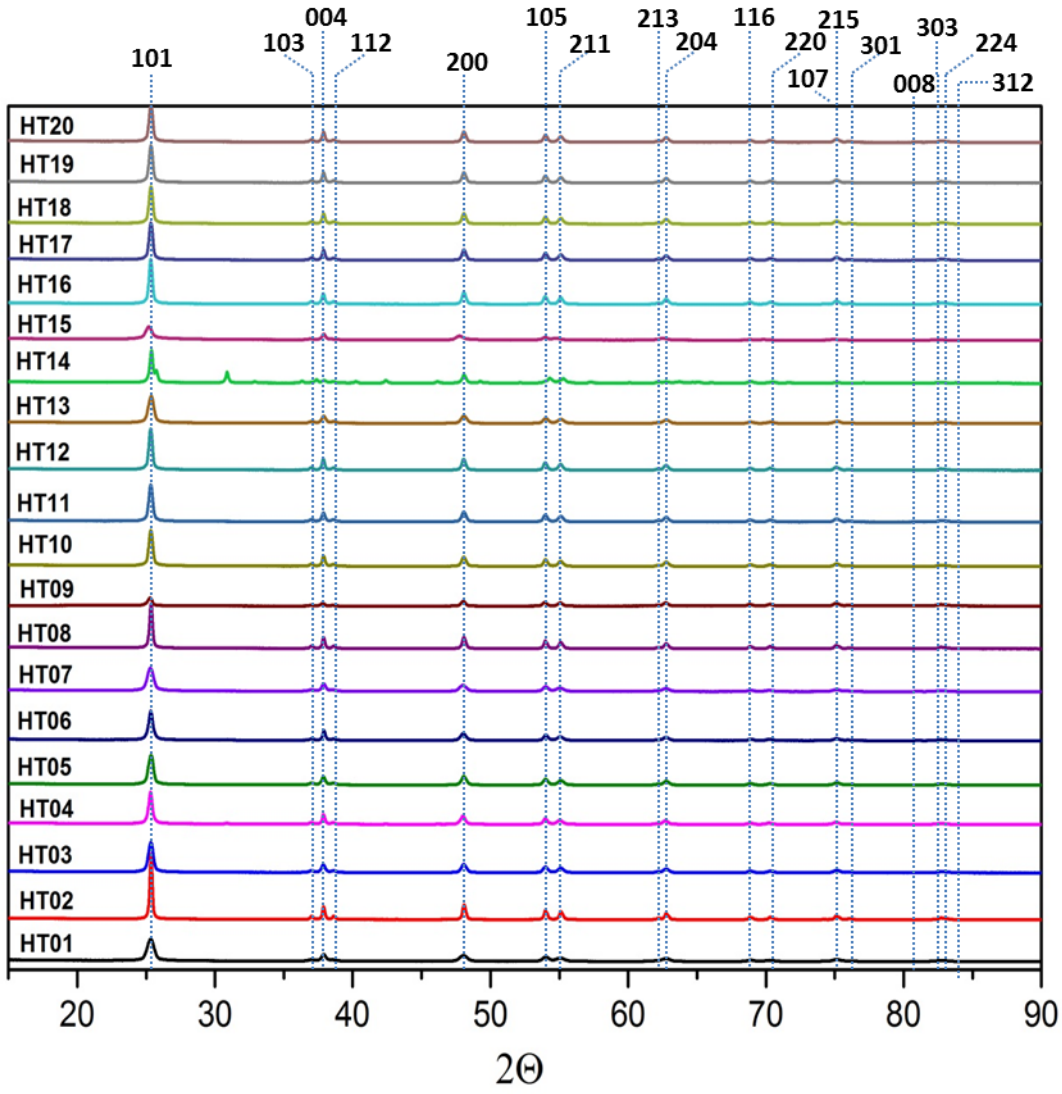

Figure 22. XRD patterns of all the synthetized materials. All the samples shown the anatase phase, only the material HT14 shows a good amount of the brookite phase. While in materials HT04, HT06 and HT08 brookite is present in traces. (Up) Anatase XRD pattern indexing is reported.

Dimensional characterization was performed with two different techniques: Dynamic Light Scattering (DLS) and Transmission Scanning Electron Microscopy (T-SEM). Shape characterization only through T-SEM.

The DLS system is an ALV (Langen Germany), NIBS model (not invasive backscattering). The hydrodynamic radius R_H of nanoparticles in aqueous suspension was obtained through the Stokes-Einstein equation. DLS data were obtained by analyzing the raw suspensions (if necessary diluting it using 200 mM NH_3 as a dispersant) after sonication for 10-30 minutes in an ultrasound bath and in a closed vial to avoid NH_3 evaporation (suggested 95 W, 37 kHz). The reported sizes were obtained through the fit of the decay time distribution function to the integral equation relating the field correlation function and the said distribution function using a constrained regularization method (CONTIN DP algorithm) developed by Provencher[16]. The number and mass distribution functions are then obtained. The measurements and their polydispersity (as standard deviation of the relevant peak mode) are reported in Table 4 together with the shape and size parameters obtained through the microscopic analysis (T-SEM plus image elaboration). Certain distributions are bimodal due to the presence of agglomerates.

In this study, SEM and TSEM was performed, directly on the raw suspensions of the nanoparticles as obtained from the hydrothermal syntheses, through a Zeiss Supra 40 SEM (Zeiss, Oberkochen, Germany) equipped with a Schottky field emitter and, additionally to the standard Everhart-Thornley detector, with a high-resolution InLens detector. Hence, high-resolution SEM imaging of the sample surface morphology at the nanometer scale is possible. This type of microscopy is especially suited for nanoparticulate samples to get access to the size and shape of individual nanoparticle. Usually, the transmission electron microscopy (TEM) - either as the typical TEM or as the transmission mode at an SEM, i.e. T-SEM – is

successfully applied for the study of NPs able to be prepared rather separated on a conventional TEM grid.[17-19] The shape parameter can be defined as the ratio between the size along the *c*-axis and the size of the bipyramid to the base (*a*-axis). Ideally, in the case of a perfect bipyramid, the shape of the particles may be obtained by processing a three-dimensional image, adjusting the image of the particle to a truncated bipyramidal contour. For a perfect bipyramidal crystal, having the anatase lattice parameters, this ratio is equal 2.51. This procedure, however, is suitable only on three-dimensional images of excellent quality and requires ad hoc software. So, the image processing was carried out on two-dimensional images, by calculating the lengths of the major and minor axes of the elliptical perimeter fitted to the contours of the 2-D projection of the nanoparticles (Figure 23). The TSEM micrographs of all samples are reported in Appendix A.

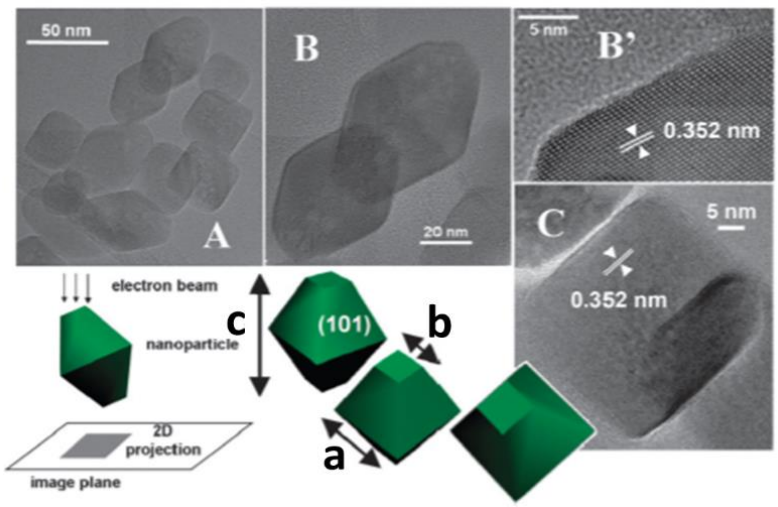

Figure 23. TEM micrographs and representation of a 2D projection of bipyramidal nanoparticle on the TEM grid. Figure from Deiana et al.[2]

The parameters *a* and *c*, however, can only be measured on particles whose c-axis is parallel or perpendicular to the TEM grid. This vision is not optimal, and leads to an underestimation of the parameters *a* and *c*, and the expected shape parameter is therefore 1.5 for a perfect bipyramid (Figure 23). Results of the dimensional and shape analysis are resumed in Table 3.

Table 3. Dimensional parameters obtained by T-SEM micrograph analysis with the corresponding standard deviations. Sample HT14 and HT15 are not listed in the table because shape and size analysis was not possible

Experiment	Minor = "b", nm	Major = "c", nm	c/a = p
HT01	15 ± 3	23 ± 7	1.5 ± 0.5
HT02	45 ± 10	89 ± 33	2.0 ± 0.9
HT03	28 ± 5	38 ± 9	1.4 ± 0.4
HT04	20 ± 4	108 ± 47	5.5 ± 2.6
HT05	21 ± 4	29 ± 8	1.4 ± 0.5
HT06	18 ± 4	100 ± 31	5.5 ± 2.1
HT07	16 ± 4	27 ± 10	1.7 ± 0.8
HT08	35 ± 6	81 ± 37	2.3 ± 1.1
HT09	32 ± 4	43 ± 11	1.4 ± 0.4
HT10	30 ± 5	52 ± 15	1.8 ± 0.6
HT11	29 ± 4	39 ± 9	1.3 ± 0.4
HT12	33 ± 4	49 ± 12	1.5 ± 0.4
HT13	21 ± 4	29 ± 9	1.4 ± 0.5
HT16	35 ± 4	49 ± 9	1.4 ± 0.3
HT17	31 ± 4	47 ± 12	1.5 ± 0.5
HT18	32 ± 4	45 ± 10	1.4 ± 0.4
HT19	32 ± 4	43 ± 10	1.4 ± 0.4
HT20	32 ± 4	44 ± 11	1.4 ± 0.4

In order to compare the results of size measurements with DLS and with T-SEM, the geometrical data determined by T-SEM analysis were converted to a hydrodynamic radius (assuming the NPs as prolate ellipsoids) with the Perrin formula:[20,21]

$$\frac{R_H}{R_S} = \frac{\sqrt{p^2-1}}{p^{1/3}\ln\left(p+\sqrt{p^2-1}\right)}$$

$$p = \mathrm{c/a} > 1\ prolate$$

where:

- R_H hydrodynamic radius of the ellipsoid,
- R_S radius of the sphere with the same volume

In this way, a direct comparison between DLS measurements (for which the measurand is the hydrodynamic radius) and T-SEM images (which give geometric size parameters) is possible. The results of the Perrin analysis together with the DLS results are reported in Table 4. The second mode observed in the DLS distributions of samples synthesized at pH < 9 and > 10.5 is due to the formation of agglomerates that the sonication treatment is not able to decluster. The agreement between the R_H determined by elaboration of the microscopic data (major and minor axes of the ellipses fitted to the NP contours) and the R_H of the first mode (for bimodal distribution) of the DLS size distribution is generally within 2 nm or 10%. The exceptions are HT02, HT04, HT07 and HT08 for which larger

differences are observed, probably due to aggregation/agglomeration phenomena.

Table 4. Hydrodynamic radii obtained through SEM analysis and DLS of the TiO_2 samples considered in the present study.

Experiment	R_H Perrin (SEM), nm	R_H ± SD number mode 1 (DLS), nm	R_H number mode 2 (DLS), nm
HT01	9	7.0 ± 0.3	24
HT02	29	20 ± 1	58
HT03	16	15 ± 1	35
HT04	22	17 ± 1	68
HT05	12	14 ± 1	35
HT06	20	18 ± 2	44
HT07	10	18 ± 4	
HT08	25	17 ± 1	126
HT09	18	20 ± 4	
HT10	19	19 ± 4	
HT11	16	17 ± 3	
HT12	19	21 ± 3	
HT13	12	13± 1	35
HT14		250 ± 20	
HT15		2.0 ± 0.3	12
HT16	20	20 ± 4	
HT17	18	19 ± 3	
HT18	18	18 ± 4	
HT19	18	19 ± 3	
HT20	18	19 ± 3	

3.1.5. Prediction Model and Validation Experiments

The soft model was obtained by using second-degree polynomials for each of the output functions Y_1, Y_2 and Y_3 that predicts final product characteristics by using least square solver built in MathCad 14 software.

The experimental Y_1 values considered are the measured hydrodynamic radius (DLS) number mode 1 (Table 4), Y_2 experimental values represent the polydispersity taken as standard deviation of the relevant mode. The experimental Y_3 values are the shape parameter in each experiment, as presented in the Table 4. The coded factors and the corresponding measured values for the synthesis outcome Y_1, Y_2 and Y_3 used for mathematical modeling are presented in Table 5.

As can be noticed, for samples number 14 and 15 (HT14 and HT15), the missing data for the shape parameter (Table 4) were taken in the range of the other experimental values, while the outlier values for Y_1 R_H number mode 1 (DLS) and Y_2 SD R_H number mode 1 in HT14 run (Table 4) were replaced with values in the range of variation in order to avoid a strong model distortion.

Table 5. Work matrix of the experimental program, based on orthogonal central composite fractional design, in normalized coordinates

Experiment	X_1	X_2	X_3	X_4	Y_1, nm	Y_2, %	Y_3
HT01	-1	-1	-1	-1	7	3.71	1.52
HT02	-1	-1	+1	+1	20	5.30	1.98
HT03	-1	+1	-1	+1	15	9.20	1.38
HT04	-1	+1	+1	-1	17	6.59	5.50
HT05	+1	-1	-1	+1	14	5.36	1.37
HT06	+1	-1	+1	-1	18	9.17	5.46
HT07	+1	+1	-1	-1	18	24.5	1.69
HT08	+1	+1	+1	+1	17	5.82	2.33
HT09	-1.525	0	0	0	20	18.15	1.38
HT10	+1.525	0	0	0	19	19.58	1.76
HT11	0	-1.525	0	0	17	17	1.33
HT12	0	+1.525	0	0	21	16.14	1.50
HT13	0	0	-1.525	0	13	5.23	1.41
HT14	0	0	+1.525	0	19	12.47	4.70
HT15	0	0	0	-1.525	2	14	3.65
HT16	0	0	0	+1.525	20	17.9	1.40
HT17	0	0	0	0	19	17.1	1.49
HT18	0	0	0	0	18	22.8	1.39
HT19	0	0	0	0	19	17.1	1.37
HT20	0	0	0	0	19	16.89	1.38

The general form of the polynomial models is:

$$\hat{Y} = b_0 + \sum_{i-1}^{4} b_i x_i + \sum_{i=1}^{4} \sum_{j=i+1}^{4} b_{i,j} x_i x_j + \sum_{i=1}^{4} b_{i,j} x_i^2$$

The ANOVA analysis proved that all three models obtained were significant and adequate, according to Fisher tests at a significance level of 0.05.

The validation of the mathematical models was realized by performing new experiments in the range of interest for the operating parameters. The experimental outcomes for the obtained TiO_2 NPs were compared with

predicted ones (Table 6). The TSEM micrographs of all samples are reported in Appendix A.

Table 6. Product predicted and measured characteristics in some test points

Experiment	Z_1, mM	Z_2, mM	Z_3	Z_4, K	Product characteristics					
					Experimentally measured			Predicted by the model		
					Y_1, nm	Y_2, %	Y_3, -	Y_1, nm	Y_2, %	Y_3, -
HT_VAL_01	85	9.1	8.3	436	13	5.4	1.4	12.2	4.6	1.41
HT_VAL_02	82	56	8	475	11	5.6	1.5	14.0	6.2	1.49
HT_VAL_03	66	80	10	473	19	6.6	1.3	19.8	12.8	1.13
HT_VAL_04	65	20	9.2	488	14	3.2	1.4	14.5	12.5	1.24
HT_VAL_05	71.90	39.5	8.2	481	12	3.1	1.4	13.1	5.5	1.5
HT_VAL_06	33.37	14.21	8.76	411	7	6.4	1.5	6.1	5.0	1.5

The data in Table 6 show a relatively good model prediction capability, especially for the particle size and shape factor. To increase the reliability of the mathematical models, the new experimental points were also included in the regression analysis. The six additional experiments were added to the initial 20 experimental points and optimized models were obtained. Having 26 experimental points instead of 20, as had the initial central composite fractional design, the experiment it is no longer an orthogonal one, but it has the advantage of including new experimental information. The final optimized models are:

$$\hat{Y}_1 = 18.311893 + 0.407102 \cdot x_1 + 1.310852 \cdot x_2 + 1.913921 \cdot x_3 + 2.726356 \cdot x_4 - 0.706556 \cdot x_1 x_2 - 1.330618 \cdot x_1 x_3 - 1.873684 \cdot x_1 x_4 - 0.108507 \cdot x_2 x_3 + 0.051493 \cdot x_2 x_4 - +0.547527 \cdot x_3 x_4 + 0.732221 \cdot x_1^2 + 0.773031 \cdot x_2^2 - 1.643796 \cdot x_3^2 - 2.74701 \cdot x_4^2$$

$$\hat{Y}_2 = 19.45097 + 1.81247 \cdot x_1 + 1.199042 \cdot x_2 - 0.715563 \cdot x_3 - 1.435496 \cdot x_4 - 2.835291 \cdot x_1 x_2 + 0.134572 \cdot x_1 x_3 + 2.12859 \cdot x_1 x_4 - 5.337425 \cdot x_2 x_3 - 2.03686 \cdot x_2 x_4 + 3.923907 \cdot x_3 x_4 - 0.652813 \cdot x_1^2 - 2.486142 \cdot x_2^2 - 4.448121 \cdot x_3^2 - 2.465596 \cdot x_4^2$$

$$\hat{Y}_3 = 1.416942 + 0.080658 \cdot x_1 + 0.074693 \cdot x_2 + 1.13782 \cdot x_3 - 0.816469 \cdot x_4 - 0.305752 \cdot x_1 x_2 + 0.076544 \cdot x_1 x_3 - 0.055872 \cdot x_1 x_4 + 0.082533 \cdot x_2 x_3 - 0.053355 \cdot x_2 x_4 - 0.461919 \cdot x_3 x_4 + 0.055628 \cdot x_1^2 + 0.025852 \cdot x_2^2 + 0.678453 \cdot x_3^2 + 0.49161 \cdot x_4^2$$

The optimized models were used to estimate the influence of operating parameters over the product characteristics and to propose optimal operating condition for predefined final product characteristics. Figure 24 and Figure 25 show the influence of pH and temperature, in dimensionless coordinates, upon the hydrodynamic radius and shape parameter at given $Ti(TeoaH)_2$ and added $TeoaH_3$ concentrations.

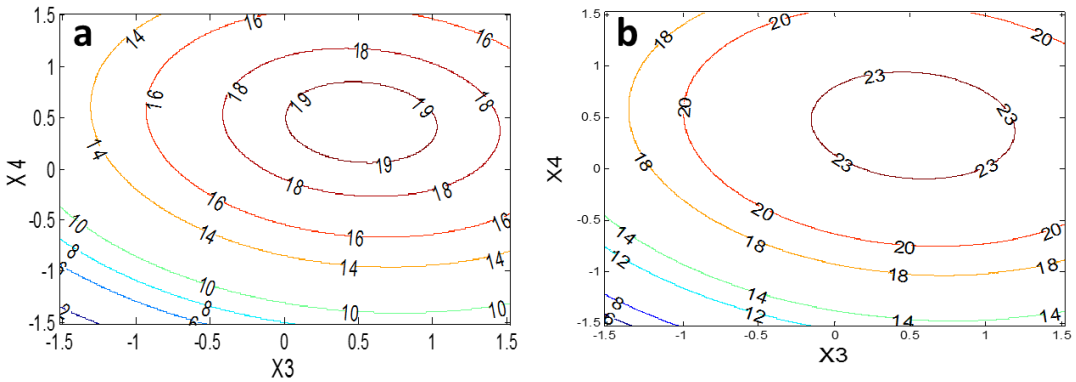

Figure 24. Variation of hydrodynamic radius (Y_1) of TiO_2 NPs as a function of pH (X_3) and temperature (X_4) for (a): $Ti(TeoaH)_2$ 65 mM (X_1=0), $TeoaH_3$ 40 mM (X_2=0) and (b): $Ti(TeoaH)_2$ 120 mM (X_1=1.52), $TeoaH_3$ 80 mM (X_2=1.52)

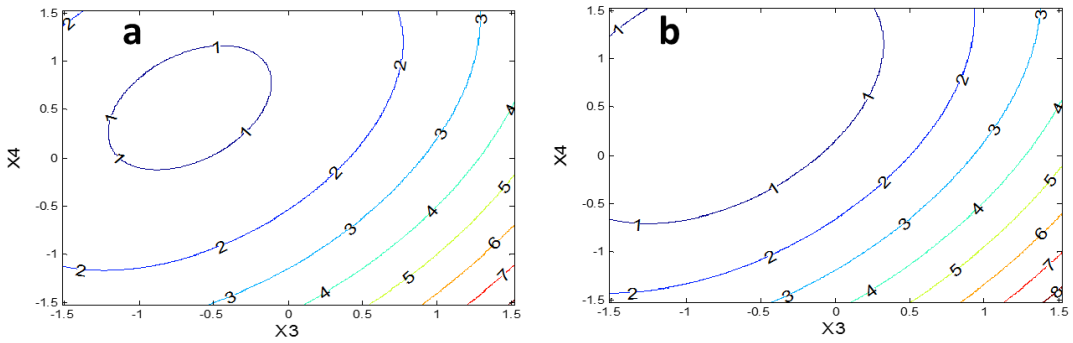

Figure 25. Variation of the shape parameter (Y_3) of TiO_2 NPs as a function of pH (X_3) and temperature (X_4) for (a): $Ti(TeoaH)_2$ 65 mM (X_1=0) and $TeoaH_3$ 40 mM (X_2=0) and (b): $Ti(TeoaH)_2$ 120 mM (X_1=1.52), $TeoaH_3$ 80 mM (X_2=1.52)

As Figure 24a shows, very low hydrodynamic radius are expected in a small region of pH and temperature variation (at low pH and low temperature), while particles with sizes between 8 and 16 nm can be obtained in several working conditions. In the whole range of temperatures and pH vales, for 65mM $Ti(TeoaH)_2$ and 40 mM added $TeoaH_3$ solutions, the expected particle size would not exceed 20nm. For higher $Ti(TeoaH)_2$ and higher added $TeoaH_3$ concentrations (Figure 24b) there is a large region in the pH and temperature variation range as where particles with sizes greater than 20 nm may be obtained. As for the shape parameter (Figure 25), shape factors between 1 and 2 are expected in a very large region of working conditions.

The optimized models were used to estimate the influence of operating parameters over the product characteristics and to propose optimal operating condition for predefined final product characteristics. Some good operating conditions can be suggested by formulating optimization problems with the objective function representing the desired product properties. For instance, the identification of possible operating condition

for obtaining TiO_2 crystals with predefined shape factor of 2, 3 and 4, and hydrodynamic radius lower than 20 nm, gave the results presented in Table 7. The optimization was performed in the frame of Matlab Release 2013a using genetic algorithms. The conditions listed in Table 7 are not unique, and, as revealed by Figure 24 and Figure 25, particles with almost the same characteristics can be obtained in different operating conditions.

Table 7. Optimal operating conditions identified for TiO_2 NPs with imposed shape factor

	Process operating conditions				**Product characteristics**	
Shape factor required	**$Ti(TeoaH)_2$, mM**	**$TeoaH_3$ added, mM**	**pH**	**T, °C**		
p=2	117	47	10.9	209	R_H, nm	14.0
					Polydisp, %	8.5
					p	2.0
p=2	79	24	10.8	190	R_H, nm	18.5
					Polydisp, %	17.2
					p	2.0
p=3	62.8	42	10.3	142.6	R_H, nm	14.3
					Polydisp, %	19.2
					p	3.0
p=4	66.0	28.5	10.25	125.0	R_H, nm	8.1
					Polydisp, %	14.8
					p	4.0

The results here discussed about the experimental design, validation experiments and the prediction model are enclosed in a manuscript that is in preparation.

3.1.6. Growth Mechanism

The evolution of crystal shape during growth is related to the nature of the species present in the synthesis environment and their concentration. As said, these species could modulate the crystal surfaces energy acting as shape controllers. Moreover, the solvent can affect the final crystals characteristics via the different interactions with different crystal planes, stabilizing preferentially one of them.[22]

Several experimental and theoretical works suggest different mechanism of TiO_2 crystal growth using hydrothermal processes.[23-28] For hydrothermal TiO_2 syntheses carried out in alkaline conditions, at 473 K and times from 2 to 16 hours, seems to be operative a growth mechanism based on crystallites oriented attachment (OA) along the [001] direction seems to be operative. This mechanism is then followed by an increase of the size due to an Ostwald ripening process, as proposed by Cho et al.[24] They noticed that pH and synthesis duration could strongly influence the size and shape of the crystal formed. Penn and Banfield[25] first noticed OA in the synthesis of nano anatase crystals in hydrothermal conditions. This mechanism was extensively studied by molecular dynamics simulation by Fichthorn et al. based upon the intrinsic nanocrystal forces that act in vacuum and facilitate alignment and aggregation[26,28].

Moreover, they also introduced in their model the interactions between water molecules and crystal surface when the process occurs in humid environment, where the growth is mediated by adsorbed water and hydroxyls[27].

Starting from the previously illustrated hydrothermal synthesis methodology and in order to infer about the growth mechanism, a study on the time evolution of size and shape of crystallites as well as on the soluble species was carried out.[7]

Table 8. Synthesis conditions of the experiments stopped at different time in order to evaluate the nanoparticles' growth mechanism

TiO_2 synthesis set	$Ti(TeoaH)_2$ (mM)	Added $TeoaH_3$ (mM)	Initial *p*H	Temperature (K)	Treatment time (hours)	Crystallographic Phase
HT_2h	59.2	40.0	10.0	443±2	2.00	Anatase
HT_5h	58.8	40.0	10.0	443±2	4.67	Anatase
HT_15h	58.6	40.7	10.0	443±2	15.0	Anatase
HT_25h	56.4	40.0	10.0	443±2	25.0	Anatase
HT_35h	60.5	40.3	10.0	443±2	35.0	Anatase
HT_50h	59.2	40.0	10.0	443±2	50.0	Anatase

In Table 9 are reported the data concerning the total Ti(IV) measured by ICP-MS of the filtered mother liquors of the hydrothermal syntheses as a function of the treatment time. After 2 hours at 443 K soluble Ti(IV) species are less than 0.3% of the initial Ti(IV) concentration. A minimum is reached after 15 hours, then, a slight rebound of the soluble Ti(IV) concentration is observed probably due to primary nuclei re-dissolution.

Table 9. Time evolution of the soluble Ti(IV) concentration during the hydrothermal treatment. The data at 50 hours is missing

Time, hours	Soluble Ti(IV), mM
0	58.7 ± 0.7
2	0.16 ± 0.01
5	0.07 ± 0.005
15	0.04 ± 0.005
25	0.09 ± 0.005
35	0.10 ± 0.005

In Figure 26 are reported the mass weighted size distributions of the TiO_2 nanoparticles size distributions at different treatment time, obtained by DLS measurements. All distribution functions are bimodal, except HT_50h, corresponding to the final synthesis time. Number-weighted size distribution functions are dominated by a small mode at 1-3 nm, except for HT_50h. It is possible to see the progressive disappearance of the mode at small sizes in the distribution function (Figure 4).

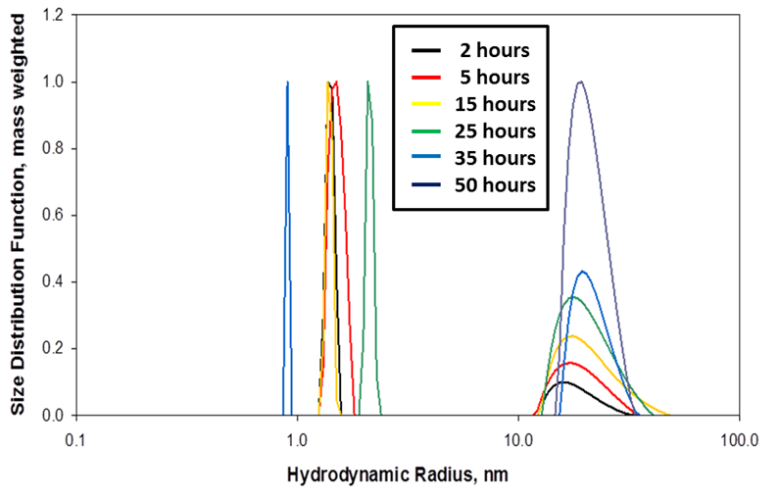

Figure 26. Mass weighted size distribution function for the synthetized materials.

X-ray diffraction (XRD) patterns of the powders were recorded, all the samples shown only the anatase phase (Figure 27).

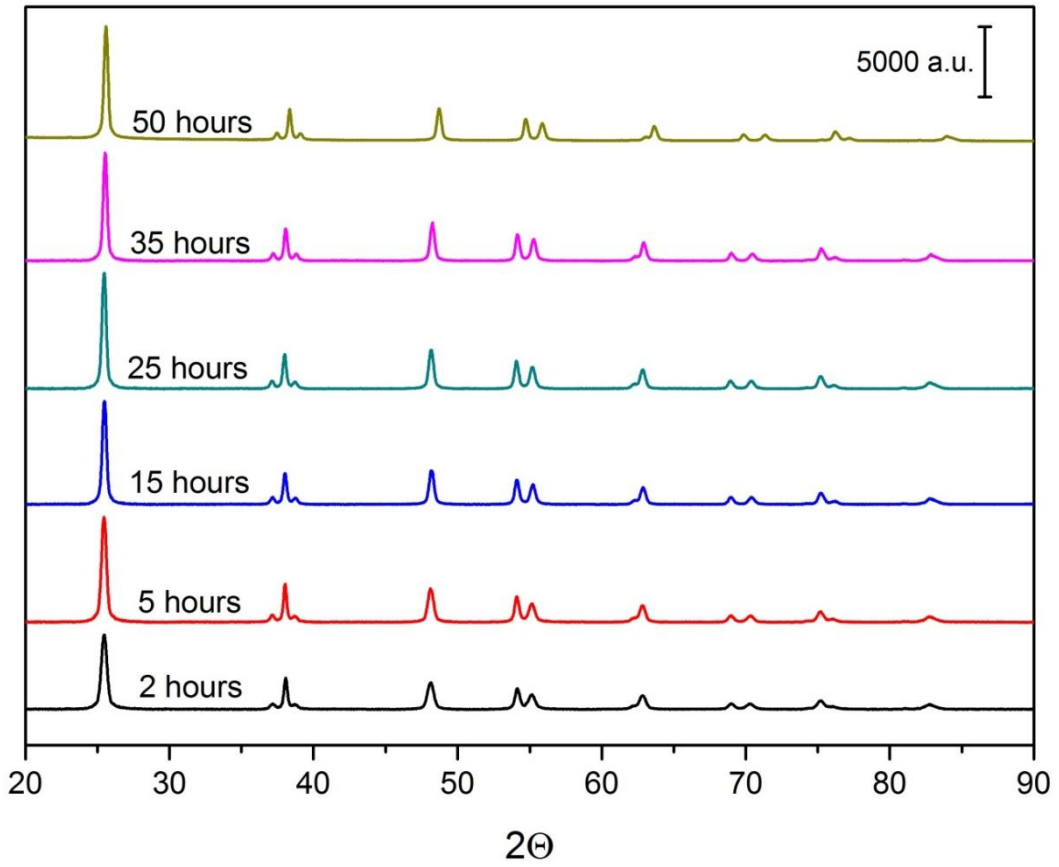

Figure 27. XRD patterns of the synthetized materials. All the samples shown only the anatase phase.

Table 10 reports all the output variables determined: average dimension of the nanoparticles (hydrodynamic radius, both from DLS measurements and T-SEM characterization), polydispersity index (expressed as standard deviation, SD, of the relevant mode of the size distribution) and shape factor.

Table 10. Time evolution of the morphological characteristics during the hydrothermal process

Time, h	RH (major-minor) as measured by T-SEM /nm	RH number mode 2 /nm	SD RH number mode 2 /nm	RH number mode 1 /nm	RH mass mode 2 /nm	SD RH mass mode 2 /nm	RH mass mode 1 /nm	Shape factor Major/Minor
2	15	16	3	1.4	18	4	1.4	2.60
5	15	17	3	1.5	19	5	1.5	2.26
15	20	17	4	1.4	21	6	1.4	1.60
25	18	19	4	2.1	20	5	2.1	1.58
35	18	20	3	0.9	21	4	0.9	1.47
50	18	18	3	n/a	21	4	n/a	1.38

The shape factor evolves from 2.6 (at 2 hours) to 1.4 (at 50 hours). Prolate ellipsoids with high shape factors have lower volumes in comparison to ellipsoids with low shape factor. In Figure 28 and Figure 29 it is possible to see the TSEM micrographs and a graph of the shape factor evolution.

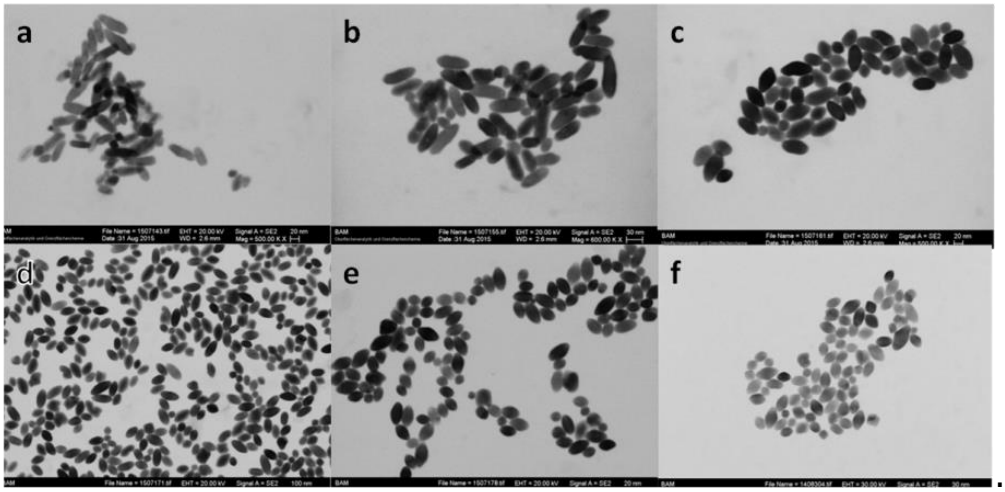

Figure 28. TSEM images of the materials: a. HT_2h; b. HT_5h; c. HT_15h; d. HT_25h; e. HT_35h; f. HT_50h.[7]

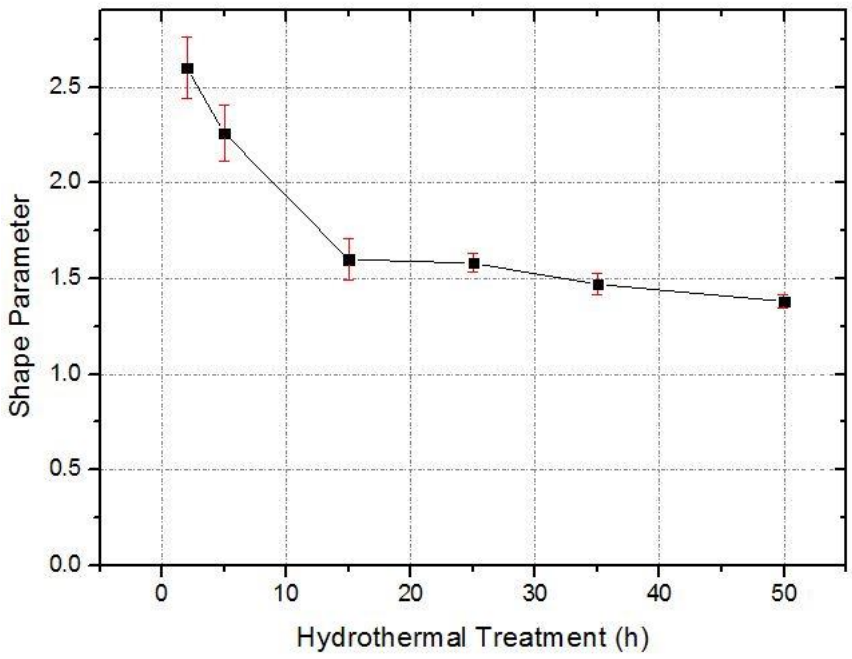

Figure 29. Shape factor evolution depending on synthesis time.[7]

These evidences suggest that there is a fast nucleation step in the early stages of the hydrothermal treatment. This fast nucleation step induces the generation of cuboidal nuclei of TiO_2. An oriented attachment (OA) of these cuboidal nuclei occurs with the generation of elongated nanoparticles. Increasing the treatment time an Ostwald ripening occurs, with a re-dissolution of free cuboidal nuclei and evolution of elongated to bipyramidal NPs.[7]

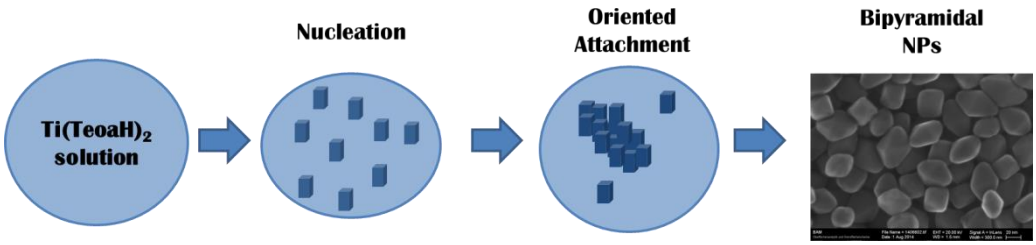

Figure 30. Growth mechanism of bipyramidal nanoparticles[7]

3.2. Solvothermal Synthesis of TiO_2 Nanosheets

The synthesis of TiO_2 nano-sheets was carried out with a solvothermal method following an established literature procedure.[29,30] In a typical synthesis a precise volume of $Ti(OBu)_4$ (Aldrich reagent grade 97%) was added in a 150 mL Teflon pot and the desired volume of concentrated hydrofluoric acid (Aldrich reagent grade 47%) was added dropwise under stirring. The Teflon pot was sealed and kept under stirring at high temperature (523 K) for 24 hours in autoclave. The resulting bluish paste was triply centrifuged and washed with acetone and with water (Milli-Q) to remove the residual organics. The aqueous suspensions are then freeze-

dried obtaining a bluish powder. The blue color is due to the CB electron absorption associated to F^- doping.

To remove the fluorides from the surface, the as-synthesized material was washed with NaOH 0.1 M (2 hours at r.t.). The reaction is an exchange of the OH^- group with the surface F^- group. The resulting material was then washed with 0.1 M HNO_3 solution and ultrapure water, finally freeze-dried. In order to evaluate if the 0.1 M NaOH treatment could modify the NP morphology by etching the surface, the presence of Ti in the alkaline solution kept in contact with the TiO_2 NPs was evaluated by ICP-MS spectrometry, resulting in the removal of less than 0.015 atoms of Ti for nm^2 of TiO_2. The data confirm that no significant etching occurs at the surface of the TiO_2 NPs.

The other way used to completely remove the fluorides from the nanoparticles, is a heat treatment at 873 K for 1 hour in air atmosphere (temperature gradient for 1h 30'). The resulting powder is white. The fluoride removal was confirmed by chemical analysis.

The three samples obtained will be labeled from now on respectively:

- n-sh: as synthetized nanosheets, this sample has fluorides both on bulk and surface;
- n-sh_NaOH: sample washed with a 0.1 M NaOH solution (surface fluoride removal);
- n-sh_873K: sample calcined 1 hour at 873K

3.2.1. Shape and Size Characterization

Figure 31A shows a SEM image of the as-synthesized TiO_2 n sh NPs, which have an average dimension of 75 nm in the basal plane with a thickness (along the c-axis) of 9 nm (see Table 11). HR-TEM images with lattice fringes 0.2370 nm apart (d004= 0.2378 nm, PDF 00-021-1272) parallel to the side view of the basal facets, and related FT (Figure 31B) confirm that these facets are normal to the c-axis and, thus, should correspond to {001} surfaces. The lateral boundaries form an angle of ~130°, compatible with the projection of intersecting (101) and $(10\bar{1})$ surfaces for a nanoparticle with the a-axis forming a small angle with the image plane. The sample washed in a 0.1 M NaOH solution to remove surface fluorides exhibits a similar morphology (Figure 31C), whereas the pristine nano-sheet shape was almost lost by subsequent calcination at 873 K (Figure 31D). Therefore, the calcined TiO_2 n sh_NaOH will no longer be considered. Conversely, direct calcination of the fluorinated TiO_2 n-sh does not lead to evident morphological changes (Figure 31E), retaining basal {001} surfaces normal to the c-axis (Figure 31F). It appears that surface fluorides are essential to stabilize the morphology of these nanosheets.

All samples were found to be pure anatase TiO_2 phase by XRD (Figure 32). However, the Scherrer analysis, applied as an integral method, highlights that the average crystallite dimension in the [001] direction is approximately doubled for TiO_2 n-sh_873K (Table 11), suggesting that the primary nanoparticles could have sintered in pairs along the c-axis. This is consistent with the decrease of the specific surface area (SSA_{BET}) from 53

to 34 m^2/g, despite any significant change in size and shape of nanoparticles observed as stacked primary particles in SEM/TEM images.

This sintering should have a relevant impact on the relative amount of lateral {101} surfaces and the basal {001} ones. By a geometric modeling of nanoparticles pairing (see Appendix B), the {101}:{001} ratio was estimated to change on an average from 20:80 to 40:60 (Table 11). The resulting relative change in calculated specific surface area was in excellent agreement with the experimental one (see APPENDIX B).

Table 11 resumes all the geometrical characteristics of the obtained nanoparticles and the characteristics of obtained bipyramidal anatase TiO_2 nanoparticles (TiO_2 bipy), mainly exposing {101} facets. For details, see Deiana et Al.[2]

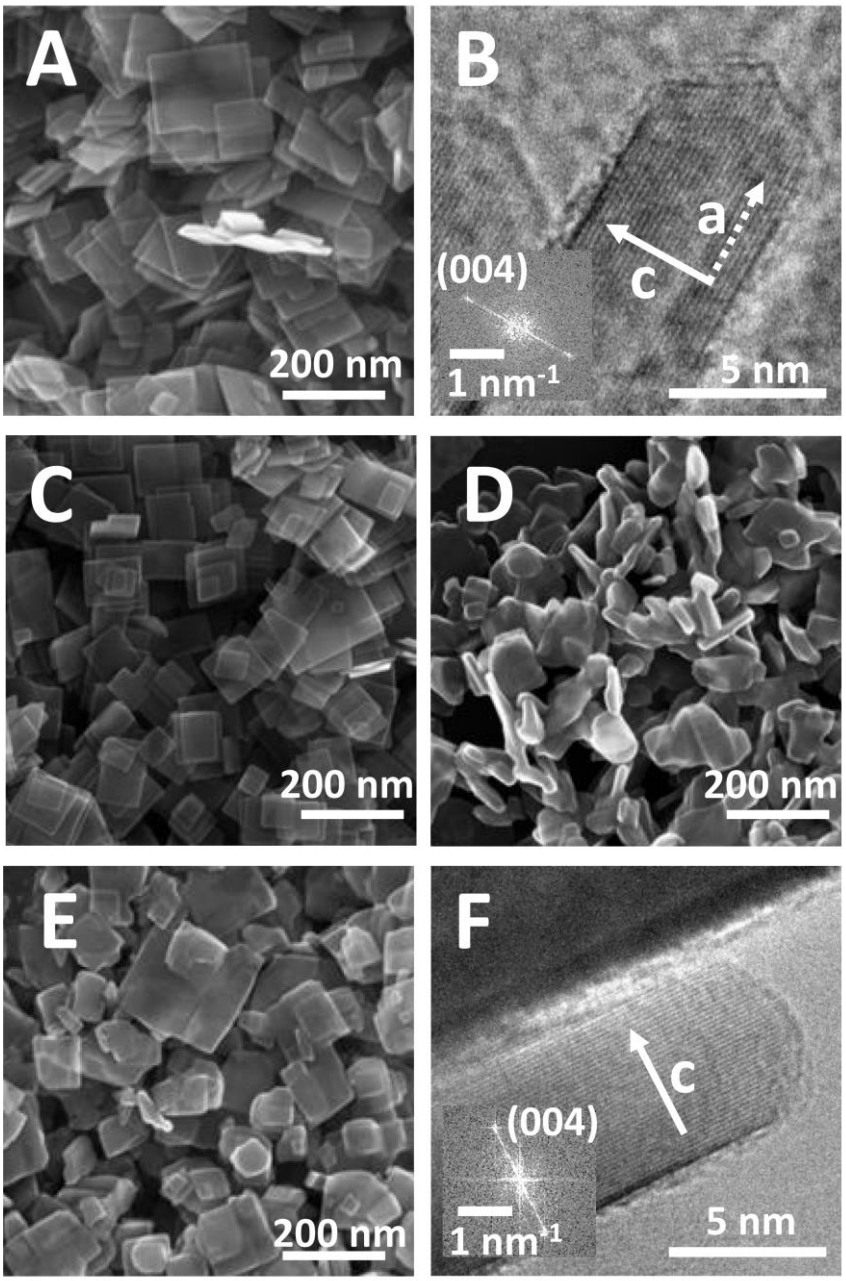

Figure 31. (A) SEM image of the as-synthesized TiO_2 nanosheets sample. (B) HR-TEM image and related FT of the as-synthesized TiO_2 nanosheets sample. (C) SEM image of the TiO_2 nanosheets sample washed in a NaOH solution. (D) SEM image of the TiO_2 n sh_NaOH sample after subsequent calcination at 873 K. (E) SEM image of the TiO_2 n sh calcined at 873 K (F) HR-TEM image and related FT of the TiO_2 n-sh calcined at 873 K.

Table 11. Average particle dimension obtained by Scherrer analysis of the (004) and (200) XRD peaks, particle thickness (T) and basal length (L) measured from SEM images, specific surface area, calculated average percentage of {001} facets (APPENDIX B).

Sample	d_{004} (nm)	d_{200} (nm)	T (nm)	L (nm)	SSA_{BET} (m^2/g)	%{001}
n-sh	18	> 100	9.4 ± 1.6	75 ± 25	53	78
n-sh_NaOH	21	> 100	8.4 ± 1.7	73 ± 27	57	79
n-sh_873K	46	> 100	10 ± 2	64 ± 25	34	58
bipy	36	29	40 ± 9	30 ± 5	43	10
bipy_873K	32	26	35 ± 5	45 ± 9	37	13

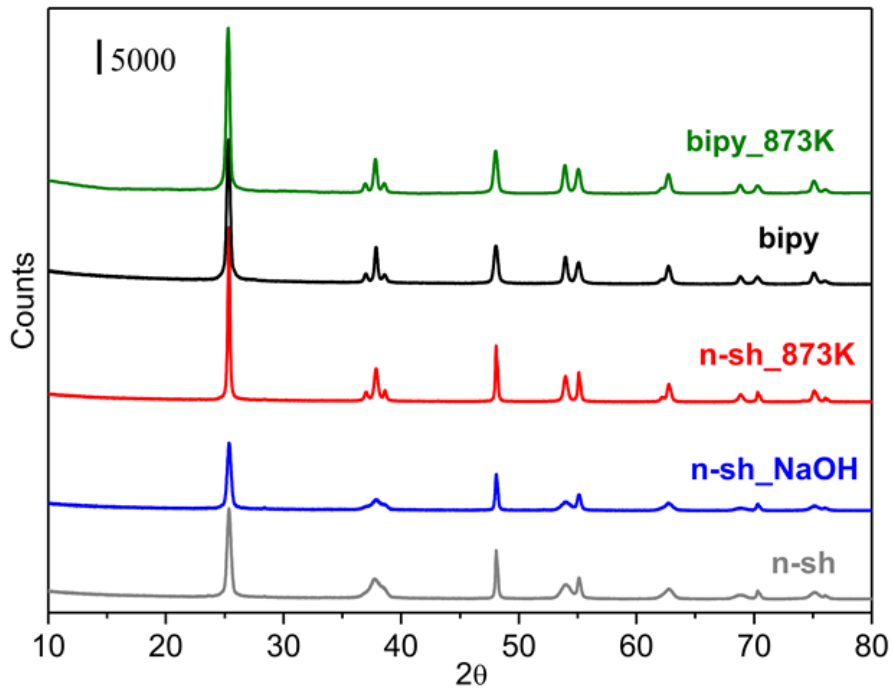

Figure 32. XRD patterns of the n-sh and bipy TiO_2 samples employed to perform the Scherrer analysis.

3.2.2. Fluorides doping measurement

The fluorine content and its evolution after treatments were determined by complementary techniques, also probing different depths (APPENDIX C). By ion chromatography, pristine TiO_2 n sh is found to contain 16 mg F^-/g TiO_2, decreasing to 7 mg F^-/g TiO_2 for TiO_2 n sh_NaOH, where is expected fluorides removal only from the surface. As a result, an initial F- surface concentration of ~5 F^-/nm^2 is calculated. This surface fluorination is relevant since the Ti^{4+} density is 7 and 5 nm^{-2} on {001} and {101} surfaces, respectively.[31] The significant decrease in the ToF-SIMS signal of F^- in the mass spectra of n-sh_NaOH sample, normalized to the TiO_2^- intensity (Table 12), supports partial removal of fluorine as found with IC. Note that Auger Electron Spectroscopy (probing 3-4 nm depth) as well as EDX (probing ~1 μm depth) cannot distinguish between the levels of fluorine signals as detected in the two samples n-sh and n-sh_NaOH. A reliable quantification into absolute chemical composition of fluorine with all three techniques, ToF-SIMS, AES and EDX is impossible mainly due to the strong matrix effect (see APPENDIX C).

All methods agreed in indicating the removal of fluorine in the sample calcined at 873 K down to or below the detection level of each method (Table 12), from both the bulk and the surface. Accordingly, the VIS-NIR electronic absorption due to the presence of Ti^{3+}, resulting from the substitution of O^{2-} ions by F^- ions,[32] present in the optical spectra of pristine and washed TiO_2 n-sh, disappeared (Figure 33).

Table 12. Fluoride concentration for the different samples obtained by ion chromatography and fluoride signals as detected by ToF-SIMS, AES and EDX.

Sample	IC (mg F^-/g TiO_2)	ToF-SIMS I_{F^-}/I_{TiO2^-} (a. u.)	AES $I_{F\ KLL}$ (a. u.)	EDX $I_{F\ K\alpha}$ (a. u.)
n-sh	16.1 ± 1.2 (5 F^-/nm^2)	73 ± 6	Yes	Yes
n-sh_NaOH	7.0 ± 0.8	54 ± 4	Yes	Yes
n-sh_873K	<0.4	3.6 ± 0.4*	Not Detected	Not Detected
bipy	<0.4	5.7 ± 0.6*	Not Detected	Not Detected

* Specifically for the extremely element-sensitive ToF-SIMS, this concentration level, differing from 'zero' also for the originally F-free TiO_2 bipy, was found also in the Si (100) blank substrate used for analysis, i.e. I_{F^-}/I_{TiO2^-}= 6.5, this demonstrating that this level of F^- represents the rest contamination present at the instrument used. LoD= limit of detection.

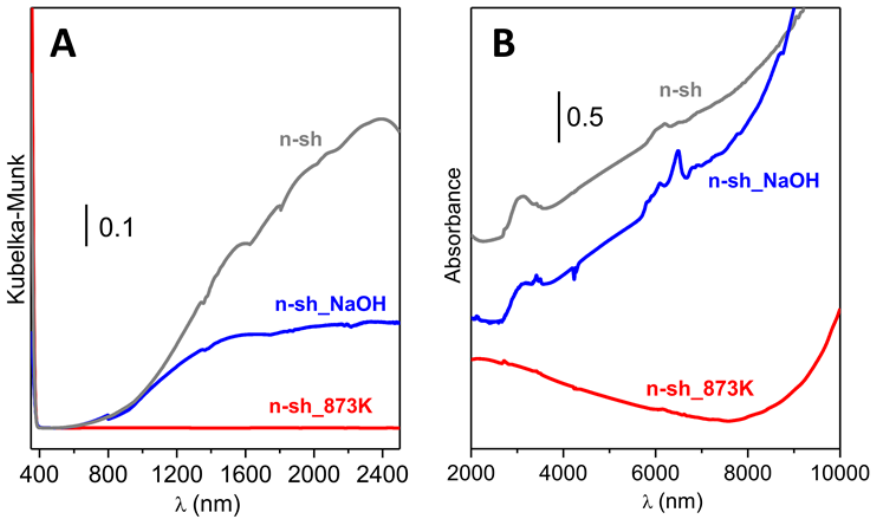

Figure 33. Diffuse reflectance Vis-NIR spectra (A) and transmission MIR spectra (B) of TiO_2 n-sh, TiO_2 n-sh_NaOH and TiO_2 n-sh_873K. On the X-axis of panel B, where spectra in the MIR range are shown, wavelength values are reported, instead than conventional wavenumber values, for the sake of consistency with spectra in panel A (being wavelength values commonly used for electronic spectra in the UV-Vis-NIR ranges). Note on the MIR spectrum of TiO_2 n-sh_873K: the apparent decrease in absorbance from 8000 to 2000 nm is the typical effect of decreased scattering of the samples at higher wavelengths, observed when measuring the spectrum in transmission, instead of in diffuse reflectance.

3.3. Spectroscopic Analysis of Bipyramids and Nanosheets

3.3.1. Interaction of H_2O with {001} and {101} surfaces

The interaction of surfaces with water can impact several functional properties of TiO_2, ranging from surface hole/electron transfer to water and other adsorbates to osseointegration.

The interaction between water and fluorinated (TiO_2 n-sh) and F^- free (TiO_2 n-sh_NaOH and TiO_2 n-sh_873K) was investigated by measuring the amount of H_2O molecules that can be reversibly adsorbed at room temperature (Figure 34A). This amount depends on the adsorptive properties of the "first hydroxylation/hydration layers", constituted by surface hydroxyl groups and strongly adsorbed water which are not desorbed by outgassing at r.t. Pristine TiO_2 n-sh adsorbs up to ~8 H_2O molecules/nm^2 when in contact with 15 mbar of H_2O. The removal of F^- by the two different methods impacts in two opposite directions the surface hydrophilicity: for TiO_2 n-sh_NaOH, the substitution of surface F^- by exchange with OH^- results in an increase to ~12 H_2O molecules/nm^2, whereas for calcined TiO_2 n-sh_873K the water adsorption capacity becomes limited to only ~5 H_2O molecules/nm^2. This finding is in agreement with DFT calculations which suggested that in the terrace region of the (1×4) reconstructed (001) surface, which should be obtained after calcination, water is physisorbed or not adsorbed at all.[33] It is worth

mentioning that TiO_2 bipyramids, overwhelmingly exposing {101} surfaces, adsorbs up to ~10 H_2O molecules/nm^2. Thus, for TiO_2 n-sh_873K, where these facets {101} account on an average for 40% of the surface, the actual amount of H_2O molecules adsorbed on fluorine free calcined {001} terminations might be of the order of ~2 H_2O molecules/nm^2. A similar consideration holds for TiO_2 n-sh_NaOH, which exposes on average 20% of {101} facets, but in this case the F^- free unreconstructed {001} surface exhibits an affinity towards water similar or slightly higher that the {101}. No definitive conclusions can be derived for the pristine TiO_2 n-sh since F^- can modify also the properties of {101} surfaces.[34]

The amount of H_2O per nm^2 found reversibly adsorbed on TiO_2 bipy in contact with 15 mbar H_2O might correspond to the formation of 2 molecular layers, in addition to the first hydration layer, as evaluated on the basis of molecular dynamic calculations of H_2O on a (101) surface, resulting in an average density of ~5.3 molecules/nm^2 for each of the three layers.[35,36] For H_2O on (001) TiO_2 anatase, a radial distribution function was found only for an unreconstructed hydroxy-free surface,[35] resulting in an average density of ~9.3 molecules/nm^2 per each of the first three layers. This result cannot be compared with experimental results on neither TiO_2 n-sh_NaOH nor TiO_2 n-sh_873K, where {001} surfaces are expected to be hydroxylated or (1 x 4) reconstructed, respectively. Nevertheless, an additional insight on the state of water on TiO_2 n-sh_873K in comparison with TiO_2 bipy was obtained by NIR spectroscopy (Figure 34B). The $\nu_{asym}+\delta(H_2O)$ band observed for TiO_2 bipy in equilibrium with 15 mbar H_2O (i.e. ~3 molecular layers of adsorbed water) is composed by a main absorption at ~5180 cm^{-1}, and a shoulder at ~5300 cm^{-1}, this latter due to

the H-bonding free OH pointing towards the exterior of the upmost water layer.[37-39] This component accounts for ~3.7% of the overall integrated intensity, but this value increases to ~8.5% for H_2O on TiO_2 n-sh_873K. In agreement with the microgravimetric data, this feature should be related to a decrease of the amount of water molecules underneath the upmost layer, i.e. a decreased number of H_2O layers on TiO_2 n-sh_873K. Moreover, a different networking among water molecules on the two samples can also contribute to the relative change in intensity of the two sub-bands.

Information on the relative amount of water molecules left irreversibly adsorbed at r.t. on the various samples and on their hydroxylation state was provided by mid-IR spectroscopy. For direct comparison with microgravimetric data, which concern H_2O reversibly adsorbed at r.t., also spectra of samples in contact with 15 mbar H_2O were collected (Figure 35A). Relevant spectral feature are: i) a weak, sharp band at ~3700 cm^{-1} due to the ν(OH) of H-bonding free H_2O molecules at the surface of the upmost water layer (see above), ii) an intense and broad absorption spread over the 3600-2800 cm^{-1} range, due to the ν(OH) of H-bonded water molecules and surface hydroxyl groups, iii) the $\delta(H_2O)$ signal of adsorbed H_2O molecules, with maximum at ~1635 cm^{-1}.[40,41] In addition, also the $\delta(H_2O)$ of water left adsorbed irreversibly by outgassing at r.t. is reported, for the sake of comparison (dashed lines). For each sample, the integral of the area between the full and dotted lines is proportional to the amount of reversibly adsorbed H_2O molecules. The relative values obtained (1.0/bipy, 0.7/n-sh, 0.9/n-sh_NaOH, 0.3/n-sh_873K) are in good agreement with those provided by microgravimetry (1.0/bipy, 0.7/n-sh, 1.1/n-sh_NaOH, 0.4/n-sh_873K).

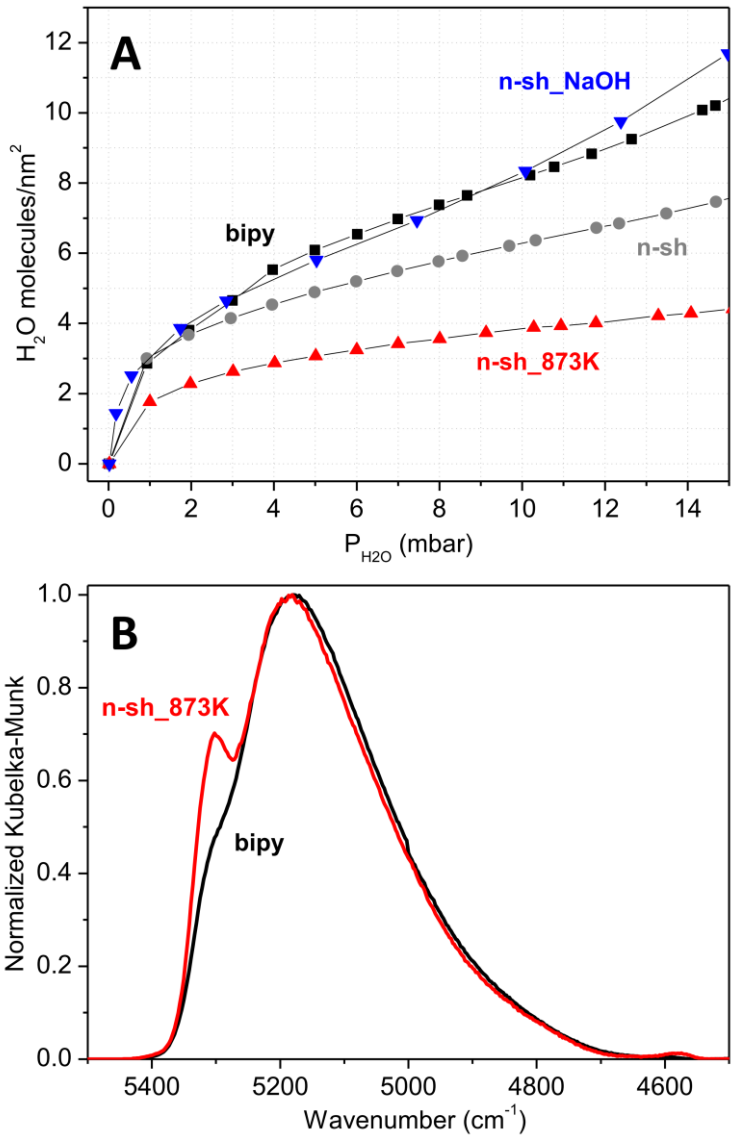

Figure 34. (A) Water adsorption isotherms at 298 K obtained from microgravimetric data. The samples have been previously outgassed at r.t. (B) Normalized NIR spectra of the TiO_2 bipy (black) and TiO_2 n-sh_873 K (red) samples in contact with 15 mbar of H_2O.

Thus, also the relative integrated intensity of the $\delta(H_2O)$ signals obtained for samples outgassed at r.t. (Figure 35B) should correspond to the relative amount of H_2O molecules left adsorbed in this condition, that was not

possible to determine by microgravimetry. With respect to the pristine TiO_2 n-sh, the removal of fluorides by NaOH washing resulted in an increased capability of retaining water in the first hydration layer, becoming similar to that of TiO_2 bipy. Moreover, the upshift in position of the $\delta(H_2O)$ band indicates that water molecules are experiencing a weaker coordinative interaction with surface cationic sites.[42,43] Conversely, the amount of water molecules retained by the surface of TiO_2 n-sh calcined at 873 K appears rather low. This well agrees with DFT calculations which suggested that, on the reconstructed (001) surface in the terrace region, water is physisorbed or not adsorbed at all.[33] Concerning the 3800-2700 cm^{-1} ν(OH) spectral profile of samples outgassed at r.t., TiO_2 bipy exhibits the well-known pattern made of a series of sharp bands at $\nu \geq 3600$ cm^{-1} due to isolated hydroxyl groups, a band at 3470 cm^{-1} assigned to water molecules strongly coordinated with Ti^{4+} sites on {101}, superimposed to the onset of a broad absorption due to an extended network of hydrogen bonding between OH groups and water molecules.[40,41] This absorption becomes the dominant component of the ν(OH) profile of TiO_2 n-sh, at the expenses of signals due to isolated hydroxyl groups. These signals are totally absent in the spectrum of TiO_2 n-sh_NaOH, indicating that the treatment in basic solution affected also the hydroxylation of {101} surfaces. Conversely, bands due to isolated OH are the main feature of the ν(OH) pattern of TiO_2 n-sh_873K, characterized by an overall weak intensity.

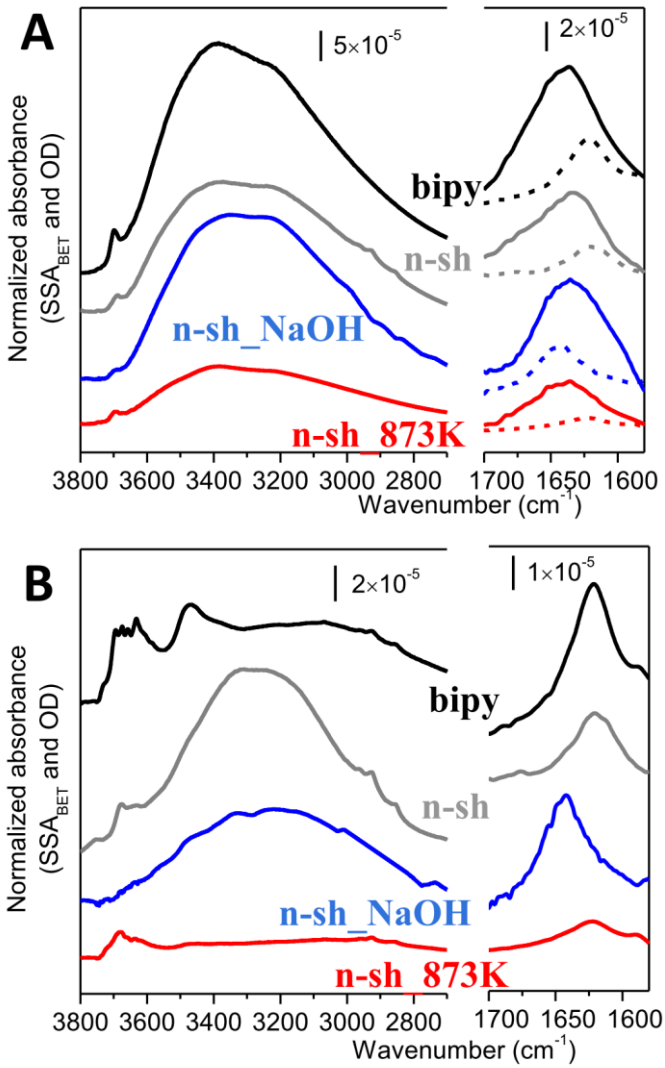

Figure 35. FT-IR spectra of the samples in contact with 15 mbar of H_2O (A) and after outgassing for 1 hour at r.t. (B). To facilitate the comparison, the spectra after outgassing for 1 hour are also reported in part (A) as dashed curves in the H_2O bending region.

3.3.2. Interaction with CO

Finally, the Lewis acidity of surface Ti^{4+} sites was probed by IR spectroscopy of adsorbed CO.[44,45] This method requires the pre-outgassing at high temperature, and then it was applied only to TiO_2 n-sh_873K, that already experienced a thermal treatment, and to TiO_2 bipy, for the sake of comparison. Surprisingly, the main feature of the spectrum of CO adsorbed at ~100 K on TiO_2 n-sh_873K is the peak at ~2180 cm^{-1} due to probe molecules on {101} surfaces,[46,47] similar in position to the dominant peak of CO on TiO_2 bipy, whereas {001} surfaces seem to be silent (Figure 36A). Details on the assignment of the other minor components are reported in Table 13. By further decreasing the adsorption temperature down to ~60 K (Figure 36B) the dominant spectral feature of CO on TiO_2 n-sh_873K becomes a new band at ~2155 cm^{-1}, thus falling in a frequency range expected for CO adsorbed on Ti^{4+} sites on (1x4) reconstructed (001) surface as predicted by DFT calculations.[46] This band is fully reversible upon CO outgassing at 60 K, whereas the peak at ~2180 cm^{-1} remains almost unaffected (appearing reversible upon outgassing in the experiment at 100 K). Moreover, the maximum moves from ~2155 to ~2160 cm^{-1}, because of the fading away of adsorbate-adsorbate interactions, i.e. approaching the singleton ν(CO).[48] The very limited upshift of the singleton signal with respect to the stretching mode of CO in gas phase (2143 cm^{-1}) indicates that Ti^{4+} on such surfaces are rather weak as Lewis acid sites. This agrees with the weakness of their interaction with CO, actually scarce at a temperature as low as ~100 K.

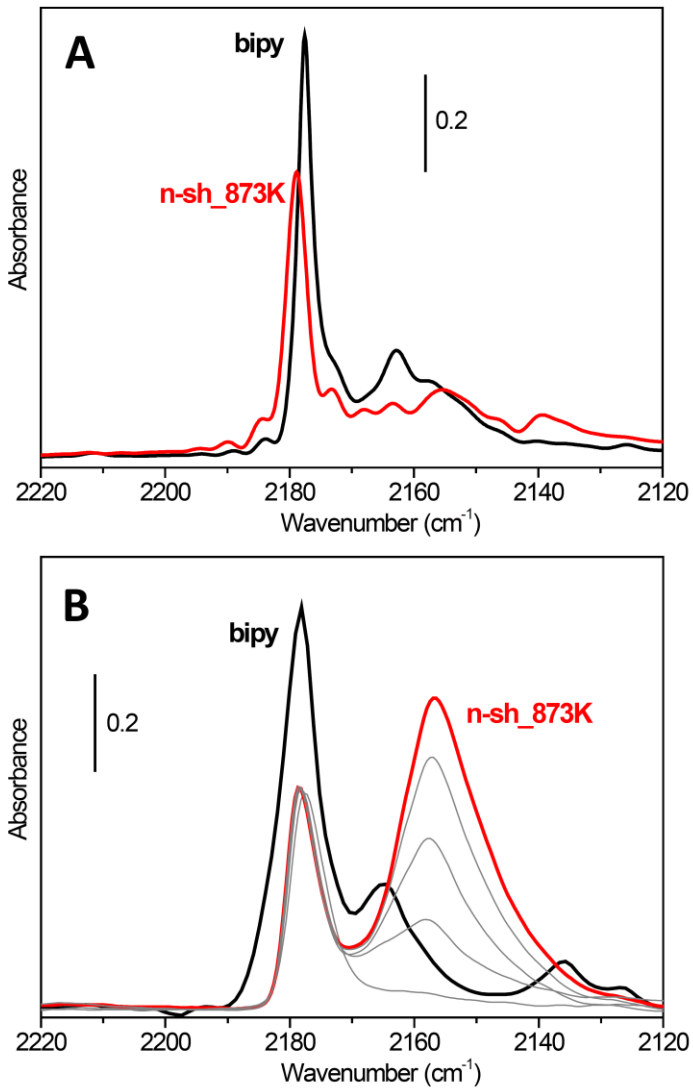

Figure 36. IR spectra of CO adsorbed on TiO_2 bipy (black) and TiO_2 n-sh_873 K (red) at 100 K (A) ad 60 K (B). In both cases the sample was put in equilibrium with 15 mbar of CO at 100 K and then, for (B), the temperature was decreased to 60 K. The gray spectra in part (B) refer to progressive CO outgassing at 60 K for sample TiO_2 n-sh_873 K.

Thus, calcination at 873 K of F^- templated TiO_2 n-sh with prevailing {001} facets allows the complete removal of fluorides from both surface and bulk without modifying the NPs morphology. However, the resulting {001} surfaces are poorly hydroxylated and expose Ti^{4+} sites with a weaker Lewis

acidity than those on {101} ones. This results in a weak interaction with H_2O molecules in forming the first hydration layer that, in turn, decreases the capability to further adsorb water. These features agree with the occurrence of a (1x4) reconstruction of {001} surfaces upon calcination, as predicted by DFT calculations.[33,49]

Conversely, it is possible to obtain TiO_2 n-sh with highly hydroxylated {001} surfaces, as hydrophilic as the {101} ones, by washing pristine fluorinated NPs with a NaOH solution. However, the nanoparticles remain doped with F^- in their bulk, still affecting the electronic features, and their morphology is not stable against possible subsequent calcination treatments.

Table 13. Assignment of the main IR spectral features of CO adsorbed on TiO_2 NPs (Figure 36).[2,41]

Band position (cm^{-1})	**Assignment**
2180-2178	^{12}CO on {101} surfaces
2165-2163	^{12}CO on {100} surfaces
2156-2155	^{12}CO on {001} surfaces
2139-2138	Liquid-like CO
2127-2126	^{13}CO on {101} surfaces

3.3.3. Electron Paramagnetic Resonance of TiO_2 nanosheets

Among the spectroscopic techniques, Electron Magnetic Resonance techniques can be of fundamental in order to describe at a molecular level the structure and the reactivity of paramagnetic species. Such species, which shown the presence of an unpaired electron (at least), are frequently present in some catalytic systems either as active species or catalytic intermediates, often associated to transition-metal ions. The structure that surrounds the active site of the catalyst has a great influence on the activity, selectivity and specificity of the catalyst.[50] If the paramagnetic species are important within the catalytic cycle, EPR techniques can provide a unique characterization of the geometric and electronic structure, the interaction with the environment and the dynamical processes of the active species.[51]

Different EPR approaches can be used for the characterization of heterogeneous catalysts, ranging from the study of model systems under ultra-high vacuum conditions[52] until real catalysts under operando conditions,[53,54] or also catalysts under controlled conditions.[55-57] Some methodologies include thermal treatments in a controlled atmosphere, solid-gas interface reactivity tests and the use of isotopic enrichment. Moreover, controlled-conditions approaches allow the use of high resolution pulse EPR techniques, which are able to resolve weak magnetic interactions, which usually are not resolvable in conventional CW-EPR experiments. In particular, ENDOR (Electron Nuclear Double Resonance)

and ESEEM (Electron Spin Echo Envelope Modulation) techniques allow detecting the nuclear magnetic resonance (NMR) transition frequencies of those nuclei that are coupled to unpaired electrons, providing information about the local structure of the chemical bond between the active site and its ligands.[51]

Concerning the chemistry of low valence states of titanium, an important aspect concerns the photo-catalytic reactions that occur at the surface of titanium dioxide (TiO_2). The TiO_2 photocatalytic properties are based on the light-induced charge separation.

$$TiO_2 + h\nu \rightarrow e_{cb}^- + h_{vb}^+$$

Both charge carriers (if they do not recombine) can be trapped at surface or bulk position of the solid. Holes are trapped by oxygen anions, while electrons are trapped by cations forming Ti^{3+} ions.

$$O^{2-} + h_{vb}^+ \rightarrow O^-$$

$$Ti^{4+} + e_{cb}^- \rightarrow Ti^{3+}$$

This process of charge separation causes the formation of two separated paramagnetic species; both the trapped electron and the trapped hole are observed by EPR.[51,58] By means of CW-EPR the rationalization of the g values of the EPR active species present in the titania crystals is possible. Table 13 reports the g-tensor values of the main electron trapping sites for the three natural TiO_2 polymorphs.

Table 14. g-tensor values of the main electron trapping sites in titanium dioxide polymorphs (from [51]).

Polymorph	Trapping site	g Matrix		
		g_1	g_2	g_3
Anatase	Regular Lattice Site	1.992	1.992	1.962
	Surface sites (disordered environment)	g_{av}=1.93		
Rutile	Regular Lattice Site	1.969	1.960	1.949
	Interstitial Lattice Site	1.9787	1.9750	1.9424
Brookite	Bulk Lattice Site	1.989	1.989	1.960
	Surface sites	1.939	1.929	1.893

3.3.3.1. EPR measurements

X-band CW-EPR spectra were detected on a Bruker EMX spectrometer (MW frequency ~9.75 GHz) equipped with a cylindrical cavity. A modulation frequency of 100 kHz, a modulation amplitude of 0.2 mT and a microwave power of 0.1 mW were used. Pulse EPR experiments were performed on an ELEXYS 580 Bruker spectrometer operating at X-band (MW frequency 9.4 GHz), equipped with a liquid-helium cryostat from Oxford Inc. The magnetic field was measured by means of a Bruker ER035 M NMR gauss meter. Electron-spin-echo (ESE) detected EPR spectra were recorded with the Hahn echo sequence $^{\pi}/_{2}\,\tau-\pi-\tau-$echo. Microwave pulse lengths $t_{\pi/2}$= 16 ns, t_{π} = 32 ns, and a shot repetition rate of 0.5 kHz were used. Two-pulses electron-spin-echo envelop modulation (2P-ESEEM) experiments were carried out with the Hahn echo pulse sequence, in which the π value was incremented in steps of 8 ns starting from 100 ns. The

time traces of the 2P-ESEEM spectra were baseline corrected, apodized with a Hamming window and zero filled; after two-dimensional Fourier transformation, the absolute value spectra were calculated.

The quantification of the amount of EPR-active Ti^{3+} centers in the samples was performed employing as a reference Ti^{3+} standard solutions obtained dissolving the $Ti(tmhd)_3$ complex in anhydrous toluene at five different molar concentrations in the range 2 - 20 mM. The standard solutions were prepared operating in glove-box. The EPR spectra of the standard frozen solutions were recorded under the same experimental conditions used for the samples (the microwave power was selected in order to avoid saturation effects of both the standard and the samples).

3.3.3.2. EPR Characterization. Ti^{3+} in Anatase Generated by Valence Induction

The alteration of the ionic charge caused by the presence of an aliovalent element into an ionic lattice is a well-known phenomenon in solid-state chemistry. In the case of titanium dioxide, the introduction of F^- ions in the oxide matrix during the synthesis, leads to the formation of Ti^{3+} ions revealed by characteristic EPR spectra[32,59]. The concentration of F^- (hence Ti^{3+}) in the solid can be tuned using different preparation methods. In particular, in the present work high doping levels are achieved via a hydrothermal synthesis leading to highly fluorinated, blue coloured, TiO_2 platelets exposing {001} facets.

After high vacuum treatments at 373 K (residual pressure $<10^{-3}$ mbar) to remove surface adsorbates, the as prepared F-TiO_2 samples display EPR spectra (Figure 37a) characterized by a powder-like axial pattern with $g_{zz} = g_{\parallel} = 1.962$ and $g_{xx} = g_{yy} = g_{\perp} = 1.992$, in line with typical F-doped TiO_2 systems, although displaying unusually broad line widths, associated to dipole-dipole broadening and indicating a large concentration of Ti^{3+} species. Quantitative evaluations indicate a Ti^{3+} concentration of the order of 1.14×10^{18} spin/g. In the case of F-TiO_2 prepared by wet chemistry methods, it is crucial to discriminate between the possible formation of both surface and bulk F^- dopants and the correlated Ti^{3+} surface and bulk states. Clearly surface states will deeply affect the chemistry at the solid/adsorbate interface, while bulk impurities will alter the electronic structure of the solid, both situations impacting, in different ways, on the chemical reactivity of the modified solid. The insertion of fluorine in the TiO_2 matrix has been demonstrated to generate localized electrons in the t_2g orbitals of the cations without generating oxygen vacancies. On the other hand, surface diamagnetic F_{surf}-TiO_2 centres have been identified by the X-ray photoemission spectroscopy technique (XPS)[32]. However, no evidence of surface Ti^{3+} ions has been obtained so far for F doped TiO_2 samples.

Reduced titanium species localized at the surface are characterized by distinctive broad EPR spectra, which are best observed by means of electron spin echo (ESE) detected EPR experiments[59]. The ESE-detected EPR spectrum corresponds to the absorption of the conventional CW-EPR spectrum and is more effective in detecting broad signals, which become

hardly observed in conventional CW-EPR experiments, which provide the absorption derivative.

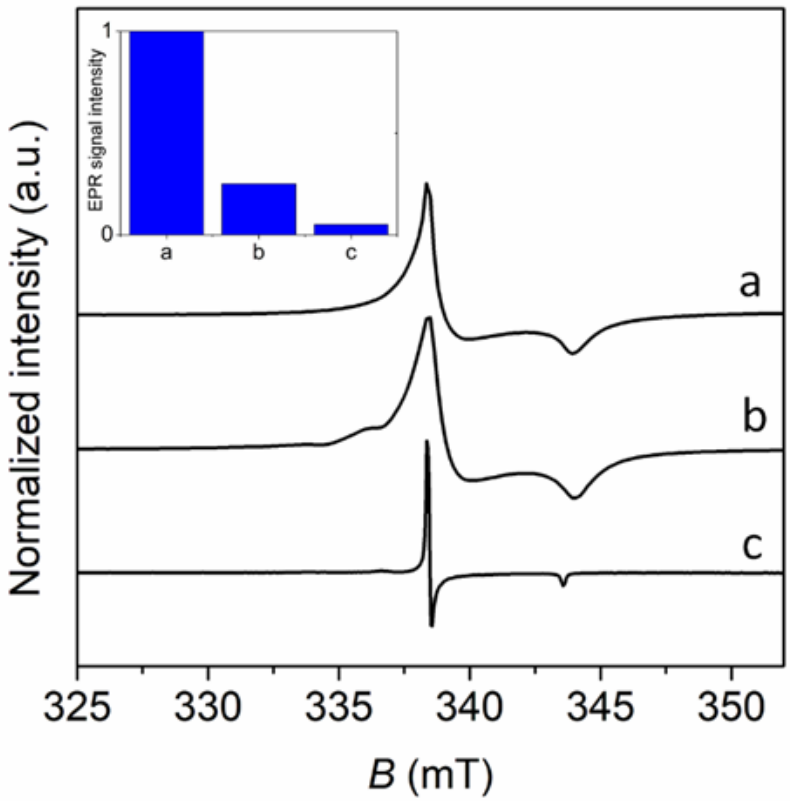

Figure 37. X-band CW EPR spectra of different F-TiO_2 samples recorded at 77 K of a) F-TiO_2 as prepared; b) NaOH washed; c) calcined. All samples were treated under high vacuum at 373 K.

The ESE detected EPR spectrum is reported in Figure 38a and clearly shows the presence of a broad absorption centered approximately at g=1.93. This broad signal, undetectable in the conventional CW EPR experiment, has been assigned to a collection of surface and subsurface reduced Ti^{3+} centers whose heterogeneity derives from several factors including the local coordination of the ion, the symmetry of the particular crystal face hosting the reduced ion, and the presence of magnetically active nuclei

located in the vicinity of the paramagnetic centers. In our case magnetically active nuclei are associated to surface F ions, whose presence can be revealed by means of Electron Spin Echo Envelope Modulation (ESEEM) experiments. Two-pulse ESEEM (2P-ESEEM) spectra were then taken at magnetic field settings corresponding to the maximum absorption of bulk Ti^{3+} and of the broad resonance at g=1.93 (indicated by the arrows in Figure 38a), respectively. The 2P-ESEEM measurements of ^{19}F modulation of the two different Ti^{3+} provide compelling evidence of the surface nature of the broad species, which is characterized by a ^{19}F rich environment. The 2P-ESEEM patterns recorded at field positions corresponding to the two different species are shown in Figure 38c,e respectively, whereas the corresponding Fourier transform is shown in Figure 38d,f. Despite the low echo intensity, the ^{19}F modulations are clearly visible, indicating a high number of ^{19}F nuclei interacting with the Ti^{3+} centers. The same experiment, performed at a magnetic field setting corresponding to the narrow feature of the Ti^{3+} bulk species, does not show such modulations, as already observed in the past.

Further evidence of the surface nature of the Ti^{3+} species is obtained by performing the same experiment after washing the sample with a NaOH solution (0.1 M). This treatment removes surface F^- ions oxidizing the associated Ti^{3+} species to diamagnetic Ti^{4+} ions. As a result the spectral intensity is decreased to approximately 25% of the initial value (inset in Figure 37), with a strong depletion of the broad absorption feature (Figure 2b). Finally, calcination of the sample at high temperature leads to a strong depletion of the Ti^{3+} centers, which are reduced to approximately 5% of the initial value (inset in Figure 37) and diluted in the diamagnetic host

matrix as reflected by the drastic decrease of the spectral line width. In summary, combined CW and pulse EPR experiments indicate that before illumination the F-TiO_2 sample exhibits both terminating surface Ti^{3+} centers and bulk Ti^{3+} due to F-doping during the synthesis. To test the photochemical reactivity towards electron and hole transfer experiments were carried out under UV irradiation in vacuum and in the presence of O_2 and H_2, which act as electron and hole scavengers respectively.

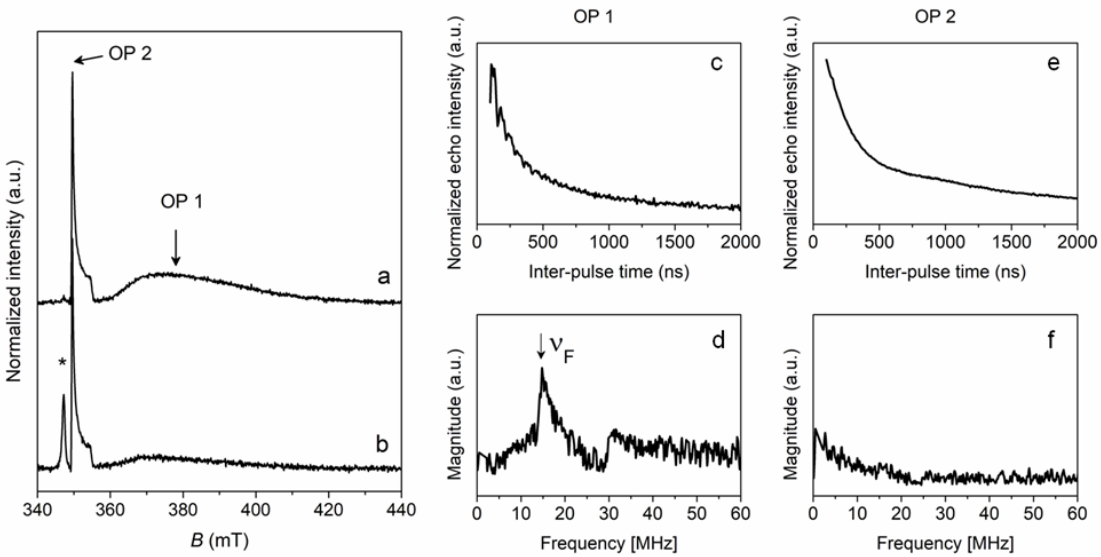

Figure 38. ESE-detected EPR spectra of F-TiO_2 as prepared (a) and NaOH washed (b). 2P-EESEEM spectra of F-TiO_2 as prepared, taken at OP1 (c) and OP2 (e) and their corresponding Fourier transform (d,f). All of the spectra were recorded at T = 10 K.

Irradiation under vacuum with above band gap energies is expected to generate paramagnetic charge separated states, which can be described in chemical terms as Ti^{3+} and O^- transient species. After 10 min of UV illumination under vacuum at 77 K of the as prepared sample, we observe the appearance of weak EPR signals at $g > g_e$ and g values typical of surface O^- species formed by hole trapping at surface O^{2-} sites[60-62]. Irradiation of the same sample under O_2 and H_2 atmosphere, leads to

similar results, indicating that the surface fluorinated sample with exposed {001} facets displays a negligible photochemical reactivity. A different situation is observed upon removal of the fluorinated surface by means of NaOH washing. Under these circumstances UV irradiation under vacuum induces minor changes in the original EPR spectrum associates to a new signal at g=2.007 and a shoulder at g= 1.999. The first peak may be ascribed to one of the spectral components of an oxygen based radical, while the signal at g=2 is likely to be associated to electrons at oxygen vacancies or so-called $V_o^{\bullet}$ centers. More interestingly, after irradiation under H_2, the EPR signals associated to localized hole centers completely disappear, while the intensity of the Ti^{3+} signal increases of a factor of 3. This result indicates that surface holes are formed, which react with H_2 according to the following reactions as already observed by Diwald et al.[63]

The complementary experiment involving O_2 as an electron scavenger, leads to the appearance of a new signal characterized by $g_{\parallel}$ = 2.036 an $g_{\perp}$ = 2.005, which is due to surface adsorbed superoxide ions, formed via a direct surface to molecule electron transfer, according to the following reaction:

$$Ti^{3+}_{surface} + O_2 \rightarrow Ti^{4+} + O_2^-(surface)$$

The intensity of the superoxide signal corresponds thus to the fraction of surface reactive Ti^{3+} species generated under irradiation. Quantitative evaluation of the EPR spectra obtained upon irradiation under H_2 and O_2 indicates that the fraction of chemically reactive surface hole centers generated under irradiation is slightly higher (approximately 1.7 times) than

that of the surface Ti^{3+} centers, suggesting a moderately higher oxidative capacity of the sample.

Finally, we notice that the reactivity of the calcined samples is strongly inhibited, and no significant spectral changes are observed upon UV illumination under the above reported conditions.

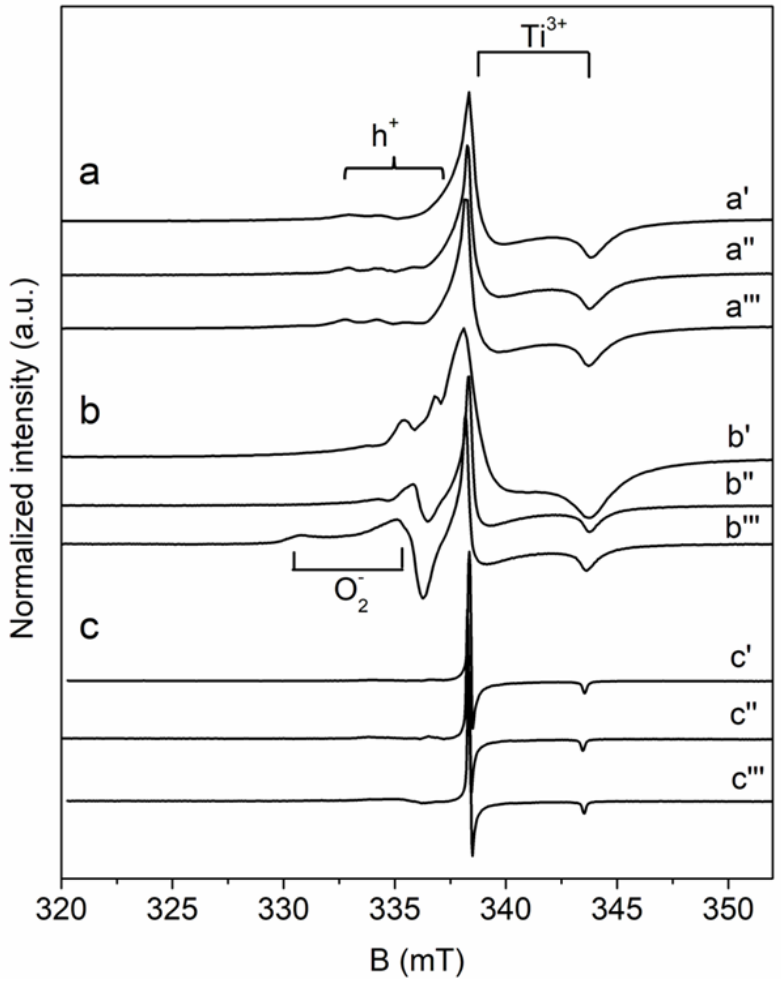

Figure 39. CW-EPR spectra of F-TiO_2 as prepared (a), NaOH washed (b) and calcined (c), recorded in dark upon 10 minutes irradiation in vacuum (') , in H_2 ('') and in O_2 (''') . All of the spectra were recorded at T = 77 K.

3.4. Effect of fluorination on the photo-electrochemical properties of nanosheets TiO_2 electrodes

In order to evaluate the rate constant of recombination and transfer to solution for electrons and holes generated upon illumination of the studied TiO_2 nanoparticles, we carried out electrochemical measurements. For this purpose, the method developed by Gomez[64] was used. It is based on the combination of voltammetric measurements (CV) in the dark and open circuit photopotential (OCP) relaxation tests. In this way, it is possible to obtain the density of charge carriers generated and their recombination rate. In our specific case, the fluorination of the TiO_2 nanoparticles can change the recombination rate of the photogenerated electrons and holes and the carrier transfer to solution. The complete theory used by Gomez is beyond the purpose of this thesis, where only the measurements and the results obtained following this model are reported.

3.4.1. Preparation of TiO_2 films

TiO_2 electrodes were prepared following the procedure described below:

- Preparation of 5 mL of TiO_2 suspension 10 g L^{-1} and sonication for 30 min;
- Deposition of a thin TiO_2 film on a fluorine doped tin oxide (FTO) glass using the doctor-blade technique and drying in air at room temperature;

- Dropping of the TiO_2 suspension over the first layer until the generation of a thick film and drying in air at room temperature. In this way all the UV irradiation was extinguished and it was possible to weight the deposited sample, but only the first layers of the film are effectively active in the photocatalytic process, decreasing the yield of the reaction;
- The illuminated area of the electrodes is 4 cm^{-2};

3.4.2. Apparatus and Test Conditions

The electrochemical measurements were performed using a standard photo-electrochemical setup, composed of a computer-controlled potentiostat, AUTOLAB PGSTAT12, and a fluorescent source with λ_{max} = 365 nm (Philips PL-S 9W BLB, integrated irradiance = 20 W m^{-2}). The electrochemical cell was a conventional three-electrode cell with a 1 mm thick fused silica window. The counter and reference electrodes were a Glassy Carbon and a Ag/AgCl/KCl (3M) electrode, respectively. Both CV and OCP measurements were carried out under a N_2 atmosphere (flux 100 mL min^{-1}); also the solution (KNO_3 0.1 M as electrolyte) was purged with N_2 for 20 min before each measurement in order to eliminate the residual O_2 present in the solution, to obtain the recombination rate of the photogenerated carriers. The experiments are carried out at unadjusted pH (i.e. without any correction) and at pH 3.5.

3.4.3. Results

Figure 40 shows the OCP measurements of the three considered materials at unadjusted pH.

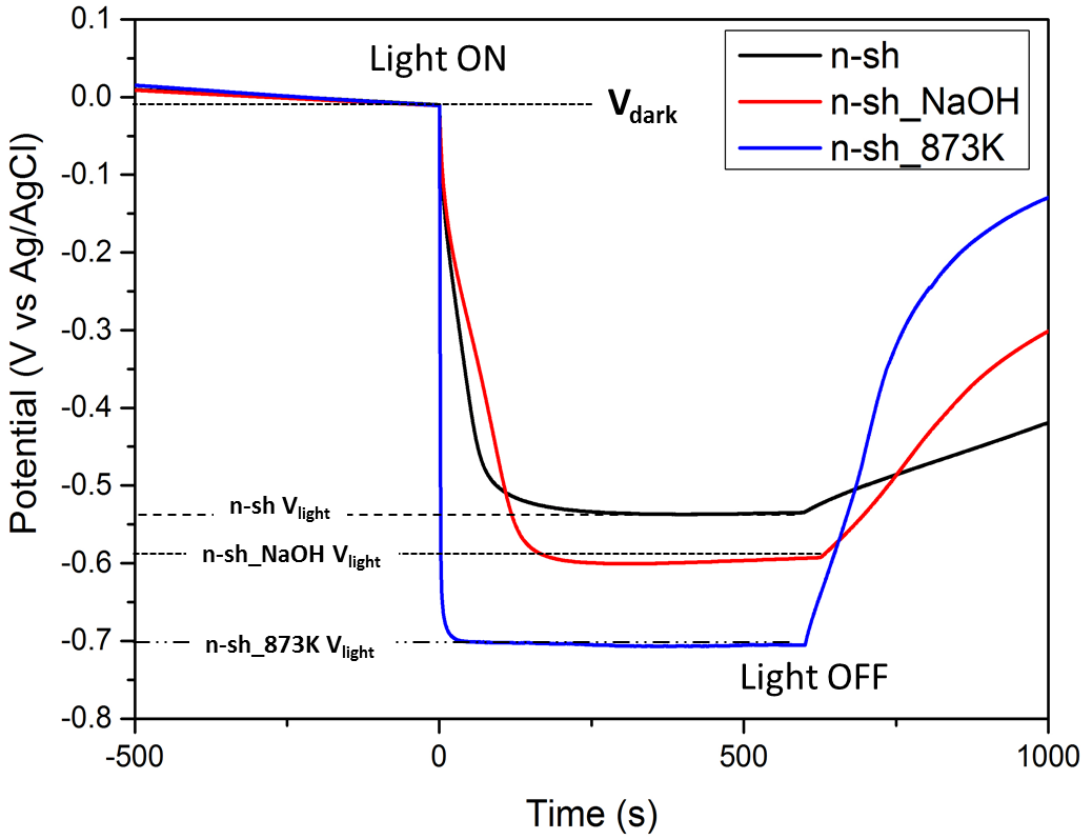

Figure 40. Open Circuit Potential (OCP) of the three considered materials under N_2 atmosphere and an UV illumination (365 nm) of 20 W m^{-2}. Unadjusted pH.

The OCP measurements carried out under a N_2 atmosphere can be used to evaluated the effect of fluorides on the charge carriers recombination in the semiconductor and on the ability of the materials to accumulate electrons. Indeed, the potential obtained under irradiation, is an equilibrium between electrons accumulation (hole are transferred to the solution with faster

timescales) and recombination.[64] If the rate of the recombination process is lower than the electrons accumulation rate, the result is a net storage of electrons that pushes the photo-potential towards more negative values. In order to evaluate the effect of the fluorides, the comparison between the materials n-sh and n-sh_NaOH was carried out. Figure 40 highlights that decreasing the presence of fluorides lowers the photo-potential ($\Delta V = V_{light} - V_{dark}$). This means that fluorides stabilize the photogenerated electrons that, consequently, are less reducing. As a consequence the fluorides slow down the recombination rate of the carriers when the irradiation is turned off (lower recovery rate of the potential). This phenomenon was already observed[64,65] and it is relevant on the photocatalytic activity of fluorinated materials as we will see later in the chapter dedicated to the photocatalysis. Figure 40 reports also the OCP of the material n-sh_873K, the photo-potential obtained for this material is higher than for the fluorinated materials, and with an apparent increased recombination rate.

In order to quantify the charge carrier recombination and the density of photo-generated carriers, the method developed by Gomez[57] was used, based on the combination of CV in the dark and the rates of OCP rise and decay.

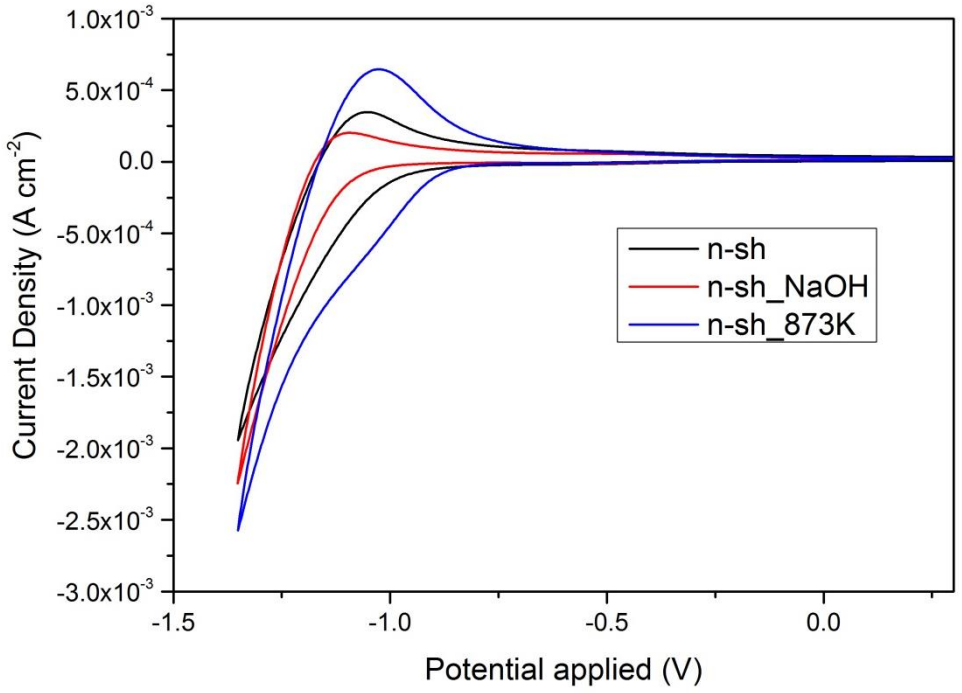

Figure 41. CV carried out on the three materials under a N_2 atmosphere. Unadjusted pH

In Figure 41 the CVs carried out on the three materials under a N_2 atmosphere are shown. The relevant information is given by the cathodic branch, in particular between V_{dark} and V_{light} obtained in the OCP test.

The integration of the cathodic branch voltammogram gives the charge accumulated in the electrode in a defined ΔV or, equivalently, the electron density as a function of the applied potential.

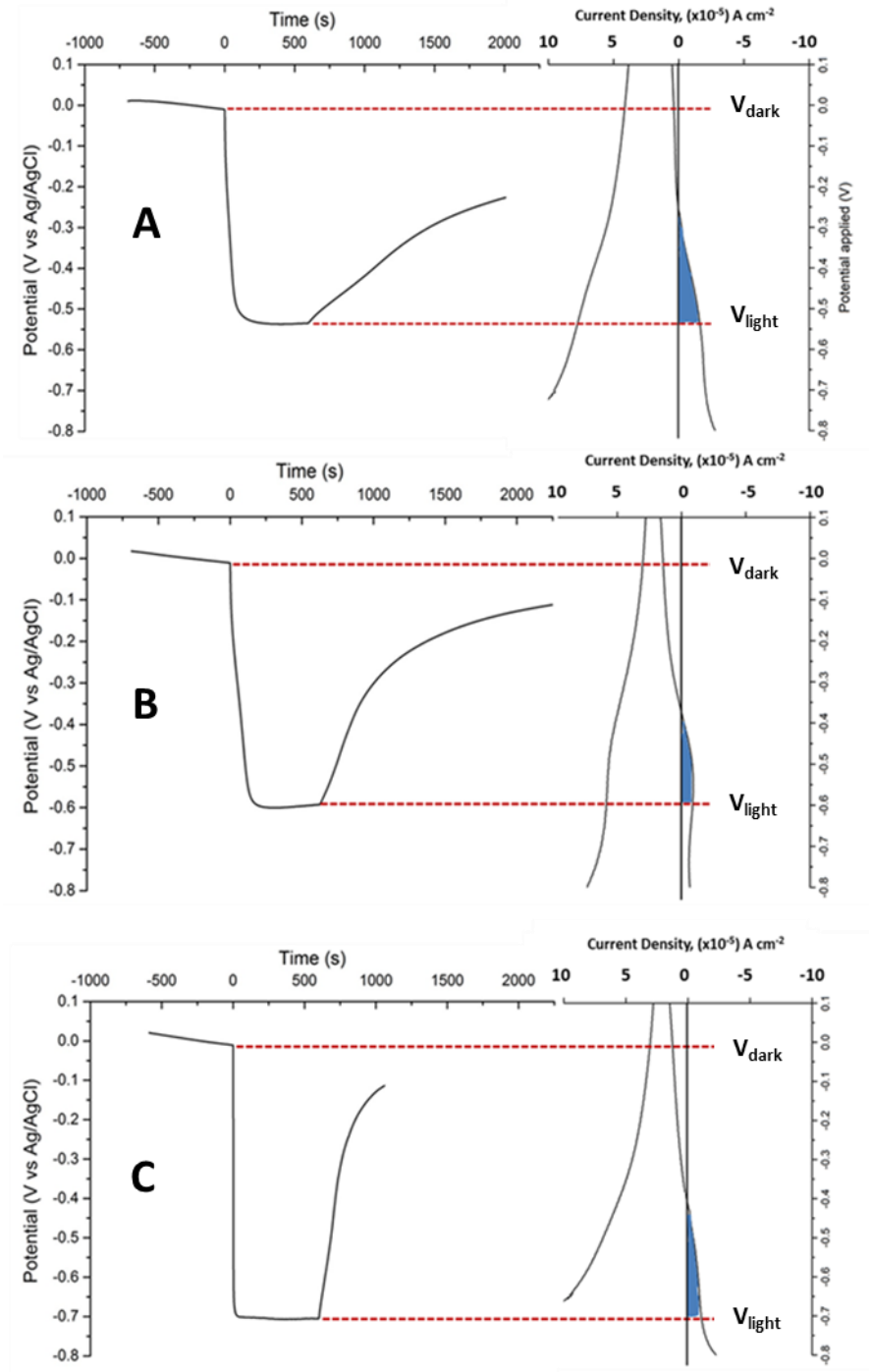

Figure 42. Combination of CV in the dark and OCP relaxation tests. The integrated area is highlighted in blue and delimited by V_{dark} and V_{light}. A) n-sh; B) n-sh_NaOH; C) n-sh_873K. Current density scale is expressed in 10^{-5} A cm^{-2}.

Integrating from V_{dark} to V_{light}, it is possible to calculate the density (cm^{-3}) of photoelectrons produced under illumination. Whereupon it is possible to monitor the decay of the carriers' density integrating gradually a lower area in the CV, following the return of the V_{light} to more positive potential. The integration process is well described in Figure 43 for the material n-sh_873K.

From the decay curve of the photogenerated carriers density it is possible to calculate a recombination rate constant for the materials considered. Table 15 reports the photogenerated carriers density (n_{ph}) at steady-state irradiation and the photogenerated carriers density at the same potential (-0.5 V), the recombination rate constant calculated taking into account the linear decay trend of the process in the OCP measurements and the photo-potential induced by an irradiation of 20 W m^{-2} under a N_2 atmosphere at unadjusted pH.

Table 15. Resume of the results obtained applying the Gomez model to the material n-sh, n-sh_NaOH and n-sh_873K at unadjusted pH.

Material	n_{ph} (cm^{-3})	n_{ph} at -0.5 V (cm^{-3})	k_r*	ΔV (mV)
n-sh	$8.56*10^{16}$	$8.11*10^{16}$	$2.7*10^{-3}$	525
n-sh_NaOH	$6.59*10^{16}$	$6.24*10^{16}$	$6.5*10^{-3}$	581
n-sh_873K	$8.45*10^{16}$	$5.82*10^{16}$	$2.4*10^{-2}$	694

*k_r is calculated using data from n_{ph} max to $4.0*10^{16}$ cm^{-3}

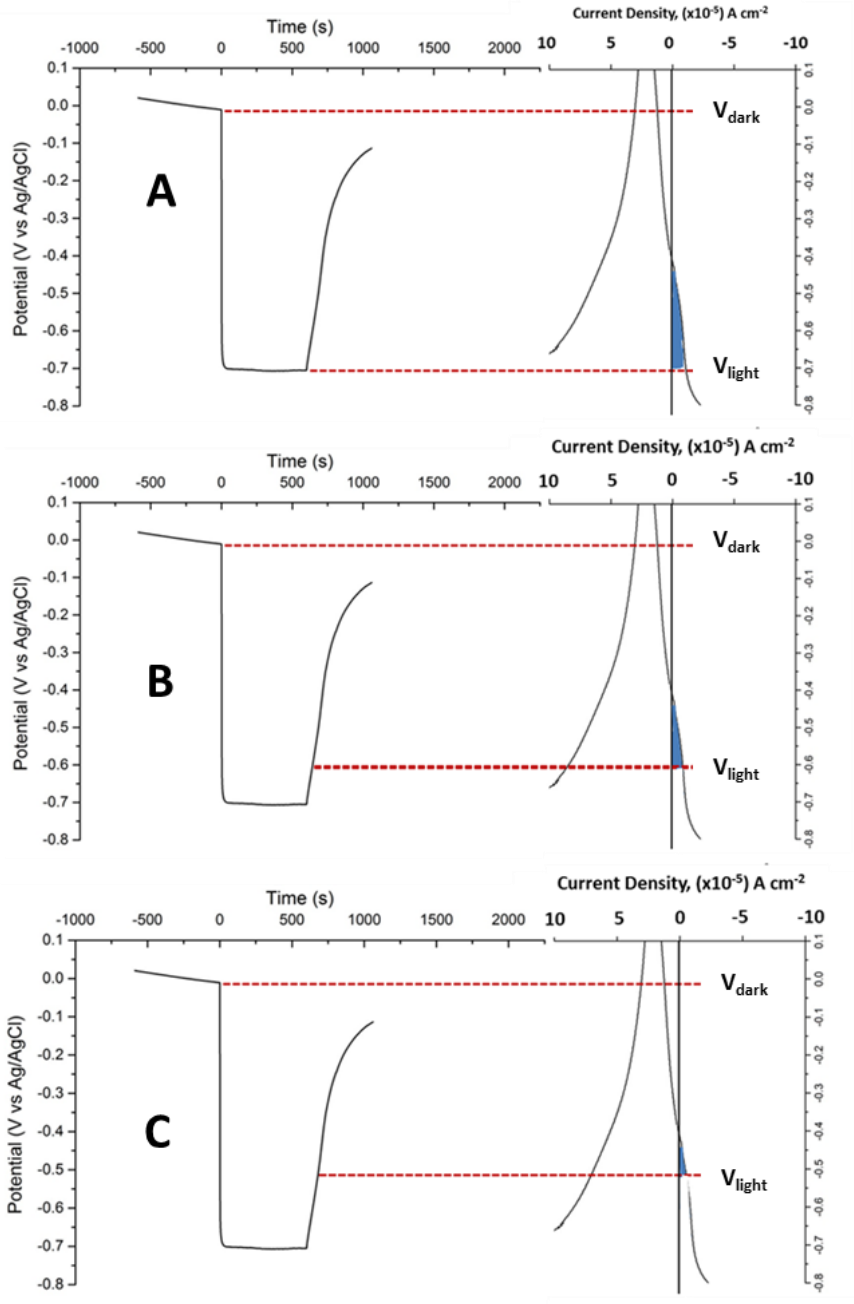

Figure 43. Integration process used for calculating the charge carriers density for the material n-sh_873K. In the panel A is calculated the number of carriers density at steady-state irradiation, in the panels B and C is calculated the carriers density during the recombination at two different potentials. Current density scale is expressed in 10^{-5} A cm^{-2}.

In Figure 44 are shown the trends of the charge carriers density decay and the trends of the k_r vs n_{ph} (inset). As already seen in Table 15 the charge carrier density generated is near the same for the fluorinated material and the calcined one, slightly lower for the n-sh_NaOH. However, the recombination rate is very low for the material n-sh comparing to the others, due to the higher presence of fluorides. The ratio between the kr of the materials n-sh and n-sh_NaOH is near 1 in the early stages of the process, to become about 2.5 after some seconds. The material n-sh_873K presents always a very high recombination rate, near 10 time than n-sh.

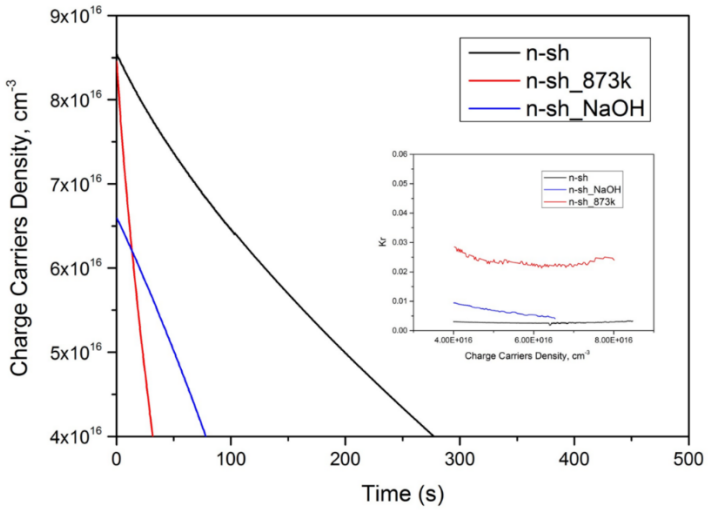

Figure 44. Charge carriers density decay vs time and trends of the k_r vs n_{ph} (inset) at unadjusted pH.

Figure 44 highlights the higher recombination rate of the material n-sh_NaOH compared with n-sh that, in effect, presents higher charge carrier density. The material n-sh_873K has the highest recombination, but also a high charge carriers density.

The OCP and CV tests were carried out also in acidic condition, pH 3.5 with $HClO_4$. The same model previously used was applied in order to quantify the charge carriers density and their recombination rate. The results are shown in Figure 45 and Table 16.

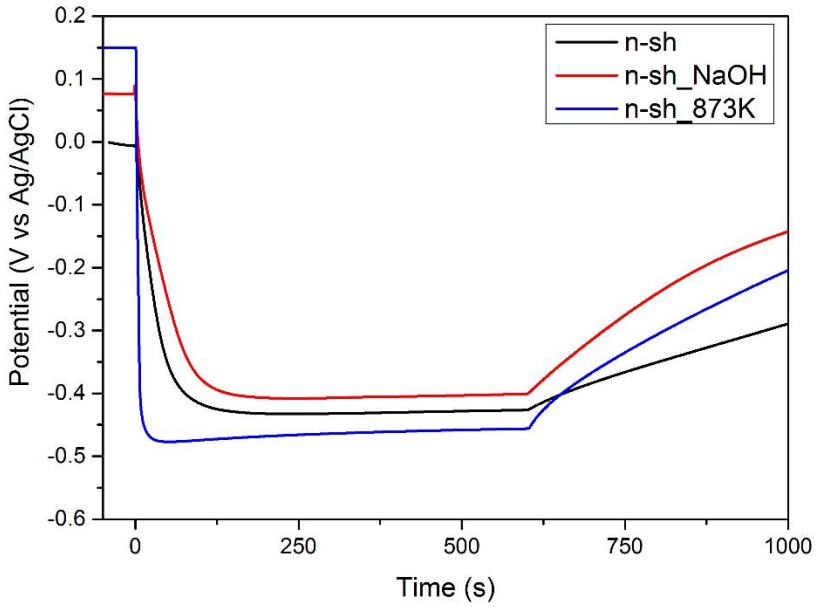

Figure 45. Open Circuit Potential (OCP) of the three considered materials under N_2 atmosphere and an UV illumination (365 nm) of 20 W m^{-2}. pH 3.5.

Table 16. Resume of the results obtained applying the Gomez model to the material n-sh, n-sh_NaOH and n-sh_873K at pH 3.5.

Material	n_{ph} (cm^{-3})	n_{ph} at -0.4 V (cm^{-3})	k_r*	ΔV (mV)
n-sh	$1.49*10^{17}$	$1.44*10^{17}$	$5.6*10^{-3}$	420
n-sh_NaOH	$5.18*10^{16}$	$4.87*10^{16}$	$1.1*10^{-2}$	478
n-sh_873K	$1.19*10^{17}$	$1.06*10^{17}$	$1.0*10^{-2}$	606

**k_r is calculated using data from n_{ph} max to $4.0*10^{16}$ cm^{-3}

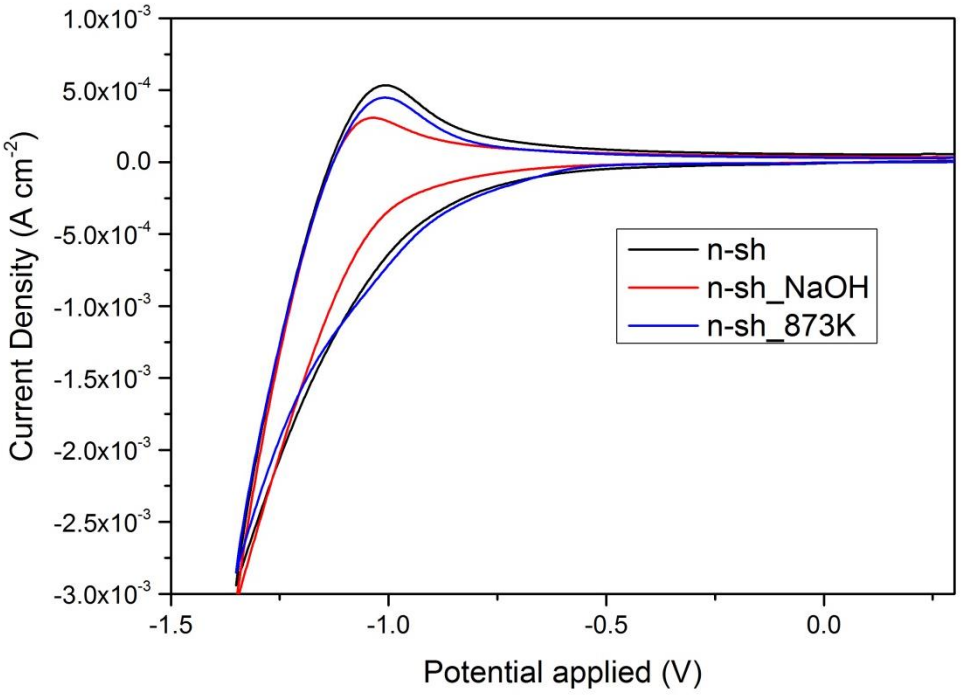

Figure 46. CV carried out on the three materials under a N_2 atmosphere. pH 3.5

The results reported in Table 16 highlight that at acidic pH the materials n-sh and n-sh_NaOH increase their average recombination rate constant (Kr), $Kr_{pH3.5}/Kr_{unadjusted\ pH}$ 2.1 and 1.7 respectively. The material n-sh_NaOH starts its recombination very slowly, however it increases its rate in few seconds after the turn off of the UV irradiation. Curiously, the calcined material greatly decrease its recombination rate, with a final ratio $Kr_{pH3.5}/Kr_{unadjusted\ pH}$ of 0.4. This reduction of the recombination rate can be responsible of its great increase of the photocatalytic activity at acidic pH (see following chapter). Figure 47 shows the charge carriers density decay with time and the trends of the Kr vs n_{ph} at acidic pH.

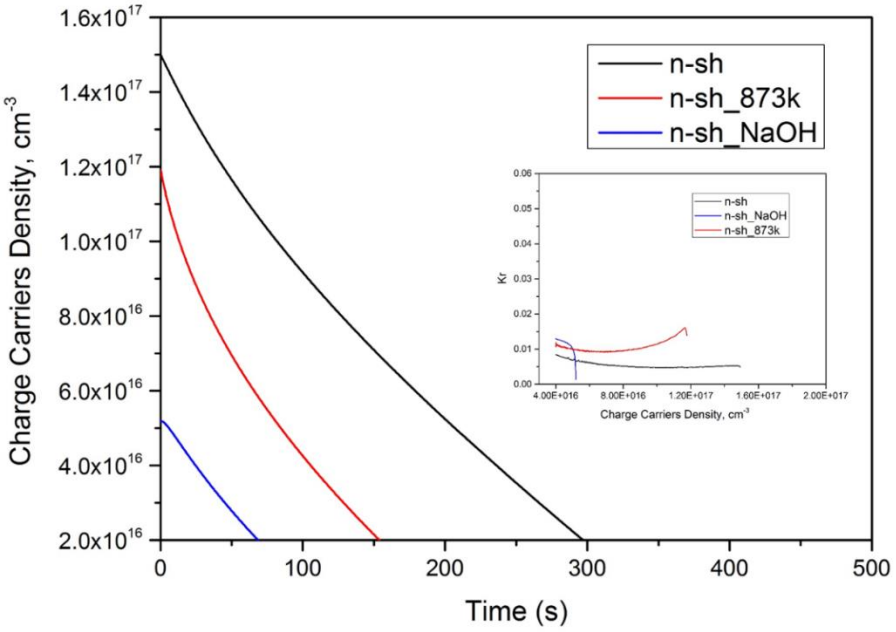

Figure 47. Charge carriers density decay vs time and trends of the k_r vs n_{ph} (inset) at pH 3.5.

In conclusion, from the electrochemical measurements carried out on TiO_2 electrodes produced starting from the three different nanosheets, it was possible evaluate the effect of the fluorides on the recombination kinetics of the photogenerated carriers. As expected, the general effect of the fluorides is a reduction of the recombination rate of the carriers due to the stabilizing effect on CB electrons. In the case of the material n-sh_873K at circumneutral natural pH the charge carriers recombination is very high due to a surface passivation. However, acidic conditions (pH 3.5) are able to modify the surface properties (surface charge) of the material decreasing the recombination rate and largely increasing its photocatalytic activity (see next chapter). Obviously, during the photocatalytic tests other factors intervene in the mechanism that can modify the results obtained in the

electrochemical tests. Indeed, the presence of different kinds of electron and hole scavengers greatly influences the material's photo-activity.

3.5. ζ Potential and PZC

The measurement of the ζ potential of the four studied colloids (n-sh, n-sh_NaOH, n-sh_873K, bipy) was carried out with a Zetasizer Nano–ZS (Malvern Instruments, Worcestershire, U.K.) in order to evaluate the changes in the surface charge at different pHs, and the role of the fluorides at the surface. The behavior of the ζ potential as a function of pH was reported in Figure 48. Some differences are apparent. This measure gives also the pH of zero charge (point of zero charge, pzc) of the materials.

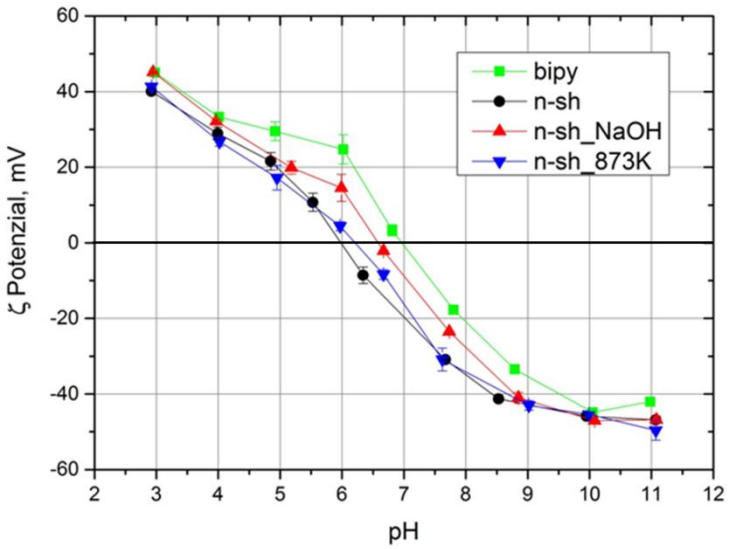

Figure 48. ζ potential values as a function of pH for the four selected materials. Conditions: TiO_2 concentration 0.01 g dm^{-3}, electrolyte NaCl 0.1 M, pH adjusted with NaOH 0.1 M or HCl 0.1 M.

From the analysis of the ζ potential – pH profiles of the samples reported in Figure 48, it is possible to see that all the samples have their ζ potentials in

the range of ± 50 mV, with pH values from 3 to 11. At extreme pH values the ζ potentials are all similar, so in such conditions all the materials have near the same surface charge. Moreover, it should be remembered that at basic and acidic pH, ions exchange on the surface take place. A saturative behavior of ζ potential, at around −50 mV, was observed only in basic solution at pH higher than 9. Conversely, on acidic solutions the saturation was not obtained in the range of pH explored. The presence of the fluorides in the sample n-sh has a significant impact on the surface charge of the material at extreme pHs. The differences in the ζ potential between the nanosheets systems disappear at pH > 9. However, at lower pH values, in particular for pHs near the neutrality the differences are marked. Consequently, the PZC of the four considered materials (Table 17) obtained from the results shown in Figure 48 have a significant difference. As expected, the presence of a certain amount of fluorides at the surface of the nanosheets decrease the PZC of the material. The treatments carried out in order to remove the fluorides increase the PZC, to 6.2 with the calcination at 873K and until 6.6 washing with NaOH 0.1 M. In particular, the higher value obtained for the calcined nanoparticles can be ascribed to a real modification of the surface characteristics, i.e. a reconstruction of the (001) surface.

Table 17. PZC of the selected materials

Material	PZC, pH
n-sh	6.0
n-sh_NaOH	6.6
n-sh_873K	6.2
bipy	7.0

Bibliography

(1) Sugimoto, T.; Zhou, X.; Muramatsu, A. *J Colloid Interface Sci* **2003**, *259*, 53.

(2) Deiana, C.; Minella, M.; Tabacchi, G.; Maurino, V.; Fois, E.; Martra, G. *Physical Chemistry Chemical Physics* **2013**, *15*, 307.

(3) Menge, W. M. P. B.; Verkade, J. G. *Inorganic Chemistry* **1991**, *30*, 4628.

(4) Naiini, A. A.; Menge, W. M. P. B.; Verkade, J. G. *Inorganic Chemistry* **1991**, *30*, 5009.

(5) Bickmore, C. R.; Waldner, K. F.; Baranwal, R.; Hinklin, T.; Treadwell, D. R.; Laine, R. M. *Journal of the European Ceramic Society* **1998**, *18*, 287.

(6) Cargnello, M.; Gordon, T. R.; Murray, C. B. *Chemical reviews* **2014**, *114*, 9319.

(7) Lavric, V.; Isopescu, R.; Maurino, V.; Pellegrino, F.; Pellutie, L.; Ortel, E.; Hodoroaba, V. D. *Cryst Growth Des* **2017**, *17*, 5640.

(8) Sugimoto, T.; Zhou, X.; Muramatsu, A. *J Colloid Interface Sci* **2003**, *259*, 43.

(9) Vogel, A. I.; Jeffery, G. H. *Vogel's Textbook of Quantitative Chemical Analysis*; Longman Scientific & Technical: Harlow, Essex, England, 1989.

(10) Perik, M. M. A.; Oranje, P. J. D. *Analytica Chimica Acta* **1974**, *73*, 402.

(11) Tim Kemmitt, N. I. A.-S., Graeme J. Gainsford *Inorg. Chem.* **2000**, *39*, 6067.

(12) Jin-Koo Park, J.-J. M., Jin-Burm Kyong, Ho-Kun Kim *Bull. Korean Chem. Soc.* **2003**, *24*.

(13) Box, G. E. P.; Wilson, K. B. *Journal of the Royal Statistical Society. Series B (Methodological)* **1951**, *13*, 1.

(14) Kuznetsova, I. N.; Blaskov, V.; Stambolova, I.; Znaidi, L.; Kanaev, A. *Materials Letters* **2005**, *59*, 3820.

(15) Xie, H.; Li, N.; Liu, B. S.; Yang, J. J.; Zhao, X. J. *J Phys Chem C* **2016**, *120*, 10390.

(16) Provencher, S. W. *Computer Physics Communications* **1982**, *27*, 229.

(17) De Temmerman, P.-J.; Verleysen, E.; Lammertyn, J.; Mast, J. *Powder Technol* **2014**, *261*, 191.

(18) Hodoroaba, V. D.; Akcakayiran, D.; Grigoriev, D. O.; Shchukin, D. G. *Analyst* **2014**, *139*, 2004.

(19) Hodoroaba, V. D.; Motzkus, C.; Mace, T.; Vaslin-Reimann, S. *Microsc Microanal* **2014**, *20*, 602.

(20) Hansen, S. *Journal of Chemical Physics* **2004**, *121*, 9111.

(21) Perrin, F. *Journal de Physique et le Radium* **1936**, *7*, 1.

(22) Lovette, M. A.; Browning, A. R.; Griffin, D. W.; Sizemore, J. P.; Snyder, R. C.; Doherty, M. F. *Ind Eng Chem Res* **2008**, *47*, 9812.

(23) Horvat, B.; Recnik, A.; Drazic, G. *J Cryst Growth* **2012**, *347*, 19.

(24) Cho, C. H.; Han, M. H.; Kim, D. H.; Kim, D. K. *Materials Chemistry and Physics*, *92*, 104.

(25) Penn, R. L.; Banfield, J. F. *Geochim Cosmochim Ac* **1999**, *63*, 1549.

(26) Raju, M.; van Duin, A. C.; Fichthorn, K. A. *Nano letters* **2014**, *14*, 1836.

(27) Fichthorn, K. A. *Chemical Engineering Science* **2015**, *121*, 10.

(28) Alimohammadi, M.; Fichthorn, K. A. *Nano letters* **2009**, *9*, 4198.

(29) Han, X.; Kuang, Q.; Jin, M.; Xie, Z.; Zheng, L. *J Am Chem Soc* **2009**, *131*, 3152.

(30) Zhang, J.; Wang, J.; Zhao, Z.; Yu, T.; Feng, J.; Yuan, Y.; Tang, Z.; Liu, Y.; Li, Z.; Zou, Z. *Physical chemistry chemical physics : PCCP* **2012**, *14*, 4763.

(31) Mino, L.; Ferrari, A. M.; Lacivita, V.; Spoto, G.; Bordiga, S.; Zecchina, A. *J Phys Chem C* **2011**, *115*, 7694.

(32) Czoska, A. M.; Livraghi, S.; Chiesa, M.; Giamello, E.; Agnoli, S.; Granozzi, G.; Finazzi, E.; Di Valentin, C.; Pacchioni, G. *J Phys Chem C* **2008**, *112*, 8951.

(33) Selcuk, S.; Selloni, A. *J Phys Chem C* **2013**, *117*, 6358.

(34) Minella, M.; Faga, M. G.; Maurino, V.; Minero, C.; Pelizzetti, E.; Coluccia, S.; Martra, G. *Langmuir* **2010**, *26*, 2521.

(35) Kavathekar, R. S.; Dev, P.; English, N. J.; MacElroy, J. M. D. *Mol Phys* **2011**, *109*, 1649.

(36) English, N. J. *Crystals* **2016**, *6*.

(37) Takeuchi, M.; Martra, G.; Coluccia, S.; Anpo, M. *Journal of Physical Chemistry B* **2005**, *109*, 7387.

(38) Schaefer, J.; Backus, E. H. G.; Nagata, Y.; Bonn, M. *J. Phys. Chem. Lett.* **2016**, *7*, 4591.

(39) Stiopkin, I. V.; Weeraman, C.; Pieniazek, P. A.; Shalhout, F. Y.; Skinner, J. L.; Benderskii, A. V. *Nature* **2011**, *474*, 192.

(40) Deiana, C.; Fois, E.; Coluccia, S.; Martra, G. *J. Phys. Chem. C* **2010**, *114*, 21531.

(41) Mino, L.; Spoto, G.; Bordiga, S.; Zecchina, A. *J Phys Chem C* **2012**, *116*, 17008.

(42) Soria, J.; Sanz, J.; Sobrados, I.; Coronado, J. M.; Maira, A. J.; Hernandez-Alonso, M. D.; Fresno, F. *J Phys Chem C* **2007**, *111*, 10590.

(43) Kevorkyants, R.; Rudakova, A. V.; Chizhov, Y. V.; Bulanin, K. M. *Chem Phys Lett* **2016**, *662*, 97.

(44) Hadjiivanov, K. I.; Klissurski, D. G. *Chem. Soc. Rev.* **1996**, *25*, 61.

(45) Xu, M. C.; Gao, Y. K.; Moreno, E. M.; Kunst, M.; Muhler, M.; Wang, Y. M.; Idriss, H.; Woll, C. *Phys Rev Lett* **2011**, *106*, 4.

(46) Deiana, C.; Minella, M.; Tabacchi, G.; Maurino, V.; Fois, E.; Martra, G. *Physical chemistry chemical physics : PCCP* **2013**, *15*, 307.

(47) Mino, L.; Spoto, G.; Bordiga, S.; Zecchina, A. *J Phys Chem C* **2013**, *117*, 11186.

(48) Hadjiivanov, K.; Reddy, B. M.; Knozinger, H. *Appl. Catal. A-Gen.* **1999**, *188*, 355.

(49) Shi, Y. L.; Sun, H. J.; Saidi, W. A.; Nguyen, M. C.; Wang, C. Z.; Ho, K. M.; Yang, J. L.; Zhao, J. *J. Phys. Chem. Lett.* **2017**, *8*, 1764.

(50) Dyrek, K.; Che, M. *Chemical reviews* **1997**, *97*, 305.

(51) Morra, E.; Giamello, E.; Chiesa, M. *Journal of magnetic resonance* **2017**, *280*, 89.

(52) Risse, T.; Schmidt, J.; Hamann, H.; Freund, H. J. *Angewandte Chemie* **2002**, *41*, 1517.

(53) Brandhorst, M.; Cristol, S.; Capron, M.; Dujardin, C.; Vezin, H.; Le bourdon, G.; Payen, E. *Catalysis Today* **2006**, *113*, 34.

(54) Bruckner, A. *Chem Commun (Camb)* **2005**, 1761.

(55) Morra, E.; Giamello, E.; Van Doorslaer, S.; Antinucci, G.; D'Amore, M.; Busico, V.; Chiesa, M. *Angew Chem Int Edit* **2015**, *54*, 4857.

(56) Pietrzyk, P.; Mazur, T.; Podolska-Serafin, K.; Chiesa, M.; Sojka, Z. *J Am Chem Soc* **2013**, *135*, 15467.

(57) Schwach, P.; Eichelbaum, M.; Schlogl, R.; Risse, T.; Dinse, K. P. *J Phys Chem C* **2016**, *120*, 3781.

(58) Howe, R. F.; Gratzel, M. *The Journal of Physical Chemistry* **1985**, *89*, 4495.

(59) Livraghi, S.; Chiesa, M.; Paganini, M. C.; Giamello, E. *J. Phys. Chem. C* **2011**, *115*, 25413.

(60) Chiesa, M.; Paganini, M. C.; Livraghi, S.; Giamello, E. *Physical Chemistry Chemical Physics* **2013**, *15*, 9435.

(61) Micic, O. I.; Zhang, Y.; Cromack, K. R.; Trifunac, A. D.; Thurnauer, M. C. *The Journal of Physical Chemistry* **1993**, *97*, 7277.

(62) Kus, M.; Altantzis, T.; Vercauteren, S.; Caretti, I.; Leenaerts, O.; Batenburg, K. J.; Mertens, M.; Meynen, V.; Partoens, B.; Van Doorslaer, S.; Bals, S.; Cool, P. *The Journal of Physical Chemistry C* **2017**, *121*, 26275.

(63) Berger, T.; Diwald, O.; Knözinger, E.; Napoli, F.; Chiesa, M.; Giamello, E. *Chemical Physics* **2007**, *339*, 138.

(64) Monllor-Satoca, D.; Gómez, R. *The Journal of Physical Chemistry C* **2008**, *112*, 139.

(65) Monllor-Satoca, D.; Lana-Villarreal, T.; Gomez, R. *Langmuir* **2011**, *27*, 15312.

Chapter 4

4.1. Photocatalytic Activity

Correct comparison of photocatalytic activity should be carried out measuring quantum yields for a given substrate in given conditions. Measurement of quantum yields (QY) is very difficult due to scattering. Besides this problem, fluid dynamic of the photoreactors used influences mass transfer and the wavelength of radiation influences the fraction of light absorbed or scattered, as well as QY. It is fundamental to choose correct set of experimental conditions to correctly define and measure photocatalytic activity.

4.2.Gas/Solid Photocatalysis

4.2.1. Gas/Solid Photoreactor

For gas/solid experiments different reactors could be envisaged, like

- Batch reactors
- Flow-through reactors:
    1. CSTR (Continuous Stirred-Tank Reactor)
    2. PFR (Plug Flow Reactor),

The basic equations governing these reactors and the rate expression for them are here presented. Batch reactors have the drawback that minimal leaks or adsorption phenomena on the reactor walls make difficult the

measure. Steady state flow-through reactors are not plagued by this problem thanks to the continuous flow of substrate. Experiments shows that a CSTR configuration presents a number of advantages for practical use, as any volume, any shape of catalyst, and any flow of gas into the reactor can be used. A CSTR configuration can be used in a turbulent fluid-dynamic regime, so is superior to the PFR as it is less dominated by resistance to mass transfer and, consequently, gives an evaluation of the photocatalytic rate more close to the intrinsic one of the material tested. For these reasons we have chosen a CSTR photo-reactor for our photocatalytic tests[1].

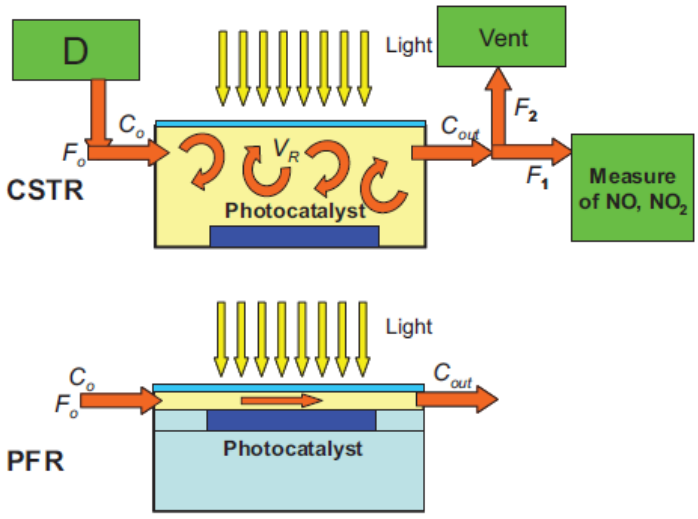

Figure 49. Models for a CSTR and a PFR reactor[1]

A CSTR reactor is normally operated:

1. Purging it with air (or some other diluent gas if needed) without the pollutant under examination (NO, NO_x, VOC etc.). This stage is required to clean the reactor form previous runs. At the end of this stage the pollutant concentration in the reactor is null[1].

2. The subsequent filling with the pollutants at the proper concentration C_0 in the diluent gas under dark. From the mass balance per unit time inside the reactor.

$$V_R \frac{d}{dt} C_{dark}(t) = F\left(C_0 - C_{dark}(t)\right)$$

where C_{dark} is the concentration measured at the output after exponential dilution inside the reactor. The straightforward solution under the initial condition that $C_{dark}(0)=0$ gives

$$C_{dark}(t) = C_0 \left[1 - exp\left(-\frac{F_t}{V_R}\right)\right]$$

from which it is evident that the equilibration time depends on the flow F and the reactor volume V_R. As larger is the reactor volume, the used flow must be larger, to avoid excessive equilibration times. From this it is evident the difficulty (and costs) to work with excessive V_R, although somehow they are unavoidable, as for performance assessment of bulky devices[1].

3. After stages (1) and (2) for a CSTR, two ways of operation are then possible: (a) batch experiments; (b) flow-through operation. The time evolution of the concentration inside the reactor under ways of operation (1) and (2) after filling and light on is reported below and exemplified in Figure 50[1].

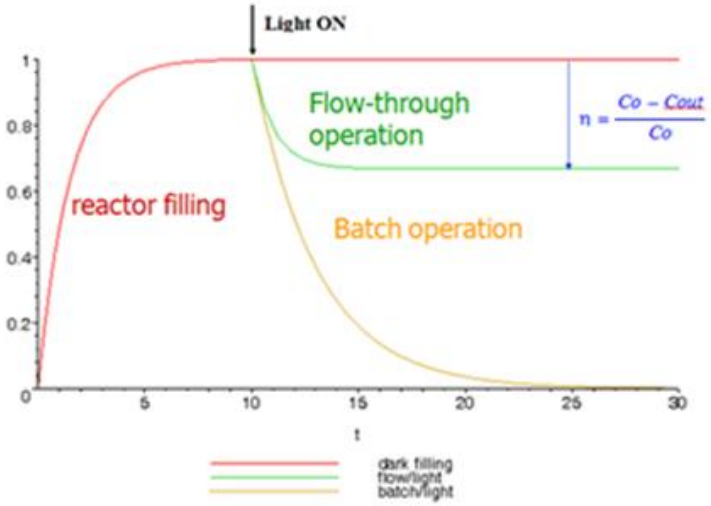

Figure 50. Time evolution of the concentration inside the reactor after filling and light on: flow-throw operation (green) and batch operation (yellow)[1]

4. The input flow is maintained, and light powered on. The output concentration of pollutant C_{out} is measured as a function of time. If the amount of pollutant consumed by the photocatalytic reaction (or other possible thermal and photolytic reactions) is constant over time, a steady state is reached at which C_{out} is constant[1].
5. Keeping the light on, step-by-step the fan speed is decreased, continuously monitoring the pollutant concentration (Figure 51). Finally for each pollutant concentration, a fan speed is associated. A plot of the inverse of the Pollutant Degradation Rate vs the inverse of the Fan Speed (Figure 52) allow us to linearly extrapolate the degradation rate at fan infinite speed, deleting limitations due to mass transfer at the gas/solid limit layer, because for the fan speed that tends to infinity the limit layer tends to be null.

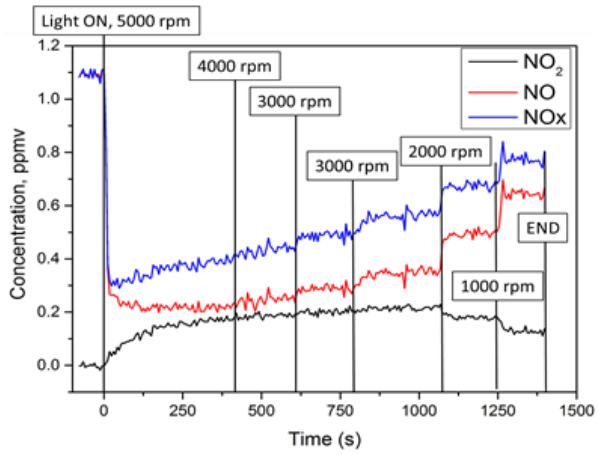

Figure 51. Example of a test using NO as substrate, note the decrease of the NO degradation decreasing the fan flow from 5000 to 1000 rpm.

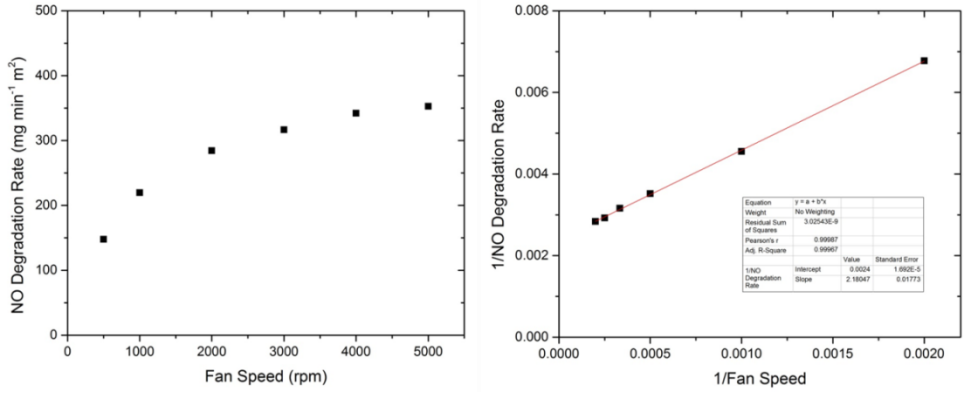

Figure 52. LEFT: A plot of the Pollutant Degradation Rate vs the Fan Speed; RIGHT: linearization of the NO degradation rate in order to extrapolate the rate at infinite fan speed, where the thickness of the limit layer is null.

The photocatalytic tests were carried out using a purposely designed reactor,[2] equipped with NO, NO_2, CO and VOC sensors (PID). The internal volume of the reactor is 15 ml, so a short time (10-30 s) is necessary for the stationary state. The humidity and temperature inside the reactor are continuously monitored, as well as the irradiation. The reaction gas mixture at proper concentrations was prepared using a Entech dynamic diluter model 4460. Total flux 0.5 l/min. The gas mixture enters the reaction

chamber where a turbine, made with UV-transparent polymer, keeps it in turbulent motion. The possibility to rotate the turbine at controlled speeds allows to reduce the diffusion limit layer above the catalytic surface, as previously described in the model. The key points of this photoreactor are the strong versatility and maneuverability due to its small size, that allow also a great measurement speed.

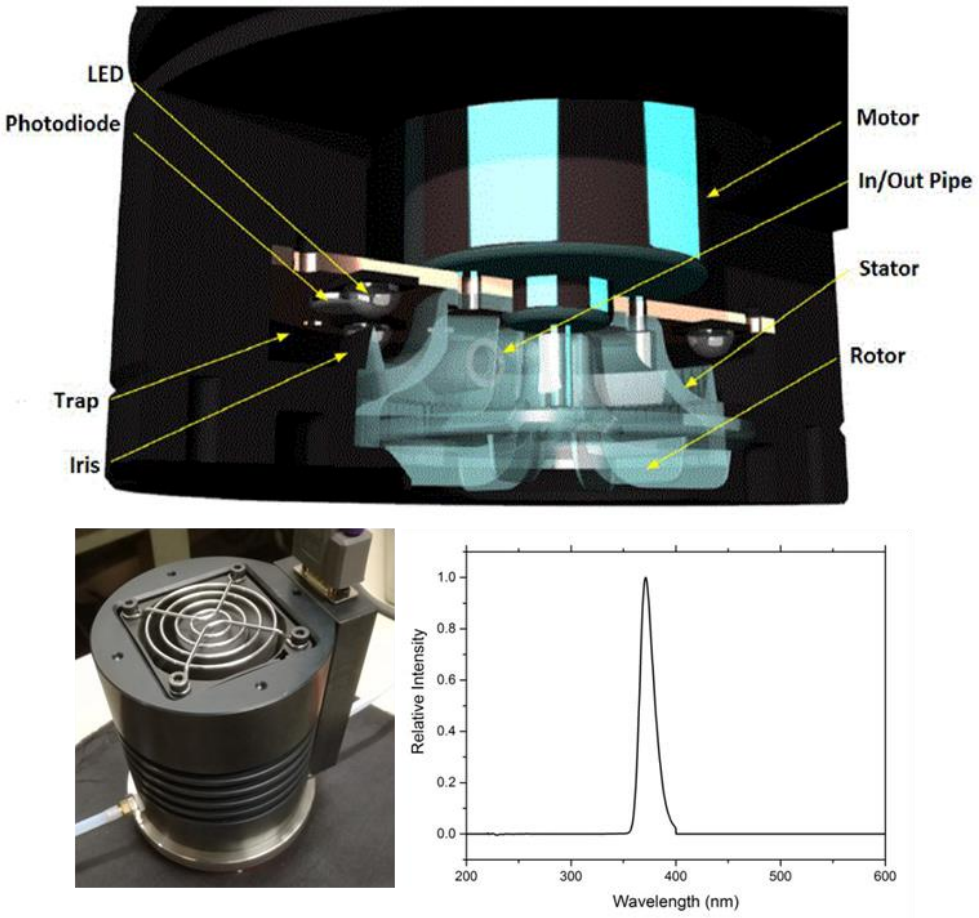

Figure 53. UP: Photoreactor scheme. BOTTOM: Photocatalytic reactor used for the gas-solid photocatalytic test (LEFT) (For a full description see Ref.2) and UV spectra emission centered at 365 nm of the photoreactor (right).

4.2.2. TiO_2 Films

TiO2 films are prepared depositing a concentrated (10 g L^{-1}) suspension of the materials on a round glass support following the here reported procedure:

1. Repeated wash of the glass support with water;
2. Preparation and sonication (1 hour) of a suspension of TiO_2 10 g L^{-1} in water;
3. Drip of 300 µL of the suspension on the support and spread using the doctor-blade technique in order to produce a thin film that adheres well at the surface of the support;
4. Drying of the film at environmental temperature;
5. Drip of the suspension until a complete coverage of the support surface and drying at environmental temperature;
6. Repetition the last operation until an homogenous thick film is observed after the drying.

The choice to use thick films is due to the need to issue independence of the measure by the amount of deposited material, in fact thick films completely absorbs the incident radiation (checked by UV-Vis absorption spectra). So, a comparison between the materials without influences by different film thickness or by small losses of material during the experiments

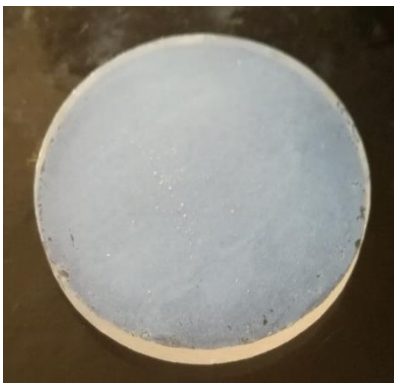

Figure 54. Example of the TiO_2 film used for the gas-solid photodegradation experiments.

it's possible. In Figure 54 is reported an example of the final film obtained following the described procedure.

4.2.3. NO photodegradation Background

Nitrogen oxides (NOx, which refers to NO and NO_2) are among the most harmful atmospheric pollutant gases. They are emitted by combustions, like for example in coal plants and automobile engines. Moreover, they contribute to several other pollution problems like acid rains, nitrogen pollution in water, smog and greenhouse effect[3-5]. They also have a relevant impact on the human health, causing diseases such as emphysema and bronchitis, but also aggravating existing heart disorders[6]. There is, therefore, a great interest in reducing the concentration of NOx especially in urban areas[7].

The photocatalytic degradation of these pollutants is a valid method for the abatement of NOx level in the atmosphere. Various studies have been carried out on the exploitation of TiO_2 as photocatalyst for the degradation of NOx, in particular on the abatement of NO, the major emission product of combustion[8]. Several investigation have shown that N_2O is the major product of the photodecomposition of NO on rutile[8-10] through a reductive pathway whereas the presence of nitrate NO_3^- and nitrite NO_2^- has been reported as major degradation products on the anatase phase, via an oxidative process[11,12]. In presence of water, NO seems to be photocatalytically oxidized to nitric acid[7]. In Figure 55 is reported the degradation pathway under UV irradiation of nitric oxide proposed by Freitag et al. in 2015[7].

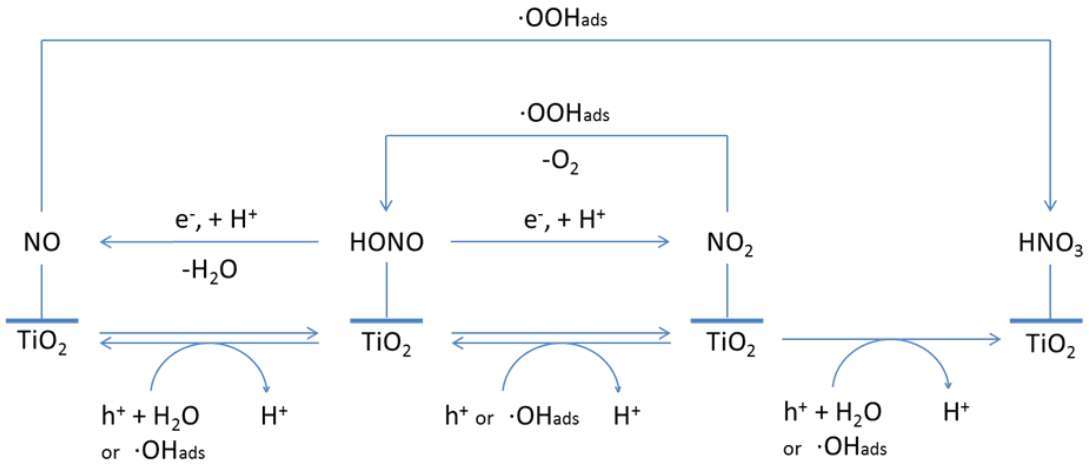

Figure 55. Scheme of the proposed degradation pathway of NO on TiO_2 under UV irradiation. From Freitag et al.[7]

In the proposed scheme the NO could be oxidized both by a direct hole transfer and an OH radical attack to generate NO_2, HNO_2 and HNO_3.

NO degradation mechanism under visible light was also described by several works, using doped TiO_2[13-15] or coupling TiO_2 nanoparticles with noble metals[16], oxide[17] and other nanostructure[18]. Nakamura et al.[19] attribute the photocatalytic activity of pure TiO_2 nanomaterials to the presence of oxygen vacancies in a plasma-treated material, able to generate infra band gap states that allow a visible light activity. This conclusion confirm the importance of the material synthesis because the presence of defects could affects the final photo-activity. In their work in 2015, Freitag et al.[7] obtained good photoactivity against NO under visible light (λ_{max} = 455 nm) using three commercial materials (P25 Evonik, UV100 Hombikat and a rutile sample by Alfa Aesar). They attributed these photoactivity to the occurrence of a charge transfer (CT) mechanism due to

the generation of a TiO_2 - NO complex. The pathway include the formation of a nitrosonium ion (NO^+) which reacting with water gives nitrous acid.

4.2.4. Results

The photocatalytic tests using NO as substrate were carried out on the four selected materials (n-sh, n-sh_NaOH, n-sh_873K and bipy) in order to investigate both the effect of the progressive defluorination of the nanosheets on the photoactivity and the effect of the shape of anatase nanoparticles (comparing nanosheets and bipyramids).

It has been decided to investigate the materials' photoactivity under four different irradiance and four different initial NO concentration, in order to monitor the effect on the activity of these two parameters. Indeed, the irradiance increment could lead to recombination phenomena, reducing the NO degradation rate until a plateau. Nevertheless, high concentration of NO could lead to a fast saturation of the active sites of the films, decreasing the resulting photocatalytic activity. To avoid the deactivation due the byproducts, each analysis was followed by a cleaning step: 30 min at 50 W m^{-2} (365 nm) under a flux of 0.5 L of pure air (79% N_2 and 21% O_2).

Table 18 reports all the experiments conditions and results of the NO photo-degradation using the four selected materials. The temperature is constantly monitored and maintained at ~298 K, while the relative humidity at ~50%.

Table 18. Experiments conditions and results of the NO photo-degradation

Material	NO Concentration, ppmv	Irradiance, W m^{-2}	NO Degradation Rate, mg min^{-1} m^{-2}
n-sh	1.10 ± 0.02	10	0.148 ± 0.006
	1.10 ± 0.02	22	0.183 ± 0.001
	1.10 ± 0.02	48	0.245 ± 0.001
	1.10 ± 0.02	82	0.297 ± 0.009
	0.55 ± 0.01	22	0.142 ± 0.001
	2.15 ± 0.01	22	0.270 ± 0.006
	4.20 ± 0.02	22	0.331 ± 0.005
n-sh_NaOH	1.10 ± 0.02	10	0.182 ± 0.019
	1.10 ± 0.02	22	0.205 ± 0.008
	1.10 ± 0.02	48	0.277 ± 0.001
	1.10 ± 0.02	82	0.315 ± 0.003
	0.55 ± 0.01	22	0.146 ± 0.007
	2.15 ± 0.01	22	0.298 ± 0.012
	4.20 ± 0.02	22	0.345 ± 0.012
n-sh_873K	1.10 ± 0.02	10	0.097 ± 0.007
	1.10 ± 0.02	22	0.124 ± 0.005
	1.10 ± 0.02	48	0.159 ± 0.000
	1.10 ± 0.02	82	0.178 ± 0.001
	0.55 ± 0.01	22	0.102 ± 0.003
	2.15 ± 0.01	22	0.181 ± 0.011
	4.20 ± 0.02	22	0.216 ± 0.001
bipy	1.10 ± 0.02	10	0.271 ± 0.013
	1.10 ± 0.02	22	0.312 ± 0.011
	1.10 ± 0.02	48	0.411 ± 0.009
	1.10 ± 0.02	82	0.462 ± 0.025
	0.55 ± 0.01	22	0.165 ± 0.014
	2.15 ± 0.01	22	0.372 ± 0.001
	4.20 ± 0.02	22	0.438 ± 0.027

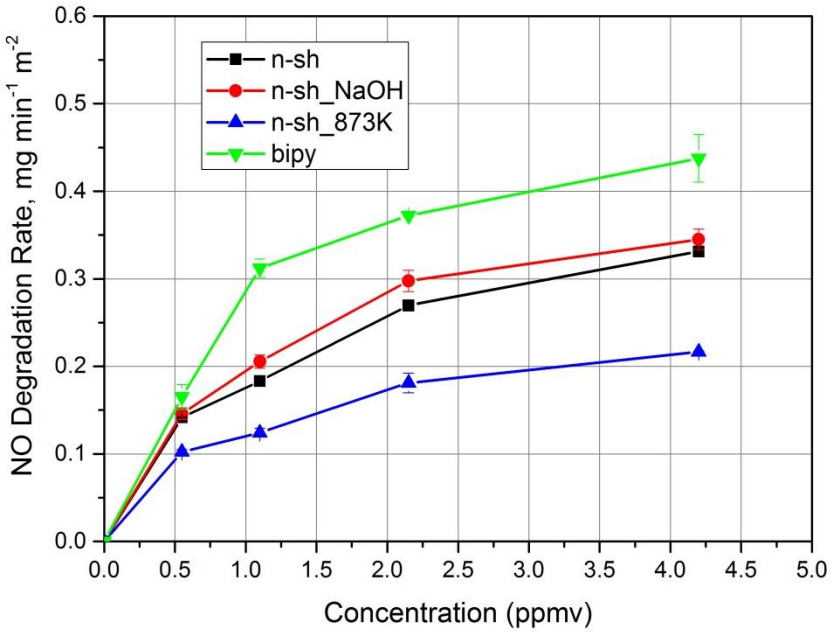

Figure 56. Dependence of the NO degradation rate from the NO initial concentration (ppmv) for the four considered materials

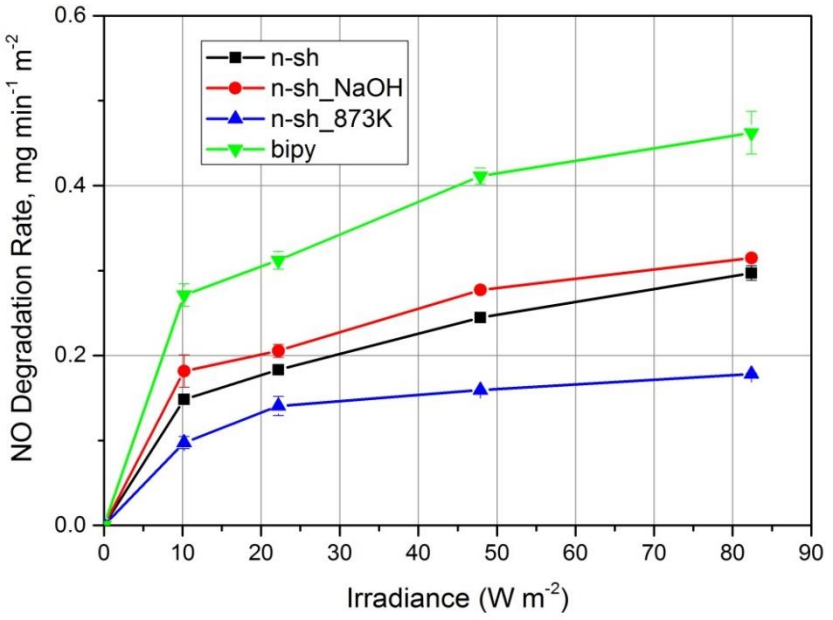

Figure 57. Dependence of the NO degradation rate from the irradiance for the four considered materials

Figure 56 and Figure 57 reports the trends of the NO photodegradation rate using different initial NO concentration (respectively 0.5, 1 and 2 ppmv) and irradiance intensity (respectively 10, 22 and 48 W m^{-2}). Figure 56 shows the common saturation-type kinetics, highlighting that at low NO initial concentration the differences between the materials are no significant, but increasing the NO initial concentration the differences become evident: the bipyramids shows the higher activity at these concentrations, whereas the nanosheets present a different photocatalytic activity depending on the treatment they have undergone, if the fluorides are removed only from the surface of the nanoparticles (n-sh_NaOH) an increase of the activity is obtained, conversely the calcination at 873K (n-sh_873K) largely decrease the activity against NO of the nanosheets. Similar trends are obtained using different irradiance (Figure 57), also in this case the bipyramidal nanoparticles shown the higher photoactivity. The nanosheets calcination drastically reduces the photoactivity, whereas the treatment with NaOH slightly increase the NO degradation.

Influence of Shape

In order to investigate the impact of the TiO_2 surface properties on the NO photocatalytic activity, features bare TiO_2 nanoparticles mainly terminated by {101} (TiO_2 bipy) or (1x4) reconstructed {001} surfaces (TiO_2 n-sh_873K) must be compared, freeing of the influence of fluorides. As it is possible to see in Figure 56 and Figure 57, the bipy sample is always more active than the calcined nanosheets. This behavior is probably due to the low concentration hydroxyl group at the surface of the material n-sh_873K that limits its hydrophilicity and its surface reactivity. Indeed, as seen in paragraph 3.3, the heating treatment reduces the affinity of nanosheets to

water, this dramatically decreases the reactivity of the TiO_2 (see EPR paragraph). Therefore, since one of the main NO degradation mechanism is the reaction with OH radicals, hydrophilicity can have a high impact on the photocatalytic degradation of NO on TiO_2. Moreover, the low hydrophilicity of the material n-sh_873K decrease the presence of H_2O molecules that can react directly with the nitrosonium ion to generate nitrous acid as described in Figure 55.

Influence of Fluorides

The influence of the fluorides on the NO photocatalytic degradation was carried out comparing the fluorinated and washed with NaOH nanosheets. Fluorides have an high impact on the surface characteristics (Chapter 3) and the photocatalytic activity of TiO_2 nanoparticles (Chapter 1). In our photocatalytic tests, de-fluorinated nanoparticles have a slightly higher activity against NO in all the conditions. The results can explained again referring to the different affinity with water of the nanoparticles due to the presence (or not) of fluorides at the surface of the material, always in the context of OH radical production mechanism. On the other hand, however, fluorination can improve the OH radical production due the lower recombination rate (see photo-electrochemical measurements). These two contrasting mechanism are responsible of the slight difference on the NO degradation rates obtained.

4.3. Liquid/Solid Photocatalysis

4.3.1. Liquid/Solid Photoreactor

The liquid/solid photocatalytic activity was evaluated by means of a purposely designed reactor using different substrates, in order to evaluate the influence of the shape and of the fluorides on the different photodegradation mechanisms. Figure 58 shows the photo-reactor setup during a test.

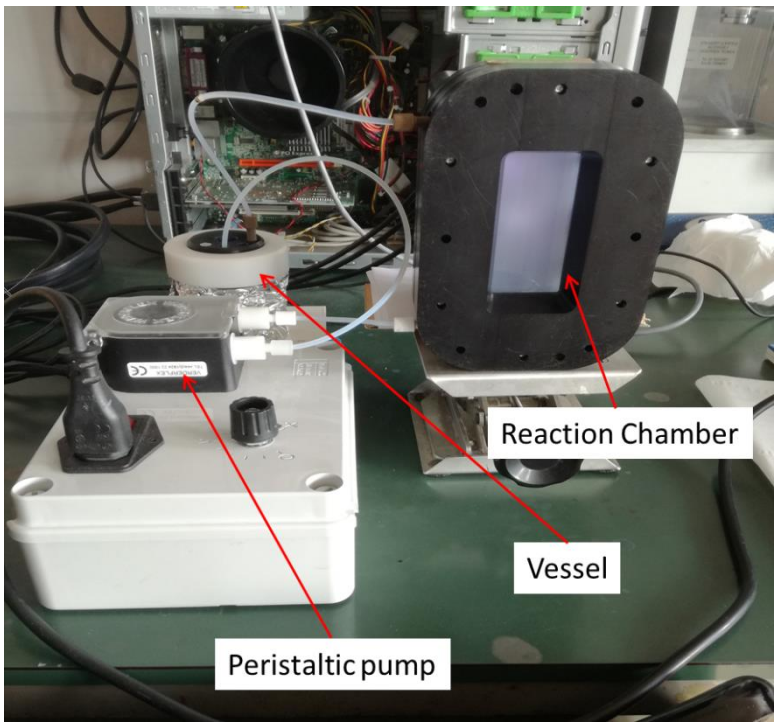

Figure 58. Home-built photoreactor used for the liquid/solid photocatalytic tests.

The freshly prepared TiO_2 suspension (sonicated 30 min and then added with the substrate) was poured in the vessel (50 ml) under stirring. A peristaltic pump (flux 40 ml/min) recirculates the suspension between the

vessel and channel photoreactor. Channel photoreactor consists in two removable polyoxymethylene (POM) covers in which two UV transparent glasses are inserted. The distance between the two glasses can be changed with a PMMA spacer. The suspension flows between the two glasses and is irradiated with a light source perpendicularly to the flow direction. A simplified scheme of the photoreactor is reported in Figure 59.

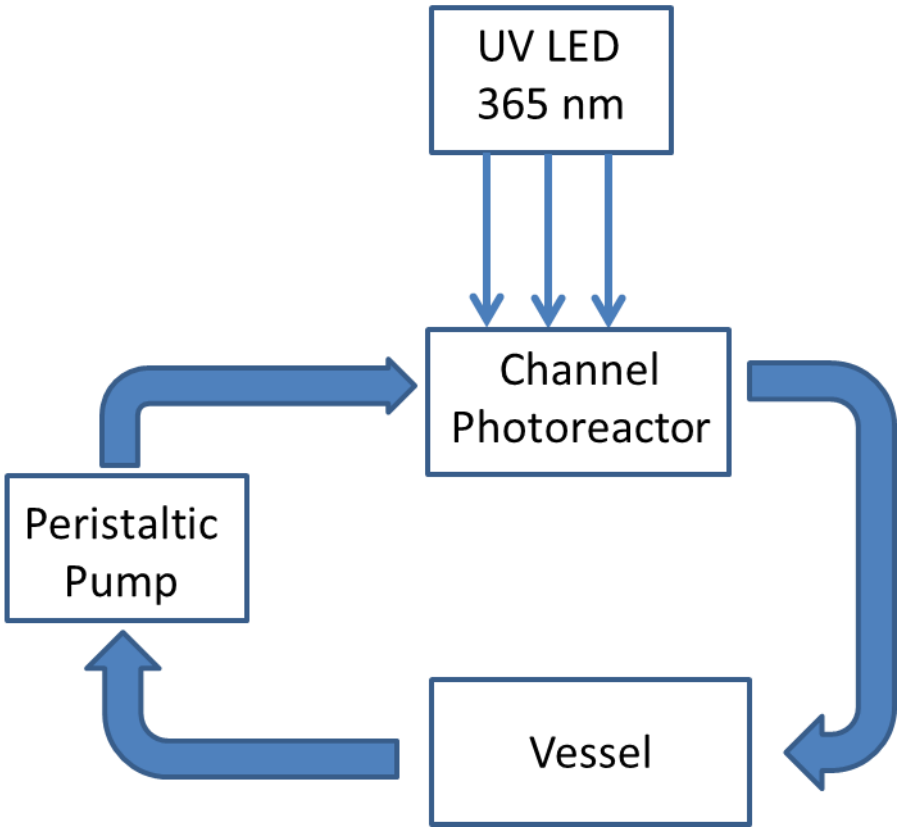

Figure 59. Scheme of the photo-reactor used for the liquid-solid photocatalytic tests

The uniformity offlow inside the photoreactor channel is assured by a flow distribution system composed by the saw tooth profile of the spacer (Figure 60a) and the flux splitters made directly on the POM structure(Figure 60b).

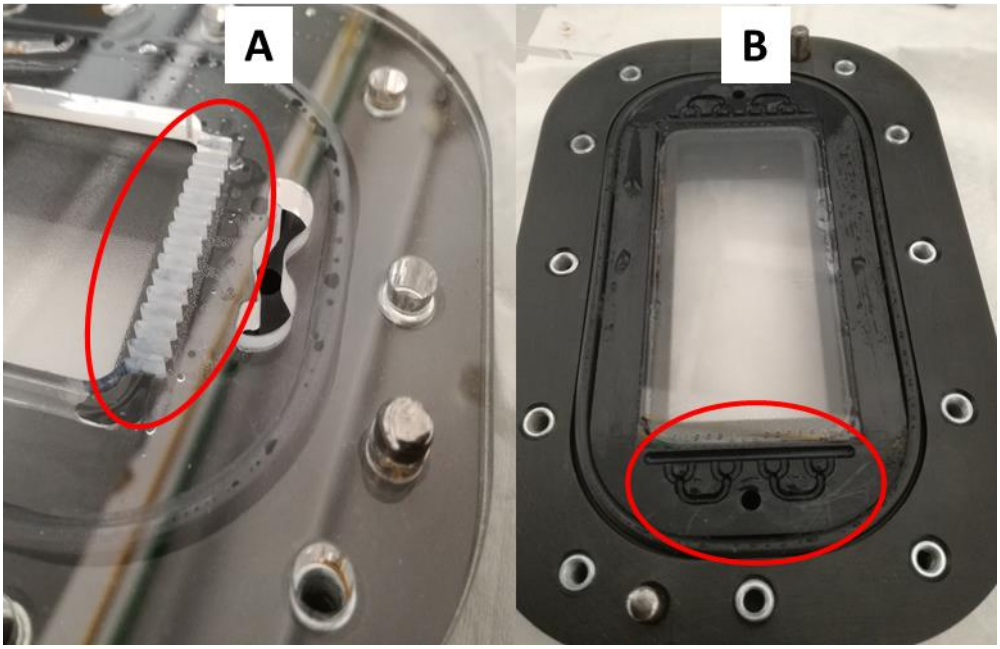

Figure 60. Particulars of the reactor's internal: a) saw tooth profile of the spacer; b) flux splitters engraved on the POM structure

The advantage of this setup is the possibility, using an external vessel, to monitor constantly the suspension for example using an electrode and/or to carried out experiments in a controlled atmosphere, sparging directly the gas in the suspension during the test.

The design of the photoreactor allows also the monitoring of the incident and transmitted radiation.

4.3.2. Phenol Photodegradation

The photocatalytic activity of TiO_2 was evaluated by irradiating the anatase bipyramids and nano-sheets suspensions (loading 100 mg l^{-1}) in the previously described photoreactor, using a fluorescent source with λ_{max} = 365 nm (Philips PL-S 9W BLB, integrated irradiance = 10 W m^{-2}). Substrate absorption at this wavelength is negligible. Photocatalytic activity was measured as the initial rate of phenol photo-transformation, by fitting disappearance curves to an exponential decay. Incident radiant power was measured in the range 290-400 nm with an Oceans Optics USB2000 spectrophotometer equipped with a cosine corrected optical fiber probe, spectroradiometrically calibrated with a NIST traceable DH-2000 CAL UV-Vis source (Ocean Optics). The initial concentration of phenol is 0.1 mM. Time profiles of phenol decay where obtained as average of three irradiation runs. Measurements at two different pH were carried out, at the natural pH of the nanoparticles (i.e. without any addiction) and at pH 3.5 for $HClO_4$. Reactor's spacer 2 mm.

HPLC determination of phenol has been carried out with an Agilent Technologies HPLC chromatograph 1200 Series equipped with a diode array detector, binary gradient high-pressure pump and an automatic sampler. Isocratic elution was carried out with a mixture of 15/85 acetonitrile/formic acid aqueous solution (0.05 % w/v), flow rate 0.5 ml min^{-1}, injection volume 20 µl. The column used was a Kinetex C18 150-2 (150 mm length, 2 mm I.D., 2.6 µm core-shell particles, Phenomenex). The detection was carried out at 220 nm.

4.3.2.1. Results

The phenol photo-degradation in the presence of fluorinated and pristine TiO_2 nanoparticles was of the most studied system.[20,21] The photocatalytic degradation of phenol is enhanced on fluorinated TiO_2. Taking into account the high reactivity of phenol with $OH^{\bullet}$ and the electrochemical properties of the $F^{-}/F^{\bullet}$ couple this effect was attributed to:[20-23]

- Elimination of the surface hole deep traps associated to the terminal Ti–OH groups (ca. 1.5 V vs NHE potential on the electrochemical scale).[24] The terminal hydroxy groups act as surface recombination centers. The substitution of Ti–OH with Ti–F should slow down the recombination rate, as seen in the photo-electrochemical characterization;
- Enhancement of production of free $OH^{\bullet}$ on TiO_2–F surfaces;

The phenol disappearance profiles at the two different pH for the selected materials are shown in Figure 61. The phenol disappearance profiles follow a pseudo first order kinetic for the bipyramids, meanwhile the low rates obtained in some tests for the nanosheets can be described with a pseudo-zero order kinetic.

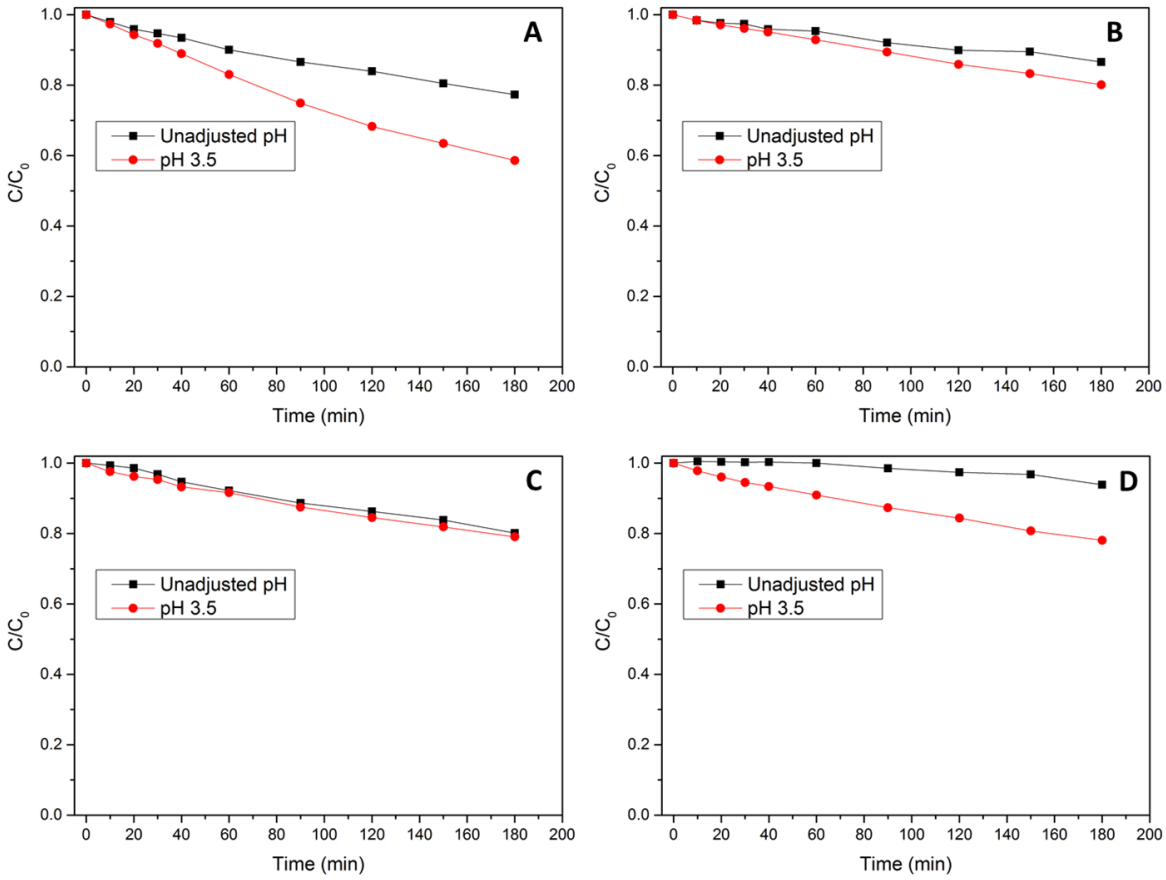

Figure 61. Phenol disappearance profiles at the two different pH for the selected materials: a) bipy; b) n-sh; c) n-sh_NaOH; d) n-sh_873K.

Table 19. Initial disappearance rates of phenol for the considered materials

	Unadjusted pH		pH 3.5	
Material	**Rate, mM min^{-1}**	**Rate, mM min^{-1} m^{-2}**	**Rate, mM min^{-1}**	**Rate, mM min^{-1} m^{-2}**
bipy	$(1.28\pm0.06)\times10^{-4}$	$(5.62\pm0.28)\times10^{-4}$	$(2.51\pm0.13)\times10^{-4}$	$(1.17\pm0.06)\times10^{-3}$
n-sh	$(7.94\pm0.40)\times10^{-5}$	$(2.88\pm0.14)\times10^{-4}$	$(1.02\pm0.05)\times10^{-4}$	$(3.83\pm0.19)\times10^{-4}$
n-sh_NaOH	$(1.17\pm0.06)\times10^{-4}$	$(4.08\pm0.20)\times10^{-4}$	$(1.14\pm0.06)\times10^{-4}$	$(4.02\pm0.20)\times10^{-4}$
n-sh_873K	$(2.04\pm0.10)\times10^{-5}$	$(1.13\pm0.06)\times10^{-4}$	$(1.19\pm0.06)\times10^{-4}$	$(6.87\pm0.34)\times10^{-4}$

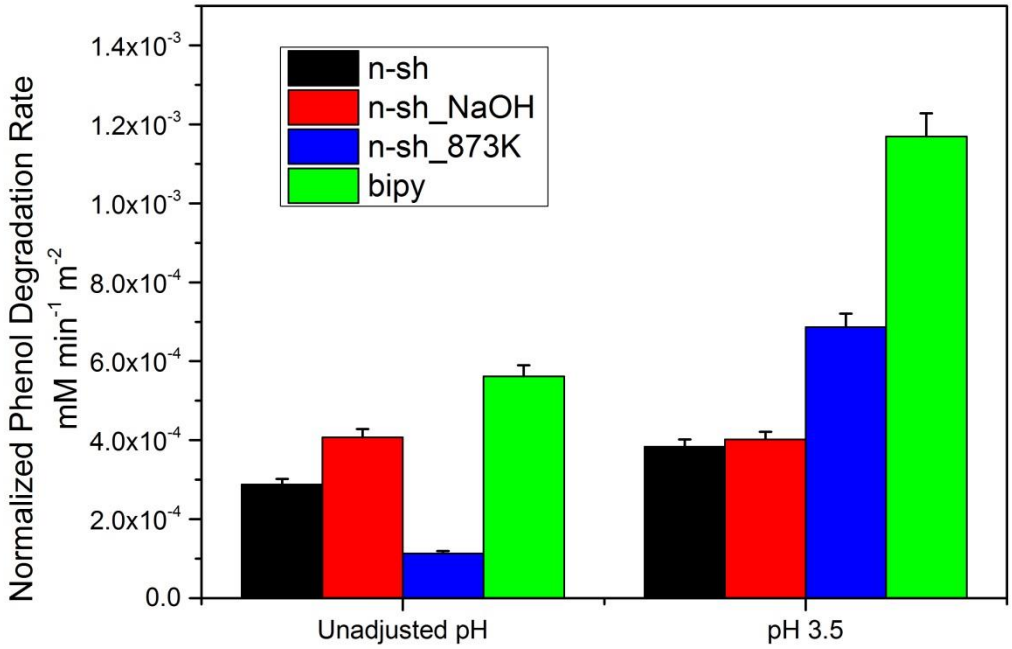

Figure 62. Initial phenol photodegradation rates, normalized by specific surface area of the samples of nanoparticles, obtained at two different pH for the four studied materials.

Table 19 and Figure 62 summarize the initial disappearance rates of phenol over the four catalysts in the two pHs conditions adopted.

Influence of shape

To investigate the impact of the differences in surface features between bare TiO_2 nanoparticles mainly terminated by {101} or (1x4) reconstructed {001} surfaces, TiO_2 bipy and TiO_2 n sh_873K must be compared, freeing of the influence of fluorides. The mechanism of phenol degradation has been widely studied demonstrating that for pure TiO_2 under UV irradiation $^{\bullet}OH$ radicals are the primary active species,[25] but the mechanism include also direct hole transfer to the substrate[20,21]. Recent studies highlighted the

crucial role of both hydroxyls and adsorbed water in stabilizing the surface hole centers.[26] Moreover, also the amount of water adsorbed at the photocatalyst surface was found to strongly influence the efficiency of the phenol degradation process.[27] Thus, hydroxylation and surface affinity towards H_2O molecules are expected to have both a relevant influence on this process. Figure 61 and Figure 62 show respectively the phenol photodegradation curves and the related initial degradation rates, normalized by specific surface area of the samples of nanoparticles. Considering the degradation carried out at unadjusted pH, i.e. without any other addiction), the effectiveness of TiO_2 n sh_873K (Panel D in Figure 61) in the phenol photodegradation is very limited, whereas TiO_2 bipy (Panel A in Figure 61) appears significantly more active (ca. 6% and 23% of C_6H_5OH, respectively, after 180 min irradiation). Noteworthy, TiO_2 bipy has an initial degradation rate ca. 5 times higher than TiO_2 n sh_873 K. Thus, the collection of data on surface features of these two types of nanoparticles carried out in the previous chapter, allows to state that low hydrophilicity, poor hydroxylation, and weak Lewis acidity of Ti sites exhibited by reconstructed {001} surfaces affect negatively at unadjusted pH the photocatalytic performance of bare TiO_2 nano sheet particles in the tested reaction with respect to the TiO_2 bipy ones, mainly exposing {101} facets.

Interestingly, the pH has a high impact on the photocatalytic performances of the two materials, mostly for the n-sh_873K TiO_2 nanoparticles. This material seems to have a sort of superficial "passivation", probably due to the surface reconstruction and reduced surface stress that can decrease the surface activity.[28,29] Acidic pH increase the phenol photodegradation

rates both for bipyramidal nanoparticles and nanosheets, but the ratio $r_{bipy}/r_{n\text{-}sh\_873K}$ decreases from 5 to 1.7. The behavior can be partially explained with the different ζ potentials at these two different pH. Indeed, at the unadjusted pH (that is a little bit more acid that the neutrality in our tests conditions) the surface of the two materials is charged in the opposite way, negatively for the calcined nanosheets and positively for the bipy. At acidic conditions (pH 3.5) instead, the ζ potentials of the two materials are similar, so we have in this case a reduction of the rate ratio. Moreover, as seen in the electrochemical paragraph, the change of the pH induces the surface activation of the material (previously passivated), decreasing its recombination rate.

Influence of fluorides

The influence of the fluorides on the phenol photocatalytic degradation was carried out comparing the other two selected materials, i.e. n-sh and n-sh_NaOH. As we have seen in the previous chapter, the basic treatment of the nanosheets exchange the fluorides of the surface with OH groups, this enrichment induce a higher hydrophilicity of the surface due to the higher hydroxylation. This higher affinity to water results in a higher photodegradation rate for the nanoparticles treated with NaOH. The pH has not high influence on the degradation; indeed the experiments performed at pH 3.5 do not affect the activity of the n-sh_NaOH (see Figure 61 and Figure 62) and slightly increase the performance of the fluorinated material. The ratio $r_{n\text{-}sh\_NaOH}/r_{n\text{-}sh}$ decreases from 1.40 to 1.05, i.e. the two materials in acidic conditions have near the same performances.

These results are different from some of those reported in literature,[20-23] where fluorides seem increase the photocatalytic degradation of phenol due to the higher production of OH radicals at the surface of the nanoparticles (lower recombination rate) and because they inhibit the adsorption of species that are able to back react with e^-_{CB}, increasing the recombination. These differences can explained with the higher hydrophilicity induced by the fluorides removal that contrasts the lower recombination rate of the fluorinated material.[30] Moreover, the fluorination reduce the direct hole transfer (DHT) mechanism that can occur on the TiO_2 surface during the phenol degradation. The entire photocatalytic process is resumed in Figure 63.

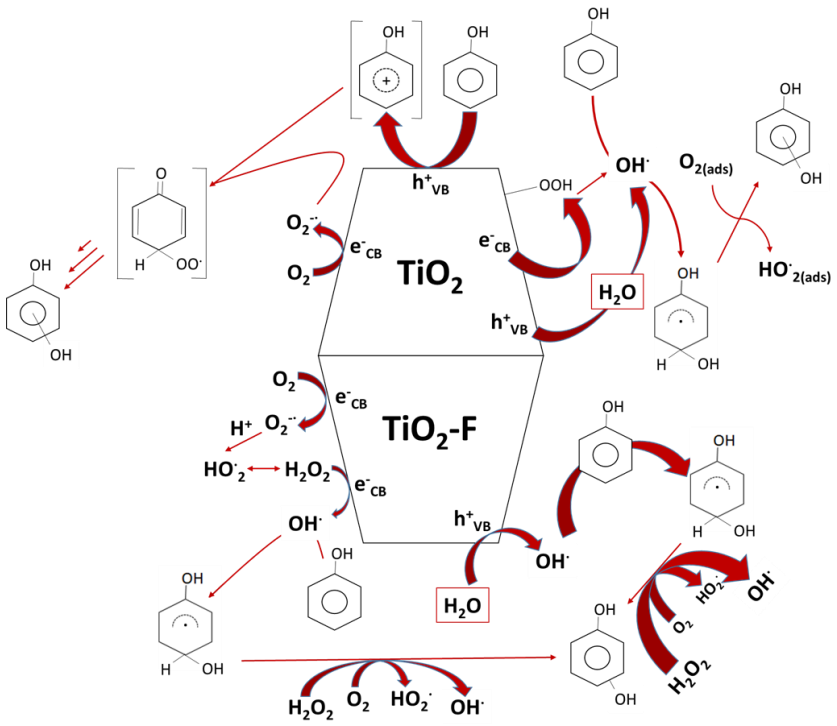

Figure 63. Schematic description of the photocatalytic phenol degradation process onto pristine (up) and fluorinated (down) TiO_2. The main mechanism (at unadjusted pH) for these studied materials is the photo-oxidation of water to produce OH radical.

It must be noted that at unadjusted pH, the photocatalytic trends shown in Figure 61 and Figure 62 follow the same order of hydrophilicity presented in Figure 34, however the change of the pH can modify this trend inducing an high increase of the photocatalytic activity of the de-fluorinated materials. The fluorination therefore mitigates the effect of the pH on the phenol degradation rate for the studied systems.

4.3.3. Melamine Photodegradation

Melamine photodegradation was evaluated using the same apparatus previously described for the phenol photodegradation. However, some conditions are different:

- Suspension: 500 mg l^{-1};
- Integrate irradiance: 20 W m^{-2};
- Reactor's spacer: 5 mm;

HPLC determination of melamine has been carried out by ion pair chromatography with a bonded phase octadecylsilica column (LiChrospher R100-CH 18/2 by Merck, 250 mm length, 10 mm i.d., 5 µm packing); the mobile phase was 0.01 M sodium hexane sulfonate (Aldrich ion-pair reagent 99+%) and 0.014 M H_3PO_4 dissolved in water aqueous solution (0.05 % w/v), flow rate 0.4 ml min^{-1}, injection volume 20 µl. The detection was carried out at 200 nm.

4.3.3.1. Results

In the first chapter of this work, it was highlighted how the intrinsic and extrinsic surface properties can affect the selectivity of the photocatalytic degradation toward different substrates. This selectivity is the result of the different ability of catalysts with different surface properties to promote free $OH^{\bullet}$ mediated or direct/indirect hole transfer oxidation. The availability of a substrate not reactive toward OH radicals and not adsorbed onto TiO_2 can help to probe the participation of a mechanism that involves an outer sphere direct hole transfer (likely promoted by shallow surface traps, also called indirect hole transfer (IHT))[31-34] in photocatalysis.

The 1,3,5-triazines (s-triazines) are organic chemical compounds with a six-membered heterocyclic aromatic ring, they are useful in a variety of applications in organic chemistry. The photocatalytic transformation of several s-triazine derivatives has been extensively investigated.[35] Moreover, its derivatives loose easily the substituents, but they retain the s-triazine ring untill to the formation of cyanuric acid, which is stable to further photocatalytic oxidation.[35] Interestingly, some advanced oxidation process like UV/H_2O_2 and Fenton reaction lead to stable products that retain the amino group and the cyanuric acid generation is not reached.[36,37] These evidences suggest to study the behavior of Melamine (2,4,6-triamino-1,3,5-triazine) under photocatalytic conditions and in $OH^{\bullet}$ generating systems. A preliminary investigation about the $UV/TiO_2/H_2O_2$ melamine degradation was proposed by Bozzi and co-workers:[38] a not complete mineralization was reported due to the formation of cyanuric acid as last product. Nothing was reported about the nature of the first steps of the photocatalytic

reaction. Studies carried out in our research group lead to the conclusion that the photocatalytic degradation of the melamine occurs with IHT, indeed Maurino et al.[39] in 2015 performed the photo-induced transformation of melamine using different advanced oxidation technologies under a variety of experimental conditions. The systems involving homogeneous hydroxyl radicals, as generated by H_2O_2/hν, Fenton reagent, and sonocatalysis are ineffective. They described a mechanism in which the first event is the oxidation of the amino-group to nitro-group through several consecutive fast oxidation steps, and that a hydrolytic step leads to the release of nitrite in solution. The experimental evidences suggest that the photocatalytic mechanism is based on an outer sphere direct hole transfer from trapped holes at the TiO_2 surface to the melamine.

This paragraph presents the study of the transformation of melamine using the four selected materials under two different pH. The melamine disappearance profiles follow a pseudo zero order due to the low photocatalytic rate obtained (Figure 64). As a measure of photocatalytic activity, the initial disappearance rate obtained was used.

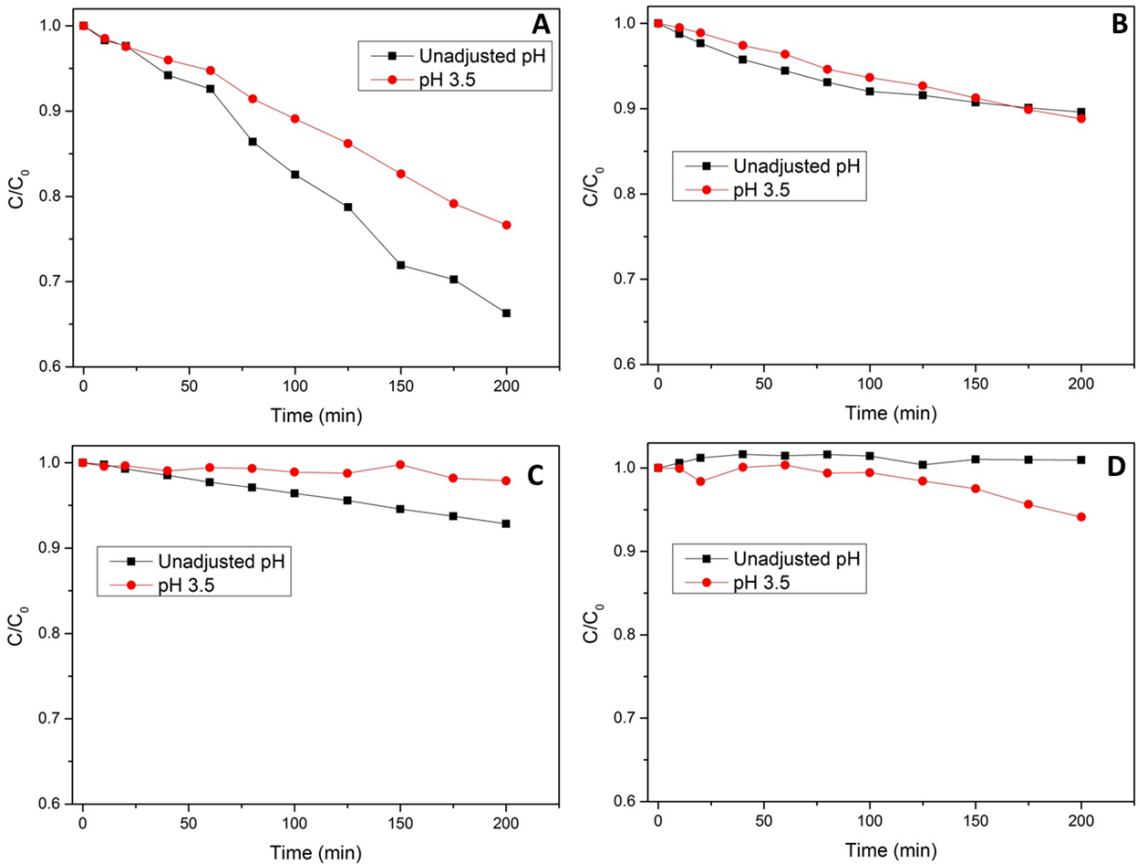

Figure 64. Melamine disappearance profiles at the two different pH for the selected materials: a) bipy; b) n-sh; c) n-sh_NaOH; d) n-sh_873K.

Table 20. Initial disappearance rates of melamine for the considered materials

	Unadjusted pH		pH 3.5	
Material	**Rate, mM min^{-1}**	**Rate, mM min^{-1} m^{-2}**	**Rate, mM min^{-1}**	**Rate, mM min^{-1} m^{-2}**
Bipy	$(1.69\pm0.07)\times10^{-4}$	$(1.58\pm0.06)\times10^{-4}$	$(1.19\pm0.04)\times10^{-4}$	$(1.10\pm0.04)\times10^{-3}$
n-sh	$(9.83\pm0.39)\times10^{-5}$	$(7.36\pm0.29)\times10^{-5}$	$(5.73\pm0.20)\times10^{-5}$	$(4.34\pm0.15)\times10^{-4}$
n-sh_NaOH	$(3.45\pm0.14)\times10^{-5}$	$(2.40\pm0.10)\times10^{-5}$	$(8.68\pm0.30)\times10^{-6}$	$(6.12\pm0.21)\times10^{-5}$
n-sh_873K	$(1.43\pm0.06)\times10^{-8}$	$(1.68\pm0.07)\times10^{-8}$	$(2.02\pm0.07)\times10^{-5}$	$(2.37\pm0.08)\times10^{-4}$

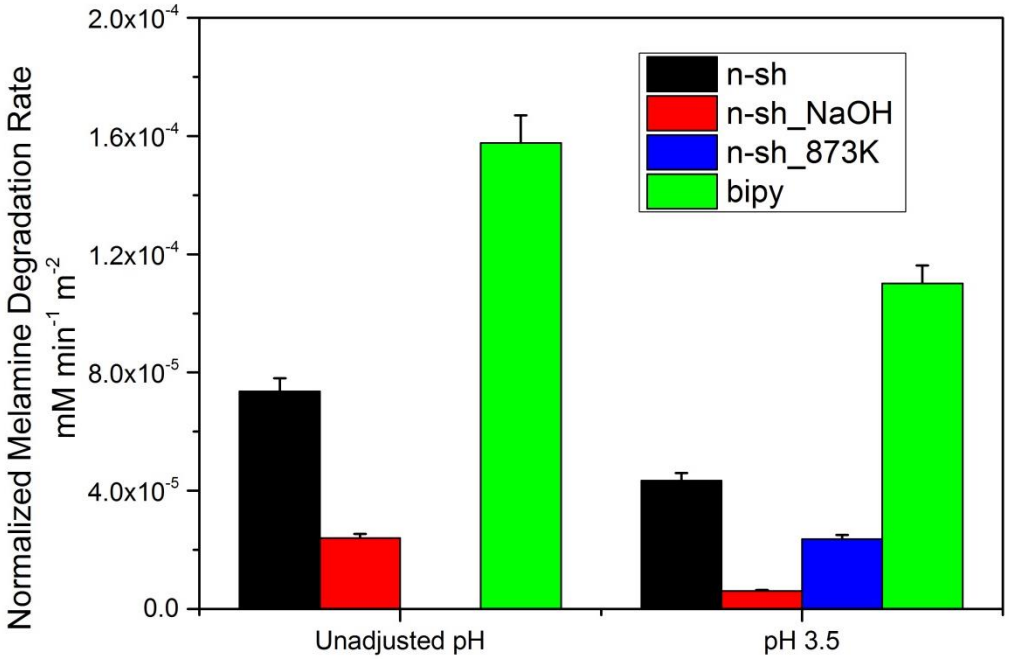

Figure 65. Initial melamine photodegradation rates, normalized by specific surface area of the samples of nanoparticles, obtained at two different pH for the four studied materials.

Table 20 and Figure 62 summarize the initial disappearance rates of phenol over the four catalysts in the two pH conditions adopted.

Influence of shape

As well as for the case of phenol, in order to investigate the impact of the differences in surface features between bare TiO_2 nanoparticles mainly terminated by {101} or (1x4) reconstructed {001} surfaces, TiO_2 bipy and TiO_2 n-sh_873K must be compared. As seen, the photodegradation mechanism of melamine over TiO_2 nanoparticles occurs with an indirect hole transfer (IHT), in which the holes generated by the UV irradiation are primary trapped at the surface and then transferred to the substrate that is

not absorbed at the surface. Therefore, we would expect that a {001} surfaces rich material has a higher photocatalytic activity against these kind of substrates, due to their oxidative behavior in photocatalysis as reported in chapter 1 and 2. However, in our tests the photoactivity of the bipy is widely higher for the bipy in which the {101} are predominant. Even, at unadjusted pH the activity of the material n-sh_873K is negligible. These results can be rationalize looking at the surface of the materials, indeed in IHT mechanism the holes must be trapped at the surface for initiating the photocatalytic process. Charge carriers are often trapped on defective sites like dopants or vacancies presents in the bulk, in the subsurface or at the surface of the crystal.[40] From all our results (IR, EPR, microbalance, electrochemistry, photocatalysis), seems that the material n-sh_873K at unadjusted pH has a sort of surface passivation induced by the thermic treatment, consistent even with a considerable reduction of bulk and surface defects that reduces the surface hole trapping increasing the recombination rate of the material.

Influence of pH

The melamine initial transformation rate is a complex function of the pH, in fact the change in the valence band position explains only partially the relationship between the melamine degradation rate and the pH. The higher rate observed at unadjusted pH can be explained as the result of the interplay among the valence band edge potential shift, the substrate acid – base properties and the amphoteric characteristics of the titania surface. The pKa_1 of melamine is 5.05,[38] so at pH below 4 more than the 90% is protonated. The reduction of the rate at acidic pH is probably due to the electrostatic repulsion between the catalysts (pzc≈6-7) and the protonated

melamine, giving a slightly decrease of the carriers transfer rate. As seen for phenol, the acidic conditions largely increase the activity (even if the rates remain very low) of the calcined nanosheets. In this case seems that the acidic conditions are able to break the "passivation status" of this material, increasing its photocatalytic activity (Figure 65). This "de-passivation" effect is so high (because this material seems to have higher UV absorption respect to n-sh and n-sh_NaOH) that can contrast the electrostatic repulsion which, instead, would tend to decrease the melamine degradation.

Influence of fluorides

The influence of the fluorides on the melamine photocatalytic degradation was, again, carried out comparing the other two selected materials, i.e. n-sh and n-sh_NaOH. It was reported that for those substrates that are oxidized through an IHT mechanism, the carriers trapping at the surface is fundamental. Surface fluorination stabilizes electron trapped at the surface of the material, decreasing the rate of the electron transfer to acceptors like molecular oxygen but decreasing also the recombination rate. Hindering of recombination favors hole transfer to solution, with a consequent increasing of the substrate photo-oxidation. Indeed, as reported in Figure 65, fluorinated nanosheets (n-sh) has higher photocatalytic activity against melamine compared to the NaOH treated ones (n-sh_NaOH) both at natural and acidic pH. However, the high level of doping of these materials are responsible of the lower photocatalytic activity compared to bipyramids, indeed the presence of fluorides at the surface favor the degradation of the substrate but when present in large amount on the crystal bulk, the can act as recombination centers. The

recombination of the carriers greatly decrease the efficiency of the entire process.

4.3.4. Formic Acid Photodegradation

Melamine photodegradation was evaluated using the same apparatus previously described for the phenol photodegradation. However, some conditions are different:

- Suspension: 500 mg l^{-1};
- Substrate concentration: 0.5 mM;
- Integrate irradiance: 20 W m^{-2};
- Reactor's spacer: 5 mm;

Each time the suspension was filtered and the solution analyzed by Ion Chromatography (IC) as formate. The instrument (DIONEX DX 500) is equipped with a GP40 pump, AS9-HC column (Dionex, length 25 cm and internal diameter of 4 mm), Suppressor ASRS-Ultra II autosuppression mode, electrochemical detection system ED40, LC30 column thermostat (temperature 303 K). The mobile phase consists of 9 mM K_2CO_3 and the eluent flow is equal to 1 mL min^{-1}.

4.3.4.1. Results

Carboxylic acids allow to probe different aspects of the photocatalytic mechanism. Indeed, a dual direct hole transfer (DHT) and a OH radical mediated oxidation of carboxylic acid was demonstrated over irradiated P25 Degussa.[41] In particular, the direct hole transfer (with an inner sphere

mechanism) is operative when the carboxylate is adsorbed over the TiO_2 surface, i.e. at pH between 3 and 5.

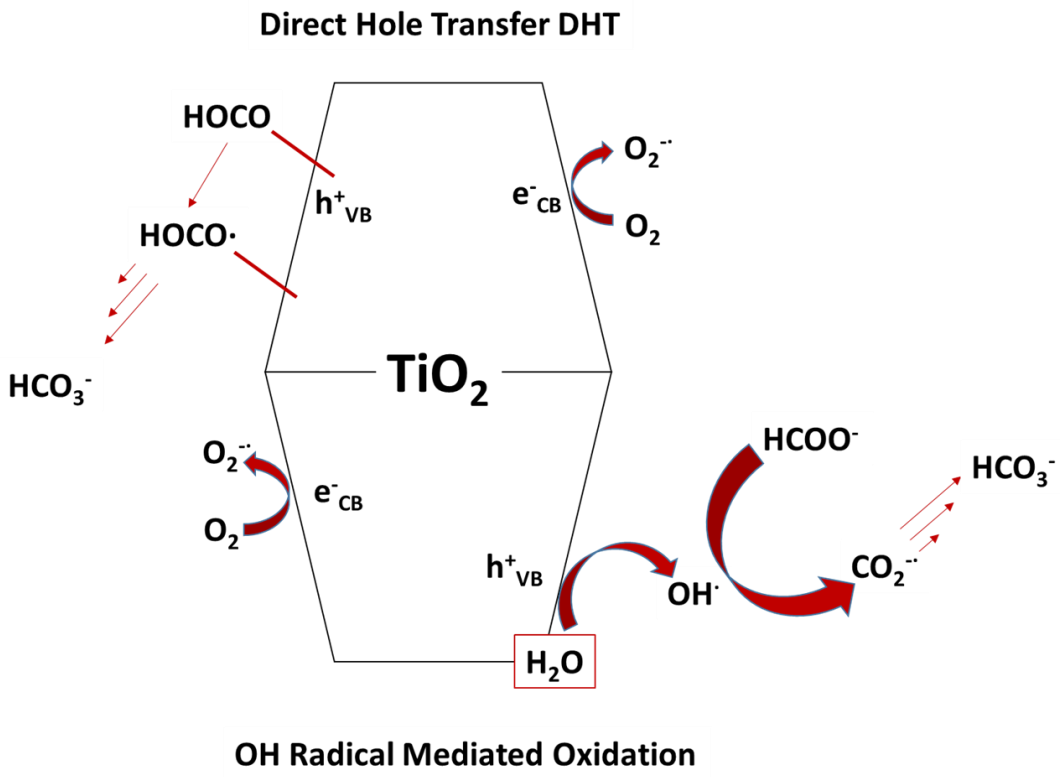

Figure 66. Schematic description of the photocatalytic formate ion degradation process through OH radical mediated oxidation and direct hole transfer (DHT).

In order to describe the formate oxidation mechanism, Perissinotti and co-workers[42] carried out a kinetic analysis of the photocatalytic degradation on TiO_2 P25 based on EPR experiments. In their conditions, 30% of formate ions oxidation occurs through the reaction with hydroxyl radicals.

$$HCOO^- + OH^\cdot \rightarrow CO_2^{\cdot-} + H_2O \qquad (4.1)$$

The carboxyl anion radicals are then oxidized by O_2 (reaction 4.2) or through the electron injection into the conduction band (reaction 4.3).

$$CO_2^{\bullet-} + O_2 \rightarrow CO_2 + O_2^{\bullet-} \quad (4.2)$$

$$CO_2^{\bullet-} \rightarrow CO_2 + e^- \quad (4.3)$$

Direct hole transfer, instead, involves a surface carboxylate complex that gives formyl-oxyl radical (reaction 4.4), that can be further oxidized by electron transfer to adsorbed O_2 (reaction 4.5) or by electron injection into the conduction band (reaction 4.6).

$$HCOO^- + h_{VB}^+ \rightarrow HCOO^\bullet \quad (4.4)$$

$$HCOO^\bullet + O_2 \rightarrow H^+ + CO_2 + O_2^{\bullet-} \quad (4.5)$$

$$HCOO^\bullet \rightarrow H^+ + CO_2 + e_{CB}^- \quad (4.6)$$

The electron injection into the conduction band by the oxidized intermediate results is called "current doubling".[43]

Figure 67 reports the formic acid/formate disappearance profiles in the presence of O_2 at natural and 3.5 pHs for the four tested materials. Table 21 and Figure 68 summarize the initial degradation rates obtained from the fit of each degradation experiment to an exponential decay.

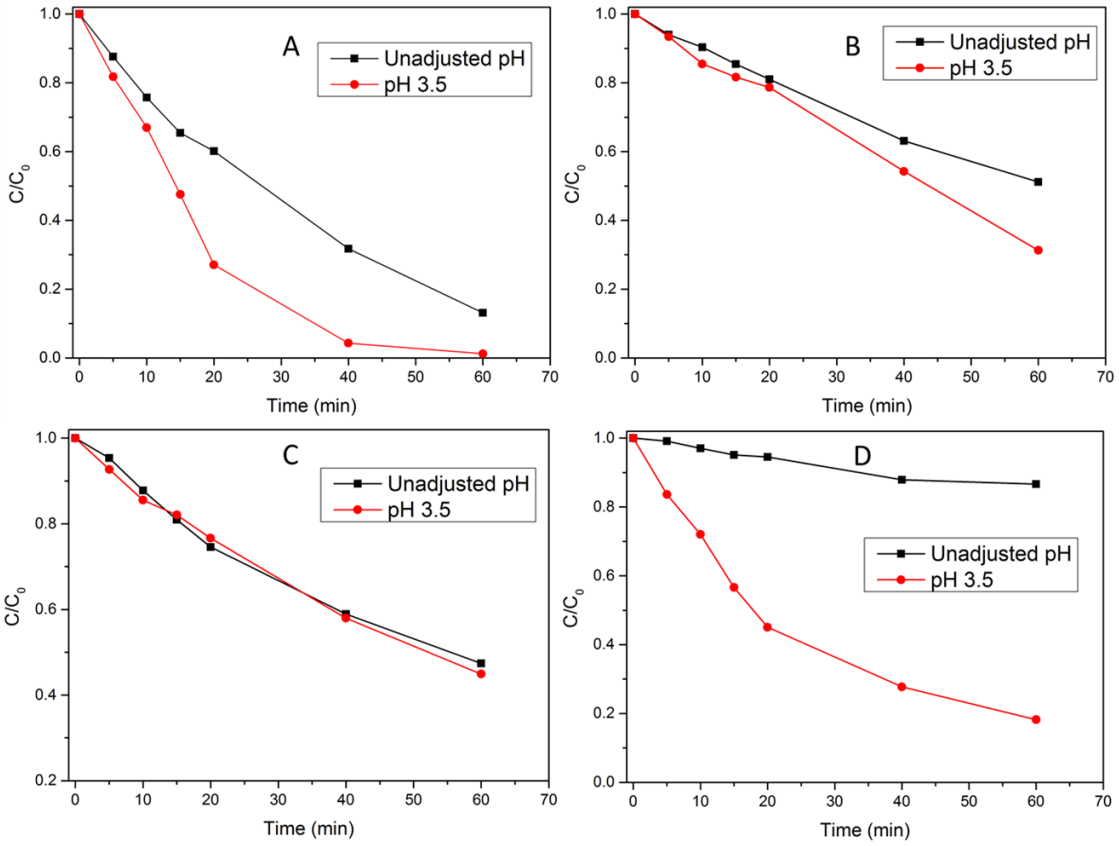

Figure 67. Formic acid/formate disappearance profiles at the two different pH for the selected materials: a) bipy; b) n-sh; c) n-sh_NaOH; d) n-sh_873K.

Table 21. Initial disappearance rates of formic acid/formate for the considered materials

	Unadjusted pH		pH 3.5	
Material	**Rate, mM min^{-1}**	**Rate, mM min^{-1} m^{-2}**	**Rate, mM min^{-1}**	**Rate, mM min^{-1} m^{-2}**
bipy	$(1.35\pm0.08)\times10^{-2}$	$(1.25\pm0.07)\times10^{-2}$	$(1.71\pm0.10)\times10^{-2}$	$(1.58\pm0.09)\times10^{-2}$
n-sh	$(5.40\pm0.31)\times10^{-3}$	$(4.05\pm0.23)\times10^{-3}$	$(5.64\pm0.37)\times10^{-3}$	$(4.29\pm0.28)\times10^{-3}$
n-sh_NaOH	$(6.71\pm0.40)\times10^{-3}$	$(4.69\pm0.28)\times10^{-3}$	$(6.72\pm0.06)\times10^{-3}$	$(4.70\pm0.43)\times10^{-3}$
n-sh_873K	$(1.56\pm0.08)\times10^{-3}$	$(1.84\pm0.10)\times10^{-3}$	$(1.40\pm0.58)\times10^{-2}$	$(1.61\pm0.07)\times10^{-2}$

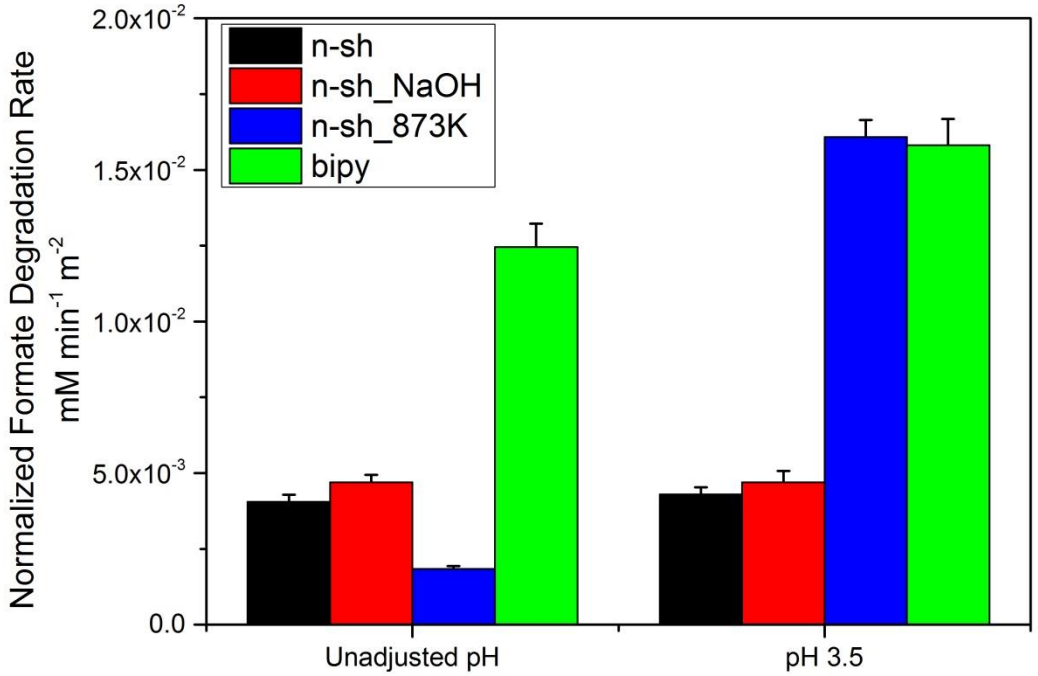

Figure 68. Initial formic/formate photodegradation rates, normalized by specific surface area of the samples of nanoparticles, obtained at two different pH for the four studied materials.

Influence of shape

As well as for phenol and melamine, in order to investigate the influence of the different surfaces, a comparison between bare TiO_2 nanoparticles mainly terminated by {101} or (1x4) reconstructed {001} surfaces must be done, i.e. a comparison between TiO_2 bipy and TiO_2 n-sh_873K. The photodegradation mechanism of the formic acid over TiO_2 nanoparticles occurs with an direct hole transfer (DHT), in which the holes generated by the UV irradiation are directly transferred to the substrate absorbed at the surface. Therefore, we would expect that a {001} surfaces rich material has a higher photocatalytic activity against these kind of substrate, due to

their oxidative behavior in photocatalysis as reported in chapter 1 and 2. In our tests with formic acid the photoactivity is widely higher at unadjusted pH for the bipy in which the {101} are predominant, the ratio between the rates is ~ 7.2. Once again, a sort of "passivation" of the surface for the sample n-sh_873K largely decreases the activity against formic acid/formate. Also in this case, seems that the acidic conditions are able to break the "passivation status" of this material (Figure 65 and Table 21), decreasing the recombination rate of the charge carriers and increasing its photoactivity. Moreover, with the pH decreasing, there is also a modification of the degradation mechanism of formate, passing from an OH radical mediated oxidation to a DHT. The low hydrophilicity and hydroxylation of the material n-sh_873K influence negatively the photocatalytic activity at unadjusted pH. Conversely at acidic pH the DHT mechanism become more and more important and the lower recombination in the calcined nanosheets allows an high improvement of the formate photodegradation, reaching the activity of the bipyramids.

Influence of fluorides

The influence of the fluorides on the formate/formic acid photocatalytic degradation was, again, carried out comparing the other two selected materials, i.e. n-sh and n-sh_NaOH. As previously seen, fluorination should decrease the photo-oxidation of species that are oxidized throughout the direct hole transfer model, which provides a strong and direct interaction of the substrate with the TiO_2 surface.[30,31,44] The surface fluorides are able to avoid that of the organic substrates can be absorbed, precluding the direct transfer of holes to the adsorbed species. This results in a change of the mechanism from direct to indirect, which is intrinsically less effective. This

change of the mechanism explain the lower photodegradation rates obtained for the fluorinated nanosheets. The lower presence of fluorides for n-sh_NaOH induces a higher photoactivity for this material both at natural and acidic pH values. At unadjusted pH this behavior can be ascribed to the increased hydrophilicity that results in higher production of hydroxyl radicals. For the tests carried out at pH 3.5, the higher photoactivity of the material n-sh_NaOH is probably due to the slightly higher absorption of the formic acid on the TiO_2 surface, that favors the direct hole transfer.

4.3.5. Liquid/Solid Photocatalysis: Summary

The following scheme summarizes the results obtained on the three probe molecules in the liquid/solid photocatalysis.

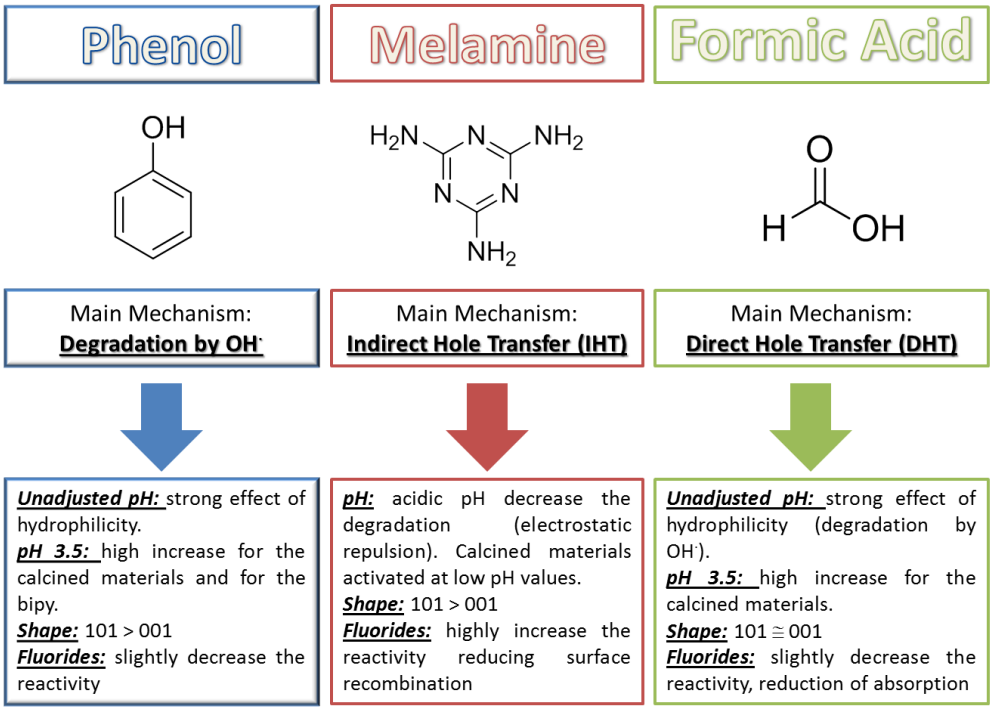

4.4. Photocatalytic hydrogen production on Pt-loaded TiO_2 shape controlled NPs

Hydrogen production experiments were performed irradiating with UV light slurries containing 1.0 g L^{-1} of TiO_2 powder of the four selected materials and 2.0 mg L^{-1} of Pt, added as H_2PtCl_6, which is reduced to Pt^0 (by the photoelectrons produced in the semiconductor) and deposited onto TiO_2 upon irradiation. The use of a co-catalyst was discussed in Chapter 1. Briefly, it helps to increase the photogenerated carriers separation improving the kinetics of H_2O reduction, which would be very slow on pristine TiO_2. Formic acid (0.1 M) was used as hole scavengers in order to reduce the electron-hole recombination. The experiments were carried out at two different pH, at pH 3.5 using formate buffer (that is also the hole scavenger) and at unadjusted pH. The irradiation experiments were carried out in magnetically stirred, cylindrical quartz cells (3.5 cm inner diameter, 2 cm height), containing 5 mL of slurry. Before irradiation the cell containing the slurry was carefully purged with nitrogen to remove oxygen from the reaction environment. The removal of oxygen is fundamental in order to obtain higher H_2 production yields, indeed the reaction of light generated electrons can react with oxygen giving rise to a competitive reaction. The photocatalytic mechanism of H_2 production was already represented in Figure 6 in the first chapter of this thesis.

Hydrogen evolution was followed withdrawing periodically 2.5 mL of gas from the irradiation cell and replacing it with the same volume of N_2. The gas sample was analyzed with an Agilent 490 Micro GC gas chromatograph

equipped with a Molsieve 5Å for H_2 analysis. During the analysis the columns were kept at a temperature of 363 K and 313 K and at a pressure of 200 kPa and 150 kPa, the carrier gases was argon. The total amount of H_2 produced as a function of time was calculated from the concentration in the sampled gas, considering the total volume of gas in the irradiation cell and the previous samplings. The irradiation was carried out with a LED source centered at 365 nm with an irradiance of 15 W m^{-2}.

The reactions that occurs at the TiO_2 surface are:

$$h\nu \rightarrow e^- + h^+ \quad (4.7)$$

$$e^- + H_2O \rightarrow 1/2H_2 + OH^- \quad (4.8)$$

$$h^+ + HCOOH \rightarrow HCOO^{\cdot} + H^+ \quad (4.9)$$

$$HCOO^{\cdot} \rightarrow e^- + CO_2 + H^+ \quad (4.10)$$

4.4.1. Results

The results obtained for the H_2 production by formic acid photoreforming on Pt-TiO_2 in absence of oxygen under UV irradiation are represented in Figure 69 and Figure 70. They show the H_2 production curves and rates (normalized for both the weight and the surface area) obtained for the four considered materials at two different pHs. Table 22 summarizes the H_2 production rates obtained at the studied conditions.

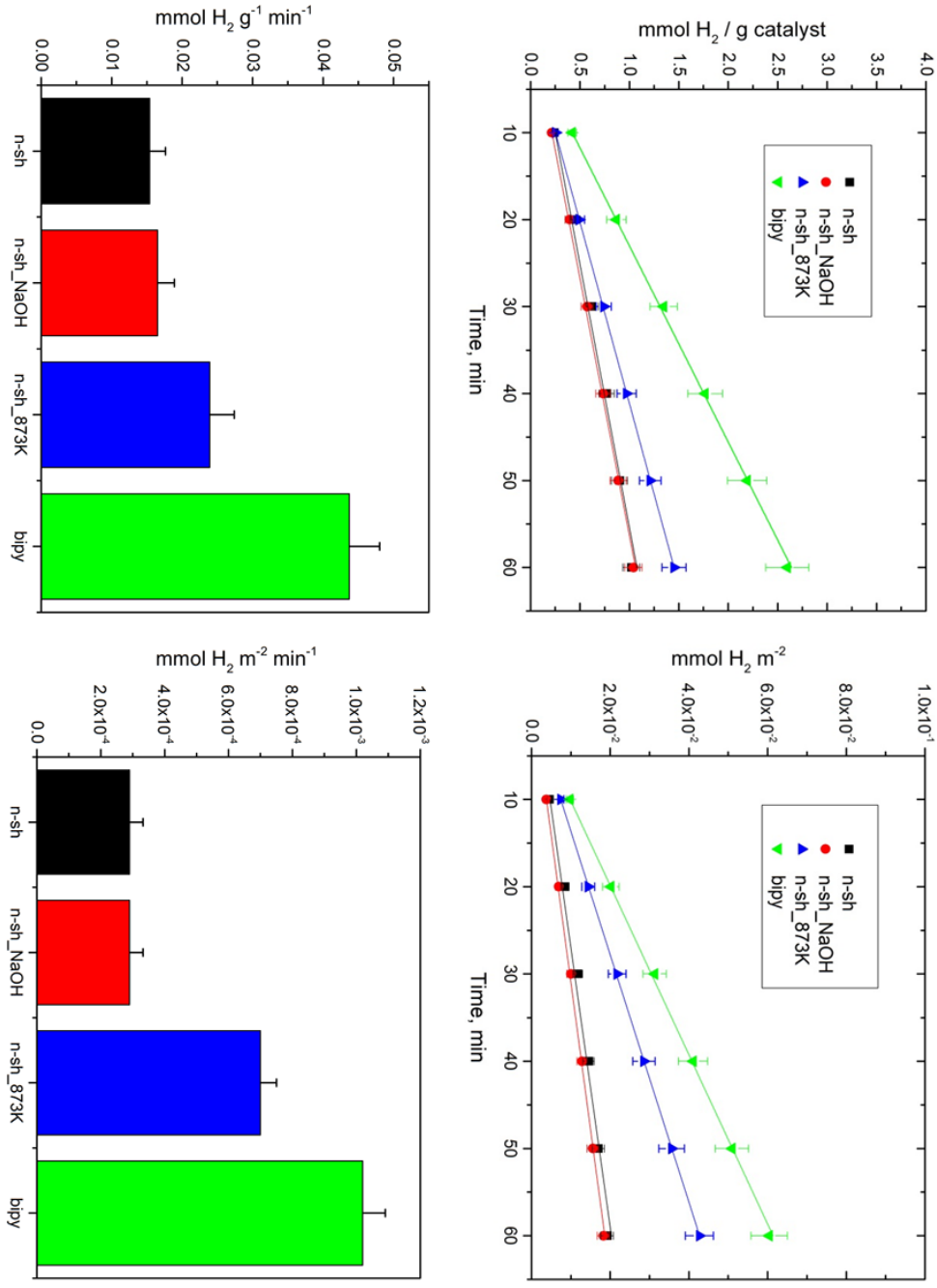

Figure 69. Photocatalytic H_2 production curves and rates obtained at pH 3.5 for the studied materials. The results are normalized for the weight (up) and for the SSA (bottom) of the TiO_2 material used.

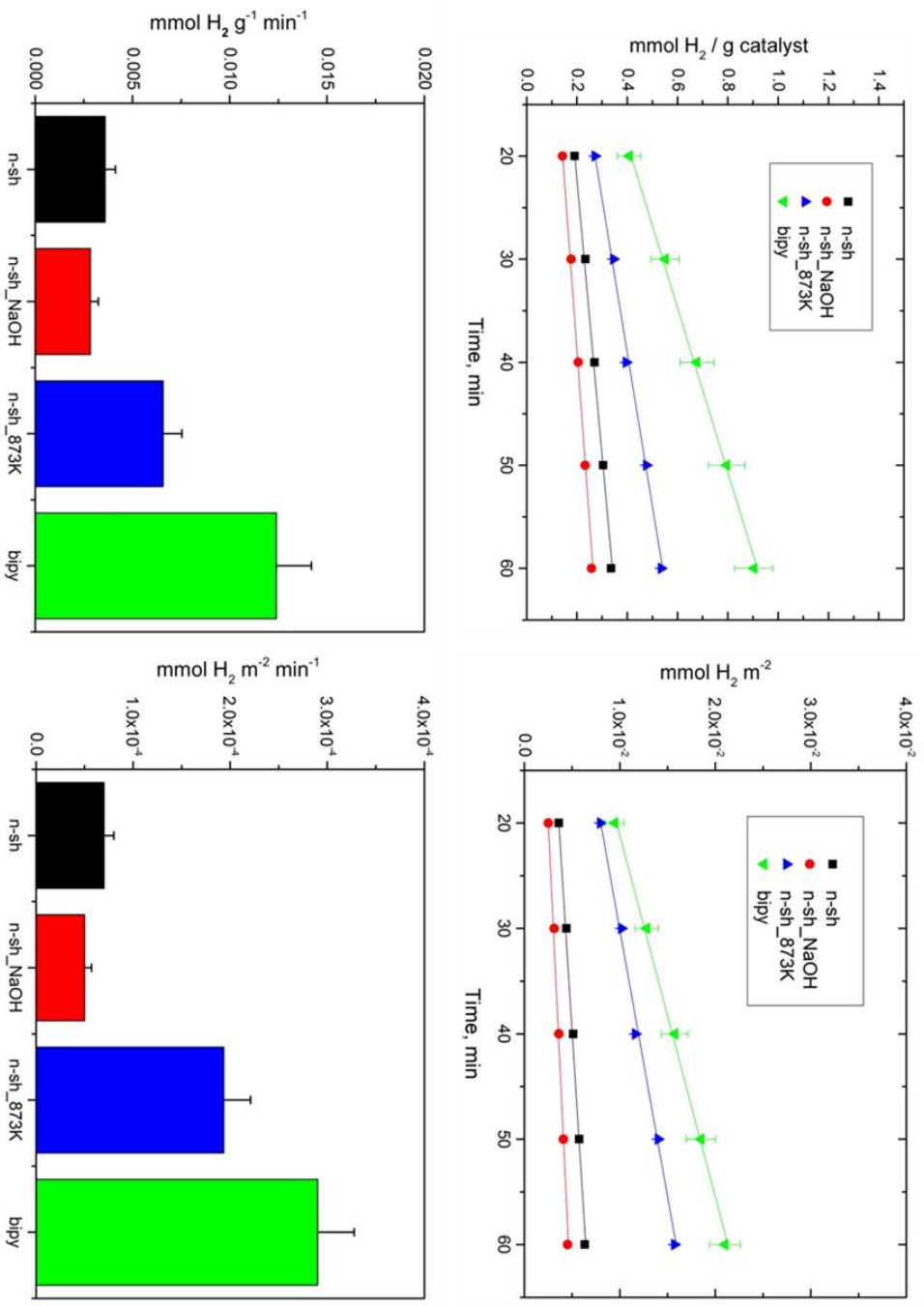

Figure 70. Photocatalytic H_2 production curves and rates obtained at unadjusted pH for the studied materials. The results are normalized for the weight (up) and for the SSA (bottom) of the TiO_2 material used.

Table 22. Photocatalytic H_2 rate evolution from the four Pt-TiO_2 samples considered at two different pH under an irradiation of 15 W m^{-2} centered at 365 nm.

	Unadjusted pH		pH 3.5	
Material	**Rate, mM H_2 g^{-1} min^{-1}**	**Rate, mM H_2 m^{-2} min^{-1}**	**Rate, mM H_2 g^{-1} min^{-1}**	**Rate, mM H_2 m^{-2} min^{-1}**
bipy	$(1.2\pm0.2)\times10^{-2}$	$(2.9\pm0.4)\times10^{-4}$	$(4.4\pm0.6)\times10^{-2}$	$(1.0\pm0.2)\times10^{-3}$
n-sh	$(3.6\pm0.5)\times10^{-3}$	$(7\pm1)\times10^{-5}$	$(1.5\pm0.2)\times10^{-2}$	$(2.9\pm0.4)\times10^{-4}$
n-sh_NaOH	$(2.8\pm0.4)\times10^{-3}$	$(5.0\pm0.7)\times10^{-5}$	$(1.7\pm0.2)\times10^{-2}$	$(2.9\pm0.4)\times10^{-4}$
n-sh_873K	$(6.6\pm0.9)\times10^{-3}$	$(1.9\pm0.3)\times10^{-4}$	$(2.4\pm0.4)\times10^{-2}$	$(7\pm1)\times10^{-4}$

In the first step of the irradiation, the photoelectrons produced reduce Pt(IV) to Pt(0), inducing the deposition of Pt islands on TiO_2. As seen in the first chapter, controlling the shape of the TiO_2 nanoparticles it is possible direct the deposition on a given surface. Therefore, it is expected that those facets that favor the electron transfer to the solution are more efficient in the Pt reduction. In the case of anatase NPs, the surface (101) is the reducing facet. During the photo-deposition, the formate buffer has the function of hole scavenger. Once the Pt is deposited and the suspension turned to a pale grey, the production of hydrogen started. The "induction time" is the reason of the non-linearity of hydrogen production in the very first minutes of irradiation, after which it follows a linear trend. The duration of the induction time depends also on the photo-activity of the material, indeed the higher is the H_2 evolution rate, lower is the induction time. This phenomenon is probably due to the slower Pt deposition rate for the lest active materials. Evidences of this mechanism are showed in the H_2 evolution curves of Figure 69 and Figure 70, where the change in the pH reduces the photocatalytic rates and increases the

induction time from 10 to 20 min. Indeed, at acidic pH the electrostatic force between TiO_2 and formate become larger, increasing the direct hole transfer (DHT) from the semiconductor to the substrate and reducing, consequently, the time of Pt reduction and deposition.

Influence of Fluorides

In order to evaluate the influence of fluorides on the H_2 evolution from formic acid photoreforming on Pt-TiO_2, the materials n-sh and n-sh_NaOH must be compared. From the results resumed in Table 22, Figure 69 and Figure 70 it is possible to conclude that fluorides has not high impact on the photocatalytic process. There is a slightly higher rate for the washed NPs at pH 3.5 (normalizing for the TiO_2 weight), but at unadjusted pH the situation is reversed. This reversal is probably due to the change on the surface charge on the catalysts and to the different hole scavenging mechanism at different pHs. However, the differences in the results are so low to be within the uncertainty range of the measurements, so they can be neglected. The reason of a so small influence of fluorides can be ascribed to the low coverage of the fluorides on the (101) for the nanosheets, which is the main active surface on the H_2 production. Indeed, as already explained, fluorides are used as shape controllers for obtaining (001) surfaces, so the large amounts of the fluorides present in the n-sh material are present on these facets, which are marginally involved on the photocatalytic process.

Influence of Shape

Given the little influence of fluorides on the entire process, in order to evaluate the influence of the shape on H_2 evolution rates, all the material

can be compared. As said, the main active surface in this process is the (101) that is a reducing facet. As a consequence, the 2 nm Pt nanoparticles are deposited predominantly on the (101) surface (see Figure 72). It follows that higher is the amount of the (101) surface on the material, the higher is the rate of the H_2 evolution. The results obtained on the four materials considered confirm the increase of the H_2 production rates with the increase of the (101) percentage in the material. Indeed, the highest rate is obtained for the bipy that has near the 90% of its surface composed by (101) facets (38.7 m^2 g^{-1}). Whereupon, among nanosheets NPs, the calcined sample has the highest photoactivity due to its larger amount of (101) surfaces (14.3 m^2 g^{-1}) induced by the thermal treatment. Meanwhile, n-sh and n-sh_NaOH that have near the same percentage of (101) surface (6.4 and 6.3 m^2 g^{-1} respectively), present near the same photocatalytic H_2 evolution rate. Figure 71 shows the trend of the H_2 evolution rates vs the calculated (101) specific surface area at the two different pH used.

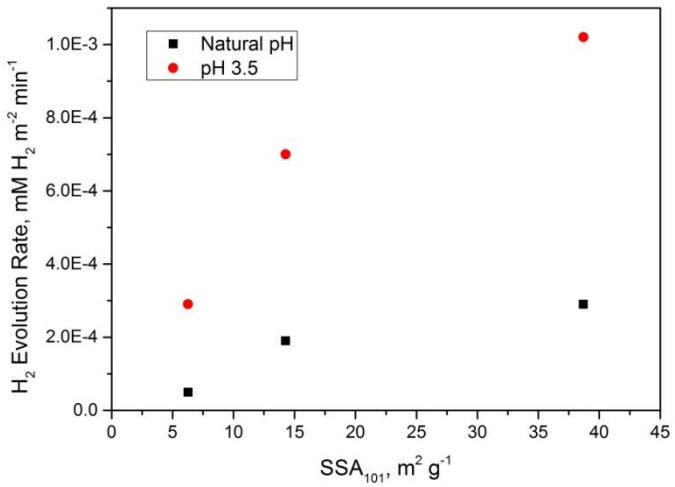

Figure 71. Trend of the H_2 evolution rate vs (101) specific surface area at the two different pH used

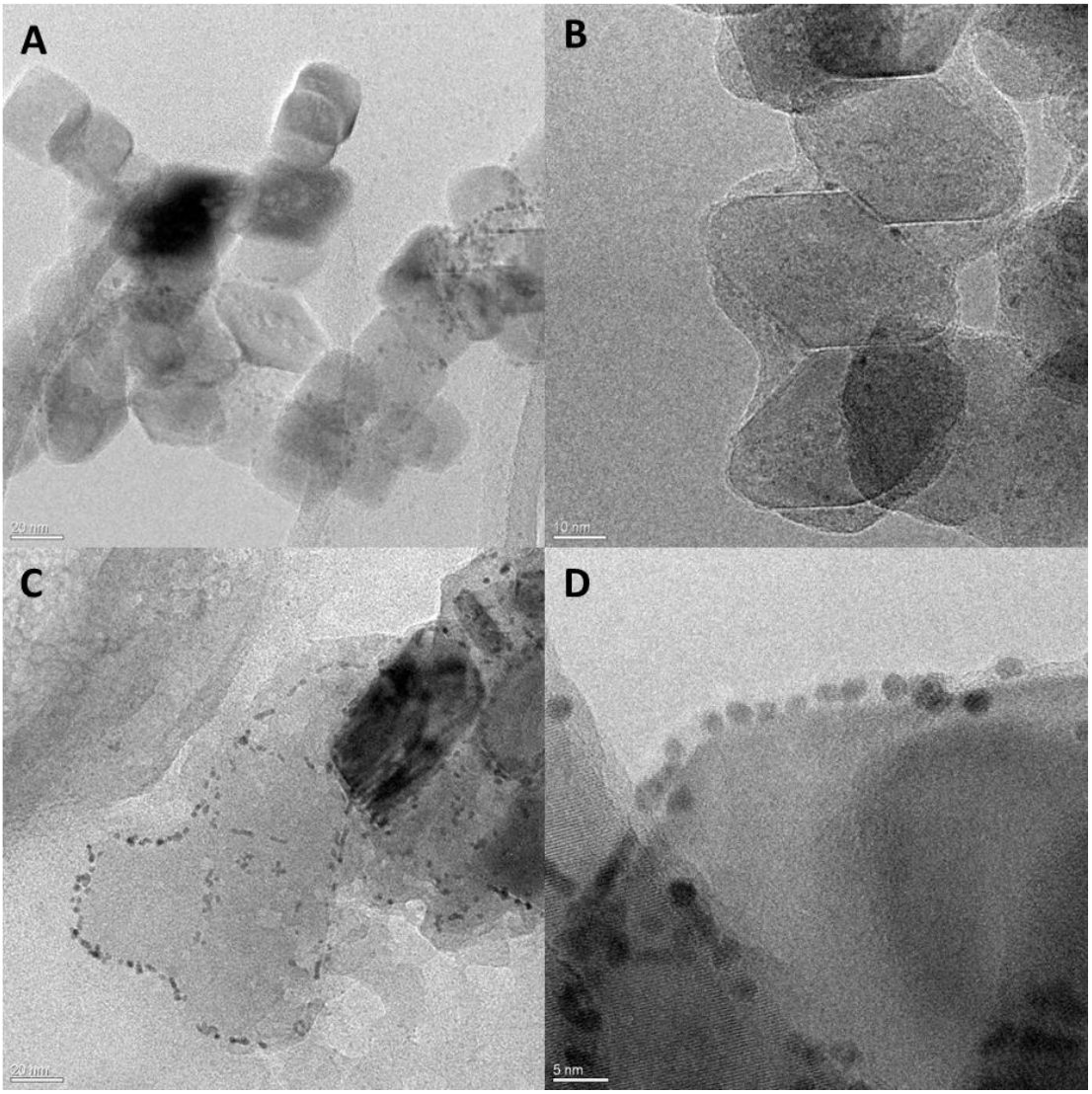

Figure 72. HR-TEM micrographs of the Pt nanoparticles deposited on the materials bipy (A and B) and n-sh_873K (C and D). The micrographs highlight that the Pt nanoparticles photo-deposition occurs mainly on the (101) surfaces of the TiO_2 nanoparticles. This is particularly evident in the case of the nanosheets, where Pt nanoparticles are deposited only on the contours, where (101) surface is present.

Bibliography

(1) Minero, C.; Bedini, A.; Minella, M. *International Journal of Chemical Reactor Engineering* **2013**, *11*.

(2) Maurino, V.; Minero, C.; Pellegrino, F.; Zangirolami, M. In *European Patent Office* 2017.

(3) Lasek, J.; Yu, Y. H.; Wu, J. C. S. *J Photoch Photobio C* **2013**, *14*, 29.

(4) Carslaw, D. C.; Beevers, S. D.; Bell, M. C. *Atmos Environ* **2007**, *41*, 2073.

(5) Lioy, P. J.; Georgopoulos, P. G. *Environmental health perspectives* **2011**, *119*, 1351.

(6) Stern, A. C.; Boubel, R. W.; Turner, D. B.; Fox, D. L. *Fundamentals of Air Pollution*; Second ed. Orlando, 1984.

(7) Freitag, J.; Dominguez, A.; Niehaus, T. A.; Hulsewig, A.; Dillert, R.; Frauenheim, T.; Bahnemann, D. W. *J Phys Chem C* **2015**, *119*, 4488.

(8) Rusu, C. N.; Yates, J. T. *Journal of Physical Chemistry B* **2000**, *104*, 1729.

(9) Lu, G. Q.; Linsebigler, A.; Yates, J. T. *J Phys Chem-Us* **1994**, *98*, 11733.

(10) Sorescu, D. C.; Yates, J. T. *Journal of Physical Chemistry B* **2002**, *106*, 6184.

(11) Dines, T. J.; Rochester, C. H.; Ward, A. M. *J Chem Soc Faraday T* **1991**, *87*, 643.

(12) Markovits, A.; Mguig, B.; Calatayud, M.; Minot, C. *Catalysis Today* **2006**, *113*, 201.

(13) Huang, J. H.; Cheuk, W.; Wu, Y. F.; Lee, F. S. C.; Ho, W. K. *J Nanomater* **2012**.

(14) Ding, X.; Song, X.; Li, P. N.; Ai, Z. H.; Zhang, L. Z. *J Hazard Mater* **2011**, *190*, 604.

(15) He, D.; Li, Y. L.; Wang, I. S.; Wu, J. S.; Yang, Y. L.; An, Q. E. *Applied Surface Science* **2017**, *391*, 318.

(16)

(17) Luevano-Hipolito, E.; Martinez-de la Cruz, A.; Lopez-Cuellar, E.; Yu, Q. L.; Brouwers, H. J. H. *Materials Chemistry and Physics* **2014**, *148*, 208.

(18) Ma, J. Z.; Wang, C. X.; He, H. *Appl Catal B-Environ* **2016**, *184*, 28.

(19) Nakamura, I.; Negishi, N.; Kutsuna, S.; Ihara, T.; Sugihara, S.; Takeuchi, E. *J Mol Catal a-Chem* **2000**, *161*, 205.

(20) Minero, C.; Mariella, G.; Maurino, V.; Pelizzetti, E. *Langmuir* **2000**, *16*, 2632.

(21) Minero, C.; Mariella, G.; Maurino, V.; Vione, D.; Pelizzetti, E. *Langmuir* **2000**, *16*, 8964.

(22) Mrowetz, M.; Selli, E. *Physical chemistry chemical physics : PCCP* **2005**, *7*, 1100.

(23) Mrowetz, M.; Selli, E. *New J Chem* **2006**, *30*, 108.

(24) Lawless, D.; Serpone, N.; Meisel, D. *The Journal of Physical Chemistry* **1991**, *95*, 5166.

(25) Grabowska, E.; Reszczynska, J.; Zaleska, A. *Water Res.* **2012**, *46*, 5453.

(26) Panarelli, E. G.; Livraghi, S.; Maurelli, S.; Polliotto, V.; Chiesa, M.; Giamello, E. *J. Photochem. Photobiol. A-Chem.* **2016**, *322*, 27.

(27) Mino, L.; Zecchina, A.; Martra, G.; Rossi, A. M.; Spoto, G. *Appl Catal B-Environ* **2016**, *196*, 135.

(28) Ibach, H. *Surf. Sci. Rep.* **1997**, *29*, 195.

(29) Shi, Y.; Sun, H.; Saidi, W. A.; Nguyen, M. C.; Wang, C. Z.; Ho, K.; Yang, J.; Zhao, J. *The journal of physical chemistry letters* **2017**, *8*, 1764.

(30) Monllor-Satoca, D.; Lana-Villarreal, T.; Gomez, R. *Langmuir* **2011**, *27*, 15312.

(31) Villarreal, T. L.; Gómez, R.; González, M.; Salvador, P. *The Journal of Physical Chemistry B* **2004**, *108*, 20278.

(32) Montoya, J. F.; Atitar, M. F.; Bahnemann, D. W.; Peral, J.; Salvador, P. *The Journal of Physical Chemistry C* **2014**, *118*, 14276.

(33) Montoya, J. F.; Peral, J.; Salvador, P. *The Journal of Physical Chemistry C* **2014**, *118*, 14266.

(34) Luan, Y.; Jing, L.; Xie, Y.; Sun, X.; Feng, Y.; Fu, H. *ACS Catalysis* **2013**, *3*, 1378.

(35) Pelizzetti, E.; Maurino, V.; Minero, C.; Carlin, V.; Tosato, M. L.; Pramauro, E.; Zerbinati, O. *Environ Sci Technol* **1990**, *24*, 1559.

(36) Arnold, S. M.; Hickey, W. J.; Harris, R. F. *Environ Sci Technol* **1995**, *29*, 2083.

(37) Zong, G.; Lusby, W. R.; Muldoon, M. T.; Waters, R.; Hapeman-Somich, C. J. *J.Agric.Food Chem.* **1992**, *40*, 2294.

(38) Bozzi, A.; Dhananjeyan, M.; Guasaquillo, I.; Parra, S.; Pulgarin, C.; Weins, C.; Kiwi, J. *J. Photochem. Photobiol. A* **2004**, *162*, 179.

(39) Maurino, V.; Minella, M.; Sordello, F.; Minero, C. *Applied Catalysis A: General* **2016**, *521*, 57.

(40) Zawadzki, P. *The Journal of Physical Chemistry C* **2013**, *117*, 8647.

(41) Sun, Y.; Pignatello, J. J. *Environ Sci Technol* **1995**, *29*, 2065.

(42) Perissinotti, L. L.; Brusa, M. A.; Grela, M. A. *Langmuir* **2001**, *17*, 8422.

(43) Hykaway, N.; Sears, W. M.; Morisaki, H.; Morrison, S. R. *The Journal of Physical Chemistry* **1986**, *90*, 6663.

(44) Villarreal, T. L.; Gomez, R.; Neumann-Spallart, M.; Alonso-Vante, N.; Salvador, P. *Journal of Physical Chemistry B* **2004**, *108*, 15172.

Conclusions

The PhD work is part of a European project named SETNanoMetro. The project stems from the importance to establish validated methods and instrumentations for detection, characterization and analysis of nanoparticles. Central for this project is the development of new synthetic procedures and paradigms for the production of shape and size controlled sets of TiO_2 NPs. In the framework of the SETNanoMetro project, the use of various measurement techniques for the determination of the NPs properties allowed to move from the currently used "trial and error" approach toward the development of well-defined and controlled protocols for the production of TiO_2 NPs.

Moreover, this PhD thesis was devoted to the study of the influence of the TiO_2 NPs shape and surface properties on their photocatalytic activity. The importance of surface properties in photocatalysis is further emphasized by the need of at least two active sites, one for the reductive, the other for the oxidative process.

The work is divided in two main sections:

1. Synthesis and characterization of shape controlled nanoparticles;
2. Photocatalytic activity characterization.

In the first section a series of design rules are developed in order to obtain sets of anatase TiO_2 NPs with low polydispersity and to tune their shape and their size through hydrothermal processing of Ti(IV)-triethanolamine complex in the presence of different shape controllers (OH-,

triethanolamine). Through a careful experimental design the influence of many process parameters (pH, temperature, shape controller type and concentration) on the synthesis outcome (size, shape and polydispersity), a predictive soft model was developed. The model is able to predict reasonably well the synthesis outcome allowing to tune the shape factor from 5.5 (elongated nanoparticles) to 1.5 (perfect bipyramids). The model was validated, it can be used to guide the synthesis of NPs with precise characteristics, if the requested morphology falls within the validated range, i.e. NP size between 2 and 25 nanometers and shape parameter between 1 and 5.5. The results here presented are valuable per se, because the NP materials of this kind can find application in catalysis and energy harvesting, but, more importantly, because these results can be extended widening the experimental ranges or applying the same procedure to different synthetic procedure or to other materials, e.g. α-Fe_2O_3 ZnO, WO_3, etc. In all these cases, the possibility to rely on materials composed of monodisperse, size and shape-controlled NPs will allow the connection between macroscopic properties and morphology at the nanoscale, with benefits for both fundamental and applied research.

In the synthesis and characterization section is also included the method employed to obtain TiO_2 nanosheets that expose the {001} surfaces. Fluorides are used in order to control the shape of TiO_2, they are selectively absorbed on the {001} surface, modifying the growth mechanism of the NPs. Whereupon it is reported a comprehensive experimental study at the molecular level of the evolution of interfacial/surface features of TiO_2 anatase nano-sheets with dominant {001} facets from the pristine fluorinated to the F^--free nanoparticles, obtained by calcination at 873 K. A

comparison with bipyramidal TiO_2 anatase nanoparticles highlights that the resulting reconstructed {001} surfaces are poorly hydroxylated, show a limited capability to adsorb water and expose Ti^{4+} sites with a weaker Lewis acidity than those on {101} ones. Conversely, by washing pristine fluorinated nano-sheets with a NaOH solution, it is possible to remove fluorine from the surface, obtaining highly hydroxylated {001} surfaces, as hydrophilic as the {101} ones. However, the nanoparticles remain doped with F^- in their bulk, which affects their electronic properties. Moreover, the three materials obtained (pristine, washed with NaOH and calcined) were characterized both by EPR spectroscopy and electrochemical methods in order to study the effect of the fluorides and of the calcination from an electronic point of view. In particular, it was assigned with high certaintly the signal due to Ti^{III} surface and bulk centres.

The second section is dedicated to the photocatalytic activity of shape controlled nanoparticles. The tests were carried on four selected materials: one material (named "bipy") that largely expose the {101} facets, and the three materials which expose mainly {001} facets (n-sh, n-sh_NaOH, n-sh_873K). The four considered materials were already characterized in the previous section. The photocatalytic tests were carried out both in gas-solid (nitric oxide, NO) and liquid-solid systems (phenol, melamine and formic acid). The substrates was chosen in order to study the behavior of the catalysts with different photocatalytic mechanisms. The results can be summarized as follow:

- for the NO degradation, that could be oxidized both by a direct hole transfer and an OH radical attack, the photo-activity order is bipy > n-sh_NaOH > n-sh > n-sh_873K; this is same order of hydrophilicity

obtained using spectroscopic methods (Figure 34 and Figure 35). This result suggests that the different surface hydrophilicity and Lewis acidity of the samples in dependence on the post-synthesis treatments have a strong impact on the resulting photocatalytic activity against NO;

- the same conclusions can be drawn for the photocatalytic degradation of phenol (in which OH radicals have a crucial role) carried out at unadjusted pH. The data highlight that the lower Lewis acidity of the Ti centers exposed by the reconstructed {001} surfaces and their lower affinity towards water result in an evident decrease of the photocatalytic performance with respect to the {101} facets. These evidences suggest that a higher affinity towards water can facilitate the hole transfer process, resulting in a more abundant formation of OH·-like species. Conversely, at acidic pH the highest increase of the activity was obtained for the calcined material, it seems to have a surface "passivation" induced by the thermal treatment that is eliminated at low pHs. Acidic pH values are, indeed, able to decrease the charge carrier recombination rate in the material;
- in the case of melamine, the photodegradation occurs with an indirect hole transfer (IHT) mechanism. Fluorides, reducing the carriers' recombination rate and acting as hole traps at the surface, increase the photodegradation of the melamine, which is not strongly absorbed at the TiO_2 surface. The highest activity is obtained for the bipyramidal nanoparticles; the material n-sh_873K presents again different behavior respect to the others, increasing

incredibly its activity at pH 3.5 due to the lower recombination rate at this pH value;

- formic acid, instead, is oxidized with a direct hole transfer (DHT) mechanism, in which it is absorbed at the TiO_2 surface. Fluorides hinder the surface absorption of the substrate, slightly reducing the photodegradation rate for the material n-sh respect to n-sh_NaOH. Once again the material bipy presents the highest photoactivity at unadjusted pH and the calcined sample improves drastically is photoactivity at acidic pH.

From the obtained results of the photocatalytic tests, it is possible to conclude that the material bipy, which presents the larger amount of {101} surfaces, is almost always the most active sample in the conditions and with the used substrates. This result is in contrast with many (not all) works so far seen in literature, in which is reported that materials that largely expose {001} surfaces present a superior photo-activity. This discrepancy can be rationalized looking at the rate of electrons transfer to oxygen for n-type catalyst. As said, under irradiation, in these semiconductors there is a net accumulation of electrons due to their lower transfer rate to the solution, in particular to the dissolved oxygen. The higher presence of the reductive {101} surface increases the oxygen reduction, in this manner the recombination rate of the charge carriers is reduced and the production of reactive species in solution is enhanced. Moreover, it must be taking into account the different synthetic strategies that were used for obtaining the TiO2 materials and the high impact that the post-synthesis treatment can have on the final TiO2 sample at molecular level. In particular, as seen, the post-synthesis treatment can

affect the photoactivity of a material depending on the degradation mechanism and the conditions of the experiments.

Finally, the selected materials were tested for the H_2 production in formic acid photoreforming under UV irradiation and using Pt as co-catalyst. The results show the high influence of the shape on the H_2 evolution, confirming the increase of the H_2 production rates with the increase of the {101} surfaces amount in the material, due to the reducing character of this facet. HR-TEM micrographs highlight that 2 nm Pt nanoparticles are deposited mainly on the {101} surfaces. Therefore, the possibility to tune the shape of TiO_2 NPs obtained in this PhD work, allows to improve the hydrogen production modulating the exposition of the surface {101}.

The main result of this doctoral thesis was to demonstrate the high importance of the shape and the surface properties of TiO_2 nanoparticles in several aspects of its chemistry in fields like photocatalysis and H_2 evolution. The results obtained in this work can be employed in order to improve the exploitation of TiO_2 nanoparticles in several fields that can vary from photocatalysis to other technological applications such as the fabrication of fuel cells, microelectronic circuits, sensors, coatings against corrosion and, of course, catalysts.

APPENDIX A

Below are reported TSEM micrographs of all the materials synthetize.

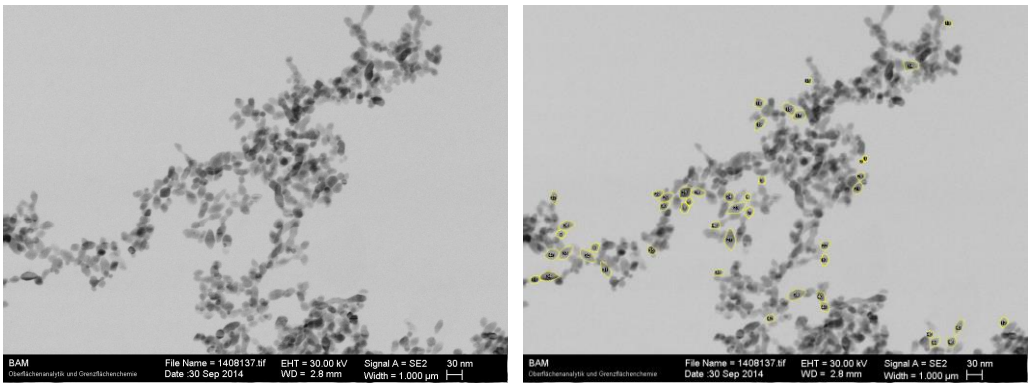

Figure Appendix A1. T-SEM images of sample HT01.

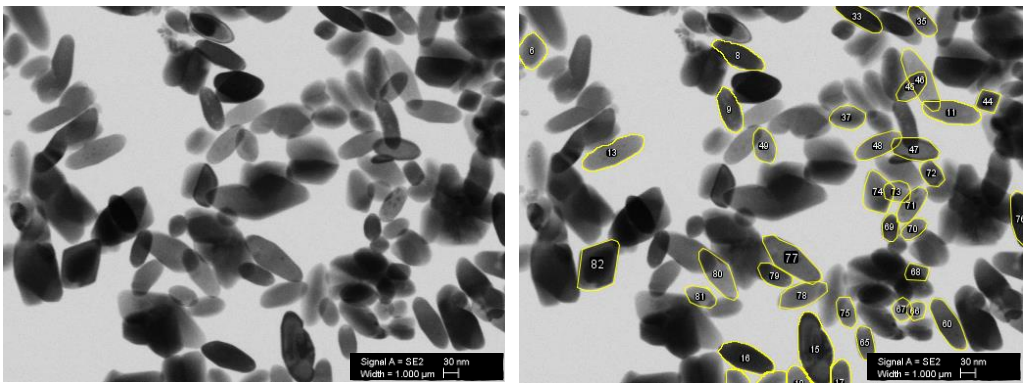

Figure Appendix A2. T-SEM images of sample HT02.

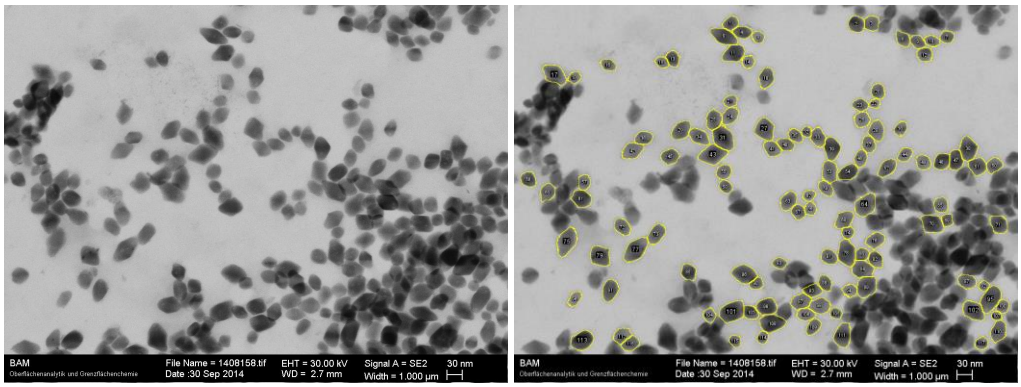

Figure Appendix A3. T-SEM images of sample HT03.

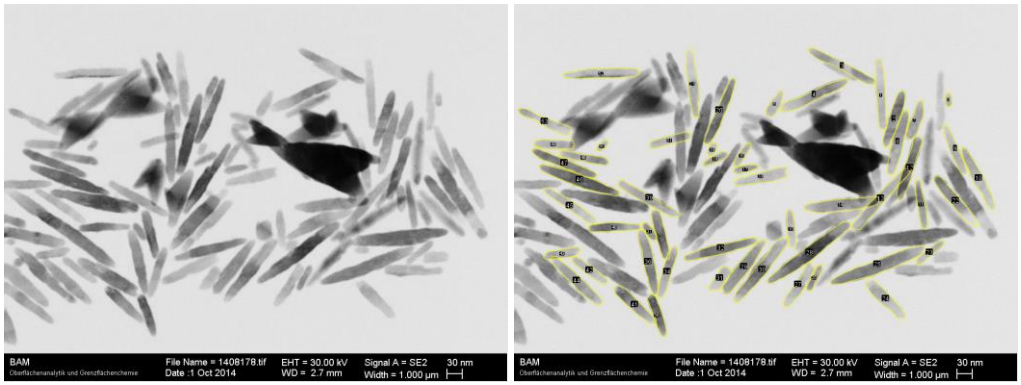

Figure Appendix A4. T-SEM images of sample HT04.

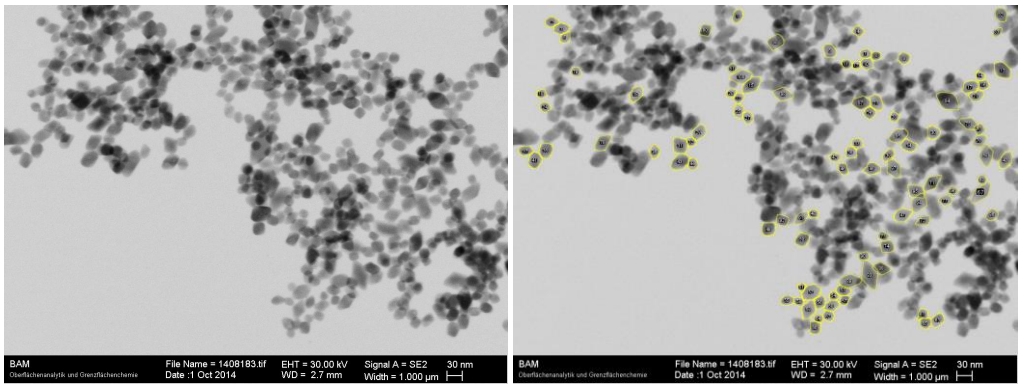

Figure Appendix A5. T-SEM images of sample HT05.

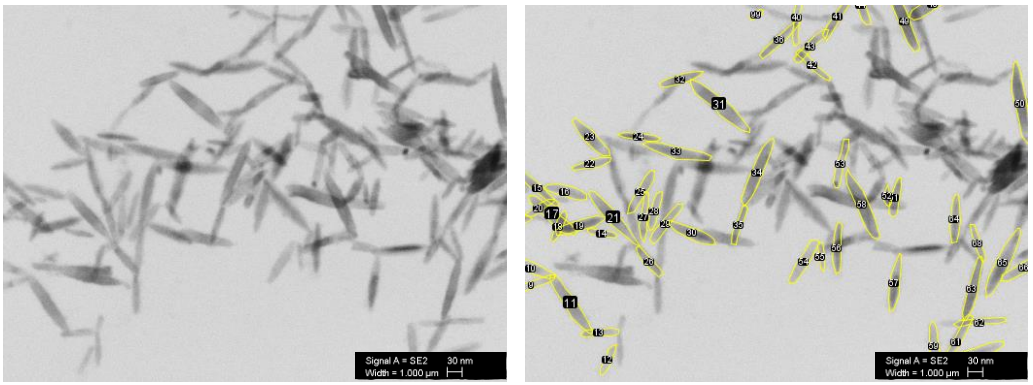

Figure Appendix A6. T-SEM images of sample HT06.

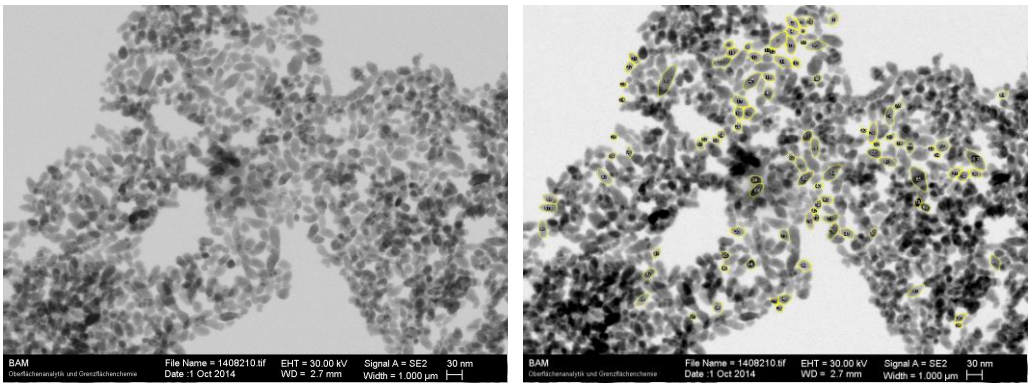

Figure Appendix A 7. T-SEM images of sample HT07.

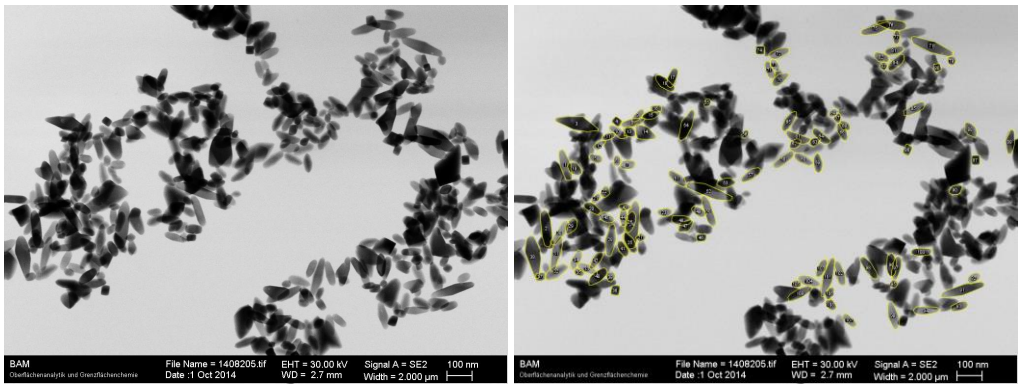

Figure Appendix A 8. T-SEM images of sample HT08.

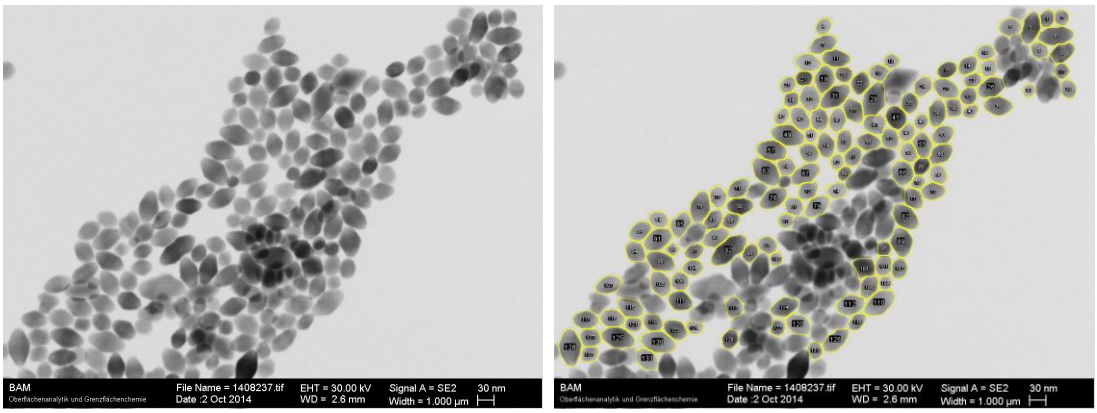

Figure Appendix A 9. T-SEM images of sample HT09.

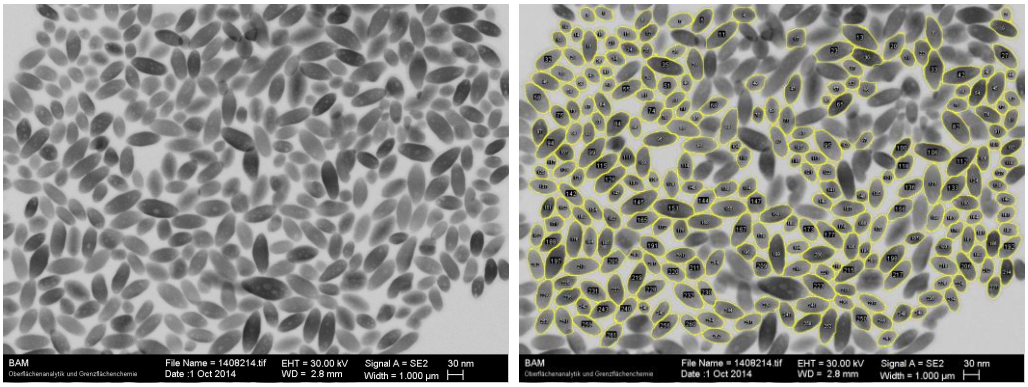

Figure Appendix A10. T-SEM images of sample HT10.

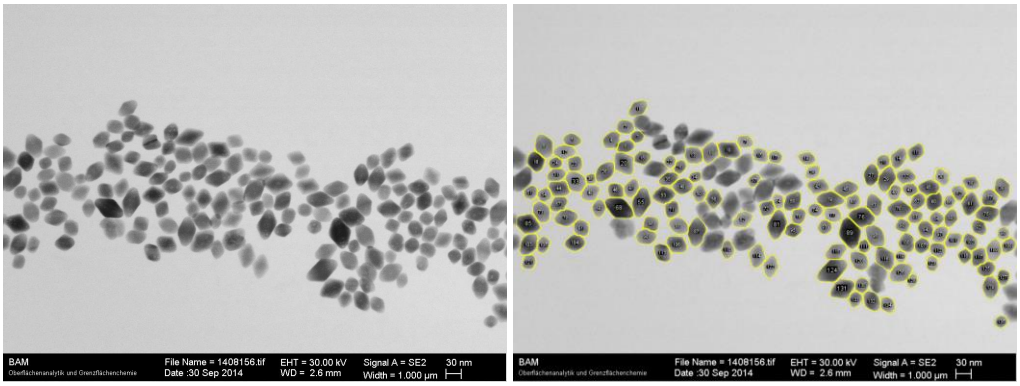

Figure Appendix A11. T-SEM images of sample HT11.

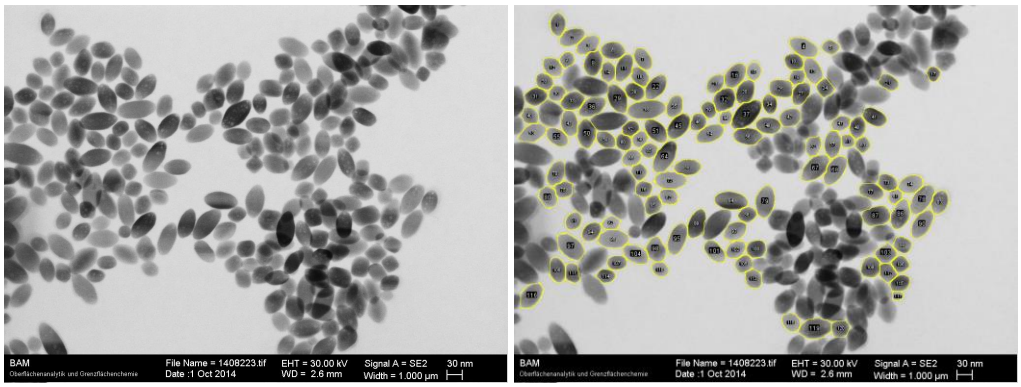

Figure Appendix A12. T-SEM images of sample HT12.

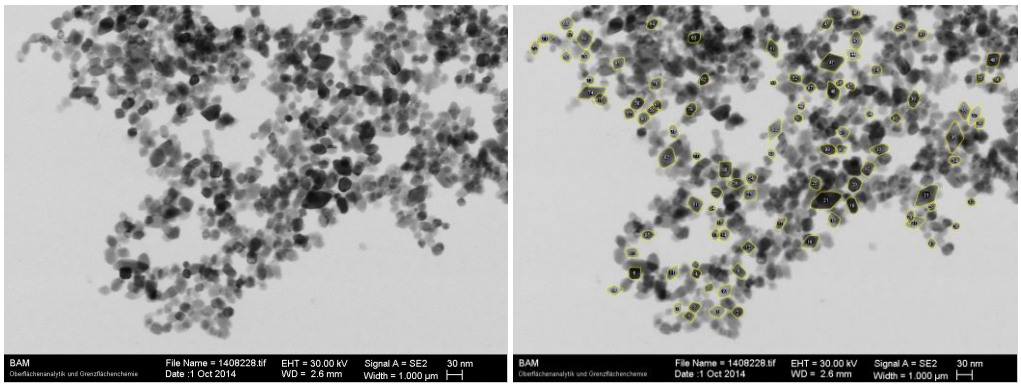

Figure Appendix A13. T-SEM images of sample HT13.

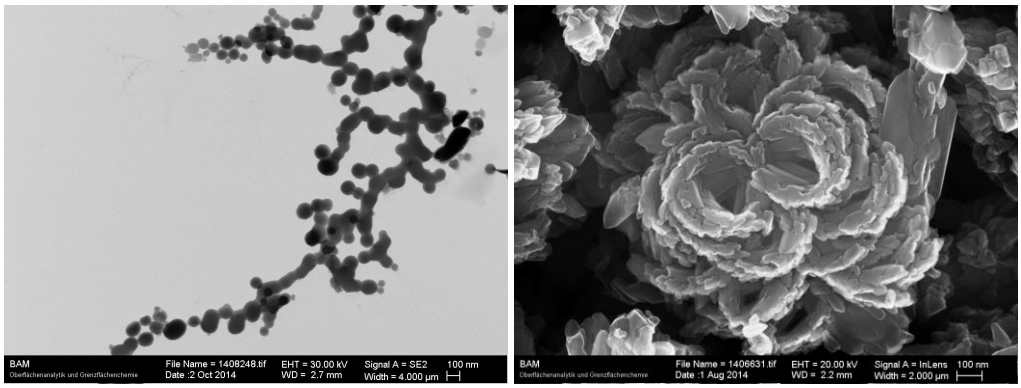

Figure Appendix A14. T-SEM images of sample HT14.

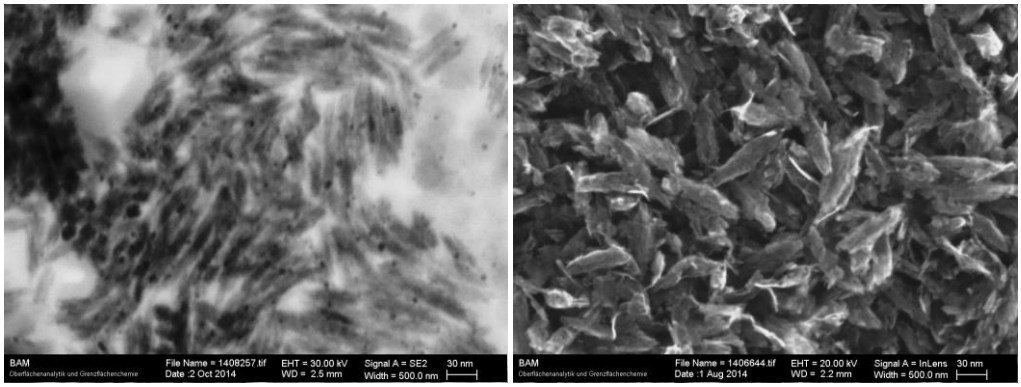

Figure Appendix A15. T-SEM images of sample HT15.

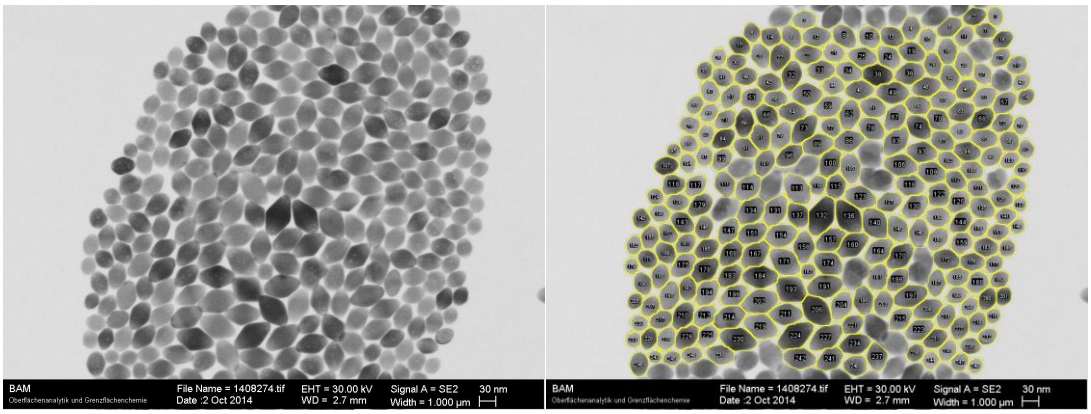

Figure Appendix A16. T-SEM images of sample HT16.

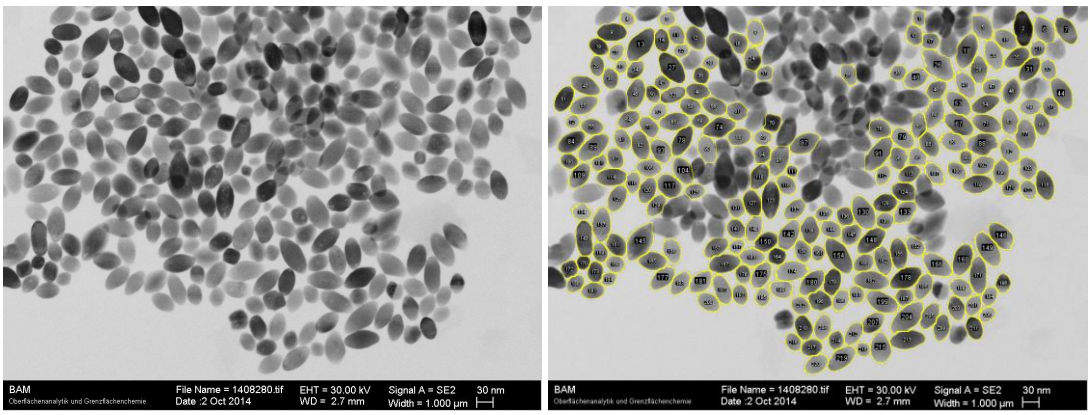

Figure Appendix A17. T-SEM images of sample HT17.

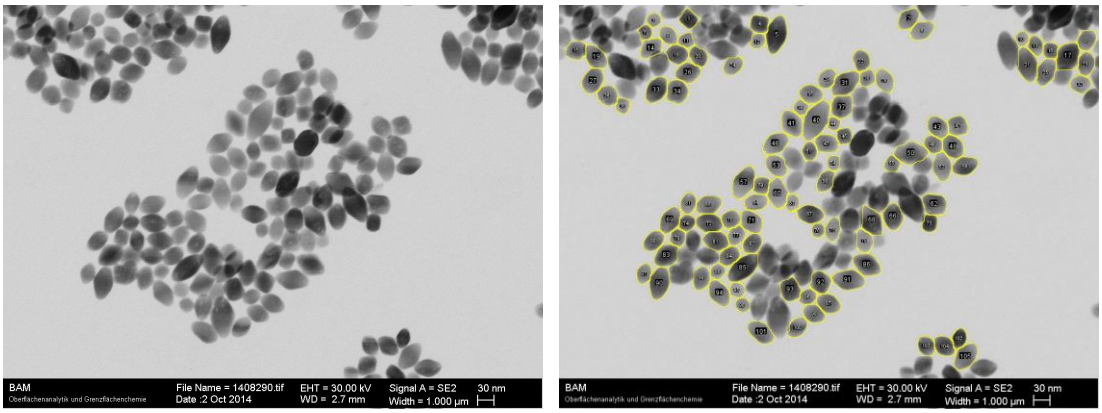

Figure Appendix A18. T-SEM images of sample HT18.

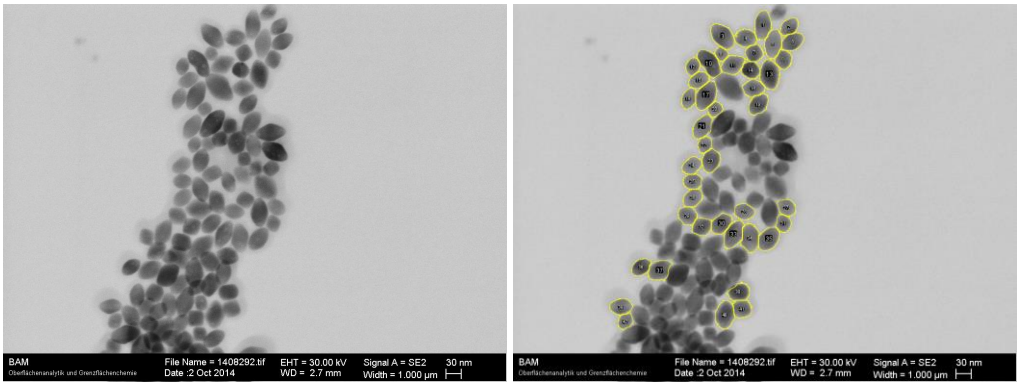

Figure Appendix A19. T-SEM images of sample HT19.

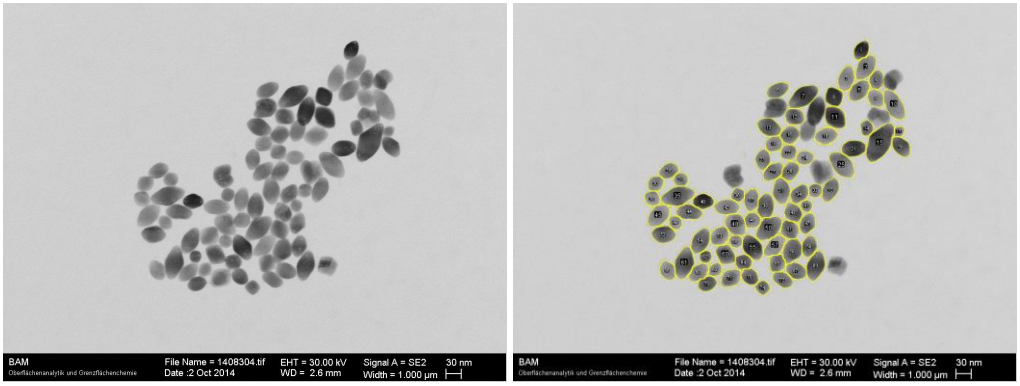

Figure Appendix A20. T-SEM images of sample HT20.

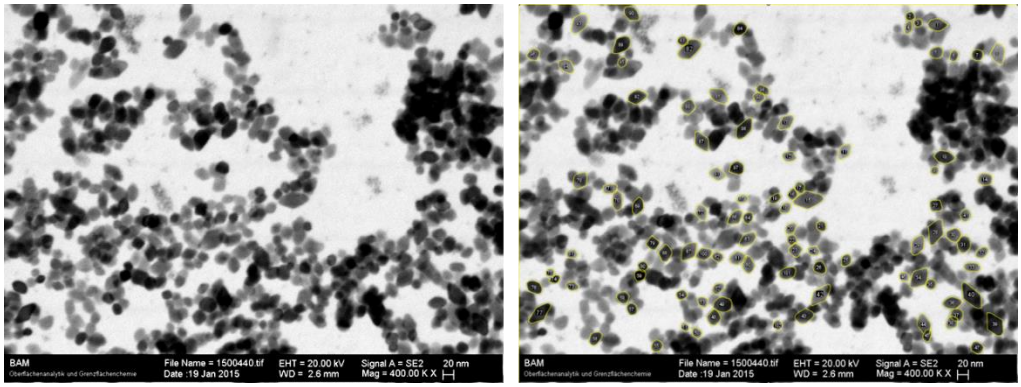

Figure Appendix A21. T-SEM images of sample HT_VAL_01.

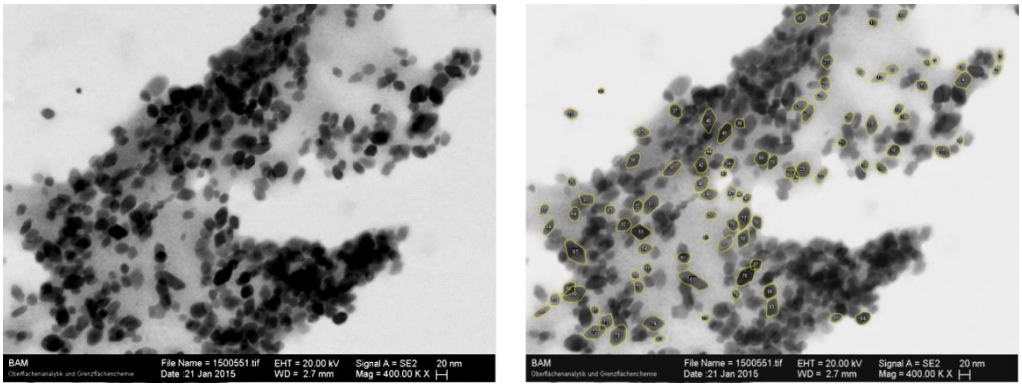

Figure Appendix A22. T-SEM images of sample HT_VAL_02.

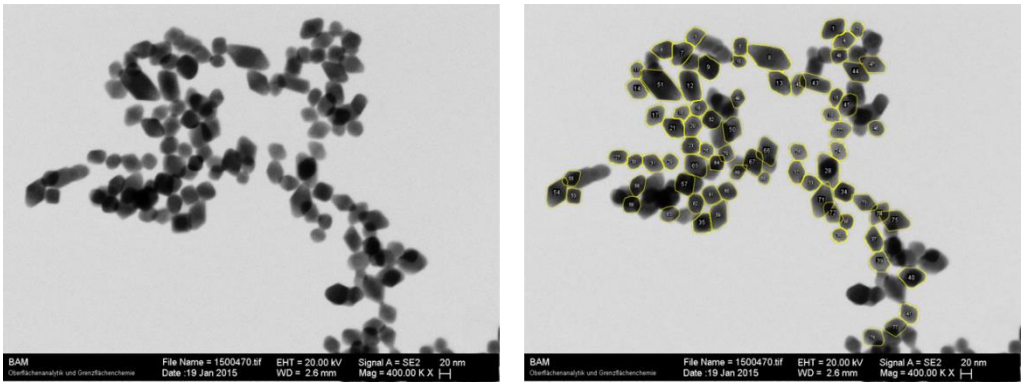

Figure Appendix A23. T-SEM images of sample HT_VAL_03.

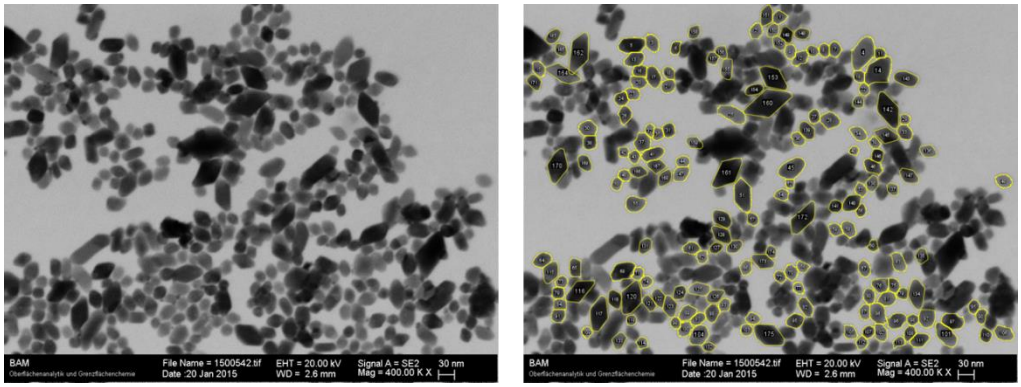

Figure Appendix A24. T-SEM images of sample HT_VAL_04.

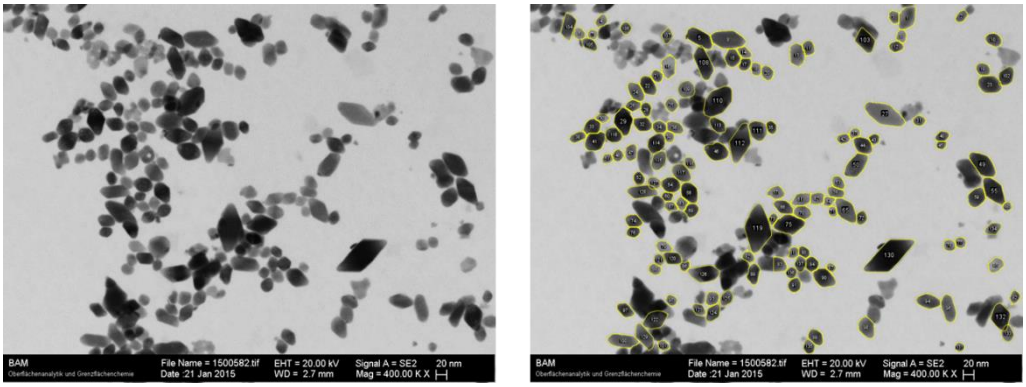

Figure Appendix A25. T-SEM images of sample HT_VAL_05.

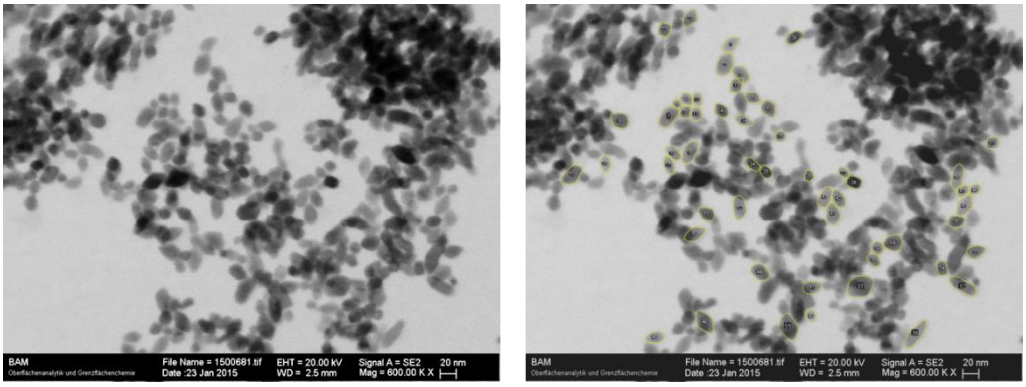

Figure Appendix A26. T-SEM images of sample HT_VAL_06.

APPENDIX B

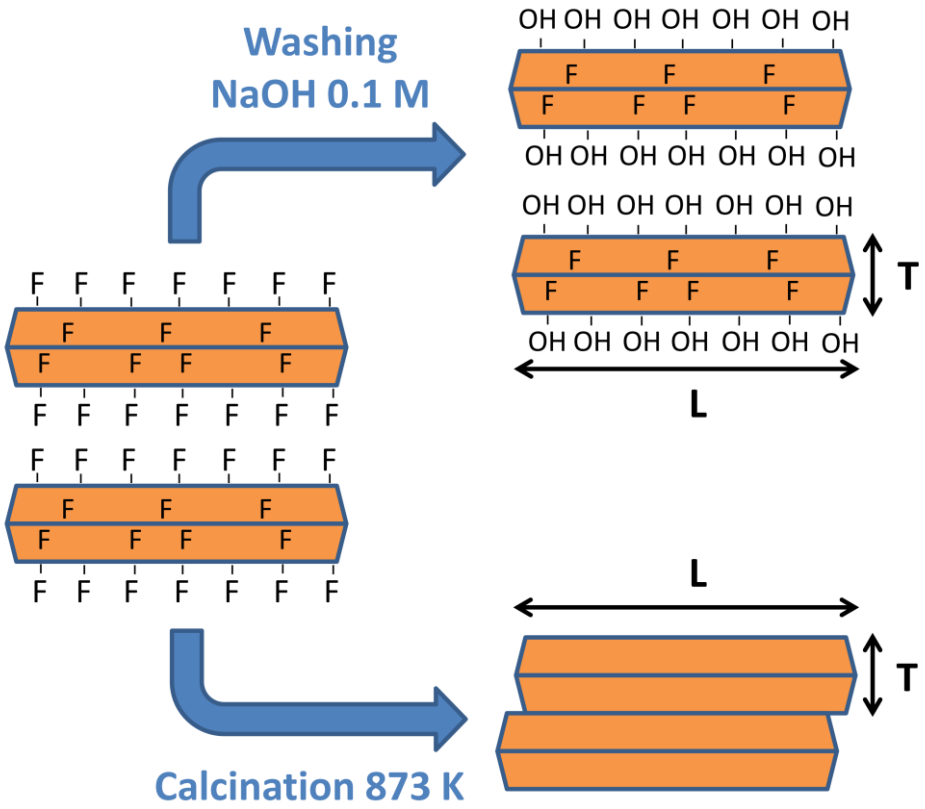

Figure Appendix B1. Schematic representation of the effect of the treatments performed to remove fluorides from the as-synthesized TiO_2 n-sh. T and L are the thickness and length of the NPs determined by electron microscopy (see Table 11).

To calculate the expected specific surface area (SSA_e) and percentage of exposed {001} surfaces, we built a geometric model using the electron microscopy dimensional data (see Table 11). The formulas employed in the calculations are reported in the following:

$$l_{101} = \frac{T}{2sin\alpha}$$

$$l_{001} = L - 2l_{101}cos\alpha$$

$$A_{tot} = 2{l_{001}}^2 + 2\left[\frac{(4L + 4l_{001}) * l_{101}}{2}\right]$$

$$V_{tot} = \frac{1}{3}\frac{T}{2}\left(L^2 + {l_{001}}^2 + \sqrt{L * l_{001}}\right) * 2$$

$$SSA_e = A_{tot} * \frac{1}{\rho * V_{tot}}$$

where ρ is the TiO_2 density and the other symbols are reported in Figure Appendix B2.

The result of the calculation is SSA_e = 66 m^2/g for the TiO_2 n-sh sample.

For the TiO_2 n-sh_873K sample we considered a model in which couples of NPs share one (001) facet (see Figure Appendix B1) and therefore we employed a modified formula to calculate the total exposed surface area for a pair of sintered NPs:

$$A_{tot} = 2{l_{001}}^2 + 4\left[\frac{(4L + 4l_{001}) * l_{101}}{2}\right]$$

In this case the result of the calculation is SSA_e = 41 m^2/g. The trend is in excellent agreement with the experimental SSA_{BET} data (see Table 11) and confirms the XRD data which suggest that the primary NPs could have sintered in pairs.

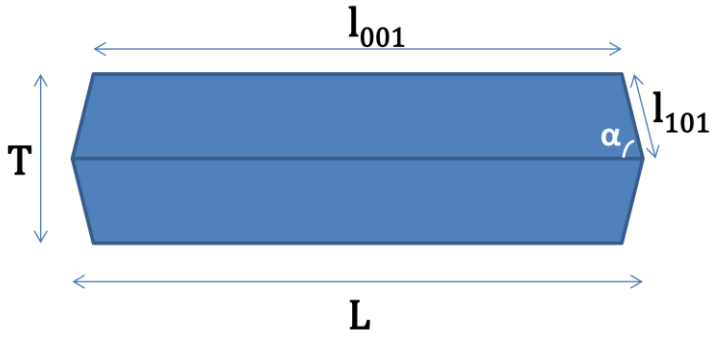

Figure Appendix B1. Schematic representation of the geometrical model employed to calculate the expected specific surface area (SSA_e) and percentage of exposed {001} surfaces.

APPENDIX C

IC

In order to evaluate the total amount of fluorides a complete mineralization in microwave was performed heating the samples for 90 min at 473 K under vigorous stirring in NaOH 10 M. After the treatment a dilution 1:10 of the solution was analyzed by Ionic Chromatography (IC). The instrument (DIONEX DX 500) is equipped with a GP40 pump, AS9-HC column (Dionex, length 25 cm and internal diameter of 4 mm), Suppressor ASRS-Ultra II autosuppression mode, electrochemical detection system ED40, LC30 column thermostat (temperature 303 K). The mobile phase consists of 9 mM K_2CO_3 and the eluent flow is equal to 1 mL min^{-1}.

SEM/EDX

For SEM and EDX sand paper Al holders were used, then they were cleaned by sonication in ethanol and subsequently sample powder was pressed on the Al holder with spatula. SEM images and EDX spectra have been collected with a Zeiss Supra 40 (Carl Zeiss, Oberkochen, Germany), equipped with a Schottky field emitter and having attached a silicon drift detector energy dispersive X-ray spectrometer (SDD-EDS) from Thermo Fisher Scientific (Thermo Fisher Scientific Inc., Waltham, MA, USA, energy resolution at Mn Kα of 128 eV and 100 mm2 crystal active area). SEM images were acquired with an accelerating voltage of 10 kV for all samples.

Energy dispersive X-ray spectroscopy has been applied on microscopic (500 µm x 500 µm) sample areas defined on scanning electron micrographs. The

information depth associated to the X-ray signals reaches typically the sub-micrometer range. F K X-ray line was detected only in the samples n-sh and n-sh_NaOH at a comparable intensity level. Similar to the AES analysis, the other two samples n-sh_873K and bipy have provided only 'noise' signals. The limit of detections of electron probe microanalysis are in the range of 0.1 mass-%. The quantification of the X-ray signals detected cannot be applied accurately due to the strong sample morphology at the sub-micrometer scale.

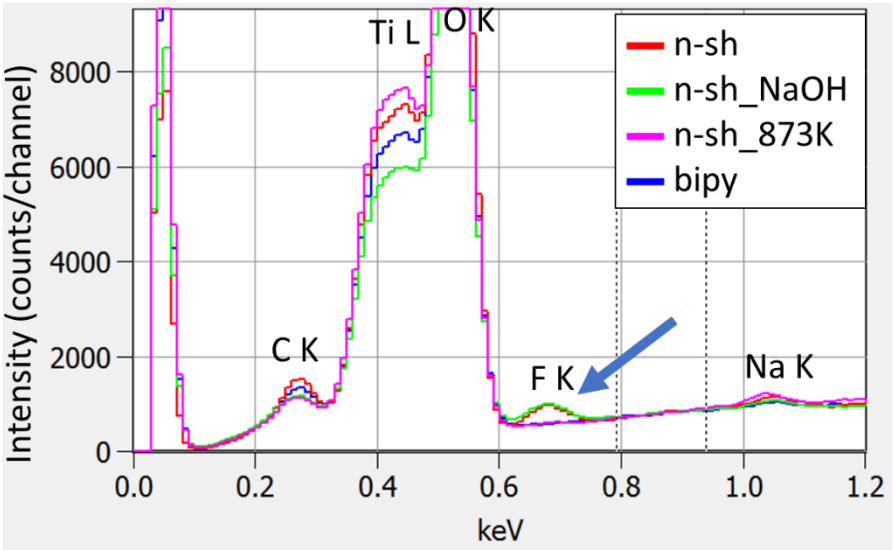

Figure Appendix C1. 10 kV EDX spectra of the samples n-sh, n-sh_NaOH, n-sh_873K and bipy (measured over a 500 µm by 500 µm area of the nanoparticulate material prepared on silicon wafer as a substrate). The spectra have been normalized to the background signal between 0.79 and 0.95 keV.

Auger electron spectroscopy

The powder was deposited on a cleaned Si-wafer (sonicated in isopropanol) by slightly pressing the powder with a spatula on the wafer surface. AES analysis was carried out with a PHI 700 Auger Scanning Probe (ULVAC-PHI Inc.) equipped with a coaxial cylindrical mirror analyzer. Auger electrons spectra were excited by a primary electron beam at different locations on the sample surface. To evaluate the presence of Fluorine on the TiO2 NPs surface, AES survey spectra as well as window spectra (5 keV, 20 nA and 20 keV, 1 nA) of energy region corresponding to F KLL were recorded.

Auger electron spectroscopy (AES) has been applied in order to take advantage of both excellent lateral resolution of the Auger probe (in the range of 10 nm) as well as of the information depth (about 3-4 nm). Hence, areas significantly smaller than that of individual TiO_2 nano-sheets could be analyzed. Figure S6 shows two examples of AES analysis where individual nano-sheets of the samples n-sh and n-sh_873K have been inspected. Note the distinct Auger signal detected on the n-sh sample. Under the same analysis conditions, the calcined sample does not show any F KLL signal. It should be noticed that the limits of detection of AES are in the range of sub-percent, so that any presence of fluorine at ultra-trace level cannot be detected.

In general, a level of fluorine similar to that in the sample n-sh has been detected in n-sh_NaOH sample. The quantification of the Auger signals into absolute concentrations constitutes a challenging task. Particularly for the TiO_2 nano-sheets as in the present study, the strong sample morphology at the nanometer scale makes the reliability of quantification very poor, so

that direct comparison of spectra taken under same experimental conditions remains a means for reliable semi-quantitative evaluation. Further, the 'noise' level of fluorine as detected for the n-sh_873K sample, indicating the removal of fluorine from the 3-4 nm depth sampled by AES, has been confirmed by measurements on the bipy sample, also showing no F KLL signal.

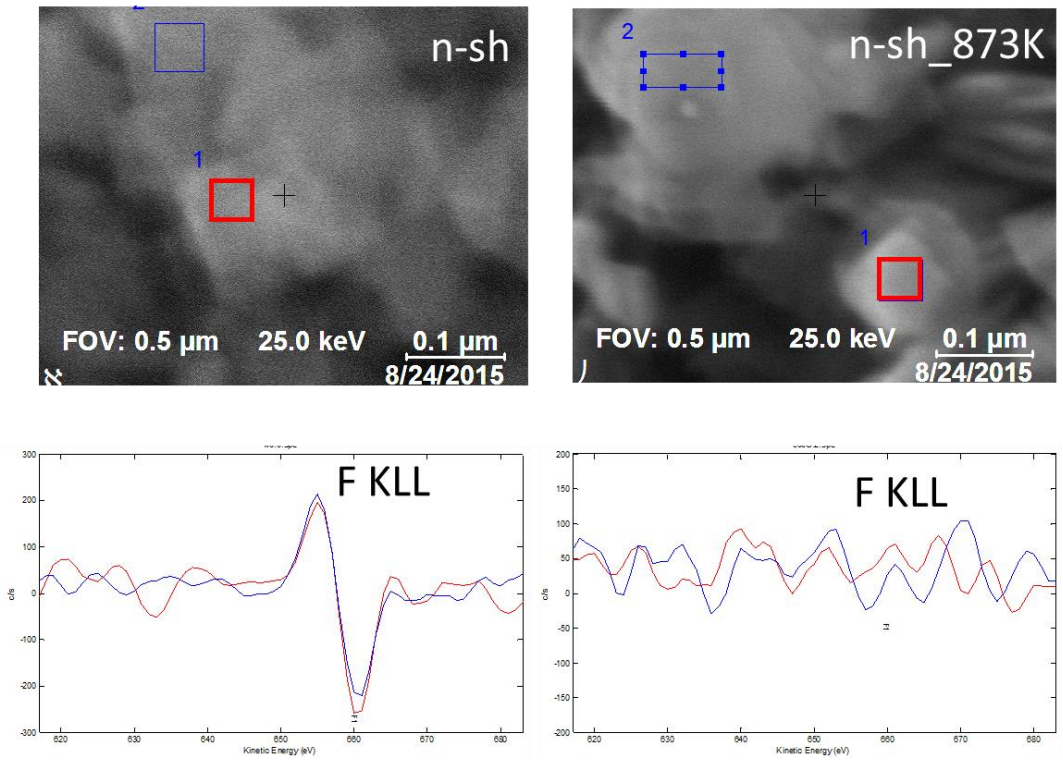

Figure Appendix C2. 25 kV Auger electron spectra of the samples n-sh and n-sh_873K (measured over a 400 nm by 400 nm area on two nano-sheets, respectively). Due to the poor (typically) signal-to-background Auger peaks, the Auger spectra have been differentiated.

ToF-SIMS

Samples were prepared on silver foil as well as on silicon wafers by slightly pressing the powder with a spatula on the wafer surface. The substrates were cleaned by sonication in isopropanol prior to sample deposition. ToF-SIMS measurements were performed on a ToF-SIMS IV instrument (ION-TOF GmbH, Münster, Germany) of the reflectron type, equipped with a 25 keV bismuth liquid metal ion gun as a primary ion source.

The highest elemental sensitivity of all analytical methods employed in the present study is offered by ToF-SIMS (time-of-flight secondary ion mass spectrometry). Elements present in the outermost 1 nm at the sample surface can be detected at the ppm (sometimes even ppb) level. The strong matrix effects are well-known to hamper seriously an accurate SIMS quantification. Similar to the other analytical techniques, in order to be able to compare the results obtained for different samples at least in a semi-quantitative manner, normalization to a signal of an internal element and/or relation to reference materials measured under the same conditions are necessary. Figure Appendix C3 shows the peak of the negative fluorine ion as detected in the samples n-sh and n-sh_873K after normalization to the TiO_2 signal from each ToF-SIMS spectrum acquired at different 9 locations on each sample. Note the clear difference by a factor of about 20 between the F intensity corresponding to sample n-sh and the n-sh_873K sample. As resumed in Table 12, sample n-sh_NaOH provides a significantly lower signal of F^-. Further, the low level of F^- found in sample n-sh_NaOH is comparable to the level of F^- detected in the sample bipy, but also in the fluorine-free silicon substrate. Hence, the conclusion drawn is that this fluorine level is sample independent and shows the limits of

detection of the ToF-SIMS instrument used in the conditions given as a rest level. Note that all the other analytical techniques IC, EDX, and AES could not detect presence of fluorine in both samples n-sh_873K and the reference bipy.

The reproducibility of the ToF-SIMS results has been confirmed by measurements carried out at different times and by preparing the samples on alternative substrates (e.g. silver foils).

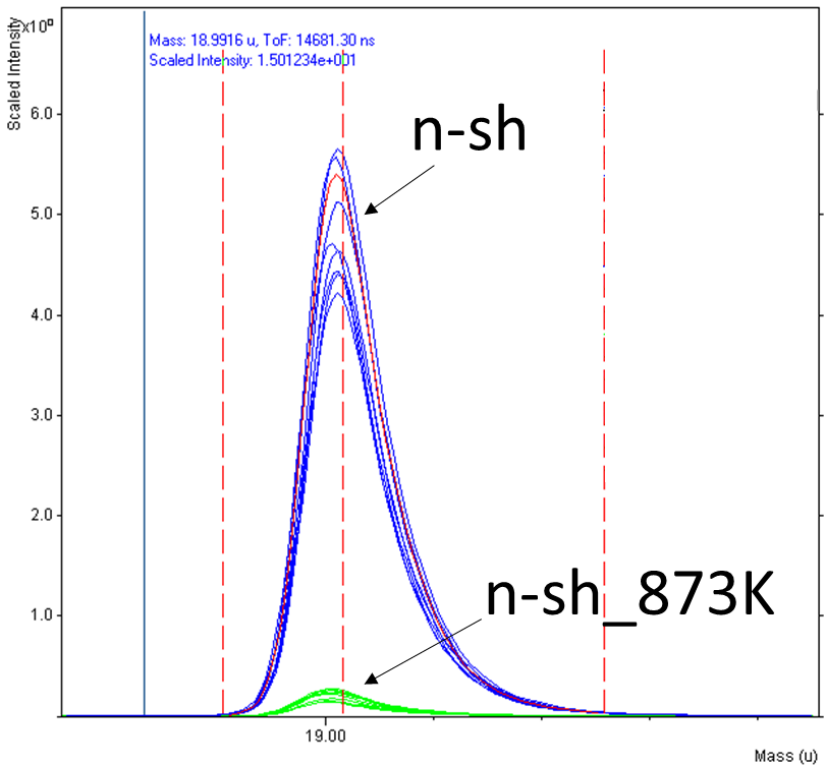

Figure Appendix C3. Fluorine signal in the ToF-SIMS spectra of the samples n-sh (blue) and n-sh_873K (green) measured over a 100 µm x 100 µm area at nine different locations on each sample prepared on a silicon substrate. For comparison purpose, the F signal (recorded in a window around 18.9916 a.m.u.) has been normalized to the TiO_2 signal at 79.9374 a.m.u.

Acknowledgements

I would like to express my sincere gratitude to my supervisor Prof. Valter Maurino for the advices and support.

A huge THANK YOU to Letizia who taught me life in the laboratory. Her knowledge, precision and meticulousness were a great example for me.

Thanks to Fabrizio (thanks a thousand times!!) and Marco, their knowledge and their advice have been of fundamental importance in these three years.

Thanks to Prof. Martra and Dr. Mino for the helpful discussions related to the phisico-chemical characteristics of the nanoparticles.

Thanks to Dr. Hodoroaba from BAM (Berlin) for the SEM/T-SEM characterization of the nanoparticles and the continuous and fruitful collaboration.

I am grateful to Prof. Isopescu and Prof. Lavric from Polytechnic University of Bucharest for the great help with the experimental design and the develop of the soft model.

Thanks to Prof. Chiesa and Dr. Morra for the EPR investigation of the TiO_2 nanosheets.

Finally, a special thanks to my colleagues and friends "organics": Stefano (thanks a thousand times!!), Emanuele and Annamaria, for fun and educational lunches.